MEASUREMENT, MODELING AND MITIGATION OF INSTABILITIES AND MALDISTRIBUTION IN MICROCHANNEL CONDENSERS

A Dissertation
Presented to
The Academic Faculty

by

Allison Jasmine Mahvi

In Partial Fulfillment
of the Requirements for the Degree
Doctor of Philosophy in the
Woodruff School of Mechanical Engineering

Georgia Institute of Technology
December 2018

MEASUREMENT, MODELING AND MITIGATION OF INSTABILITIES AND MALDISTRIBUTION IN MICROCHANNEL CONDENSERS

Approved by:

Dr. Srinivas Garimella, Advisor
G.W.W. School of Mechanical Engineering
Georgia Institute of Technology

Dr. S. Mostafa Ghiaasiaan
G.W.W. School of Mechanical Engineering
Georgia Institute of Technology

Dr. Samuel Graham
G.W.W. School of Mechanical Engineering
Georgia Institute of Technology

Dr. Gregory Nellis
Department of Mechanical Engineering
University of Wisconsin - Madison

Dr. Asegun Henry
Department of Mechanical Engineering
Massachusetts Institute of Technology

Date Approved: [September 15, 2018]

To my husband, Eric

ACKNOWLEDGEMENTS

First and foremost, I would like to thank my advisor, Dr. Srinivas Garimella, for his guidance throughout my PhD. His advice and insights will be invaluable to me throughout the rest of my career. Additionally, I would like to thank all the past and present members of the Sustainable Thermal Systems Lab who have provided both technical assistance and moral support throughout my time at Georgia Tech. In particular, I would like to express my appreciation to Jeff Milkie, Brian Fronk, Alex Rattner, David Forinash, and Bachir El Fil for helping me define and reach the goals of my project.

Finally, I would like to thank my family – especially Chris, David, Sasha, Jonathan and Eric. They have fostered my interests and supported the paths I have chosen throughout my life. Without them, I certainly would not be where I am today.

TABLE OF CONTENTS

LIST OF TABLES

LIST OF FIGURES

LIST OF SYMBOLS AND ABBREVIATIONS

A	area [m^2]
AAD	absolute average deviation [%]
Br	Brinkman Number ($\mu u^2/k\Delta T$) [-]
$\dot{C}$	capacitance rate [W kg K^{-1}]
c_p	specific heat [J kg^{-1} K^{-1}]
D	diameter [mm]
d	Depth [mm]
F	fraction [-]
f	friction factor [-]
Fr	Froude number [-]
Fr^*	Modified Froude number [-]
G	mass flux [kg m^{-2} s^{-1}]
g	gravitational acceleration (9.81) [m s^{-2}]
h	enthalpy [J kg^{-1}]
H	height [mm]
$H(t)$	Heavyside function [-]
htc	heat transfer coefficient [W m^{-2} K^{-1}]
j_l	superficial liquid velocity ($G_{in}(1-x)/\rho_l$) [m s^{-1}]
j_g	superficial gas velocity ($G_{in}x/\rho_v$) [m s^{-1}]
JC	jet-correction [-]
K	loss coefficient [-]
k	thermal conductivity [W m^{-1} K^{-1}]
L	length [mm]

LMTD	log mean temperature difference [^{o}C]
M	Mass [kg]
$\dot{m}$	mass flow rate [kg s^{-1}]
MC	momentum-correction [-]
n	number of data points [-]
N_{ch}	number of channels [-]
NSTD	normalized standard deviation [-]
P	pressure [kPa]
Pe	Peclet number ($L\bar{u}/\alpha$) [-]
Pitch	outlet channel pitch [mm]
$\dot{Q}$	heat transfer rate [W]
$\dot{Q}_o''$	heat flux [W m^{-2}]
R	thermal resistance [K W^{-1}]
r	radius [m] or radial direction [m]
Re	Reynolds number [-]
s	dimensionless Laplace parameter [-]
std	sample standard deviation [s]
t	time [s]
T	temperature [^{o}C]
th	thickness [mm]
TOF	time of flight [s]
u	velocity [m s^{-1}]
U	uncertainty
UA	heat exchanger conductance [W K^{-1}]

$\dot{V}$ volumetric flow rate [mL min^{-1}]

W width [mm]

We Weber number [-]

x quality [-] or axial direction [m]

X Eigenfunction [-]

z axial position [m]

Greek Symbols

α void fraction [-]

β eigenvalue [-]

γ arbitrary measured variable [-]

δ Dirac delta function [-]

δ_l $\dot{m}_{l,ch}[i]/\dot{m}_{l,header}[i]$ [-]

$\delta_{baseline}$ baseline prediction for δ_l [-]

ΔP pressure drop [Pa]

ΔT temperature difference [K]

ε thermal emissivity [-]

θ^* normalized temperature difference [K]

κ thermal diffusivity [m^2 s^{-1}]

λ unknown function to characterize Gaussian position [-]

μ dynamic viscosity [kg m^{-1} s^{-1}]

ρ density [kg m^{-3}]

σ Stephan-Boltzmann constant (5.67×10^{-8}) [W m^{-2} K^{-4}]

ϕ two-phase multiplier [-]

φ unknown function in correlation development [-]

χ	unknown function to characterize Gaussian height [-]
ω	unknown function to characterize Gaussian width [-]

Superscripts

*	normalized variable

Subscripts

adi	adiabatic
amb	ambient
amb-w	ambient to water
assb	assembly
base	base temperature
ch	outlet channel
ch/tube	Number of channels in multiport tube
chiller	chiller setpoint
cond	condensation
cs	cross section
decel	deceleration
dist	distributed
ΔP	pressure drop
down	downstream
eff	length of heater assembly before measurement ports
exit	exit
exp	expected
feed	feeder tube

fric	frictional
g	gas
grav	gravitational
H	hydraulic
h	heater
header	header
HT	heat transfer
i	channel number or node number
in	at inlet or internal
ins	insulation
int	intermediate
∞	far from source
j	specifies phase (l, v, or g)
l	liquid
lat	latent
ld	liquid depth
lo	liquid only
local	at a specific axial position (z)
loss	loss to ambient
m	manifold
max	maximum
meas	measured
mix	mixture
NC	natural convection
off	when the heater is turned off

op	orifice plate (at channel entrances)
orifice	nozzle orifice
out	at outlet or outer
peak	peak temperature
pred	predicted
preh	preheater
prot	protrusion
r	radial
rad	radiation
rect	rectangular header
ref	refrigerant
ref-w	refrigerant to water
s	surface
sat	saturation condition
seg	segment
sens	sensible
surr	surroundings
tap	pressure tap
total	through full facility
tri	triangular header
TP	two-phase
TS	test section
tube	tube (for flat tubes with several flow channels)
up	upstream
v	vapor

w	water
wall	wall
wavy	stratified wavy – intermittent/annular transition
x	axial direction
0	initial

SUMMARY

Mini- and microchannel heat exchangers have the potential to drastically decrease the size and cost of energy systems, but they often underperform because of flow maldistribution. Maldistribution can be particularly acute when a two-phase mixture enters a heat exchanger header, which is difficult to address because the flow phenomena in these situations are poorly understood. In the present study, flow distribution in mini- and microchannel heat exchanger manifolds is investigated. The work focuses on two-phase flow regimes and distribution characteristics of air-water mixtures and saturated refrigerants in plate-type heat exchanger headers. The results quantify the effects of inlet mass flux, inlet quality, header flow regime and header pressure drop on distribution. Additionally, several header geometries are investigated to identify pathways to mitigate maldistribution in heat exchangers.

A comprehensive study on the distribution of air-water mixtures and saturated refrigerants in multi-channel heat exchangers was conducted. The heat exchangers considered here contain vertical parallel minichannels connected to a common horizontal header with a rectangular cross section. The header geometries are based on those commonly seen in plate-type heat exchangers. In this study, fluid flowed through the parallel channels in the direction of gravity (downward). Distribution experiments were conducted on air-water mixtures with varying inlet mass fluxes ($2.60 < G_{in} < 200$ kg m^{-2} s^{-1}), inlet qualities ($0.05 < x_{in} < 0.35$), outlet channel diameters ($1 < D_{ch} < 3$ mm), and header geometries (rectangular and triangular). Experiments on the distribution of saturated refrigerants were conducted for multiple inlet mass fluxes ($23.9 < G_{in} < 95.7$ kg m^{-2} s^{-1}),

inlet qualities ($0.10 < x_{in} < 0.90$), and header geometries (rectangular, triangular, and vane) for ten parallel 1-mm diameter channels functioning as a counterflow water-cooled heat exchanger.

Using insights from the experimental work, a modeling framework is developed for predicting the distribution of saturated refrigerants in horizontal plate-type heat exchanger headers. The proposed approach considers the effects of the path pressure drop (predicted using a detailed heat transfer and pressure drop model of the heat exchanger) and the header flow regimes to calculate the liquid and vapor flow rates into each channel. The resulting model predicts both the magnitudes and trends of the channel flow rates for the conditions tested.

The findings of this study advance the understanding of two-phase flow distribution in heat exchangers. This understanding will facilitate future development of low pressure drop methods to evenly distribute both the liquid and vapor in manifolds. Mitigating flow maldistribution in mini and microchannel heat exchangers can help enable the development of extremely compact, cost effective heat exchangers for a variety of power production, heating, and/or cooling systems.

CHAPTER 1. INTRODUCTION

Mini- and microchannel heat and mass exchangers have been proposed for many applications, including electronics cooling, compact refrigeration systems, and industrial processing equipment. Interest in small-diameter channels for heat transfer applications has been driven by the high heat transfer coefficients that are achievable in these geometries ($htc \propto D_{ch}^{-1}$). Increasing the heat transfer coefficient reduces the size and cost of heat exchangers and allows for the development of extremely compact and efficient energy conversion systems for power production, heating and/or cooling. Such systems will be critical in the future as the available energy resources decrease and the environmental externalities associated with traditional fossil fuel sources starts to have a larger societal impact.

Although small-diameter channels can improve transport in heat and mass transfer components, reducing the flow area increases the frictional pressure drop. To maintain reasonable pressure losses across the component, microchannel heat exchangers usually split the flow into many parallel flow paths. Ideally, multi-channel heat exchangers should be designed so that the fluid is equally distributed to all the channels by an inlet header (also called a manifold). However, many researchers have found that the flow can be maldistributed in multi-channel heat exchangers (Vist and Pettersen, 2004; Tong *et al.*, 2009; Tuo and Hrnjak, 2013), which can significantly degrade their performance (Kærn *et al.*, 2011; Nielsen *et al.*, 2012; Forinash, 2015). There has been progress over the past several decades on the development of effective header designs to mitigate maldistribution in heat exchangers, especially for single-phase flows (Bassiouny and Martin, 1984; Habib

et al., 2008; Jones *et al.*, 2008; Dharaiya *et al.*, 2009; Said *et al.*, 2015; Anbumeenakshi and Thansekhar, 2016). Unfortunately, the design methodology used for single-phase flows cannot be applied when the component has a two-phase inlet condition because the flow characteristics inside the header are significantly more complex (Webb and Chung, 2005). Additionally, maldistribution is often more severe when gas-liquid mixtures enter a header. For example, many authors have reported cases where some heat exchanger channels only receive liquid and others only receive vapor from the inlet manifold (Marchitto *et al.*, 2008; Ahmad *et al.*, 2009; Dario *et al.*, 2015; Mahvi and Garimella, 2017). In evaporators and condensers, poor distribution can lead to localized dry-out and non-uniform heat transfer rates across the component. In absorbers and desorbers, the effects of maldistribution are even more acute because it decreases the interfacial area and interaction between the two fluids, thereby reducing the mass transfer between them.

Several researchers have conducted experimental and numerical studies to examine the effects of operating conditions, fluid properties, and geometric parameters on two-phase flow distribution. Although this work offers some insight into the driving forces involved in distribution, there are discrepancies in the reported trends even in simple header geometries (Vist and Pettersen, 2004; Hwang *et al.*, 2007). Additionally, many authors have studied modified header designs that aim to improve the distribution of liquid-vapor flows. One approach to improving distribution is to force the fluid to be more homogeneous in the header. This is typically accomplished by adding an expansion device at the inlet. Although expansion devices have been shown to improve distribution (Fei and Hrnjak, 2004; Vist and Pettersen, 2004; Ahmad *et al.*, 2009), the additional pressure drop across the device is usually not reported. Another common approach to improving distribution is

to modify the header geometry by adding baffles (Fei and Hrnjak, 2004), allowing the outlet channels to protrude into the header (Lee and Lee, 2004; Kim and Han, 2008; Zou and Hrnjak, 2013) or changing from a rectangular to a triangular or tapered manifold (Dharaiya *et al.*, 2009; Manikanda Kumaran *et al.*, 2013; Mahvi and Garimella, 2017). Some of these studies have demonstrated improvement, but the results are mixed and there has not been agreement on an optimal design for a given inlet condition.

Flow maldistribution must be understood and mitigated to design high-performance compact heat and mass exchangers for real systems. This study aims to quantify and understand flow distribution through the careful observation of header flow patterns and measurement of the pressure drop and phase flow rates in the heat exchanger channels. Additionally, a model is developed to predict the distribution of two-phase flows in headers that combines the effects of both the path pressure drops and the flow characteristics in the header, which both play an important role in flow distribution.

1.1 Organization of Dissertation

The remainder of this dissertation is organized as follows:

- Chapter 2 presents a review of previous research on two-phase flow distribution in heat exchanger manifolds. The review covers both the results from past experimental studies and the different modeling approaches that attempt to predict distribution. The need for additional research is discussed and the objectives of the present study are stated.

- Chapter 3 presents the results from an experimental study on the distribution of air-water mixtures in heat exchanger manifolds. This chapter includes a description of the experimental setup and a discussion of the experimental results.
- Chapter 4 details the experimental approach used to measure the distribution of a saturated refrigerant in a plate-type heat exchanger manifold. The experimental facility, all measurement devices and the data analysis approach are discussed.
- Chapter 5 presents the experimental results from the refrigerant study and discusses the effects of the inlet operating conditions on pressure drop and flow distribution.
- Chapter 6 describes the development of a pressure drop and flow regime-based modeling approach for the distribution of two-phase flows in mini- and microchannel plate-type heat exchangers.
- Chapter 7 provides conclusions from the present study and recommends areas for future research.
- The appendices present detailed information about an analytical model used to investigate the flow measurement devices developed and used in the refrigerant study and a sample calculation stepping through the data analysis method used in this work.

CHAPTER 2. LITERATURE REVIEW

Flow maldistribution in header systems has been studied by many researchers over the last three decades. Effective manifold designs and models have been developed for single-phase flow (Bassiouny and Martin, 1984; Jones *et al.*, 2008; Dharaiya *et al.*, 2009; Said *et al.*, 2015; Anbumeenakshi and Thansekhar, 2016), and these models and good design practices can successfully mitigate single-phase flow maldistribution (Habib *et al.*, 2008). Unfortunately, these models cannot be used for two-phase inlet conditions because the flow characteristics inside the header are significantly more complex (Webb and Chung, 2005). Although there have been experimental and numerical studies examining the effects of operating conditions, fluid properties, and geometric parameters, there is currently no generally applicable method for predicting two-phase flow distribution in heat exchanger manifolds.

This chapter presents the findings from previous research on two-phase flow distribution in heat exchanger headers. First, the results from past experimental studies are discussed, with an emphasis on the effect of the inlet conditions (mass flux and quality) and geometry on distribution. This is followed by a description of alternative header designs presented in the literature. Finally, modeling techniques for two-phase flow distribution in manifolds are summarized and discussed.

2.1 Experimental Studies

A summary of important experimental studies on two-phase flow distribution of gas-liquid mixtures (mostly air-water) and saturated refrigerants in heat exchanger

manifolds is presented in Table 2.1 and 2.2, respectively. The table includes information about the inlet conditions, geometries, and header modifications investigated by each author. The next sections discuss the conclusions from these studies and highlight some of the discrepancies in the literature.

2.1.1 Header Inlet Conditions

Most experimental studies quantify flow distribution for a range of inlet mass fluxes and qualities. The inlet conditions tested in twenty prominent studies on two-phase flow distribution are compared in Figure 2.1. Most previous work has focused on low inlet qualities ($x_{in} < 0.5$) over a large range of inlet mass fluxes.

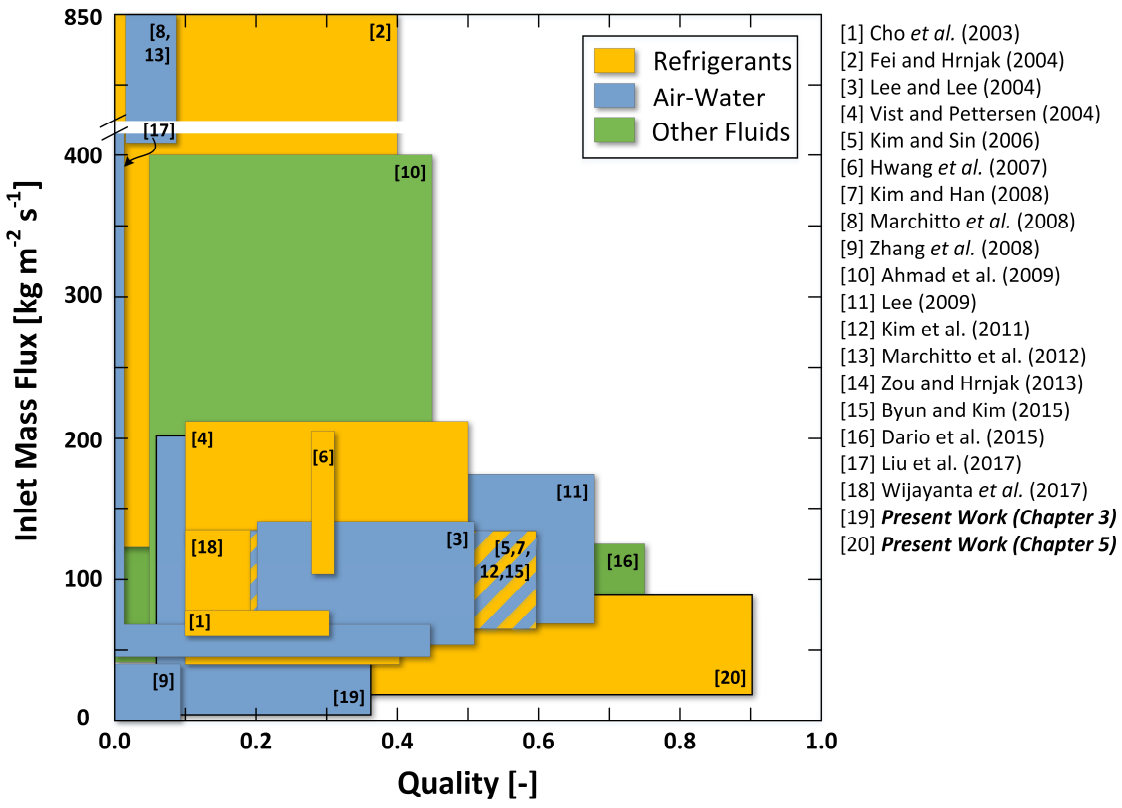

Figure 2.1: Summary of inlet conditions tested in the current and previous experimental two-phase flow distribution studies

Table 2.1: Summary of experimental studies on gas-liquid mixture distribution in heat exchanger headers

Reference	Fluid	Operating Conditions	Header Type	Header Geometry	Channel Geometry	Modifications
Rong *et al.* (1995)	Air-Water	Adiabatic G_{header} < 337 kg m^{-2} s^{-1} x_{in} < 0.22	Tubular	D_{header} = 12.3 mm *Orientation*: Horizontal	W_{ch} = 75 mm H_{ch} = 2.6 mm L_{ch} = 230 mm N_{ch} = 7 *Orientation*: Vertical ↑↓	Channels contained 8.2 mm diameter dimples on surface
Lee and Lee (2004)	Air-Water	Adiabatic G_{in} = 54 – 134 kg m^{-2} s^{-1} x_{in} = 0.20 – 0.50	Rectangular	W_{header} = 24 mm H_{header} = 24 mm *Orientation*: Vertical ↑	W_{ch} = 1.8 mm H_{ch} = 22 mm N_{ch} = 6 d_{prot} = 0, 6, & 12 mm $Pitch_{ch}$ = 9.8 mm *Orientation*: Horizontal	Rectangular channels protrude into the header
Kim and Sin (2006)	Air-Water	Adiabatic G_{in}= 70 – 130 kg m^{-2} s^{-1} x_{in} = 0.20 – 0.60	Tubular	D_{header} = 17 mm D_{feed} = 17 mm L_{feed} = 1000 mm *Orientation*: Horizontal	$D_{H,ch}$ = 1.32 mm L_{ch} = 910 mm N_{tube} = 30 $N_{ch/tube}$= 8 $Pitch_{tube}$ = 9.8 mm *Orientation*: Vertical ↑↓	Rectangular channels protrude into the header (d_{prot} = 0, 4.25, 8.50 mm)
Marchitto *et al.* (2008)	Air-Water	Adiabatic j_g = 1.50 – 16.5 m s^{-1} j_l = 0.20 – 1.20 m s^{-1}	Tubular	D_{header} = 26 mm L_{header} = 316 mm L_{feed} = 2000 mm *Orientation*: Horizontal	$D_{H,ch}$ = 16.4 mm L_{ch} = 500 mm N_{ch} = 16 *Orientation*: Vertical ↑	Nozzle added at header inlet ($D_{orifice}$ = 12 - 20 mm) and orifice plate added at entrance to outlet channels (D_{op} = 2-6 mm)

Table 2.1: Summary of experimental studies on gas-liquid mixture distribution in heat exchanger headers (cont'd)

Reference	Fluid	Operating Conditions	Header Type	Header Geometry	Channel Geometry	Modifications
Lee (2009)	Air-Water	Adiabatic G_{in} = 70 – 165 kg m^{-2} s^{-1} x_{in} = 0.30 – 0.70	Rectangular	W_{header} = 14 mm H_{header} = 14 mm L_{feed} = 1650 mm *Orientation*: Vertical ↑	$D_{H,ch}$ = 2.82 mm N_{tube} = 15 $N_{ch/tube}$ = 6 *Orientation*: Horizontal	Studied rectangular tubes with and without internal channels - distribution was not affected
Marchitto *et al.* (2012)	Air-Water	Adiabatic j_g = 1.50 – 16.5 m s^{-1} j_l = 0.20 – 1.20 m s^{-1}	Tubular	D_{header} = 26 mm D_{feed} = 26 mm L_{feed} = 2000 mm *Orientation*: Horizontal	W_{ch}= 18 mm H_{ch}= 15 mm L_{ch} = 500 mm $Pitch_{ch}$ = 18 mm N_{ch} = 16 *Orientation*: Vertical ↑	Orifice plate added at entrance to outlet channels (D_{op} = 3 mm) and "flute" added inside header
Dario *et al.* (2015)	Air-Water	Adiabatic G_{in} = 72 – 216 kg m^{-2} s^{-1} x_{in} = 0 – 0.75	Tubular	D_{header} = 50 mm L_{header} = 120 mm D_{feed} = 5 mm L_{feed} = 2500 mm *Orientation*: Several	D_{ch} = 0.80 mm L_{ch} = 150 mm N_{ch} = 9 $Pitch_{ch}$ = 21 mm *Orientation*: Several	
Liu *et al.* (2017)	N_2 - SDS	Adiabatic j_g = 0.20 – 16.0 m s^{-1} j_l = 0.03 – 0.65 m s^{-1}	Tubular	W_{header} = 0.5 mm H_{header} = 1.0 mm L_{header} = 12 mm $D_{H,feed} = D_{H,header}$ L_{feed} > 333 mm *Orientation*: Several	W_{ch} = 0.5 mm H_{ch} = 0.5 mm L_{ch} = 70 mm N_{ch} = 3 $Pitch_{ch}$ = 6 mm *Orientation*: Several	
Current Work (Chapter 3)	Air-Water	Adiabatic G_{in} = 2.6 - 200 kg m^{-2} s^{-1} x_{in} = 0.05 – 0.35	Rectangular	W_{header} = 3.50 mm H_{header} = 11.3 mm L_{header} = 52.8 mm D_{feed} = 6.35 mm L_{feed} = 942 mm *Orientation*: Horizontal	D_{ch} = 1 – 3 mm L_{ch} = 212 mm N_{ch} = 3 $Pitch_{ch}$ = 15 mm *Orientation*: Vertical ↓	Rectangular and triangular headers

Table 2.2: Summary of experimental studies on refrigerant distribution in heat exchanger headers

Reference	Fluid	Operating Conditions	Header Type	Header Geometry	Channel Geometry	Modifications
Cho *et al.* (2003)	R22	Adiabatic T_{sat} = 7°C G_{in} = 60 kg m^{-2} s^{-1} x_{in} = 0.10 – 0.30	Tubular	D_{header} = 19.4 mm L_{header} = 148 mm *Orientation*: Vertical ↑ and Horizontal	$D_{H,ch}$ = 1.32 mm N_{tube} = 15 $N_{ch/tube}$ = 8 $Pitch_{tube}$ = 9.8 mm L_{tube} = 900 mm *Orientation*: Horizontal and Vertical ↑	Tested three different inlet port locations in horizontal header
Fei and Hrnjak (2004)	R134a	Adiabatic T_{sat} = 22°C G_{header} = 10 – 100 kg m^{-2} s^{-1} x_{in} = 0.00 – 0.40	Rectangular	$D_{H,header}$ = 25.4 mm L_{header} = 305 mm D_{feed} = 3.2, 6.4, & 9.5 mm L_{feed} = 120 mm *Orientation*: Horizontal	N_{ch} = 5 *Orientation*: Vertical ↓	Studied generic rectangular header and baffled header
Vist and Pettersen (2004)	R134a	Evaporating G_{in}= 124 – 209 kg m^{-2} s^{-1} & 458 – 656 kg m^{-2} s^{-1} x_{in} = 0.11 – 0.50	Tubular	D_{header} = 8 & 16 mm D_{feed} = 8 & 16 mm L_{feed} = 50 & 250 mm *Orientation*: Horizontal	D_{ch} = 4 mm N_{ch} = 10 $Pitch_{ch}$ = 21 mm *Orientation*: Vertical ↑↓	
Hwang *et al.* (2007)	R410a	Evaporating T_{sat} = 7.2°C G_{header} = 106 – 212 kg m^{-2} s^{-1} x_{in} = 0.30 $\dot{Q}_{in}$ = 0 to 10 kW	Tubular	D_{header} = 19 mm *Orientation*: Horizontal	$D_{H,ch}$ = 1.7 mm L_{ch} = 1000 mm N_{tube} = 18, 24, & 30 $N_{ch/tube}$ = 6 $Pitch_{ch}$ = 8, 10, 12 mm *Orientation*: Vertical ↑	Investigated distribution characteristics with side and central inlet port
Ahmad *et al.* (2009)	HFE 7100	Evaporating G_{in} = 70 – 400 kg m^{-2} s^{-1} x_{in} = 0.05 – 0.45	Tubular	D_{header} = 17.5, 30, 50 mm L_{header} = 127 mm D_{feed} = 17.5 mm L_{feed} = 1600 mm *Orientation*: Horizontal	$D_{H,ch}$ = 3.85 mm N_{ch} = 8 *Orientation*: Several	Added expansion device at header inlet (orifice nozzle and splash grid).

Table 2.2: Summary of experimental studies on refrigerant distribution in heat exchanger headers (cont'd)

Reference	Fluid	Operating Conditions	Header Type	Header Geometry	Channel Geometry	Modifications
Kim *et al.* (2011)	R134a	Adiabatic G_{in} = 70 – 130 kg m^{-2} s^{-1} x_{in} = 0.20 – 0.60	Tubular	D_{header} = 17 mm D_{feed} = 17 mm L_{feed} = 1000 mm *Orientation*: Horizontal	$D_{H,ch}$ = 1.32 mm L_{ch} = 910 mm N_{tube} = 10 $N_{ch/tube}$ = 8 *Orientation*: Vertical ↓	Studied distribution in flat outlet channels with parallel, normal and vertical inlet locations
Zou and Hrnjak (2013)	R134a	Evaporating T_{sat} = 10ºC G_{header} = 22 – 64 kg m^{-2} s^{-1} $x_{in,int}$ = 0.20 – 0.80	Tubular	D_{header} = 14.9 – 15.4 mm L_{header} = 170 & 300 mm *Orientation*: Vertical	$D_{H,ch}$ = 0.52 mm $N_{ch/tube}$ = 17 N_{tube} = 5 & 10 $Pitch_{tube}$ = 13 mm *Orientation*: Horizontal	Intermediate header in multi-pass heat exchanger. Varied protrusion depth of outlet channels
Byun and Kim (2015)	R410a	Evaporating G_{header} = 73 – 143 kg m^{-2} s^{-1} $x_{in,int}$ = 0.40 – 0.60	Tubular	D_{header} = 17 mm d_{prot} = 8.5 mm *Orientation*: Horizontal	$D_{H,ch}$ = 1.24 mm $N_{ch/tube}$ = 8 N_{tube} = 22 $Pitch_{tube}$ = 9.8 mm L_{tube} = 900 mm *Orientation*: Vertical ↓	Intermediate header in multi-pass heat exchanger
Wijayanta *et al.* (2017)	R134a	Adiabatic T_{sat} = 21ºC G_{in} = 44 – 130 kg m^{-2} s^{-1} x_{in} = 0.10 – 0.40	Tubular	D_{header} = 9.0 mm D_{feed} = 9.0 mm L_{feed} = 70 mm *Orientation*: Horizontal	D_{ch} = 0.85 mm L_{tube} = 200 mm N_{tube} = 3 & 6 $N_{tube/ch}$ = 6 $Pitch_{tube}$ = 15 mm *Orientation*: Vertical ↓	Investigate how protrude depth effects distribution (d_{prot} = 0 and 4.5 mm)
Current Work (Chapter 5)	R134a	Condensing T_{sat} = 30ºC G_{in} = 24 – 96 kg m^{-2} s^{-1} x_{in} = 0.1 – 0.9	Rectangular	W_{header} = 2.00 mm H_{header} = 8.33 mm L_{header} = 155 mm D_{feed} = 4.57 mm L_{feed} = 63 mm *Orientation*: Horizontal	D_{ch} = 1 mm L_{ch} = 500 mm N_{ch} = 10 $Pitch_{ch}$ = 15 mm *Orientation*: Vertical ↓	Rectangular, triangular and vaned header shapes

Although inlet conditions have been broadly studied, there are discrepancies between the results. For example, many authors conclude that increasing the inlet mass flux improves the overall distribution (Lee and Lee, 2004; Hwang *et al.*, 2007; Kim *et al.*, 2011; Wijayanta *et al.*, 2017), but others find that it does not have a significant effect (Vist and Pettersen, 2004). This disagreement can be explained by the ranges of inlet mass fluxes tested in each study. Ahmad *et al.* (2009) and Mahvi and Garimella (2017) evaluated the distribution of HFE 7100 and air-water mixtures over a relatively large range of inlet mass fluxes (70 to 400 kg m^{-2} s^{-1} and 2.6 to 200 kg m^{-2} s^{-1}, respectively). These studies report that the inlet flow rate influences distribution at relatively high mass fluxes, but has little effect at low mass fluxes. Vist and Pettersen (2004) measured the distribution of R134a flowing through a 16 mm diameter tubular header attached to 10 vertical channels and found that increasing the mass flux from 124 to 207 kg m^{-2} s^{-1} resulting in nearly the same flow distribution. However in later experiments, Vist (2004) tested an 8-mm diameter header subjected to higher inlet mass fluxes (458 – 656 kg m^{-2} s^{-1}) and found that the distribution improved with increasing inlet flow rates, leading to agreement with previous work.

The effect of inlet quality on two-phase flow distribution is also commonly reported in the literature, and again there is a range of conclusions. For example, some studies find that the liquid distribution improves with increasing inlet quality (Fei and Hrnjak, 2004; Ahmad *et al.*, 2009), others show that it worsens (Lee and Lee, 2004; Vist and Pettersen, 2004; Wijayanta *et al.*, 2017), and some conclude that the distribution is not affected by the inlet quality (Cho *et al.*, 2003; Lee, 2009). The overall degree of maldistribution can have different trends depending on the inlet quality ranges tested, which could partially

explain the results. At an inlet quality of 0 (pure liquid) or 1 (pure vapor), the channel flow rates should be nearly equal because the flow in the header is in a single phase. For two-phase inlet conditions, the distribution is usually poor and is highly dependent on the flow regime in the header (Fei and Hrnjak, 2004; Ahmad *et al.*, 2009; Mahvi and Garimella, 2017). As the quality increases from 0, the distribution should get worse, level off, and then improve as the quality approaches 1. However, after further inspection, the tested quality ranges do not fully explain the discrepancies. For example, Fei and Hrnjak (2004) and Wijayanta *et al.* (2017) both measured the flow distribution of R134a in horizontal headers over nearly the same range of inlet qualities (x_{in} = 0 – 0.40 and x_{in} = 0.10 – 0.40, respectively), but Fei and Hrnjak (2004) concluded that the flow distribution improves, while Wijayanta *et al.* (2017) found that it worsens with increasing inlet qualities. This discrepancy can be explained by the different flow regimes in the header. The flow expands as it enters the header investigated by Fei and Hrnjak (2004) because of a large change in cross sectional area. This design often produces a liquid jet inside the header that in many cases interacts with the far end of the header. The header studied by Wijayanta *et al.* (2017) had a constant cross sectional area, which resulted in different header flow patterns. Comparing these two studies highlights the importance of the manifold geometry on two-phase flow distribution.

2.1.2 Orientation and Geometry

As noted in the previous section, the header orientation and geometry can affect the flow regimes, which changes the flow distribution characteristics in heat exchangers. There are many geometric parameters that can affect flow distribution, including the header length, the number of outlet channels, the position of the feeder tube in relation to the

header, the orientations of the header and channels, and the cross-sectional areas of the feeder tube, header, and channels. Two-phase flow distribution is not very well understood, in part because of the large number of geometric parameters that must be considered. Unlike inlet conditions, the effects of heat exchanger geometry on distribution have not been as systematically studied, as shown in Figure 2.2. The geometric parameters are usually held constant for each study because it is costly and time intensive to change them. Additionally, to thoroughly study the effects of heat exchanger geometry on distribution for a range of inlet conditions would require a large test matrix that is generally not practical for a single study. Some authors have quantified the effects of a subset of the important geometric parameters relevant to two-phase flow distribution. Their findings are summarized in the following sections.

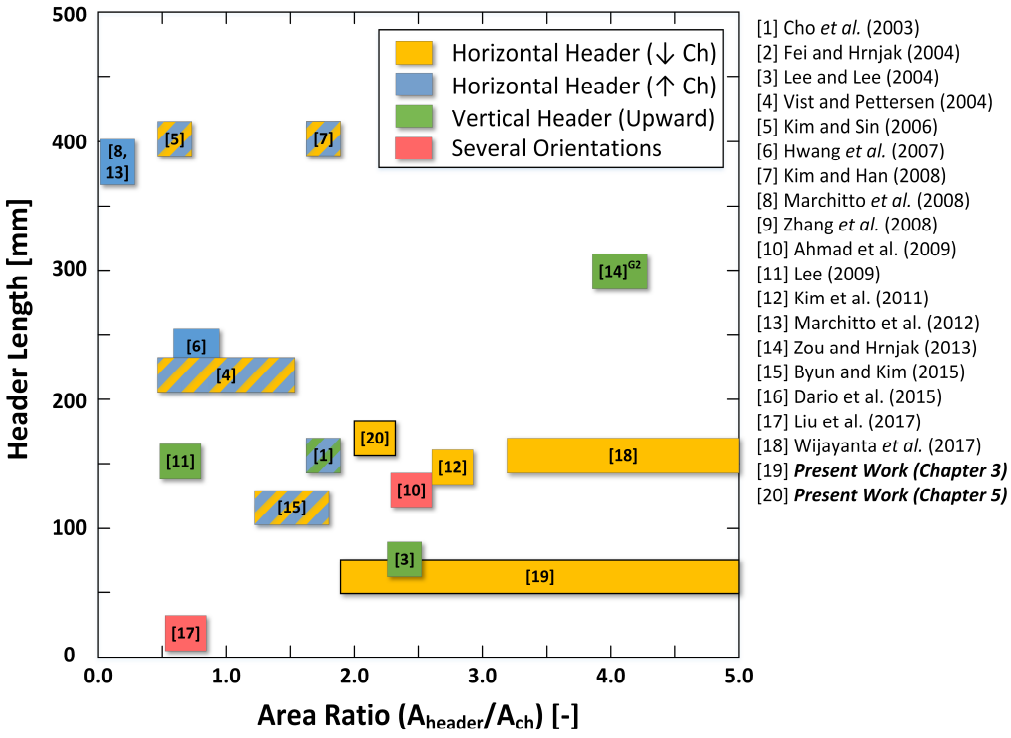

Figure 2.2: Summary of some of the important geometric parameters in the current and previous experimental two-phase flow distribution studies

2.1.2.1 Orientation of Header and Channels

Dario *et al.* (2015) conducted the most comprehensive study on the effect of heat exchanger orientation on two-phase flow distribution. They measured the liquid distribution of an air-water mixture into 9 parallel outlet channels when subjected to inlet mass fluxes between 72 and 216 kg m^{-2} s^{-1} and qualities between 0 and 0.75. The experiments were repeated on a vertical-downward header with horizontal channels and a horizontal header with horizontal, vertical-upward and vertical-downward channels. They found that the header and channel orientations affect the flow patterns in the header, which results in different distribution characteristics. It should be noted that the flow experiences a large expansion when it enters the test section in their header design ($A_{header,cs}/A_{feed,cs}$

= 100), which also affects the flow pattern. Dario *et al.* (2015) found that horizontal headers generally outperform vertical headers, which was also concluded in an earlier study by Cho *et al.* (2003). Additionally, Dario *et al.* (2015) concluded that a horizontal header with horizontal channels was the ideal orientation for the test conditions considered in the study.

Similar studies have also investigated the influence of heat exchanger orientation for different header designs on two-phase flow distribution. Vist (2004) measured distribution in a horizontal header (D_{header} = 8 to 16 mm) connected to vertical-upward and vertical-downward channels and found that the liquid distributes best into downward channels for R134a and into upward channels for CO_2. Ahmad *et al.* (2009) measure the distribution of HFE 7100 in a 30-mm diameter horizontal header attached to horizontal, vertical-upward and vertical-downward channels. At low qualities (x_{in} = 0.10), they showed the liquid phase distributes best in the vertical-downward configuration, but at higher qualities (x_{in} = 0.35) the best liquid distribution occurred in the horizontal channel configuration. Finally, Liu *et al.* (2017) studied the distribution of a nitrogen – sodium dodecyl sulfate solution (0.03 wt%) mixture in a rectangular header (D_H = 0.67 mm) connected to three parallel outlet channels. They found that the liquid and gas phases were most uniformly distributed in a horizontal header with vertical-downward channels when slug flow enters the test section and in a vertical-upward header with horizontal channels when slug-annular flow enters the test section.

Although heat exchanger orientation has been experimentally studied by several authors, there is no consensus on which orientation performs best. It is evident from previous work that distribution is dependent on many geometric characteristics of a heat

exchanger, not orientation alone. Most previous studies present their results for a single heat exchanger design, but do not provide a discussion of the driving factors that affect distribution for different orientations. Additional research is needed in this area to understand the relationship between orientation, header flow regimes and distribution for a wider array of heat exchanger designs.

2.1.2.2 Feeder Tube Diameter

In some proposed designs, the cross-sectional area of the feeder tube is smaller than the header, causing the flow to expand as it enters the heat exchanger. This expansion can substantially change the flow regime in the header, which in turn will change the distribution characteristics. Fei and Hrnjak (2004) and Ahmad *et al.* (2009) measured liquid and vapor flow distribution for different expansion ratios. Fei and Hrnjak (2004) investigated the effects of expansion using three different feeder tube diameters (D_{feed} = 9.5, 6.4, and 3.2 mm). Decreasing the feeder tube diameter increases the velocity at the header inlet and increases the expansion ratio ($A_{header,cs}/A_{feed,cs}$ = 9.10, 20.1, and 80.22), which can result in an abrupt expansion that homogenizes the inlet flow. This study concluded that decreasing the feeder tube diameter can improve distribution when the fluid enters the header at low qualities and mass flow rates. In this case, the liquid momentum with a large diameter feeder tube may not be sufficient to transport it to the channels farthest from the inlet. However, when the fluid enters the heat exchanger at a relatively high quality and mass flow rate, decreasing the inlet cross sectional area will result in very high velocities, which can produce strong jets in the header and lead to unfavorable flow regimes for distribution (for example – liquid pooling at the far wall of the header). This

work suggests that there may be an optimum feeder tube diameter for a given set of inlet conditions, but they did not suggest a method for determining it for an arbitrary heat exchanger geometry.

Ahmad *et al.* (2009) measured the liquid and vapor flow rates in ten parallel channels connected to a common header. They studied the effect of flow expansion by increasing the size of the header from 17.3 mm to 50 mm ($A_{header,cs}/A_{feed,cs}$ = 1.00, 3.00, and 8.35). Ahmad *et al.* (2009) found that the liquid and vapor distribution improved in headers with larger area ratios due to the changing flow regimes. When the cross-sectional area of the feeder tube is smaller than that of the header, a liquid jet tends to form in the header. The jet impact length increases with the diameter of the header, transporting more liquid away from the inlet port.

2.1.2.3 Channel Protrusion Depth

Most experimental studies on flow distribution focus on tubular header designs common in crossflow evaporators and condensers. In these components, the tubes often protrude partway into the header to facilitate the manufacturing process (usually brazing). A representative image of this type of header is shown in Figure 2.3.

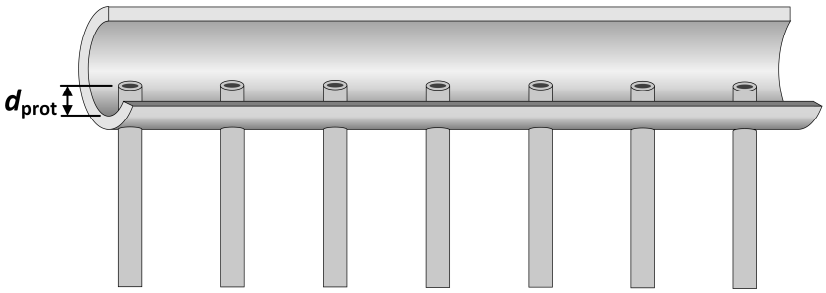

Figure 2.3: Typical header design for a crossflow heat exchanger (with channels protruding into header)

Several authors have investigated the effect of protrusion depth (d_{prot}) on the distribution of the liquid and vapor phases in crossflow heat exchanger headers (Lee and Lee, 2004; Bowers *et al.*, 2006; Kim and Sin, 2006; Kim and Han, 2008; Zou and Hrnjak, 2013; Wijayanta *et al.*, 2017). These studies show that when liquid impinges on a protruding channel, a portion of the stream is forced into the central part of the header and transported away from the inlet. When the channels are in the downward orientation, this generally improves the liquid distribution (Bowers *et al.*, 2006; Wijayanta *et al.*, 2017), especially for low inlet qualities and mass fluxes (Kim and Han, 2008). The distribution also improves when the channels protrude into vertical-upward headers (Zou and Hrnjak, 2013); however, Lee and Lee (2004) found that if the protrusion depth is too large, the distribution starts to deteriorate.

Inserting the channel into the header region can be an effective method to improve flow distribution; however, further work is needed to understand how the protrusion depth can be optimized for different geometries and inlet conditions. Additionally, this approach is only practical for crossflow heat exchangers and generally cannot be integrated into plate-type heat exchanger headers, which would need different designs.

2.1.3 Header Modifications

Previous work has established that two-phase flow distribution in smooth, unmodified headers (for both crossflow or plate-type heat exchangers) is usually poor. Many authors have proposed header modifications to improve distribution. These modifications include expansion devices at or near the header inlet (Fei and Hrnjak, 2004; Marchitto *et al.*, 2008; Ahmad *et al.*, 2009), restrictions at the entrance of each channel (Marchitto *et al.*, 2008), header inserts (Vist, 2004; Marchitto *et al.*, 2012; Kim *et al.*, 2013), and alternative header geometries (Mahvi and Garimella, 2017). Most of the proposed header modifications attempt to mitigate flow maldistribution in heat exchangers, with varying degrees of improvement. However, each modification is generally evaluated for a single header geometry and it is unclear how it can be applied and optimized for a different heat exchanger. Furthermore, adding devices or restrictions to the header inevitably increases the pressure drop, which should generally be minimized as much as possible. Many previous studies do not report the additional pressure drop resulting from header modifications. Finally, the addition of some of the proposed devices complicates the manufacturing of these components. Future work should focus on developing practical, low pressure drop distributors that operate over a large range of inlet conditions and heat exchanger geometries.

2.2 Modeling Approaches

Several modeling approaches have been proposed to predict two-phase flow distribution in manifolds. These approaches span from simple empirical correlations to complex computational fluid mechanics models. This section presents some of the

proposed empirical correlations and also discusses other more complex modeling approaches.

Some experimental work on two-phase flow distribution in manifolds has been leveraged to develop empirical correlations for common header geometries. These correlations generally predict the take-off ratio, which is the fraction of the inlet flow rate in the header (immediately upstream of the T-junction containing the channel of interest) that enters a branch channel. One of the first correlations for the liquid take-off ratio in a manifold was developed by Watanabe *et al.* (1995), which depends solely on the header gas Reynolds number. The resulting model is shown in Equation 2.1,

$$\frac{\dot{m}_{ch,l}[i]}{\dot{m}_{header,l}[i]} = 2.74 \times 10^{-5} Re_v[i] - 0.0124\sqrt{Re_v[i]} + 1.37 \qquad (2.1)$$

where $\dot{m}_{ch,l}[i]$ is the liquid mass flow rate in the channel, $\dot{m}_{header,l}[i]$ is the liquid mass flow rate in the header immediately upstream of the channel, and $Re_v[i]$ is the vapor Reynolds number in the header immediately upstream of the channel. Although the correlation predicts their data well, it does not include variables that could influence distribution in manifolds, including the inertia of the liquid phase, gravity, surface tension, and the effects of geometry. As a result, the model has poor predictive capabilities for geometries and operating conditions other than those for which it was developed (Vist, 2004; Panghat and Mehendale, 2016).

Kim *et al.* (2012) developed a similar empirical model based solely on the vapor Reynolds number for the liquid and vapor take-off ratio in a tubular header with protruding channels. Models were developed using a regression analysis for headers with a parallel,

normal, and vertical inlet feeder tube. The results for the normal inlet condition are shown in Equations 2.2 and 2.3. The model predictions fit their data relatively well, with average R^2 values of ~78% (although errors are large in some cases, especially at low vapor Reynolds numbers).

$$\frac{\dot{m}_{ch,l}[i]}{\dot{m}_{header,l}[i]} = 2.01 Re_v[i]^{-0.550} \tag{2.2}$$

$$\frac{\dot{m}_{ch,v}[i]}{\dot{m}_{header,v}[i]} = 3.38 Re_v[i]^{-0.920} \tag{2.3}$$

Again, the Kim *et al.* (2012) model oversimplifies the flow in the header by just considering the inertial and viscous forces of the vapor phase. This could result in large errors when the model is applied to conditions other than those used in the regression analysis. Additionally, the model can predict non-physical results. For example, at low vapor Reynolds numbers, the model predicts take-off ratios greater than one, implying that more liquid enters the channel than is available in the header. Also, the flow distribution in a multichannel heat exchanger is constrained by pressure drop. A simple heat exchanger is shown in Figure 2.4 with the three possible flow paths shown in red, green and blue. The pressure change across each flow path must be equal so that the inlet and exit pressure are the same for each path. The path pressure drop is dependent on the liquid and vapor flow rates into each channel. The Kim *et al.* (2012) correlation proposes a method to calculate both the liquid and vapor flow rates through each path, but does not consider the path pressure drops in the calculation. This can lead to predictions that are not physically possible because the pressure drop constraint is not satisfied.

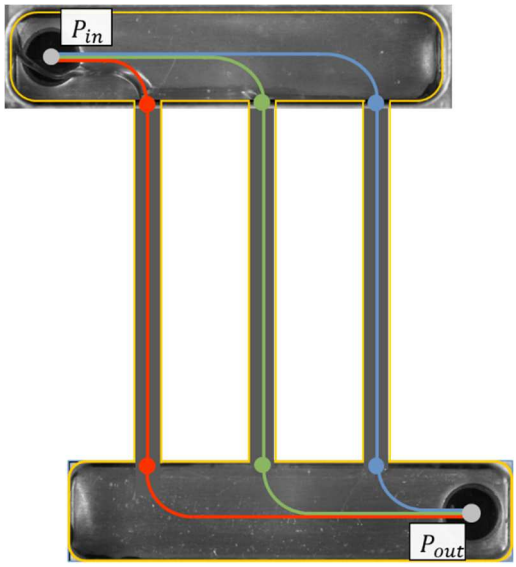

Figure 2.4: Flow paths in a simple three-channel heat exchanger

Vist (2004) developed a distribution model based on the predictions of the local flow regime in the header. Specifically, he correlated the take-off ratio in each heat exchanger channel using the used stratified wavy – intermittent/annual transition criteria proposed by Kattan *et al.* (1998). This transition criterion is shown in Equation 2.4,

$$G_{wavy} = \left(\frac{16A_{gd}^3 g D_m \rho_l \rho_v}{x^2\pi^2(1-(2h_{ld}-1)^2)^{0.5}}\left[\frac{\pi^2}{25h_{ld}^2}(1-x)\left(\frac{We}{Fr}\right)_l^{1.023}+1\right]\right)^{0.5} + 50 - 75\exp\left(-\frac{(x^2-0.97)^2}{x(1-x)}\right) \tag{2.4}$$

where A_{gd} is the dimensionless vapor cross-sectional area and h_{ld} is the dimensionless liquid height in the header. The final correlation proposed by Vist (2004) for a horizontal header with vertical-downward channels is shown in Equations 2.5 and 2.6, where $\xi[i] = \log\left(G[i]/G_{wavy}[i]\right)$. The constants *a* through *k* in the proposed model were determined using a regression analysis.

$$\frac{\dot{m}_{ch,l}[i]}{\dot{m}_{header,l}[i]} = a + b\xi[i] + c\xi[i]^2 + d\xi[i]^3 + e\xi[i]^4 + f\xi[i]^5 + \frac{g}{A_c} + \frac{h}{A_c^2} \quad if \left(\frac{G[i]}{G_{wavy}[i]}\right) > i + \frac{j}{A_c} + \frac{k}{A_c^2} \tag{2.5}$$

$$\frac{\dot{m}_{ch,l}[i]}{\dot{m}_{header,l}[i]} = 1 \qquad if \left(\frac{G[i]}{G_{wavy}[i]}\right) < i + \frac{j}{A_c} + \frac{k}{A_c^2} \tag{2.6}$$

This correlation shows good agreement with their measured data for several header geometries, showing the validity of the approach beyond a specific case.

Recently, Wijayanta *et al.* (2017) proposed another model for the liquid and vapor take-off ratios in vertical-downward channels connected to a common horizontal header. Wijayanta *et al.* (2017) found that the take-off ratios could be modeled using the local liquid Reynolds and Froude numbers and the two-phase Reynolds and Weber numbers in the header, as shown in Equation 2.7. These parameters account for the effects of inertia, viscosity, gravity and surface tension, which are all important in these types of two-phase flows.

$$\frac{\dot{m}_{ch,l}[i]}{\dot{m}_{header,l}[i]} = \frac{6}{N_{ch}} 0.426 \left(Re_{l,header}[i]^{0.5} Fr_{l,header}\right)^{-0.3} \tag{2.2}$$

$$\frac{\dot{m}_{ch,v}[i]}{\dot{m}_{header,v}[i]} = \left(\frac{6}{N_{ch}}\right)^2 0.392 e^{-0.002\left(Re_{TP,header}^{0.5}[i] We_{TP,header}[i]\right)} \tag{2.3}$$

Again, predicting the liquid and vapor flow rates in a channel with no consideration for the path pressure drop may lead to non-physical results. Caution should be used when simultaneously employing both the correlations discussed above.

Empirical models can be an effective way to predict flow distribution in heat exchangers if they account for the relevant physical phenomena. However, they are often over simplified and do not capture the underlying physics, which can lead to poor predictive capabilities outside of the data range used in the regression analysis. Another proposed model architecture discretizes the header and channels of a heat exchanger and leverages existing correlations to predict flow distribution. In these models, the header is generally modeled as a series of T-junctions, as shown in Figure 2.4. There are many models in the literature to predict the phase-splitting characteristics of two-phase flows entering a T-junction (Smoglie and Reimann, 1986; Hwang *et al.*, 1988; Tae and Cho, 2006), which can be used to predict the inlet quality into each channel. The inlet quality partially defines two-phase flow distribution, but another set of equation is required to calculate the channel mass flow rates. The mass flow rate is typically calculated using the fact that the pressure drop across each flow path in a heat exchanger must be equal. The pressure drops in the inlet and outlet manifolds are again calculated with T-junction models and the pressure drop in the channels is calculated using correlations from the literature (e.g., Friedel, 1979; Garimella *et al.*, 2005; Kim and Mudawar, 2012; Murphy, 2014). The channel mass flow rates are then calculated by equating the pressure differences across each flow path, fully defining the distribution in the heat exchanger.

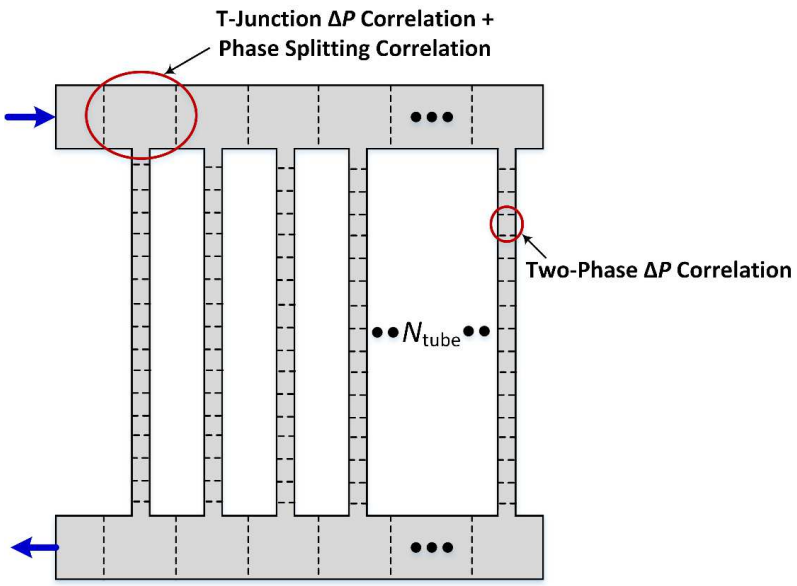

Figure 2.5: Detailed discretized model to predict flow distribution

Segmental models have been used to predict two-phase flow distribution in heat exchangers (Vist, 2004; Ablanque *et al.*, 2010), however the results are highly dependent on the correlations used. The pressure drop and phase-splitting correlations must be applicable to the flow conditions and geometry of the heat exchanger to achieve accurate results. Two-phase pressure drop in both macro- and micro-channels has been extensively studied; therefore, appropriate correlations to predict the pressure gradients in heat exchanger channels can usually be found. Pressure drop and phase-splitting models in T-junctions are usually based on experimental measurements when a fully-developed two-phase flow enters the T. Although these models can be used, they may not perform well in headers because the flow does not have the space to fully develop between consecutive Ts (Vist, 2004; Lee, 2009).

Computational fluid dynamic (CFD) models are also sometimes used to characterize flow distribution in heat exchangers. Most past work has focused on the distribution of

single-phase flows into headers (Zhang and Li, 2003; Tong *et al.*, 2009; Aslam Bhutta *et al.*, 2012; Manikanda Kumaran *et al.*, 2013; Yuan *et al.*, 2016; Luan *et al.*, 2017), with only a few studies on two-phase flows (Fei and Hrnjak, 2004; Li *et al.*, 2005; Zou and Hrnjak, 2016). Fei and Hrnjak (2004) used a 3-D Eulerian-Eulerian approach to model two-phase flow distribution in a heat exchanger using FLUENT 6 (a commercial CFD software). They compared the results with experimental data and found that the model could qualitatively predict the measured trends, but some channels had large quantitative errors. They concluded that this approach was not accurately capturing the characteristics of the inlet expansion and flow recirculation at the far end of the header. Fei and Hrnjak (2004) also showed the pressure and velocity fields inside the header for one inlet case, focusing on the formation and dissipation of the liquid jet.

Li *et al.* (2005) evaluated the applicability of algebraic slip mixture (ASM), volume of fluid (VOF) and inter-phase slip algorithm (IPSA) CFD models for refrigerant two-phase flow distribution. Models were first developed for turbulent air-water flow through an upward circular pipe and the void fraction distribution was compared with experimental data from the literature. The ASM and VOF models both performed poorly, but the IPSA model was able to predict the correct trends. The ASM and VOF models were also compared with experimental data for phase-splitting in a T-junction. Again, both models performed poorly and did not capture the correct trends; however, Lahey (1990) previously showed that ISPA CFD model can correctly predict phase splitting in T-junctions. With this information, the ASM model and the ISPA model were compared for a Y-type refrigerant distributor. Li *et al.* (2005) computed similar results with the two models when very high velocities entered the distributor inlet (~50 m s^{-1}) and concluded that both model

types could be used to predict two-phase flow distribution for high-momentum inlet flows. Although this work showed some interesting results, it would benefit from experimental validation in the geometry of interest for a larger set of inlet conditions.

Zou and Hrnjak (2016) studied the flow distribution of R134a and R410a in the intermediate vertical header of a two-pass evaporator experimentally and numerically. A 3-D numerical model was developed in FLUENT using an Eulerian-Eulerian multiphase model with the standard k-ε turbulence model for both phases. Although the model does correctly predict the flow rate in some channels, the errors between the measured inlet qualities and the CFD predictions are large in many cases and generally do not follow the same trends. Zou and Hrnjak (2016) also presented the local liquid volume fractions and velocity profiles computed by the numerical model, which show some interesting flow phenomena, but further work is needed to develop a CFD simulation that accurately predicts the experimental results.

CFD studies could help improve the understanding of two-phase flow distribution by providing detailed information about the local pressures and velocities in headers; however, past work in this area is limited. Additionally, the models that have been developed either have not been specifically validated in distributors or do not accurately match experimental data. Future work is needed to advance this area of research so that it can be leveraged to help explain the factors affecting two-phase flow distribution.

2.3 Objectives of Present Study

Although several researchers have investigated two-phase flow distribution in multichannel heat exchangers, there are still significant gaps in the literature. There is

disagreement on the effects of inlet conditions (specifically quality) and heat exchanger geometry on flow distribution. Additionally, there has been limited work on flow distribution in plate-type heat exchangers and only a handful of studies that investigate header modifications that are applicable to these types of components. Modeling work in this area has also lagged, and new, computationally efficient approaches are needed that consider the complex forces that affect distribution in heat exchangers.

This study aims to quantify and understand the underlying mechanisms involved in two-phase flow distribution in horizontal plate-type heat exchanger manifolds with vertical-downward channels. The specific objectives of this study are listed below:

1. Develop an experimental approach and data analysis procedure to accurately measure two-phase flow distribution in a representative plate-type heat exchanger header, including the development of compact sensors capable of measuring refrigerant flow rates in multiple parallel channels.
2. Conduct distribution experiments with air-water mixtures and saturated refrigerants for a range of inlet mass fluxes and qualities.
3. Identify major flow regimes in plate-type heat exchanger headers using high-speed visualization techniques.
4. Develop and validate a flow mechanism-based model for predicting the liquid and vapor flow rates of a refrigerant into each channel of a microchannel heat exchanger.

CHAPTER 3. AIR-WATER EXPERIMENTS

This chapter presents the results from an experimental study on the distribution of air-water mixtures in plate-type heat exchanger headers attached to 1-, 2-, and 3-mm diameter downward vertical channels. Rectangular and triangular headers are both evaluated to understand the effect of manifold geometry on distribution. The distribution is quantified in these headers for average channel mass fluxes ranging from 50 to 300 kg m^{-2} s^{-1} (corresponding to inlet mass fluxes between 2.6 and 200 kg m^{-2} s^{-1}) and header inlet qualities ranging from 0.05 to 0.35. Air and water flow rates are measured at the outlet of each channel, and the flow regimes present in the header and the parallel outlet channels are characterized using high-speed flow visualization. The effects of header geometry and operating conditions on two-phase flow distribution are assessed based on these measurements.

3.1 Experimental Approach

A test facility was constructed to determine the degree of two-phase flow maldistribution in heat exchanger manifolds under a variety of operating conditions. The facility contains instrumentation to measure air and water flow rates in each channel, and the pressure drop across the header. A description of the facility and the test section are provided below.

3.1.1 Flow Loop and Experimental Procedure

The test facility used for this study is shown schematically in Figure 3.1. Liquid water enters the facility through a small centrifugal pump and air enters the facility from a

laboratory compressed air line. The air and water inlet flow rates are estimated using gas and liquid rotameters and are controlled using plug and needle valves. Although the rotameters are used to set the inlet flow rates for each test, the sum of the measured outlet flow rates is used in the data analysis to reduce uncertainty. The water and air are combined in a mixing section and sent to the test section through the inlet feeder tube. The feeder tube has an inner diameter of 6.35 mm and a length of 942 mm. A large length-to-diameter ratio was chosen for the feeder tube to achieve fully developed two-phase flow at the test section inlet. An accumulator is attached to the feeder tube to prevent large pressure fluctuations at the inlet of the test section. At the entrance of the test section, the mixture temperature is measured using a T-type thermocouple. After the flow passes through the inlet tube, it enters the test section and is distributed into three parallel channels. The differential pressure between the inlet of the test section and 7.11 mm down the length of each parallel channel is measured with a Rosemount 3051CD differential pressure transducer (shown as an inset in Figure 3.1). The three channels are connected to the pressure transducer through a series of valves, used to select the appropriate pressure tap for each measurement. After the two-phase mixture exits each channel, it enters a separator. The liquid exits the system through the bottom of the separator and is collected and weighed. The gas exits through the top of the separator and a turbine flow meter measures the flow rate. Four sets of turbine flow meters with different specified ranges were used in these experiments to collect data over the entire range of interest with a low uncertainty. Specifications and uncertainties of the measurement devices are presented in Table 3.1.

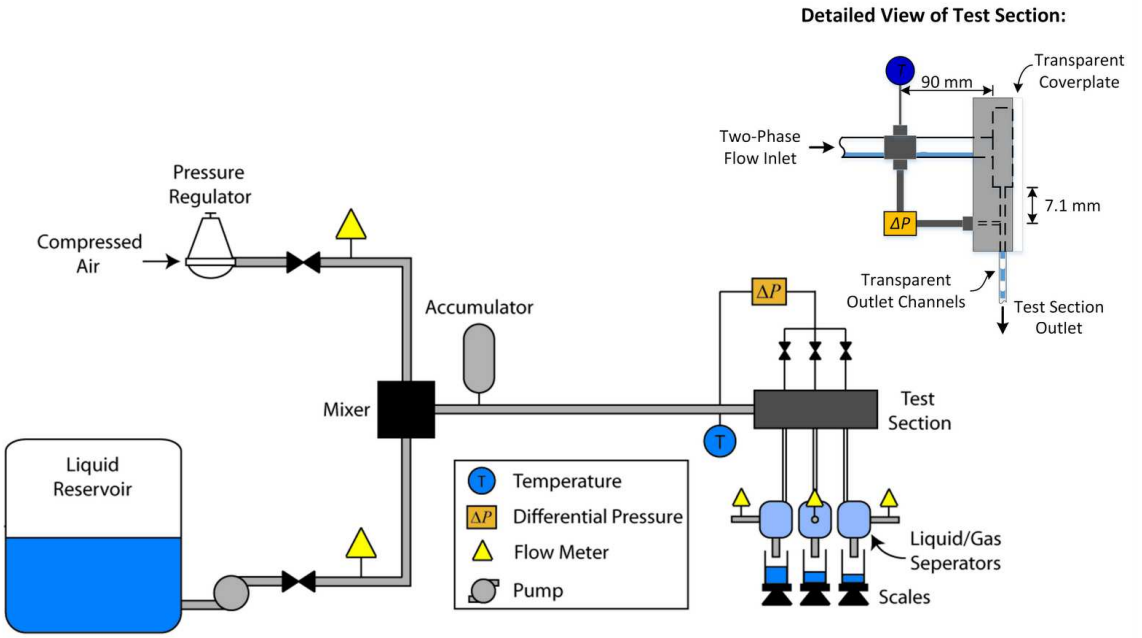

Figure 3.1: Schematic diagram of test facility with a detailed view of the test section.

Instrument signals from the pressure transducer, the thermocouple and the outlet air flow meters are recorded using a National Instruments data acquisition system. After steady state is achieved, four data sets are taken for 30 seconds each. The first data set is taken when all of the valves to the pressure transducer are closed to ensure that the pressure ports do not interfere with the flow distribution measurements. The pressure drop from the inlet of the test section to the entrance of each channel is then collected by opening one valve at a time and collecting 30 seconds of data. During each test, the liquid mass flow rate is determined by subtracting the initial and final weight of the water displayed by the scales. This procedure is repeated for both header geometries and three different outlet channel sizes for average channel mass fluxes between 50 and 300 kg m^{-2} s^{-1} and qualities between 0.05 and 0.35.

Table 3.1: Summary of instrument specifications

Physical Parameter	Instrument	Range	Uncertainty
Inlet Air Volumetric Flow Rate	Rotameter	0.472 – 5.19 L min^{-1} 2.36 – 9.44 L min^{-1} 9.44 – 94.4 L min^{-1}	0.208 L min^{-1} (4% FS) 0.283 L min^{-1} (3% FS) 1.89 L min^{-1} (2% FS)
Inlet Water Volumetric Flow Rate	Rotameter	5.0 – 46 cm^3 min^{-1} 50 – 496 cm^3 min^{-1}	2.33 cm^3 min^{-1} (5% FS) 24.8 cm^3 min^{-1} (5% FS)
Outlet Air Volumetric Flow Rate	Turbine Flow Meter	0.1 – 0.5 L min^{-1} 0.4 – 2 L min^{-1} 2 – 10 L min^{-1} 10 – 50 L min^{-1}	0.015 L min^{-1} (3% FS) 0.06 L min^{-1} (3% FS) 0.3 L min^{-1} (3% FS) 1.5 L min^{-1} (3% FS)
Outlet Water Mass Flow Rate	Scale	0.1 – 2000 g	0.1 g readability
Test Section Differential Pressure	Differential Pressure Transducer	0 – 15000 Pa	15 Pa
Thermocouple	T-Type	0 – 100ºC	0.3ºC

After data collection, high speed videos are taken of the header and the parallel channels. A high-speed video camera (Photron FASTCAM SA4 with Nikon Micro-NIKKOR 105 mm lens) is aligned perpendicular to the flow and high intensity lights are used to illuminate the test section. The Photron FASTCAM viewer software is used to capture the videos and to adjust the image resolution, frame rate, and shutter speed. All videos are one second in duration and are taken at a frame rate of 3600 fps and a shutter speed of 1/5000.

3.1.2 Test Section

The test sections consist of an inlet header and three parallel outlet channels. Rectangular and triangular header geometries were investigated because of their common use in plate-type heat exchangers. Schematics of the different geometries are shown in

Figure 3.2. The test section dimensions were determined using a pressure drop model similar to the model developed by Ablanque et al. (2010). This model divides the header into a series of T-junctions. The pressure drop through each T-junction is calculated using the Tae and Cho (2006) correlation, while the void fraction at the inlet of each channel is calculated using the Hwang et al. (1988) phase splitting model. The pressure drop in the parallel outlet channels is calculated using the Mishima and Hibiki (1996) correlation, and the pressure drops through all flow paths are set to be equal. The rectangular header has a height of 11.3 mm, a width of 52.8 mm, and a depth of 3.50 mm. The triangular header has the same base dimensions, but a wedge is added to change the manifold shape. The header is machined out of a block of aluminum and sealed on the top face by a polycarbonate window so that the header flow patterns could be recorded using the high-speed video camera. Major flow regime categories were defined through visual observation of the two-phase flow characteristics inside the header.

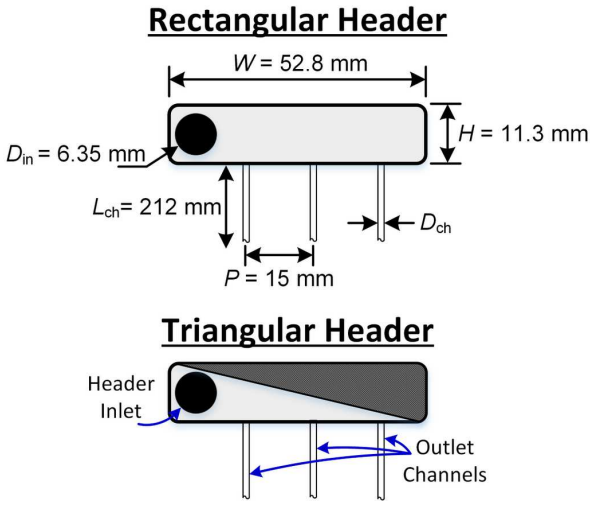

Figure 3.2: Schematic of header geometries tested with key dimensions.

For both geometries, the two-phase mixture enters the test section through a horizontal feeder tube positioned perpendicular to the header flow direction. The fluid is distributed in the test section and exits through the three parallel outlet channels on the bottom face of the header. The parallel channels are 212 mm long, have an inner diameter of 1, 2, or 3 mm, and are made of glass for flow visualization purposes. A summary of the important geometric and operational parameters used in this study are presented in Table 3.2.

Table 3.2: Important operational and geometric parameters

Parameter	Values
Inlet Quality	0.05 – 0.35
Average Channel Mass Flux	50.0 – 300 kg m^{-2} s^{-1}
Outlet Channel Diameter	1 – 3 mm
Inlet Mass Flux	2.60 – 200 kg m^{-2} s^{-1}
Feeder Tube Diameter	6.35 mm
Rectangular Header Dimensions ($L \times W \times H$)	52.8 mm × 3.50 mm × 11.3 mm

3.1.3 Data Analysis

The recorded flow rates are non-dimensionalized with respect to the perfectly distributed flow rate, which represents the phase flow rate if the header distributed the fluid equally in all the channels. This is shown in Equation 3.1, where *j* is the channel number, $\dot{m}$ is the phase mass flow rate in a given channel, and *N* is the total number of channels.

$$\dot{m}_j^* = \frac{m_j}{m_{in}/N} = \frac{m_j}{\sum_{i=1}^{N} m_i/N} \tag{3.1}$$

Although the non-dimensional flow rates provide information about the liquid and gas distribution in the header, it is difficult to compare the results with these values alone. A distribution parameter, the normalized standard deviation (NSTD), is used to quantify the overall degree of liquid and gas maldistribution in these experiments. This value is the ratio of the standard deviation of the flow rates and the maximum possible standard deviation, as shown in Equation 3.2, where $\dot{m}^*$ is the non-dimensional phase flow rate in a given channel and *N* is the total number of channels.

$$NSTD = \sqrt{\frac{\sum_{j=1}^{N}\left(m_j^* - 1\right)^2}{(N-1)N}} \tag{3.2}$$

The normalized standard deviation was chosen because it bounds the distribution parameter between 1 (worst case) and 0 (best case). It has also been used by other authors (Marchitto *et al.*, 2008) to quantify flow distribution in header geometries.

3.2 Results and Discussion

3.2.1 Header Flow Regimes

Flow patterns in heat exchanger headers differ from those in horizontal channels because of the complex geometry. Several authors have concluded that header flow regimes have a significant effect on distribution (Fei and Hrnjak, 2004; Ahmad *et al.*, 2009; Kim *et al.*, 2011); however, there is little information in the literature on the flow regimes present in plate-type heat exchanger headers. To understand the flow mechanisms pertinent to two-phase flow distribution, the header flow regimes observed in this study are categorized into five major groups, as shown in Figure 3.3.

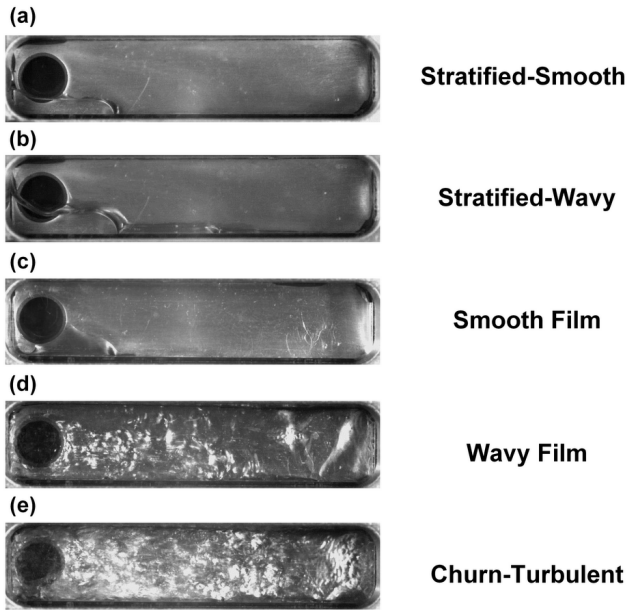

Figure 3.3: Photographs of flow regimes observed in the rectangular header.

At low superficial phase velocities ($j_l < 0.05$ m s^{-1} and $j_g < 4.5$ m s^{-1}), which generally correspond to conditions with low inlet mass fluxes, the flow regime in the header is stratified-smooth, as shown in Figure 3.3(a). This flow pattern occurs when the liquid and gas phases are separated by a relatively smooth and stable interface. Liquid only flows through one channel in this regime because the liquid momentum and the gas shear stresses are not sufficient to carry the liquid past the first header outlet.

In most cases, liquid enters the channel closest to the inlet in the stratified-smooth regime. However, the first channel occasionally becomes blocked by liquid slugs, forcing the liquid into the second channel. An image of the header and the channel flows for this condition is shown in Figure 3.4. In this image, the left channel is blocked, the middle channel contains liquid and gas flow, and the right channel is dry. Channel blockage generally occurs in smaller diameter outlet channels experiencing slug flow. In these channels, gas plugs span the entire channel diameter and cause a surface-tension-induced

pressure difference between the gas immediately above and below each liquid slug. When the pressure drop due to surface tension is equal to the pressure drop in the remaining outlets, the channel becomes blocked. The liquid slugs can be discharged from the blocked channel by increasing the pressure in the header; however, in these experiments no attempt was made to clear a channel if the condition persisted at the desired flow rates. In evaporators or condensers, this condition would likely not continue during steady-state operation due to the ongoing phase change, but it could cause instabilities in the component.

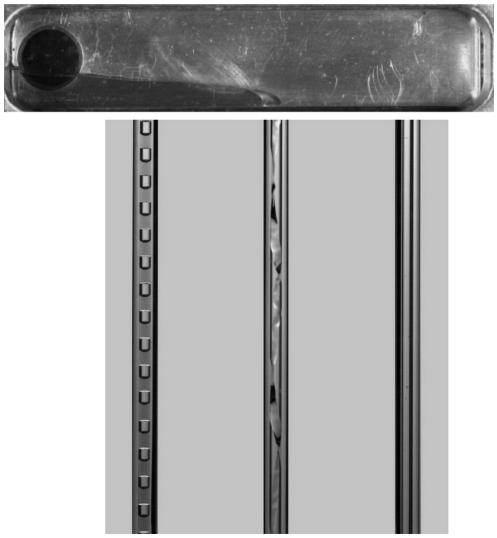

Figure 3.4: Photographs of the header and channels when one channel is blocked by liquid slugs (left channel).

At higher inlet mass fluxes and low qualities, corresponding to conditions with higher superficial liquid velocities ($0.05 < j_l < 0.10$ m s^{-1} and $j_g < 4.5$ m s^{-1}), the interface between the two phases becomes wavy as Helmholtz instabilities develop. This flow regime is classified as stratified-wavy and is shown in Figure 3.3(b). If the amplitude of

the interfacial waves is large, the waves crest over the first header outlet and liquid flows through downstream channels, improving liquid distribution.

At relatively low superficial liquid velocities ($j_l < 0.10$ m s^{-1}) and higher superficial gas velocities ($4.0 < j_g < 30$ m s^{-1}), the header flow regime transitions to film flow, as shown in Figures 3.3(c) and 3.3(d). In this regime, the liquid forms a thin film against the back wall of the header, which occurs when the gas dynamic pressure is significantly higher than the liquid dynamic pressure at the header inlet. This flow pattern may be caused by a pressure gradient that forms between the front and back faces of the header with a stagnation point directly adjacent to the header inlet. The gas has a higher dynamic pressure at the inlet in this regime; therefore, it may also have a higher stagnation pressure causing it to flow near the front face of the header. At the lower range of superficial gas velocities present in this regime (< 10 m s^{-1}), the interface of the film is relatively smooth and the film only wets the back surface of the header near the inlet. This subcategory of the film flow regime is classified as smooth-film flow. As the inlet gas velocity increases, the interface again becomes wavy as Helmholtz instabilities develop. This regime is categorized as wavy film. The distribution is usually better for the wavy film flow regime than for the smooth-film regime because the shear stresses at the interface pull more of the liquid away from the inlet and distribute it to downstream channels.

Finally, at high superficial gas (> 4.0 m s^{-1}) and liquid velocities (> 0.10 m s^{-1}), the header flow regime is churn-turbulent, as shown in Figure 3.3(e). The flow begins to transition to this regime when liquid droplets break off from the wavy-film or stratified-wavy interface and are propelled to the back of the header. As the gas and liquid superficial velocities increase past the transition velocities, the two phases become well mixed in the

header. Typically, churn-turbulent flow forms when the flow regime in the feeder tube is annular; however, an intermittent form of churn flow occurs when the regime in the feeder tube is slug flow.

The flow regimes observed in the rectangular and triangular headers are plotted as a function of inlet liquid and gas superficial velocities in Figure 3.5. The plots show distinct regions where each flow regime is present. The main difference between the rectangular and triangular geometries is the locations of regime transitions. This is discussed in more detail in a subsequent section.

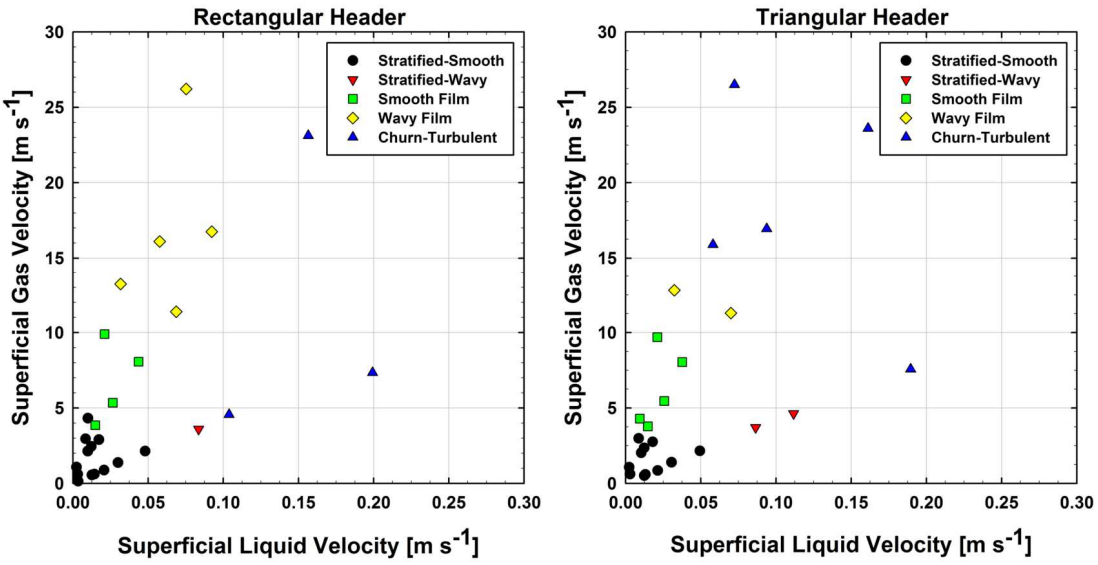

Figure 3.5: The observed flow regimes as a function of superficial liquid and gas velocities for the rectangular (left) and triangular (right) header geometries.

3.2.2 Effects of Average Channel Mass Flux on Distribution

Figure 3.6 shows the liquid and gas phase flow rates in each channel at a constant inlet quality of 0.20 over the full range of average channel mass fluxes tested. These data were collected using a rectangular header connected to 1-, 2-, and 3-mm diameter outlet

channels. The inlet feeder tube diameter was held constant; therefore, increasing the channel diameters while keeping the average channel mass flux constant represents an increase in the header inlet mass flux.

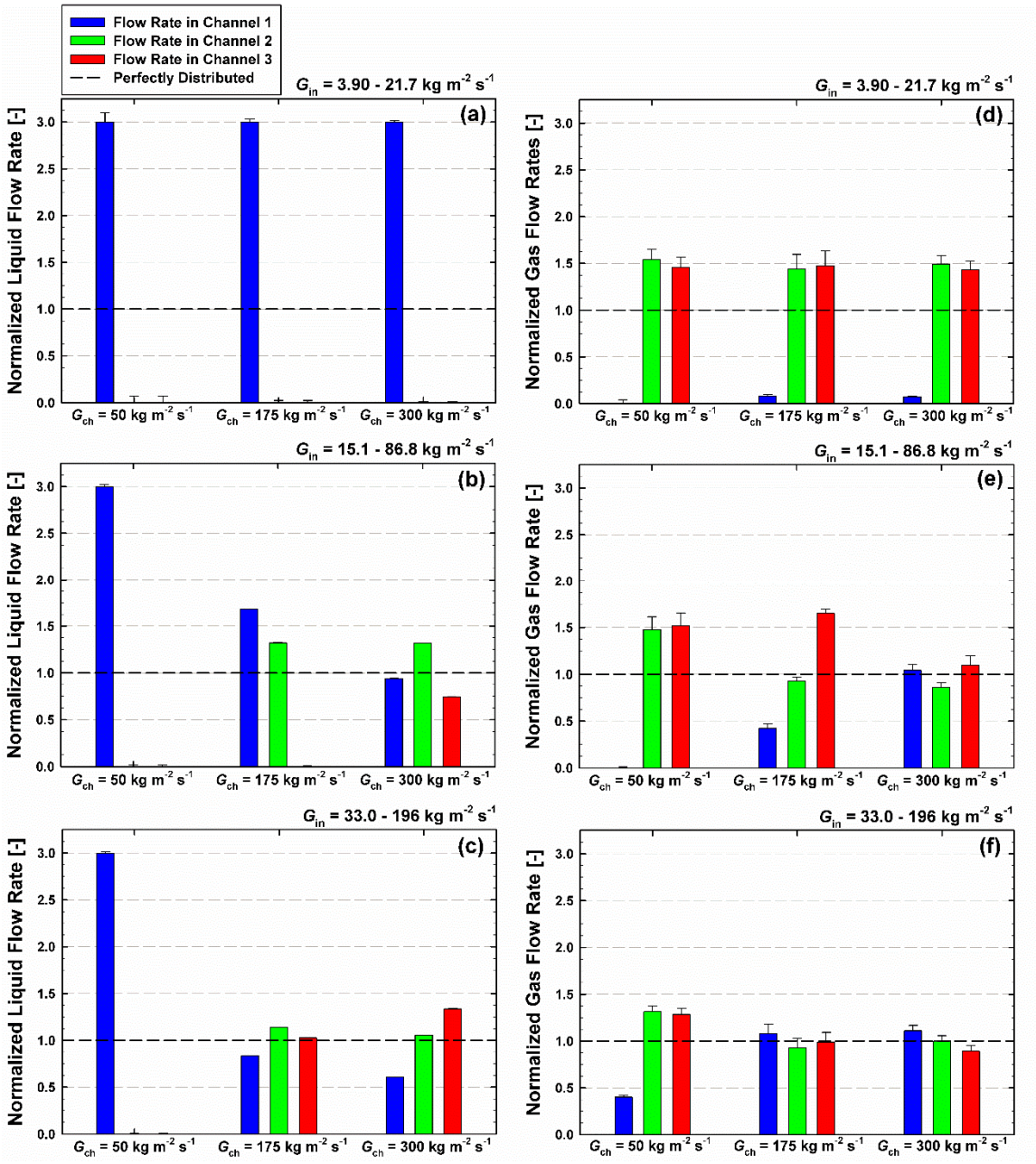

Figure 3.6: Normalized liquid and gas flow rates through each channel in the rectangular header connected to 1- (a and d), 2- (b and e), and 3-mm (c and f) diameter outlet channels with an inlet quality of 0.20.

The average channel mass flux does not affect the gas or liquid distribution for the smallest (1 mm) outlet channel diameters, as shown in Figures 3.6(a) and 3.6(d). For these conditions, the mass fluxes entering the header are relatively low (between 3.6 and 22.3 kg m^{-2} s^{-1}), causing the header flow regime to be stratified-smooth for all three cases. The stratified-smooth flow regime forces all the liquid to enter the first outlet channel, resulting in the worst possible liquid distribution. The gas distribution is better because the air is distributed relatively evenly between the channels free of water; however, the gas distribution is still among the worst observed in these experiments.

The average channel mass flux has a significant effect on distribution for the headers connected to the 2- and 3-mm diameter outlet channels. At the lowest average channel mass flux in the 2-mm diameter outlet channels (50 kg m^{-2} s^{-1}), the flow regime in the header is stratified-smooth and the distribution of the liquid and gas is poor. As the mass flux increases, the regime transitions to stratified-wavy flow. This condition exhibits better distribution characteristics because the higher momentum and interfacial shear stress transports more liquid to downstream channels. Finally, at an average channel mass flux of 300 kg m^{-2} s^{-1}, the flow transitions to wavy-film flow and the distribution improves significantly. In this case, all the outlet channels receive both liquid and gas and the phase flow rates are within 32% of the mean.

The mass flux trends are similar in the header connected to the 3-mm diameter outlet channels, as shown in Figures 3.6(c) and 3.6(f). At an average channel mass flux of 50 kg m^{-2} s^{-1}, liquid only flows through the first channel causing the liquid distribution to be poor. However, since the flow is in the smooth-film regime, gas can enter all the outlet channels and the gas distribution is better than the low flow rate conditions in the other test sections.

At average channel mass fluxes of 175 and 300 kg m^{-2} s^{-1}, the distribution again improves significantly. This improvement can be attributed to the flow regime transitions to wavy-film and churn-turbulent flows in the intermediate and high mass flux cases, respectively.

From the data presented above, two-phase flow distribution seems to be more dependent on the header flow regime and the inlet mass flux than on the average channel flow rates. The effect of inlet mass flux on the degree of maldistribution (quantified using the *NSTD*) at an inlet quality of 0.20 is shown in Figure 3.7. The header flow regimes are overlaid on the figure with representative images for each classification. Flow regime transition lines are shown for clarity; however, specifying a distinct mass flux where the transition occurs is an oversimplification. Transitions occur over a continuum and there are ranges of conditions where aspects of more than one primary regime are present, depending on several parameters including inlet mass flux, quality, fluid properties and pressure drop.

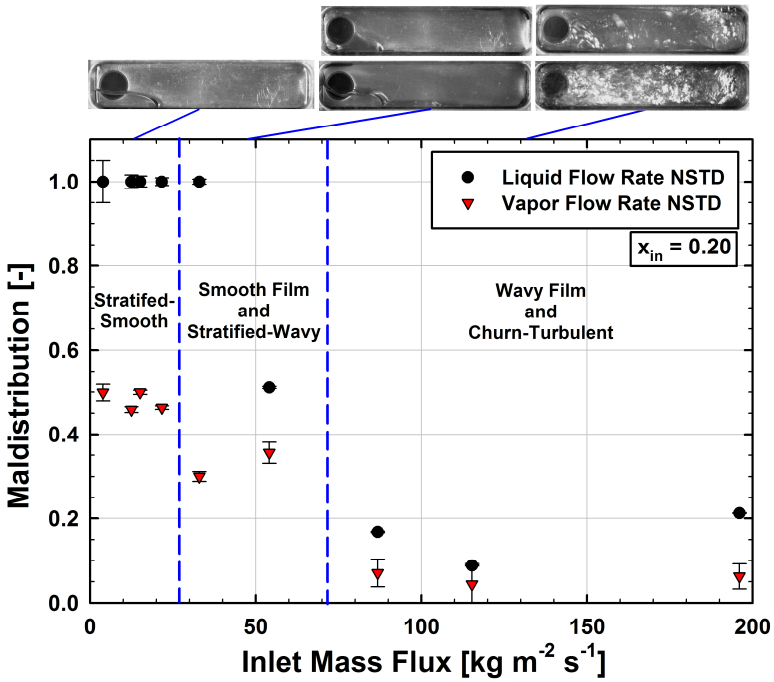

Figure 3.7: Normalized standard deviation of the liquid and gas flow rates at an inlet quality of 0.20, overlaid with flow regime classifications.

The results show that the header does not perform well in the stratified-smooth flow regime, with poor distribution of both the liquid and gas phases. As the inlet mass flux increases, the header flow transitions from stratified to wavy-film and churn flow regimes. The liquid and gas distribution improve significantly in these cases, with maximum liquid and gas normalized standard deviations of 0.21 and 0.07, respectively.

3.2.3 Effects of Inlet Quality on Distribution

Similar to the channel mass flux effects, inlet quality does not affect flow distribution at low inlet mass fluxes, corresponding to the smallest diameter outlet channels. At higher inlet mass fluxes (above about 20 kg m^{-2} s^{-1}), the phase distributions generally improve with increasing quality. The distribution improves because higher qualities correspond to higher superficial gas velocities and more favorable flow regimes for distribution. This is

shown graphically in Figure 3.8, which shows the phase distribution as a function of the inlet mass flux at qualities of 0.05 and 0.35. At a quality of 0.05, more than half of the data are in the stratified-smooth flow regime and the flow does not transition to a more favorable flow regime until an inlet mass flux of ~70 kg m^{-2} s^{-1}. However, at higher qualities, the transition line between stratified-smooth and film flow shift to an inlet mass flux of ~20 kg m^{-2} s^{-1}, resulting in fewer data points with extremely poor distribution characteristics.

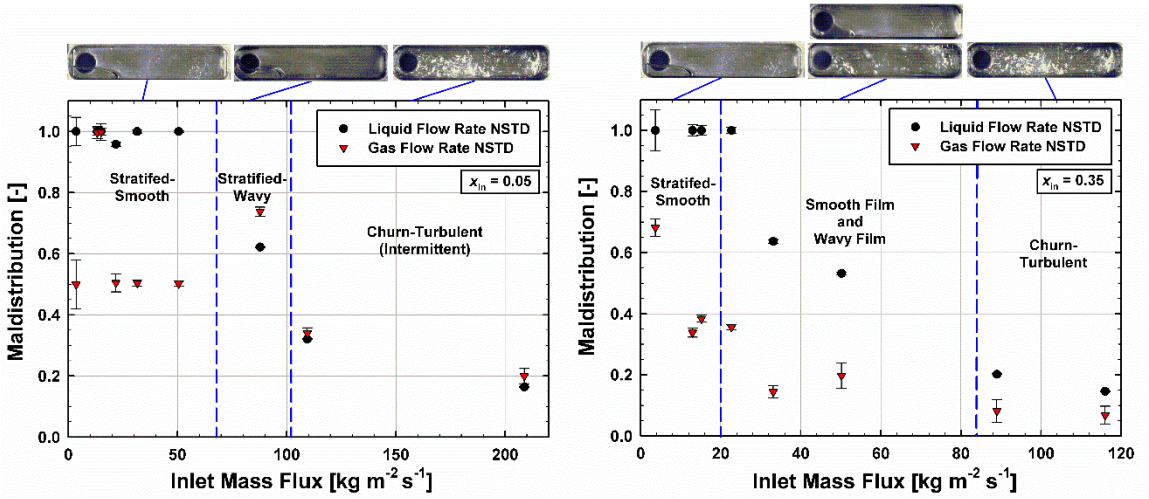

Figure 3.8: Normalized standard deviation of the liquid and gas flow rates at inlet qualities of 0.05 (left) and 0.35 (right), overlaid with flow regime classifications.

3.2.4 Effects of Header Geometry on Distribution

The overall effect of header geometry on distribution is quantified using the difference between the normalized standard deviations of the phase flow rates for the rectangular and triangular headers. This parameter is called the distribution difference for the *i*-phase and is given as:

$$Distribution\ Difference_i = NSTD_{i,rect} - NSTD_{i,tri} \tag{3.3}$$

When the distribution difference is positive, the triangular header has better distribution characteristics because well distributed flows have low NSTD values. The liquid and gas distribution differences are plotted as a function of inlet superficial liquid and gas velocities in Figure 3.9. The red data points indicate that the triangular header performs better, the blue points indicate that the rectangular header performs better, and the white data points indicate that the geometry does not affect the distribution.

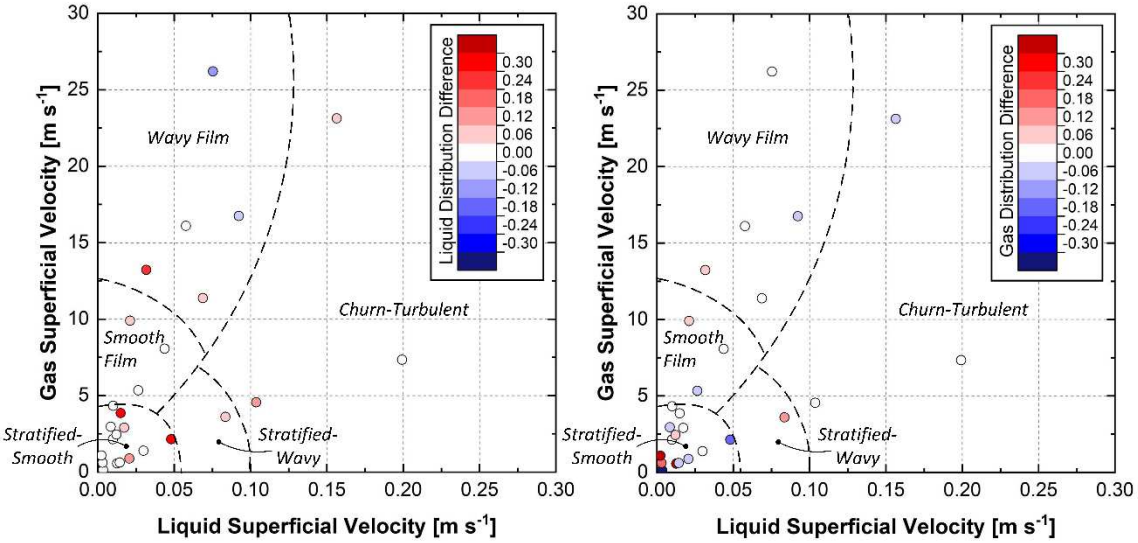

Figure 3.9: Color map showing the difference between the normalized standard deviation of the liquid (left) and gas (right) flow rates in the rectangular and triangular headers as a function of phase superficial velocities.

The results show that the triangular header either does not change or improves the distribution of the liquid phase for about 92% of the data collected. Furthermore, the triangular header has zero or a positive effect on the gas distribution for about 77% of the data. The average distribution differences for the liquid and gas phases are 0.060 and 0.042, respectively. Although the average distribution difference indicates that the triangular header has a slight positive impact on the flow distribution when considering all the

conditions tested, it has the largest effect near flow regime transitions. This is evident when comparing the distribution differences with the flow regime map shown in Figure 3.5. The areas that exhibit characteristics of each primary flow regimes are redrawn on Figure 3.9 with dashed lines. These lines are shown for the sake of discussion but are not meant to specify the precise locations of flow regime transitions. Significantly more data are needed to make strong conclusions about the locations of the transition regions between different regimes, which is outside the scope of this study.

The conditions with the largest liquid distribution difference occur at the outer boundaries of the stratified-smooth flow region and the transition between the smooth-film and wavy-film regimes. This effect can be attributed to the local phase velocities in the header. As the air-water mixture flows away from the inlet in the rectangular header, the local liquid and gas superficial velocities decrease because some of the fluid exits through the first outlet channels. This decrease in velocity can lead to transitions in the local flow regimes in the header. For example, at an inlet mass flux of 86.8 kg m^{-2} s^{-1} and an inlet quality of 0.21 (j_l = 0.07 m s^{-1} and j_v = 11.7 m s^{-1}), the flow enters both test sections as wavy-film flow. In the triangular header, this flow regime persists throughout the header because the phase velocities stay relatively constant. In the rectangular header, the flow transitions to smooth film, and even has areas of complete dryout downstream of the inlet. When this occurs, downstream channels are starved of liquid and the flow is more maldistributed. This phenomenon is shown in Figure 3.10, which compares the normalized liquid flow rates for this condition in both header geometries. The normalized standard deviations of the liquid flow rates in the rectangular and triangular tests sections are 0.168 and 0.072, respectively.

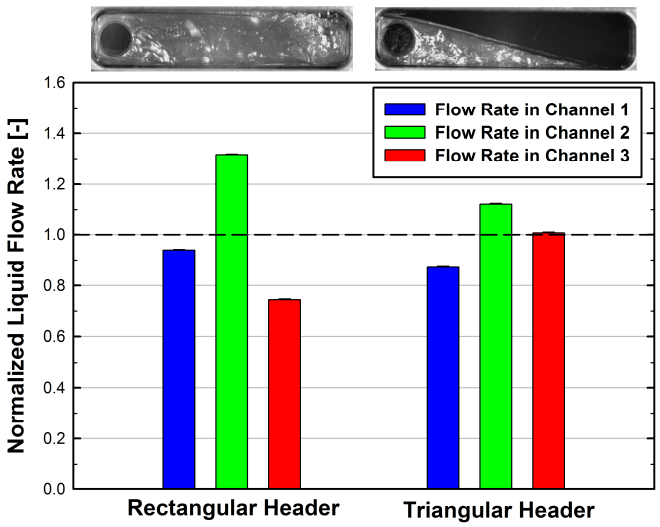

Figure 3.10: Normalized liquid flow rates for rectangular and triangular headers connected to 2 mm outlet channels. Images of the header flow regimes for this condition are shown above the plot.

Although the largest changes in liquid distribution between the rectangular and triangular header generally occur around flow regime transitions, the largest changes in gas distributions occur at very low superficial phase velocities (Figure 3.9). This is a result of the slug-induced channel blockages that occur for these conditions, as described in Section 3.2.1. In some cases, one channel is blocked in the rectangular header and is clear in the triangular header, or vice-versa. A blocked channel has a profound effect on the gas distribution because it forces most of the air flow into a single channel. This change is likely not caused by the manifold geometry because the pressure drop characteristics are nearly identical in the two test sections and channel blockages were observed for low flow rate conditions in both geometries.

3.2.5 Header Pressure Drop

Flow distribution in headers is dictated by transport properties, which are dependent on phase velocities and header flow regimes, and by pressure drop. Pressure drop in headers is difficult to predict because of the complex three-dimensional geometries involved. To date, there is no straightforward way to predict two-phase pressure drop in header systems.

As a part of this study, the pressure drop across the header was measured (as shown in the Figure 3.1 inset). Due to spatial limitations, this measurement includes the pressure drop in a portion of the feeder tube and outlet channels. These pressure drop contributions are estimated using the correlations developed by Friedel (1979) and Mishima and Hibiki (1996), respectively. The predicted values are assigned a 25% uncertainty and are subtracted from the total measurement to isolate the pressure drop in the header, as shown in Equation 3.4. The total header pressure drop includes frictional losses, minor losses due to the complex flow patterns and the contraction into the outlet channels, and effects of fluid deceleration in the header.

$$\Delta P_{header} = \Delta P_{meas} - \phi_{lo,F}^2 \left(\frac{2 f_{lo} G_{in}^2}{\rho_l D_{feed}} \right) L_{feed,out} - \phi_{l,MH}^2 \left(\frac{2 f_l G_l^2}{\rho_l D_{ch}} \right) L_{ch,in} \qquad (3.4)$$

The average pressure drop across the header is shown in Figure 3.11. The plot includes data for average channel mass fluxes between 50 and 300 kg m^{-2} s^{-1} and an inlet quality of 0.20. The results show that for a given channel diameter, the average pressure drop across the header increases with inlet mass flux. This trend can be attributed to the higher phase velocities in the header. Additionally, the channel diameter is found to have

a strong influence on pressure drop, suggesting that the minor loss resulting from the fluid contraction into the outlet channels contributes significantly to the total pressure drop. When compared with the maldistribution data in Figure 3.7, the results show that conditions with better distribution generally have higher average pressure drops. At these conditions, the phase velocities are relatively large, which allows the flow to transition to a more favorable flow regime for distribution (wavy film or churn-turbulent), but also increases both the frictional and minor losses in the header.

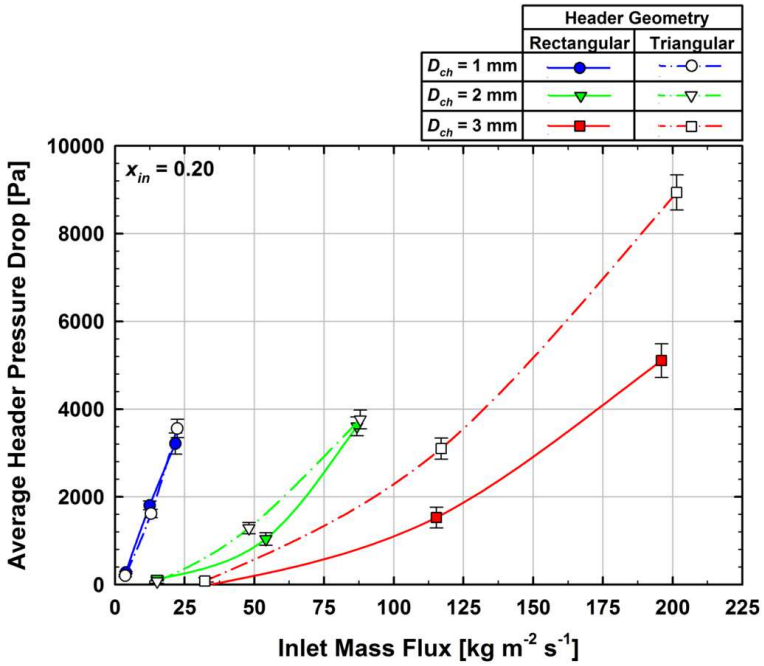

Figure 3.11: Average pressure drop across the test section for the rectangular and triangular test sections. The lines are added for clarity but are not fit to the data.

Figure 3.11 also compares the pressure drop in the rectangular and triangular headers. At inlet mass fluxes < 100 kg m^{-2} s^{-1}, the average pressure drop is approximately equal in both geometries for a given condition. However, at higher inlet mass fluxes, the pressure drop in the triangular header is significantly greater. This effect is examined

further using information about the pressure drop between the header inlet and the entrance of each channel. Figure 3.12 shows these measurements for the case with the largest average pressure drop deviation between geometries (G_{in} = 196 kg m^{-2} s^{-1}). In the rectangular header, the pressure decreases between the inlet and the first channel because of frictional losses and the area contraction into the outlet pipe. When some fluid leaves through the first channel, the total mass flow rate in the header downstream decreases. This causes the fluid to decelerate and the pressure to rise. Again, the pressure then drops due to frictional losses and the area contraction into the second outlet pipe. The results show that the pressure recovery due to fluid deceleration is significant for this case because the pressure drop is lower for channels further from the inlet. In the triangular test section, the velocity of the fluid stays relatively constant as it flows away from the inlet because of the decreasing header cross sectional area; therefore, large pressure recoveries are not expected. In this case, the pressure drop between the header inlet and the entrance of the first and second channels is ~7,700 Pa, but jumps to ~11,000 Pa for the last channel. This large increase in pressure drop is likely due to the decreasing cross-sectional area in the header, which increases the frictional component of the pressure drop. The comparison between the two geometries suggests that the pressure drop in the triangular header is higher than that in the rectangular header when the frictional pressure drop is dominant.

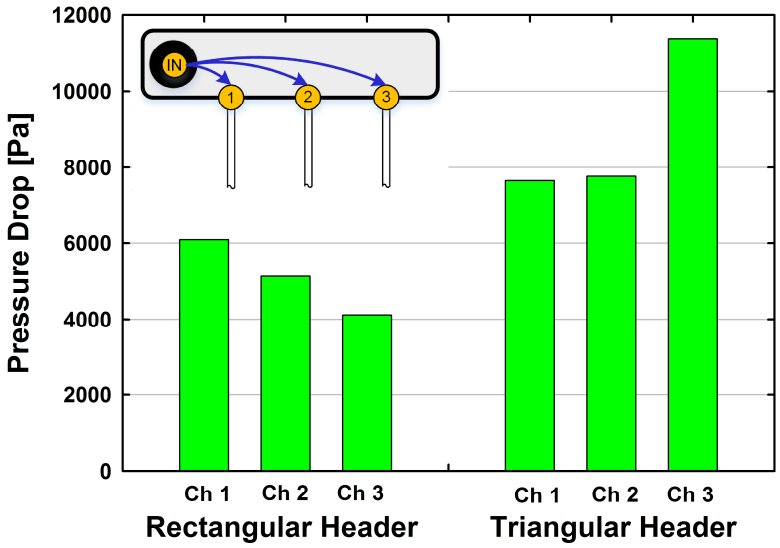

Figure 3.12: Pressure drop between header inlet and channel entrances at an inlet quality of 0.20 and an average channel mass flux of 300 kg m^{-2} s^{-1}

3.3 Conclusions from Air-Water Experimental Study

The results from this experimental study found that the flow regimes in the header have a large impact on liquid and gas distribution in heat exchangers. After observing the fluid dynamics in the header, five primary flow patterns were identified for horizontal plate-type heat exchanger manifolds with a horizontal inlet port that is perpendicular to the header flow direction. These flow regimes were mapped based on the inlet superficial phase velocities, as shown in Figure 3.5. At low inlet mass fluxes and qualities, corresponding to liquid superficial velocities < 0.05 m s^{-1} and gas superficial velocities < 5 m s^{-1}, it is found that the flow in the header is gravity dominated and the distribution in the header is poor. At higher inlet mass fluxes and qualities, the flow transitions from stratified to film or churn-turbulent flow, and distribution improves substantially because the high phase velocities increase the momentum and the interfacial shear stress, transporting more liquid to downstream channels. However, the improved distribution at

higher inlet flow rates comes with a pressure drop penalty, which should be considered when designing a heat exchanger manifold.

This study also investigated the effect of header geometry on distribution. Overall, the triangular header performed slightly better than the rectangular one, reducing the liquid and gas *NSTD* by 0.06 and 0.04, respectively. The largest improvement in the liquid distribution occurs when the inlet conditions are near a flow regime transition. The triangular header also had an impact on the gas distribution around flow regime transitions, but to a lesser degree.

CHAPTER 4. APPROACH AND DATA ANALYSIS FOR REFRIGERANT EXPERIMENTS

The air-water experiments described in Chapter 3 offer insights into the important parameters involved in maldistribution, but air-water mixtures are not typically of practical interest for heat and mass exchangers. Further experiments on the distribution of saturated refrigerants in manifolds were conducted to broaden the applicability of this study. This chapter discusses the experimental facility and measurement equipment developed and used to collect refrigerant distribution data and describes the data analysis approach used to calculate the inlet conditions and the distribution into each channel.

4.1 Facility Design and Instrumentation

A new test facility was constructed to measure the two-phase flow distribution of R134a in a heat exchanger header attached to ten parallel vertical channels. Measured parameters include header inlet mass flux and quality, header and test section pressure drops, channel flow rates, and channel inlet qualities. Components were sized so that the distribution could be quantified when refrigerant is supplied to the test section at a nominal saturation pressure of 770 kPa, average channel mass fluxes ranging from 50 to 200 kg m^{-2} s^{-1} (corresponding to header inlet mass fluxes between 23.9 and 95.6 kg m^{-2} s^{-1}) and qualities ranging from 0 to 1. To minimize heat losses and gains from the environment, the entire facility was insulated with fiberglass material ($k_{ins} = 0.042\ W\ m^{-1}K^{-1}$) with a minimum thickness of 25.4 mm.

4.1.1 Working Fluid Loop

A schematic of the experimental facility used to measure refrigerant distribution is shown in Figure 4.1. The refrigerant loop is shown in black, while the coolant loop is shown in blue. The refrigerant is circulated through the facility using a small gear pump. The total flow rate, temperature, and pressure of the subcooled refrigerant are measured at the exit of the pump (state point [1]) and the flow is directed into the pre-heater. The pre-heater adds heat to the fluid until it reaches the specified header inlet quality for the test. The power drawn by the heater, and the pre-heater outlet pressure are measured to fully determine the thermodynamic state at the header inlet (state point [2]). Losses to the ambient are considered in the calculation of the inlet quality and are described in more detail in Section 4.3. The pressure at the inlet of the test section is maintained at a nominal value of 770 kPa ($T_{sat} = 30°C$) using a piston accumulator connected to a compressed Nitrogen tank. The saturated refrigerant then enters the test section and is cooled by a chilled water loop. The refrigerant fully condenses and undergoes some degree of subcooling in the test section, and the temperature and pressure are measured to define the thermodynamic state at the test section exit (state point [3]). Finally, the refrigerant is further subcooled by an external chiller and returns to the pump (state point [4]). A summary of all the equipment and measurement devices in the refrigerant loop are provided in Tables 4.1 and 4.2, respectively. The measurement devices used in the test section to calculate the mass flux and inlet quality into each parallel heat exchanger channel are not included in Table 4.2 but are described in detail in Sections 4.1.3 and 4.2.

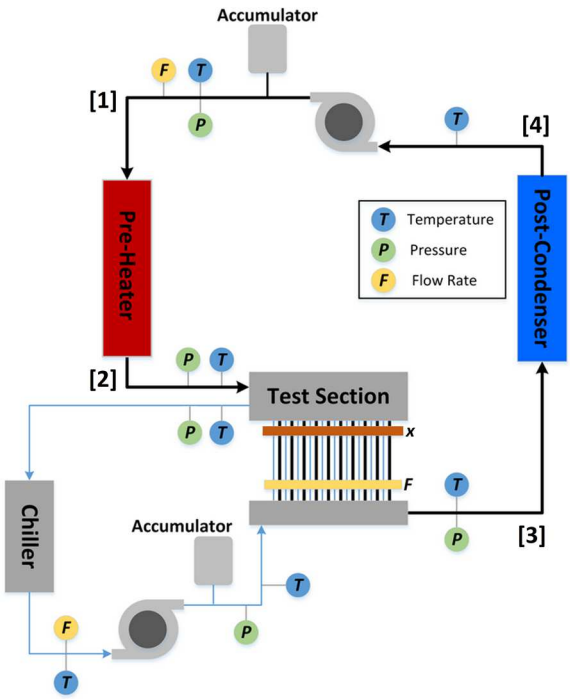

Figure 4.1: Schematic of refrigerant test facility

Table 4.1: Details of equipment in refrigerant loop

Component	Supplier	Part Number	Important Specifications
Pump Head	Micropump	GAH-V21.PFS.A	Displacement = 0.042 mL rev^{-1} Max Speed = 5500 RPM Max ΔP = 520 kPa
Pump DC Motor	Micropump	306A	Speed = 500 to 4000 RPM Power = 112 W/0.12 HP
Pump DC Power Supply	B&K Precision	1627 A	0 to 30 V Max Current = 3 amps
Pre-Heater	Watlow	SE-10705	Single Phase – 120 V Max Power = 1000 W
Variac Heater Controller	Staco Energy Products	3PN1010B	0 to 140 V Max Current = 10 amps
Chiller	Neslab	Merlin M75	Capacity = 2225 W Temperature = -15 to 35ºC
Piston Accumulator	Parker	ACP05AA050E1KTC	0.50-liter capacity

Table 4.2: Details of instrumentation in refrigerant loop

Measurement	Supplier	Part Number	Span and Uncertainty
Preheater Inlet Pressure	Rosemount	3051 CA4A22A1AM5	0 to 3500 kPa ± 2.625 kPa (Unc = ±0.075% span)
Test Section Inlet Pressure	Rosemount	3051 TA5A2B21AE5M5	0 to 3500 kPa ± 2.625 kPa (Unc = ±0.075% span)
Test Section Outlet Pressure	Rosemount	3051 TA5A2B21AE5M5	0 to 3500 kPa ± 2.625 kPa (Unc = ±0.075% span)
Header Differential Pressure	Rosemount	3051CD IA22AIAM5	0 to 6.0 kPa ± 0.005 kPa (Unc = ±0.075% span)
Test Section Differential Pressure	Rosemount	3051CD 3A22A1AB4E5M5	0 to 10.0 kPa ± 0.008 kPa (Unc = ±0.075% span)
Temperatures	Omega	TMQSS-062G-6	0 to 100°C ± 0.25°C
Mass Flow Rate	Micromotion	CMF010 H521NQBAEZZZ	0 to 100 g min^{-1} ± 0.25%
Preheater Power	Ohio Semitronics	GW5-10E	0 to 1000 W ± 0.5%

4.1.2 Coolant Fluid Loop

A chilled water loop, shown in blue in Figure 4.1, is used to fully condense the refrigerant as it flows through the test section. The water is circulated through the loop by a gear pump. The temperature and pressure of the water are measured at the inlet and outlet of the test section to determine the fluid states. Water temperatures and flow rates in each test section channel are also collected and are described in detail in Section 4.1.3. The water then flows through a heat exchanger coupled to an external chiller to reject the heat gained in the test section. Finally, the total flow rate of the water is measured using a Coriolis flow meter, and the liquid is returned to the pump. A summary of the equipment and instrumentation used in the coolant loop is provided in Tables 4.3 and 4.4, respectively.

Table 4.3: Details of equipment in water loop

Component	Supplier	Part Number	Important Specifications
Pump Head	Micropump	GB-P35.PVS.A	Displacement = 1.17 mL rev^{-1} Max Speed = 5500 RPM Max ΔP = 420 kPa
Pump DC Motor	Micropump	DP-415.A	Speed = 500 to 9000 RPM Power = 67 W/0.09 HP
Pump AC Power Supply	Micropump	DP-415.A	120 VAC, 50/60 Hz Max Current = 3.5 amps
Chiller	Neslab	Merlin M75	Capacity = 2225 W Temperature = -15 to 35°C
Diaphragm Accumulator	Accumulators Inc.	AM631003	0.10-liter capacity

Table 4.4: Details of instrumentation in water loop

Measurement	Supplier	Part Number	Span and Uncertainty
Test Section Inlet Pressure	Rosemount	2088 A3M22A1M7	0 to 2760 kPa ± 6.9 kPa (Unc = ±0.25% span)
Test Section Outlet Pressure	Rosemount	3051 CA4A22A1AM5	0 to 3500 kPa ± 2.625 kPa (Unc = ±0.075% span)
Temperatures	Omega	TMQSS-062G-6	0 to 100°C ± 0.25°C
Mass Flow Rate	Micromotion	CMFS010 M323N2BAECZZ	0 to 110 kg hr^{-1} ± 0.25%

4.1.3 Test Section

The refrigerant test section consists of an inlet header, ten parallel tube-in-tube heat exchangers, and an outlet header. A photograph of the full test section before it was insulated, and detailed views of the header and channels are shown in Figure 4.2. Saturated refrigerant enters the upper header and is distributed into 10 parallel 1-mm diameter channels. The total length of each minichannel is 0.5 m, while the active heat transfer

length is 0.41 m. The manifold has a transparent polyvinyl chloride cover plate so that the flow regimes can be visually identified and documented. Although the surface properties of the cover plate are different from those of the other surfaces in the header (aluminium), Smith *et al.* (2014) showed that the advancing and receding contact angles of R134a on low and high surface energy materials differ by about 2% and 12%, respectively. The use of a polymer cover plate could change some details of the flow patterns but should not have a significant effect on the global flow regime characteristics or distribution, because the contact angles are similar.

Once distributed, the refrigerant is cooled by chilled water flowing through an outer annulus. The annulus has an inner diameter of 2 mm and an outer diameter of 4 mm. The water flow through each annulus is measured with turbine flow meters (Omega FLR1007ST) with a measurement uncertainty of ±1% of the full scale (±1 mL min^{-1}), while the temperatures at the inlet and outlet are measured using calibrated T-type thermocouples (Omega TMQSS-062G-6). After the refrigerant exits the tube-in-tube heat exchangers, its temperature is measured with a calibrated T-type thermocouple (Omega TMQSS-062G-3), and the flow rate is measured with a thermal time of flight (TOF) flow meter. The construction and calibration of the time of flight sensors are described in Section 4.2.

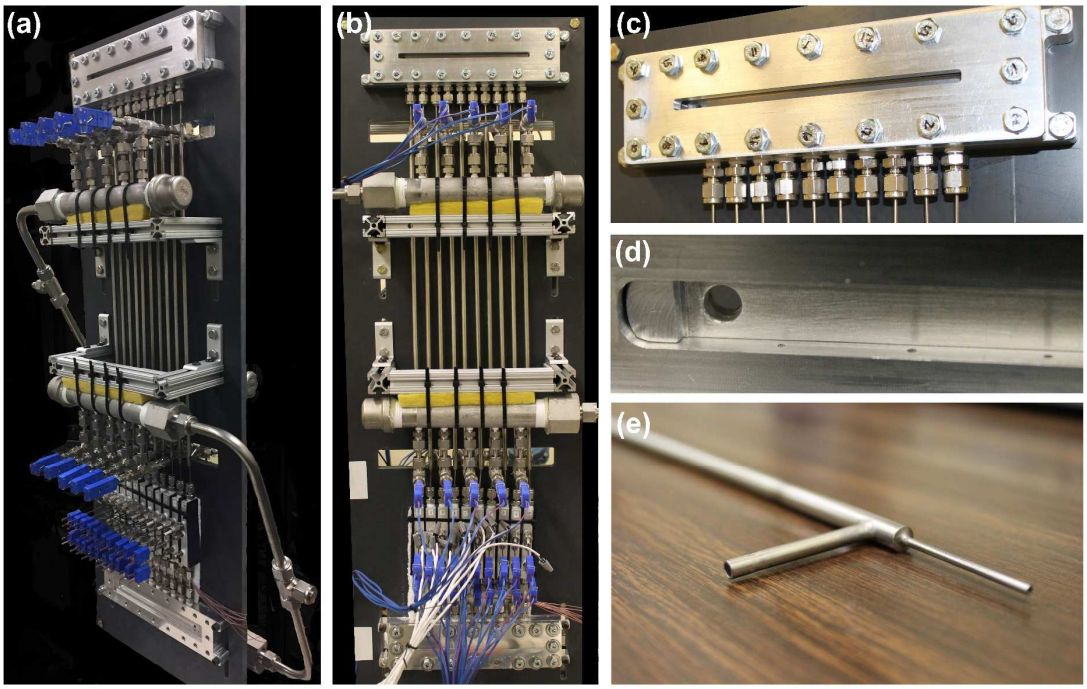

Figure 4.2: Photograph of (a, b) the full test section before it was insulated, (c) the inlet header assembly attached to 10 parallel outlet channels, (d) a detailed view of the rectangular inlet header insert and the outlet channel ports, and (e) the tube-in-tube heat exchangers attached to the inlet manifold.

The header assembly (Figure 4.2c) was fabricated so that different header shapes could be evaluated by changing the insert piece shown in Figure 4.2d. Initially a simple rectangular header was installed and tested over a wide range of operating conditions. The rectangular header has a height of 8.33 mm, a width of 155 mm, and a depth of 2 mm. The cross-sectional area of the header was designed to prevent a major constriction or expansion as the flow entered the test section, which could result in large minor losses. A detailed engineering drawing of the header assembly is shown in Figure 4.3.

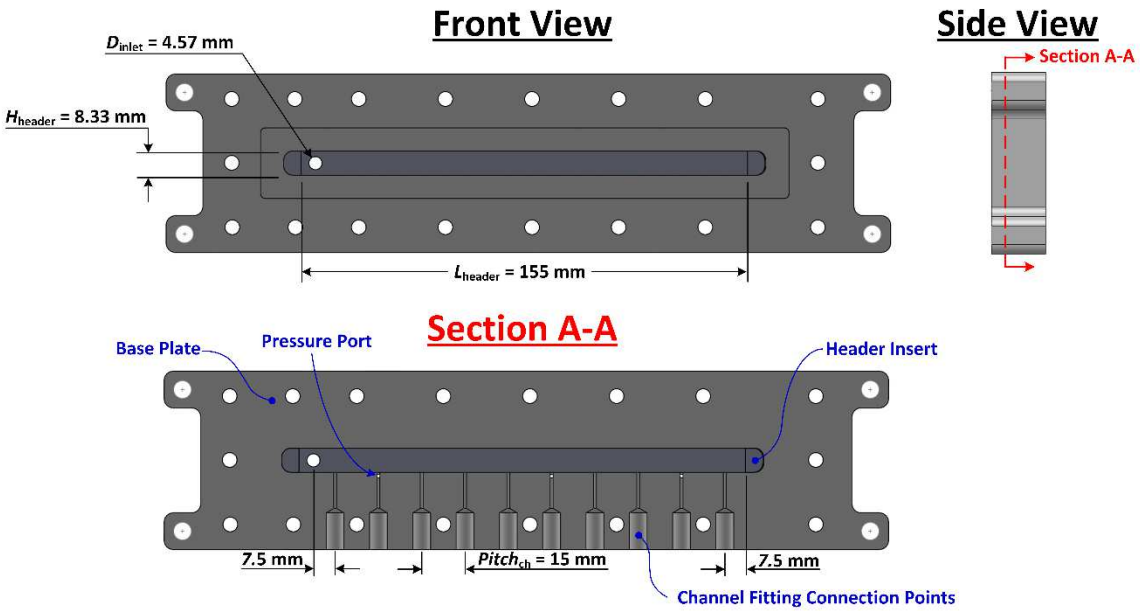

Figure 4.3: Detailed image of header base plate and insert with important dimensions

Two alternative header geometries with the same base dimensions were also fabricated and tested in the refrigerant test facility. Images of the three header inserts are shown in Figure 4.4. The triangular header has a solid wedge that reduces the cross-sectional area as the fluid flows away from the inlet. A triangular header was chosen to help maintain higher fluid velocities as the refrigerant flows away from the inlet, which could help transport more liquid to downstream channels. The vane header includes a tray with 0.4 mm slots located between adjacent refrigerant channels. The header was chosen to help promote the build-up of a liquid pool inside the header to help transport more liquid away from the inlet.

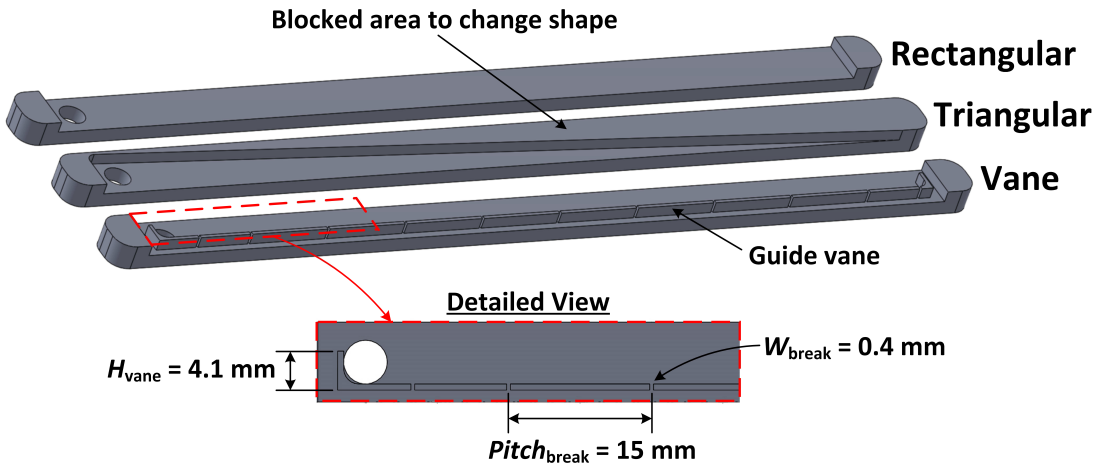

Figure 4.4: Photograph of the three header geometries investigated in this study

The pressure drops across the inlet header and the full test section were measured using Rosemount pressure transducers (Table 4.2). The upstream pressure port for both measurements is located in the preheater housing, as shown in Figure 4.5. A portion of the heater housing ($L_{assb,exit} = 25.4\,mm, D_{assb} = 17.9\,mm$) and a section of tubing ($L_{tube,in} = 50.8\,mm, D_{tube,in} = 4.57\,mm$) lie between the pressure port and the test section inlet. The downstream pressure port for the header measurement is located 2.4 mm downstream of the inlets to channels 2, 6 and 9 in the header base plate, as shown in Figure 4.3. The downstream pressure port for the test section measurement is located 178 mm downstream from the outlet manifold exit port ($D_{tube,out} = 4.57\,mm$). The pressure drops associated with flow through channels before and after the region of interest must be estimated and subtracted from the total measurement to isolate the pressure drop across the

header and test section. This is discussed in more detail in Section 4.3.4.

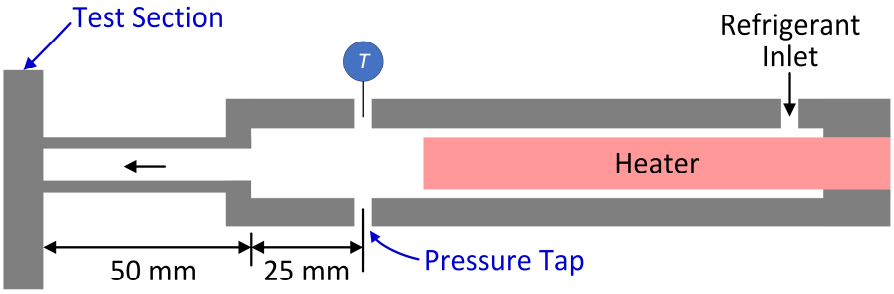

Figure 4.5: Location of upstream pressure port

The distribution in the test section is fully defined by the inlet quality and mass flux in each channel. These calculations are described in more detail in Section 4.3. The refrigerant flow rate must be measured to determine the channel distribution parameters. The refrigerant flow sensor must be compact to minimize the tube pitch as much as possible, must be relatively inexpensive because ten are required to measure the distribution, and must be compatible with R134a. No sensor on the commercial market was found that meets all these requirements; therefore, a thermal time of flight sensor was designed and fabricated for this study. A detailed description of the sensor is provided in Section 4.2.

4.2 Time of Flight Sensor

4.2.1 Overview and State of the Art

In recent years, there has been interest in developing sensors that can accurately measure flow rates in mini and microchannels for applications such as compact heat exchanger research, microelectromechanical systems, and lab on a chip (LOC) devices. Thermal flow meters are inexpensive and can be arranged in compact configurations,

making them good candidates for minichannel applications. There are three basic categories of thermal flow meters: anemometers, calorimetric sensors, and time-of-flight sensors.

The most common type of thermal anemometer is a hot-wire sensor, which consists of a single element that acts as both a heater and a temperature sensor. The steady state temperature of the element depends on the flow rate of the incident fluid through its heat transfer coefficient. Hot-wire anemometers have been used extensively in both gas and liquid flow; however, these sensors are susceptible to surface contamination and are affected by changes in the bulk fluid temperature when the surface overheat ratio is restricted (Lomas, 1986). An alternative type of thermal flow sensor is a calorimetric flow meter. These sensors typically have thermocouples installed upstream and downstream of a heater, and the flow rate is calculated based on the asymmetric temperature profile around the heating element. Calorimetric sensors have been shown to perform well at low velocities, but usually have a limited linearity range (Kim *et al.*, 2007) and require a relatively large temperature difference to maintain a low uncertainty (Lammerink *et al.*, 1993; Sabaté *et al.*, 2004).

Thermal time-of-flight (TOF) sensors calculate velocity by measuring the time for a temperature pulse to travel a known distance. These sensors generally have a relatively slow response time, but they can accurately measure low velocities without a large temperature increase across the sensor. This makes TOF flow meters ideal for measuring steady state flow of subcooled liquids near the saturation temperature. Several authors have designed and experimentally demonstrated thermal time-of-flight sensors for liquids. Early studies mounted a heater and downstream thermistors in circular channels and were

able to measure water flow rates of 0.1 to 10 mL min^{-1} using different thermistor spacings and channel diameters (Miller and Small, 1982; Yang *et al.*, 1988). More recent studies have focused on developing micro-machined silicon sensors that can measure velocity using a purely time-of-flight principle (Rodrigues and Furlan, 2009) or a combination of multiple thermal sensor principles (Yang and Søeberg, 1992; Ashauer *et al.*, 1999). The designs proposed in these studies were able to measure flow velocities as low as 1 mm s^{-1} (Ashauer *et al.*, 1999) and as high as 1500 mm s^{-1} (Rodrigues and Furlan, 2009), but the uncertainties of the measurements were either large or not reported. A review of micro-machined thermal flow meters, including information on time-of-flight sensors, is presented by Kuo *et al.* (2012).

In addition to experimental studies on time-of-flight sensors, some authors have developed analytical and numerical models to describe these devices. Although numerical models can capture complex flow patterns and temperature distributions, it is critical to also develop simple analytical models to guide the design of the device and facilitate proper calibration. It is challenging to describe the heat transfer process in time-of-flight sensors analytically because the process is spatially and temporarily dependent, and the boundary conditions also vary with time. The heat transfer characteristics of a time-of-flight sensor can be described by the advection diffusion equation with some simplifying assumptions. The first analytical solution for the 1-D advection diffusion equation subject to an impulse boundary condition was developed by Marshall (1958). Later, Kakaç and Yener (1973) solved the one dimensional unsteady advection diffusion equation for a time-dependent inlet temperature. Their form of the temperature distribution showed good agreement when compared with experimental data. They concluded that the temperature distribution can be

expressed as function of an infinite series multiplied with a decaying exponential. Numerous other studies have developed solutions to the 1-D advection diffusion equation for heat and mass transfer problems with a variety of inlet boundary conditions (Yates, 1990; Zoppou and Knight, 1997; Liu *et al.*, 2007; Guerrero *et al.*, 2009; Kumar *et al.*, 2010; Jiang *et al.*, 2012; Mojtabi and Deville, 2015). All these studies specifically analyzed either a Dirichlet (first-type) boundary condition, where the temperature or concentration is defined at the boundary, or a homogeneous Robin (third-type) boundary condition, where the sum of the temperature or concentration and its flux is set to zero. One recent study extended previous analytical work in this area by solving the 1-D advection diffusion equation for a mass transfer process with a time dependent Robin (third-type) boundary condition (Pérez Guerrero *et al.*, 2013). Although all these studies provide insight into time-of-flight sensors, there are many situations where the boundary condition can be more accurately described by a Neumann (second-type) boundary condition, where a time dependent heat or concentration flux is prescribed at the inlet boundary of a finite domain.

This work focuses on developing a measurement device for subcooled liquid refrigerant flow rates commonly seen in heat exchangers with mini (1-mm diameter) channels. This device is the first TOF sensor described in the literature that is designed and calibrated for liquid refrigerants. The performance of the TOF sensor is experimentally quantified for velocities in the sensor between 1 and 20 mm s^{-1} and refrigerant temperatures between about 10 and 25°C. In addition, the flow meter is modeled using the one-dimensional unsteady advection diffusion equation subjected to a time dependent Neumann (second-type) boundary condition at the location of the heater. Using insights from the experimental and modeling results, a calibration method for the sensor is

developed. Using this calibration approach and information from repeatability tests, the accuracy and uncertainty of the sensor are systematically quantified and reported.

4.2.2 Flow Meter Design

The flow meter developed in this study consists of a small heater and two downstream thermocouples, as shown in Figure 4.6. The heater (3.81 mm × 2.03 mm × 0.25 mm) is a 100-ohm film resistor connected to a variable power supply through a metal oxide semiconductor field-effective transistor (MOSFET) and can be turned on and off using the control system described in Section 4.2.2. The components are mounted inside a 4.83 mm diameter aluminum channel. The heater and the tips of the thermocouples are located at approximately the center of the channel and are exposed to refrigerant in cross flow. The first thermocouple is 12.5 mm from the heater (L_1), while the second thermocouple is 40.0 mm from the heater (L_2).

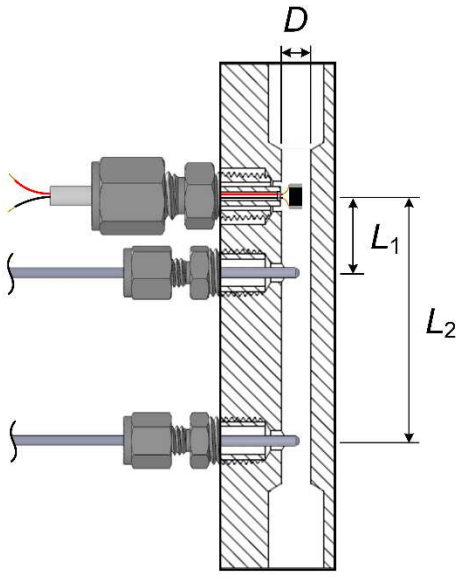

Figure 4.6: Schematic of thermal flow meter

The flow meter is activated by supplying a constant 24 volts to the heater for one second. The heater locally increases the temperature of the surrounding fluid, which acts as a thermal tracer. The temperature pulse is then convected downstream with the flow to the thermocouples. The time it takes for the tracer fluid elements to reach the thermocouples is called the "time of flight". As a first approximation, the time of flight can be calculated as the ratio of the distance traveled to the average velocity, as shown in Equation 4.1.

$$t_{peak} - t_{h,off} = \frac{L}{\bar{u}} \tag{4.1}$$

This time-of-flight estimate is also known as the advection delay. In the above equation, t_{peak} is the time at which the maximum temperature is recorded by the thermocouple, $t_{h,off}$ is the time that the heater is turned off (corresponding to the maximum heater surface temperature neglecting any thermal inertia), L is the distance between the thermocouple and the heater, and $\overline{U}$ is the average velocity. Although the advection delay can estimate the expected time of flight for a given velocity, several authors (Eaton *et al.*, 1981; Handford and Bradshaw, 1989; Byon, 2015) have reported time shifts due to thermal diffusion and the thermal capacitance of the heater and thermocouples. These phenomena, along with a discussion of the effects of radial temperature gradients in the fluid, are discussed further in the Section 4.2.4.

4.2.3 Experimental Approach

A modified version of the test facility described in Section 4.1 was used to measure refrigerant flow rates through minichannels. R134a circulates through the facility and the

flow rate is measured using both the thermal flow meter under consideration and high-accuracy Coriolis flow meters. Data are collected for average refrigerant velocities in the flow meter between 1 and 20 mm s^{-1} and chiller set point temperatures between ambient and -4°C.

4.2.3.1 Flow Loop and Experimental Procedure

The test facility used in this study is shown schematically in Figure 4.7. Liquid R134a is circulated through the facility using a small gear pump. The mass flow rate of the refrigerant is measured using Micromotion Coriolis flow meters (model CMF010H for high flow rates and LF3M for low flow rates). Both Coriolis flow meters have an uncertainty of ±0.5% of the reading. The refrigerant then enters a minichannel with an inner diameter of 1 mm and a length of 410 mm. The refrigerant in the minichannel is cooled using chilled water that flows through a concentric outer annulus. The thermal TOF sensor is attached to the exit of the minichannel, where the fluid velocity is measured. A photograph of the flow meter is also shown in Figure 4.7. Finally, the refrigerant enters a heat exchanger that is coupled to a chiller and returns to the pump. The temperature and pressure in the facility are controlled using the chiller and a piston accumulator, respectively. The temperature of the refrigerant was measured using calibrated T-type thermocouples with an uncertainty of ±0.25°C. For all data presented in this paper, the refrigerant is maintained at a nominal pressure of 800 kPa in the thermal flow meter and is in the liquid phase at all locations in the facility.

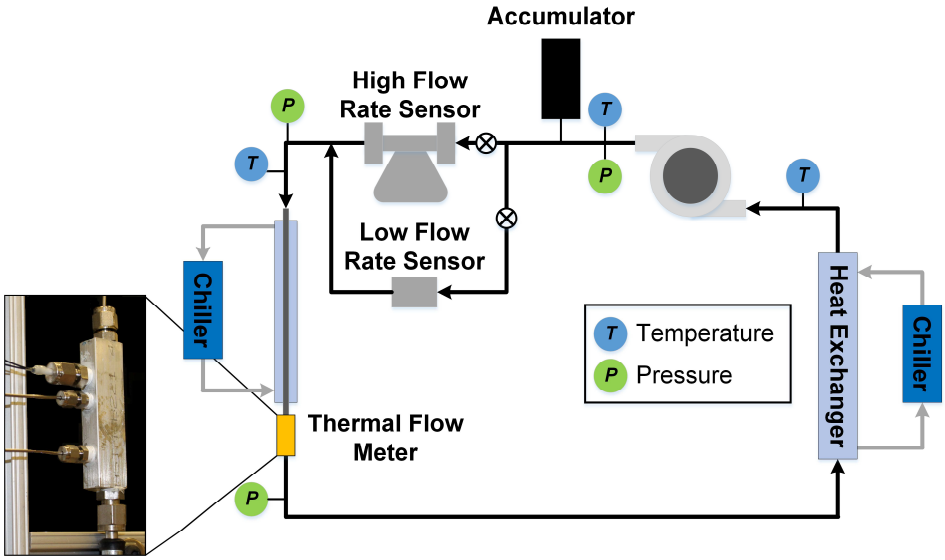

Figure 4.7: Schematic of test facility used for TOF sensor development

Instrument signals from the pressure transducer, thermocouples, and flow meters are recorded using a National Instruments data acquisition system. After the system is turned on and steady state is achieved, ten consecutive measurements are taken using the thermal flow meter and the control system described below.

4.2.3.2 Control System and Data Analysis

A control system for the thermal flow meter was developed using LABVIEW. The program initiates when the user requests that the sensor is turned on, designated as $t = 0$ sec. At that moment, a 5-volt output signal is sent to the MOSFET, which supplies the heater with 24 volts. One second later, the heater is turned off by setting the voltage supplied to the MOSFET to zero.

When the flow meter is initialized ($t = 0$ sec), the pressure, mass flow rate, and temperatures measured by the downstream thermocouples are stored in a matrix. These

data are collected at a sampling frequency of 100 Hz until the temperatures measured by both thermocouples return to the initial temperature (at t = 0 sec). The time required to return to the initial state is called the loop time. Once the loop time is reached, the temperature matrices are analyzed using a built-in peak detection program, which finds the time at which the temperature peak occurs. This value is stored, along with the average temperature, pressure and mass flow rate in the flow meter during the run.

The control program waits until twice the loop time has elapsed, and it then resets the time to t = 0 sec and pulses the heater. The same procedure is repeated until a minimum of ten data sets are collected. The peak time and average temperature, pressure and mass flow rate for each run are then exported for further analysis.

4.2.4 Sensor Calibration

Data were collected over a range of velocities and fluid temperatures to understand the best calibration method for the flow meter. This section presents the dependence of the measured time of flight on these parameters. The time of flight is defined as the difference between when the heater is turned off and when the maximum temperature is detected by the thermocouple. Repeated measurements were taken at each condition, and the time of flight and the measurement uncertainty are presented as:

$$TOF_i = \overline{TOF} \pm 1.96\frac{std}{\sqrt{n}} \tag{4.2}$$

Where *i* denotes which thermocouple location is being considered, $\overline{TOF}$ is the average time of flight from the data set, std is the sample standard deviation, and n is the number of data

points collected at each flow rate. The uncertainty is multiplied by 1.96 to incorporate a 95% confidence limit.

4.2.4.1 Velocity Dependence

An analytical model describing the performance of the time of flight sensor was developed as a part of this work. A detailed explanation of the modeling approach and the results is presented in Appendix A. The model found that the time of flight is dependent on the velocity, the sensor geometry, the energy supplied by the heater, and the thermal diffusivity of the fluid. To isolate the dependence on velocity, initial experiments were conducted at ambient temperature. Under these conditions, the refrigerant temperature is initially uniform (which is consistent with the initial condition shown in Equation A.5) and the fluid properties are approximately constant. Therefore, the model predicts that the time of flight will depend solely on the refrigerant velocity.

Fifty repeated data points were collected at velocities between 1 and 20 mm s^{-1} at intervals of 1 mm s^{-1}. The results are shown in Figure 4.8 along with the expected advection delay from Equation 4.1. The shapes of these curves offer insight into the optimal operating range for the sensor. At very high flow rates (> 15 mm s^{-1}), the time of flight becomes relatively insensitive to the velocity, which increases the uncertainty. This effect is less severe when temperature measurements are taken farther from the heater, so the operating range can be extended if the distance between the heater and the thermocouple is increased. At very low flow rates (< 4 mm s^{-1}), the time of flight increases rapidly. In this range, the time of flight is very sensitive to the velocity, but the temperature pulse has more time to diffuse into the cooler adjacent fluid, making the peak difficult to

detect. This effect increases the measurement uncertainty and eventually makes it impossible to reliably identify the precise time at which the maximum temperature occurs. Diffusion is minimized if the temperature measurement is taken close to the heater. So the range of the sensor can be extended to lower flow rates by decreasing the distance between the heater and thermocouple. Two thermocouples were included in the time of flight design to address these competing requirements that dictate the optimal thermocouple location at low and high flow rates.

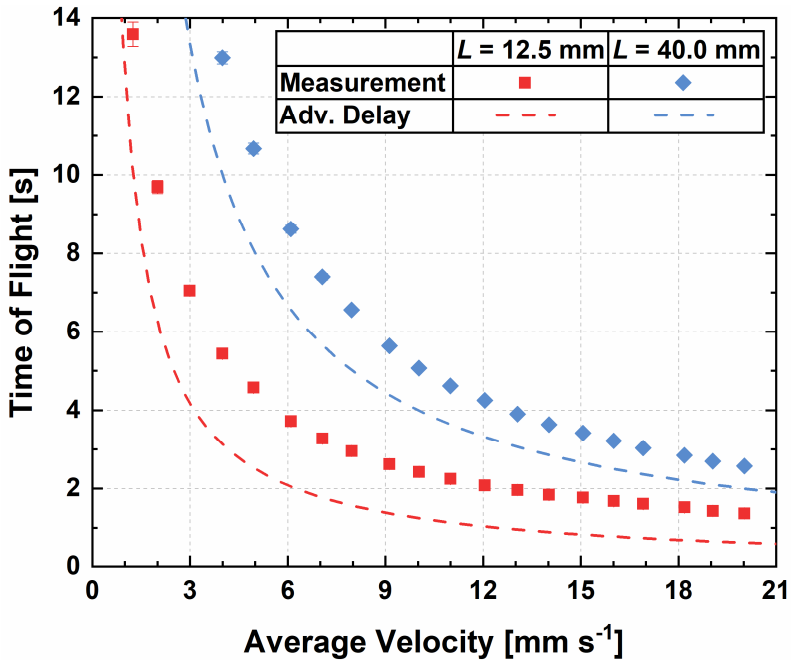

Figure 4.8: Experimental results for calibration data set and the advection delay given in Equation 4.1

Figure 4.8 also shows that the measured time of flight is greater than the theoretical advection delay for all the data collected, and that the difference increases at lower flow rates. This is shown more clearly in Figure 4.9. This effect can be partially attributed to the thermal capacitance of the thermocouples and the heater, which delays the response of these components when exposed to a change in the thermal environment. The capacitance

time constant will depend on the material, geometry, and heat transfer properties of the component. The material properties and geometry of the heater and thermocouples remain constant; therefore, the time delay should increase as the velocity decreases due to the reduced heat transfer coefficients. This general trend is consistent with the results shown in Figure 4.9. However, thermal capacitance should increase the time of flight measured by both thermocouples equally. The differences in delay times between the two thermocouples suggest other factors are at play, which may include different heat transfer coefficients caused by mixing downstream of the first thermocouple, cooling of the fluid by the first thermocouple, differences in the exact placement of the temperature sensors (off-center), and/or radial diffusion effects (discussed in the following section).

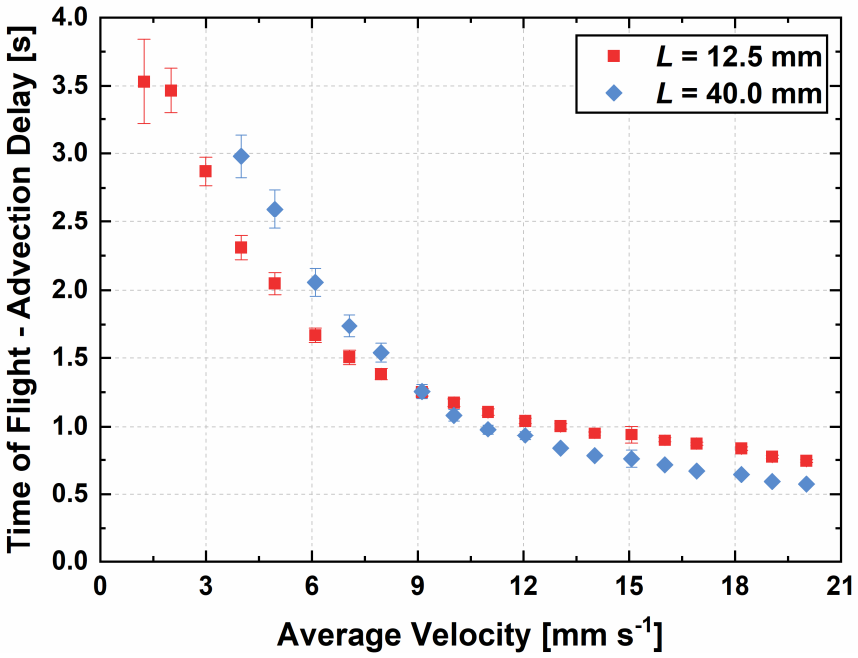

Figure 4.9: Difference between measured time of flight and the advection delay

4.2.4.2 Temperature Dependence

Data were also collected over a range of refrigerant temperatures to understand the effects of fluid properties and thermal diffusion on the time of flight. In these tests, the velocity was set and the average refrigerant temperature inside the sensor was reduced using the chiller. Ten repeated data points were collected for each condition. The first thermocouple was used to determine the time of flight for velocities less than 5 mm s^{-1}, while the second thermocouple was used for all other cases.

Three initial data sets were collected at a velocity of 5 mm s^{-1} and refrigerant temperatures between 10 and 20°C. The time of flight over this temperature range is shown in Figure 4.10(a). The results illustrate that lower refrigerant temperatures tend to have reduced times of flight; however, the trend is not consistent across data sets. These results were collected on three different days, and the only important parameter that varied significantly between days was the ambient temperature ($\bar{T}_{amb,1} = 22.2$°C, $\bar{T}_{amb,2} = 25.6$°C and $\bar{T}_{amb,3} = 25.7$°C). The same data are plotted as a function of the temperature difference between the ambient and the refrigerant in Figure 4.10(b). Here the data converges, suggesting that the time of flight is related more closely to the temperature gradient than the fluid properties.

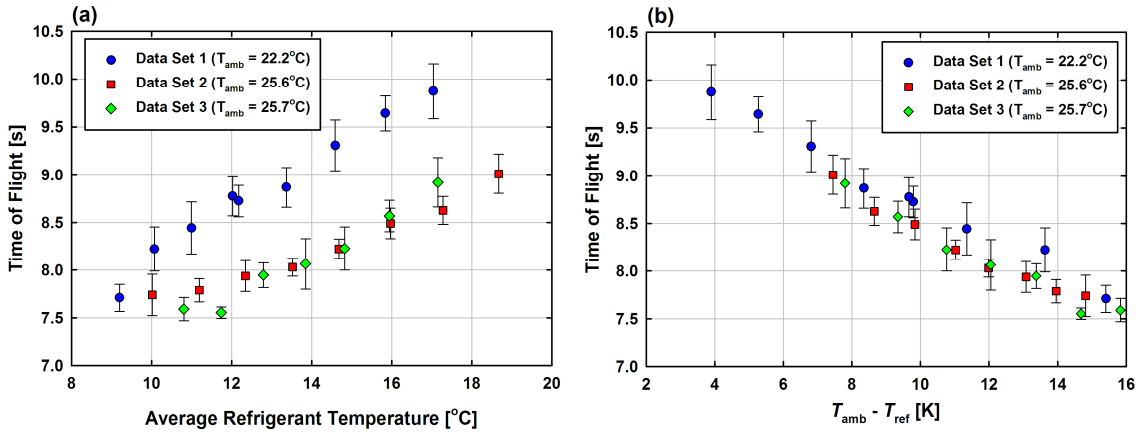

Figure 4.10: Effect of (a) average refrigerant temperature and (b) temperature difference between the ambient and the refrigerant on the measured time of flight

To better understand the mechanisms causing the observed trends, additional data were collected at different velocity set points. For these tests, a thermocouple was affixed to the outer wall so that the radial temperature gradient in the sensor could be measured more directly. Figure 4.11 shows the variation in the time of flight with the temperature difference between the outer wall and the initial fluid temperature (temperature before the heater is initiated) for select velocities. The time of flight decreases monotonically until a temperature difference of about 2.5 K and then remains relatively constant as the temperature difference increases further. The relationship between the time of flight and the radial temperature gradient is strong at low fluid velocities, but weakens at higher velocities. For example, at 4 mm s^{-1}, the time of flight changes by almost 3.75 seconds between wall-to-centerline temperature differences of 0 and 3.25 K, whereas at 12 mm s^{-1}, the time of flight changes by only about 0.35 seconds.

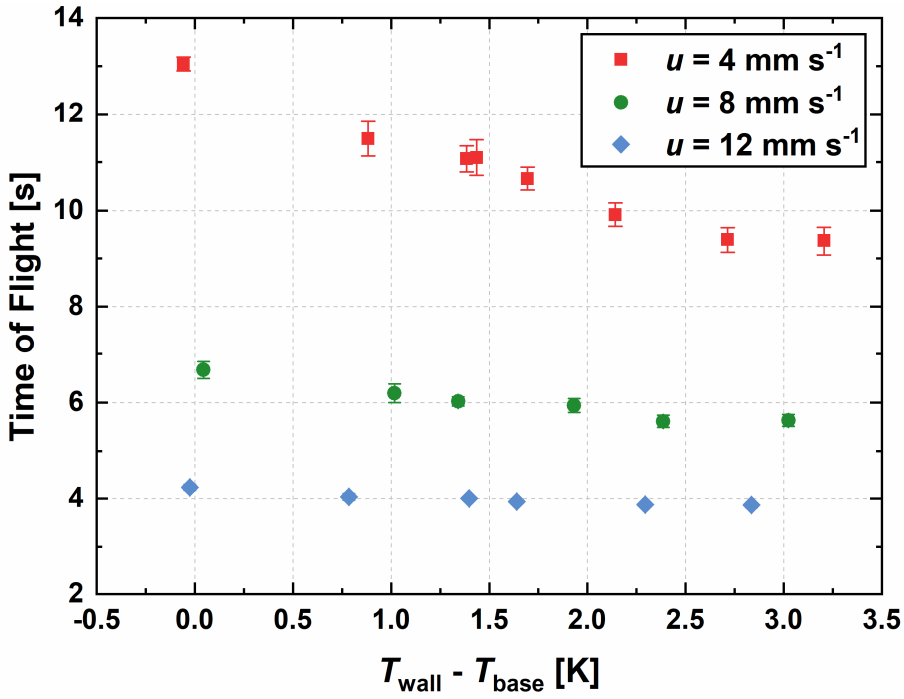

Figure 4.11: Effect of the radial temperature gradient on the measured time of flight (measured at location L_2 for all cases) at different average fluid velocities.

The dependence on the radial temperature gradient can be explained by thermal diffusion, as shown in Figure 4.12. At the leading edge and peak of the fluctuation, where the radial temperature gradient is relatively large, diffusive transport to the walls occurs rapidly. This energy is temporarily stored around the periphery of the channel and in the sensor wall. As the fluctuation passes a given location, the temperature gradient decreases because the periphery has already been warmed. This reduces or reverses diffusion from the centerline as the trailing edge passes by, which moves the location of the peak temperature in the negative *x*-direction. Radial diffusion thereby increases the time that it takes for the peak to reach the thermocouples. The magnitude of the peak shift will depend on the amount of time that the fluctuation has to diffuse; therefore, one would expect the effects of diffusion to be the most prominent at low flow rates as seen in Figure 4.11.

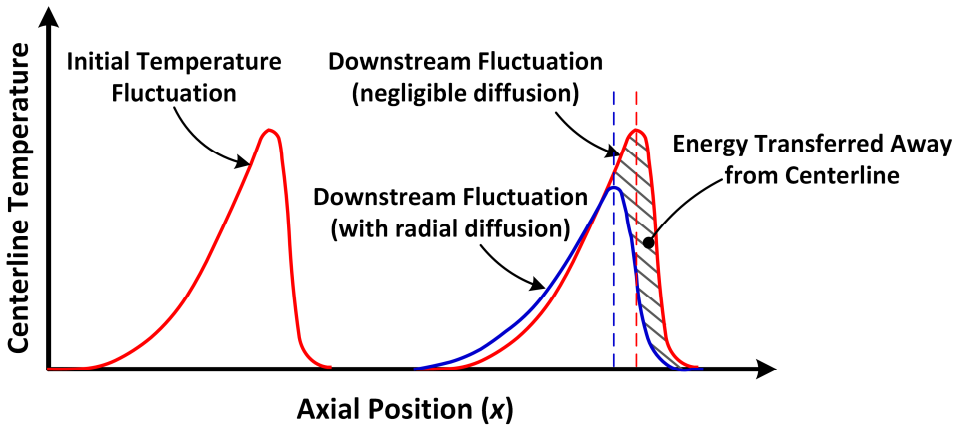

Figure 4.12: Effect of radial diffusion in the time of flight sensor

When the refrigerant is initially at the same temperature as the wall ($T_{wall} - T_{base} = 0\ K$), there is a relatively large radial temperature gradient once a temperature pulse is added to the flow. As the differences between the wall and the initial fluid temperatures increase, the driving temperature gradient between the peak and the wall decreases, hindering energy transfer away from the centerline. At some point, the peak temperature produced by the heater is lower than the wall temperature, preventing radial diffusion of the temperature pulse. A schematic representation of the temperature gradients in the fluid is shown in Figure 4.13.

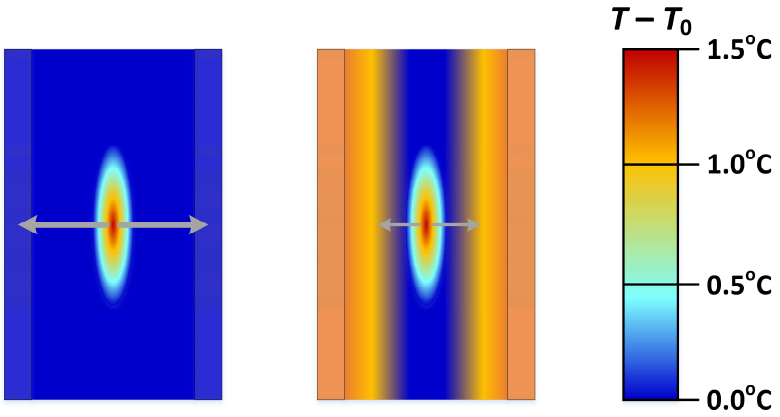

Figure 4.13: Local temperature gradients in the sensor with low (left) and high (right) radial temperature differences (The temperature values in the color bar are given as a reference, but this figure is not directly based on measured or simulated data. The actual temperatures present in the flow will depend on the ambient gains, location and fluid velocities).

This effect can be seen clearly in Figure 4.14, which shows the temperature measurements from the second thermocouple (L = 40.0 mm) as a function of time when the fluid velocity is 6 mm s^{-1}. When the difference between the base fluid temperature and the wall temperature is high, less energy is transferred away from the centerline, resulting in a higher and earlier peak. At lower temperature differences, energy is temporarily transferred to the periphery of the channel and the peak consequently has a lower amplitude and occurs later.

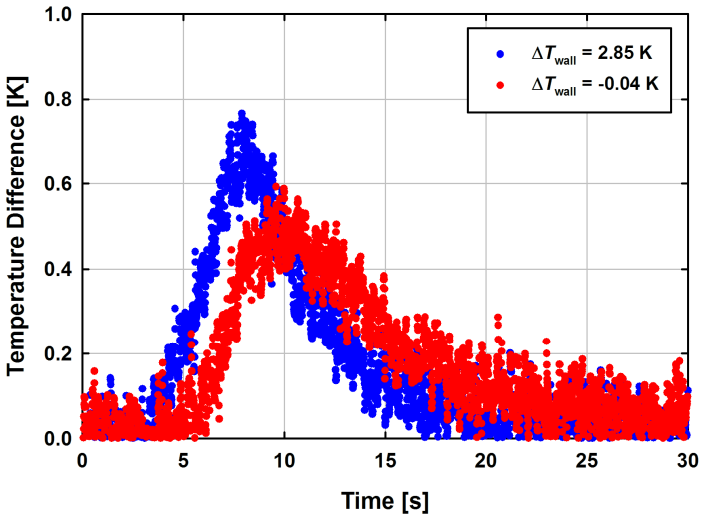

Figure 4.14: Normalized temperature measurements for the second thermocouple as a function of time when the fluid velocity is 6 mm s^{-1} and the radial temperature gradient is varied

4.2.4.3 Calibration Methodology

The time of flight is dependent on both the velocity and the local temperature gradients in the fluid. To develop a correlation to relate these parameters, dimensional analysis was used to determine the relevant Pi Groups. The important non-dimensional parameters for the sensor are the normalized time of flight, relating the time of flight to the advection delay, the Peclet number, relating advective to diffusive transport, and the normalized temperature difference. These parameters are defined in Equations 4.3 through 4.5.

$$TOF^* = \frac{TOF * \bar{u}}{D} \tag{4.3}$$

$$Pe_D = \frac{D * \bar{u}}{\kappa} \tag{4.4}$$

$$\theta^* = \frac{kD(T_{wall} - T_{base})}{\dot{Q}_h} \tag{4.5}$$

When the normalized temperature difference is held constant, the normalized time of flight follows an exponential trend, while when the Peclet number is held constant the data follows an error function trend. Additionally, an exponential term is present for the one-dimensional analytical model developed for the sensor (Appendix A). Based on these observations, Equation 4.6 was found to be the most effective correlation to relate these non-dimensional parameters. In the correlation, the constants were fit using a regression analysis. The constants are dependent on geometric parameters, which were not comprehensively investigated in this study. Therefore, a regression analysis was conducted for each thermocouple location separately. The results from the regression analysis are shown in Table 4.5.

$$TOF^* = 1 + Aerfc[(B + C\theta^*)Pe_D] + D\exp\left(-E \cdot Pe_D\theta^{*-F}\right) \tag{4.6}$$

Table 4.5: Empirical constants for correlation shown in Equation 4.6

Location (L)	A	B	C	D	E	F
12.5 mm	0.725	-3.194×10^{-5}	3.696	1.599	2.051×10^{-4}	0.370
40.0 mm	0.357	3.141×10^{-4}	3.284	1.759	9.485×10^{-5}	0.429

4.2.5 Flow Meter Uncertainty and Accuracy

4.2.5.1 Representative Results

The experimental results were examined to quantify the uncertainty of the velocity measurements and the accuracy of the proposed calibration approach. The uncertainties were calculated using Equation 4.7, considering both the uncertainty of the time of flight measurement and the uncertainty of the Coriolis flow meter used for calibration. The partial derivative in the uncertainty propagation was solved numerically.

$$U_{\bar{u}} = \sqrt{\left(\frac{\partial \bar{u}}{\partial t}\right)^2 U_t^2 + U_{coriolis}^2} \tag{4.7}$$

The velocity readings from the Coriolis and calibrated TOF flow sensors are shown in Figure 4.15. The results from the first thermocouple (L = 12.5 mm) are used for velocities less than 5 mm s^{-1}, while the results from the second thermocouple (L = 40.0 mm) are used for all other flow rates. The average and maximum uncertainties of these measurements are 2.68% and 8.92%, respectively.

The accuracy of the calibration method was studied by comparing the flow rate measurements to the Coriolis reading. The calibrated TOF sensor predicted 87.1% of the collected data within ±5% with an average deviation (AD) of 2.72% and an absolute average deviation (AAD) of 4.39%. Although the correlation captured the correct trends for most of the data, some cases were not predicted well by Equation 4.6, with errors greater than 50% at very low flow rates (1 – 2 mm s^{-1}).

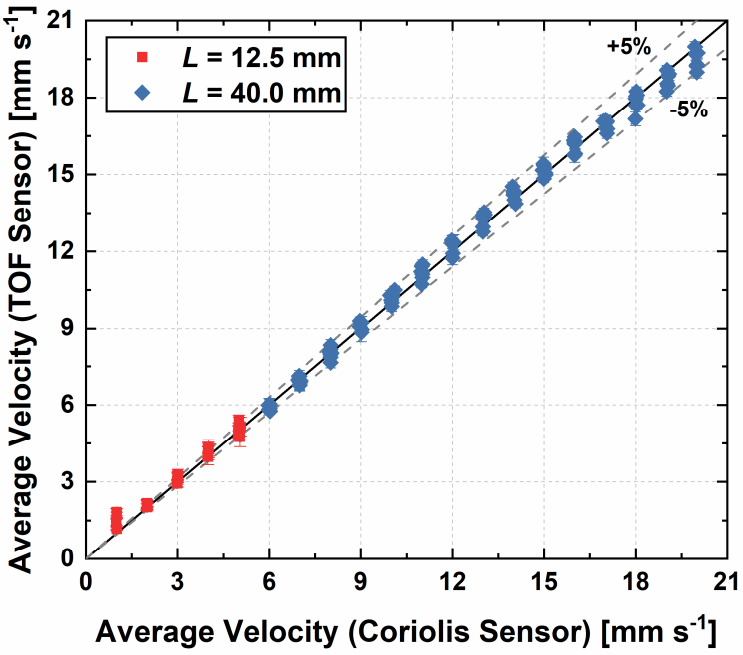

Figure 4.15: Comparison of the refrigerant velocity using the thermal flow meter and the high accuracy Coriolis sensor

These results show that the time of flight sensor can accurately measure the fluid velocities of R134a using the calibration approach shown in Equation 4.6. This thermal time of flight sensors could also be used for a range of fluids and applications, but further work is needed to develop a validated calibration approach that fully accounts for different sensor geometries (specifically the effect of L) and fluid properties. The analytical model presented in Appendix A can provide insight into an appropriate form for the calibration equation. A more robust calibration approach would allow future researchers to optimize the sensor design for different fluids and desired velocity ranges.

4.2.5.2 Final Sensor Design

After considering the performance of the time of flight sensor and the anticipated range of volumetric flow rates in the distribution experiments, the sensor design was

slightly modified. In the final design, the channel diameter was reduced to 3.81 mm and the voltage supplied to the heater was reduced to 18 volts. The channel diameter was reduced from 4.83 mm to 3.81 mm to increase the velocities in the sensor for a given mass flow rate. This enables the measurement of lower flow rates than were possible with the larger diameter sensor. The voltage was reduced from 24 volts to 18 volts to limit the maximum temperature of the refrigerant (the sensor can be damaged if boiling occurs at the heater surface; therefore, the voltage was reduced to minimize this risk.) All other aspects of the geometry and controls system remained the same. Initially, four sensors were independently calibrated using the facility described in section 4.2.2. The results for the first sensor over the range of conditions tested are shown in Figure 4.16. The trends for the final sensor design are the same as those discussed above.

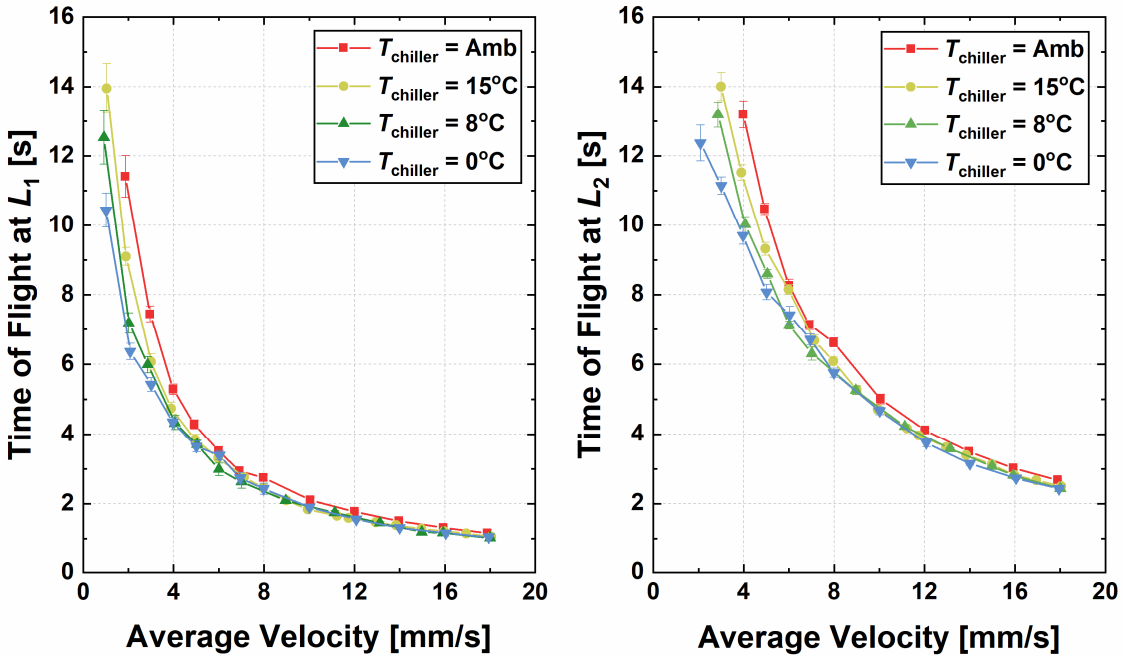

Figure 4.16: Time of flight in the final sensor design for average velocities between 1 and 18 mm s^{-1} and chiller set-point temperatures between 0°C and ambient temperature

The measured time of flight in four sensors at average velocities between 1 and 18 mm s^{-1} and a chiller set-point temperature of 8°C is shown in Figure 4.17. Although there are some small differences between sensors, likely due to variation in the precise placement of components, the results are nearly identical. These results were used to calibrate the remaining sensors in a more efficient manner. The sensors were tested at discrete flow rates and temperature differences in the full test section. In these tests, single-phase flow was distributed in the inlet manifold so that the flow rate through each parallel channel was approximately the same. The measured time of flight and the temporal temperature fluctuations at L = 12.5 mm and 40.0 mm in the sensors were then compared with the four calibration data sets. The calibration equation for the sensor that exhibited the trends closest to each uncalibrated sensor was used for all subsequent data collection.

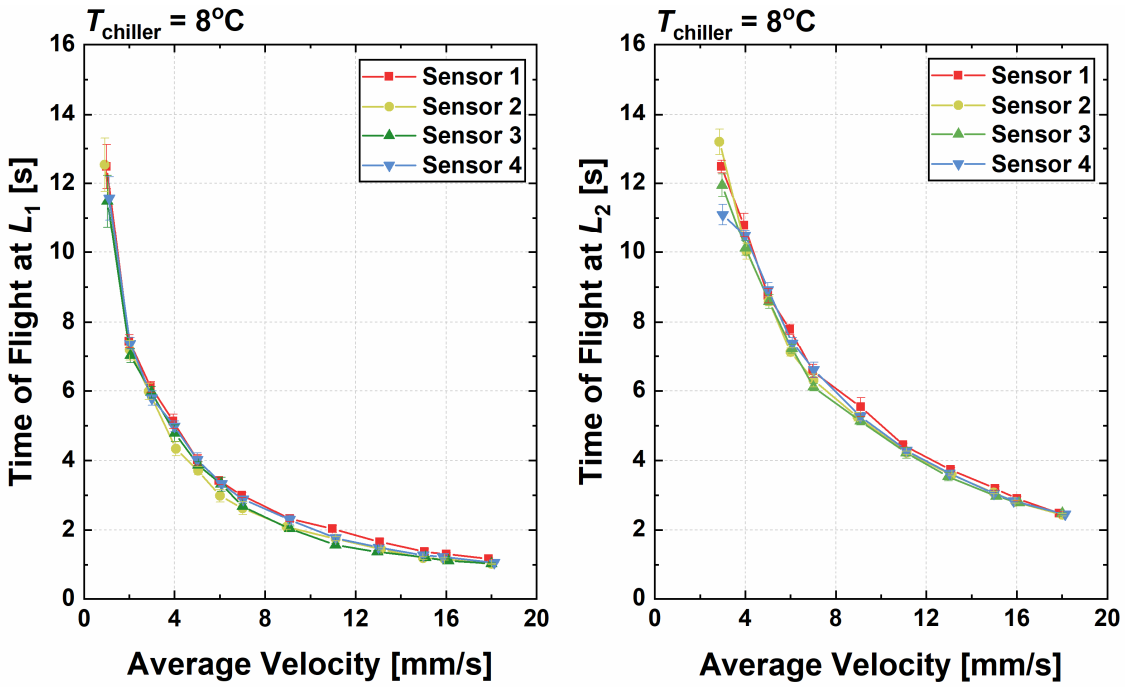

Figure 4.17: Time of flight in the four sensors tested for average velocities between 1 and 18 mm s^{-1} and a chiller set-point temperature of 8°C

The ten sensors were installed at end of the tube-in-tube heat exchangers described above. In all cases, the refrigerant fully condenses in the heat transfer section and is in the subcooled state in the TOF sensor. A schematic of one of the heat exchanger channels is shown in Figure 4.18.

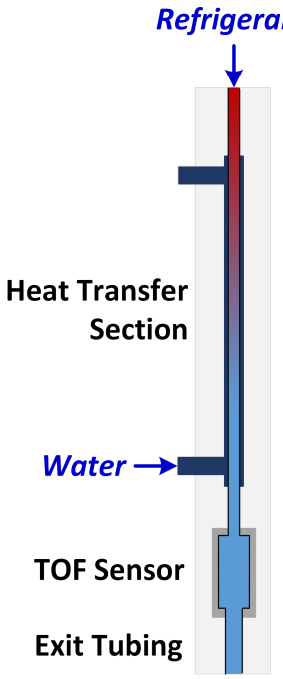

Important Geometric Parameters	
$D_{ref,ch}$	1.00 mm
$D_{w,in}$	2.00 mm
$D_{w,out}$	4.00 mm
D_{TOF}	3.81 mm
D_{exit}	1.75 mm
$L_{ref,ch}$	0.50 m
$L_{w,ch}$	0.41 m
L_{TOF}	0.09 m
L_{exit}	0.10 m

Figure 4.18: Placement of the time of flight sensor in relation to the tube-in-tube heat exchanger with important geometric parameters

4.2.6 Summary of TOF Sensor Development

A thermal time of flight sensor was developed to measure steady state refrigerant flow rates in minichannels. The one-dimensional unsteady advection diffusion equation with a time dependent Neumann boundary condition was solved to help establish a calibration technique for the sensor. The model predicts that the time of flight depends on the sensor geometry, the energy provided by the heater, the velocity of the fluid, and the thermal diffusivity of the refrigerant. The simplified 1-D analytical model accurately

predicts the thermal behavior in the sensor for cases with minimal rates of radial diffusion but tends to underpredict the average fluid velocity when the difference between the peak and wall temperature is high. Future modeling work should focus on the effects of thermal capacitance and radial diffusion to improve the calibration methodology for TOF sensors.

Using insights from the modeling and experimental work, a calibration method was developed to correlate the time of flight to the refrigerant velocity. The calibrated sensor was able to measure 87.1% of the collected data within ±5% with an absolute average deviation of 4.39%. Additionally, all of the measured data, including its uncertainty, lie within 5% of the full scale. The device developed here can therefore be recommended as a compact, inexpensive, largely nonintrusive technique to measure liquid refrigerant flow rates corresponding to average velocities between 2 and 20 mm s^{-1}.

Ten sensors were fabricated and installed in the refrigerant test section to measure the total flow rate in each channel. The uncertainty of the measurements was set to ±3% of the full scale, except for the few points that were measured above the calibrated range, where the uncertainty was set to ±3% of the measured value.

4.3 Data Analysis

The objective of the refrigerant experiments is to determine the distribution of a saturated refrigerant at a specified inlet condition. The following section describes the calculation of the inlet condition and the distribution. All data analysis and uncertainty propagation calculations are performed on the *Engineering Equation Solver* (Klein, 2018) software platform. The fluid properties of R134a are calculated using the fundamental equations of state developed by Tillner-Roth and Baehr (1994). For illustrative purposes,

a sample calculation for the conditions shown in Table 4.6 is included in this section. More details about the data analysis approach are provided in Appendix B.

Table 4.6: Experimental data for nominal conditions of $G_{in} = 59.7$ kg m^{-2} s^{-1}, $x_{in} = 0.50$, and $T_{sat} = 30$°C (channel 2)

Measurement	Measured Value	Measurement	Measured Value
$T_{preh.in}$	12.6 ± 0.25°C	$T_{ch2,out}$	9.76 ± 0.25°C
$P_{preh,in}$	774 ± 2.63 kPa	$\bar{u}_{ch2}$	13.2 ± 0.54 mm s^{-1}
$P_{preh,out}$	777 ± 2.63 kPa	$T_{w,ch2,in}$	6.04 ± 0.25°C
$P_{TS,out}$	770 ± 2.63 kPa	$T_{w,ch2,out}$	10.4 ± 0.25°C
$\dot{m}_{ref,total}$	58.9 ± 0.15 g min^{-1}	$\dot{V}_{w,ch2}$	29.1 ± 1 mL min^{-1}
$\dot{Q}_{preh}$	108.0 ± 0.54 W	$\Delta P_{header,ch2}$	0.167 ± 0.005 kPa
$P_{w,in}$	195.1 ± 5.2 kPa	T_{amb}	22.8 ± 0.25°C
$P_{w,out}$	171.7 ± 1.6 kPa		

4.3.1 Inlet Conditions

The test section inlet condition is fully defined by the saturation pressure, quality and mass flux. The inlet quality is obtained based on an energy balance across the preheater. The enthalpy of the subcooled liquid entering the preheater is determined by the measured temperature ($T_{preh,in}$) and pressure ($P_{preh,in}$), as shown in Equation 4.8.

$$h_{preh,in} = f\left(T_{preh,in}, P_{preh,in}\right) = 69011 \pm 344\ J\ kg^{-1} \tag{4.8}$$

The inlet enthalpy into the test section can then be calculated from the total mass flow rate of the refrigerant and the amount of heat gained by the refrigerant from the preheater. The heat gained by the refrigerant is a function of the power drawn by the preheater and the losses to the ambient. The losses are calculated using the thermal

resistance network shown in Figure 4.19. The thermal resistances considered in this analysis are the refrigerant convective resistance (R_{ref}), the conductive resistances through the wall (R_{wall}) and insulation (R_{ins}), the external natural convective resistance (R_{NC}), and the radiation resistance assuming the surface of the insulation is a grey surface and the surroundings behave as a large blackbody (R_{rad}).

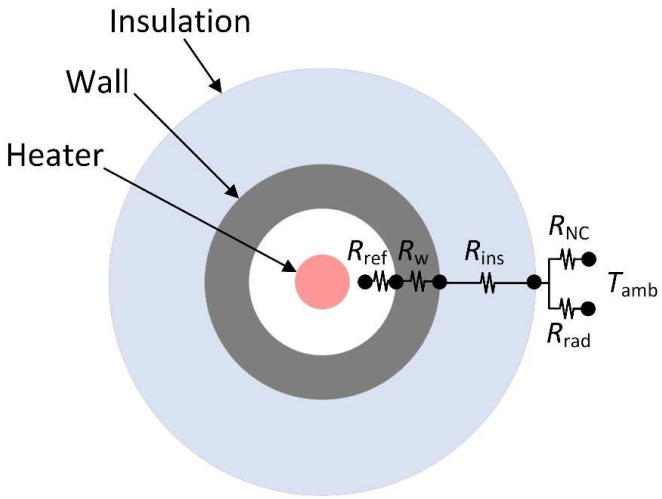

Figure 4.19: Thermal resistance network for the heat losses to the ambient through the preheater

A convective boiling heat transfer coefficient ($\overline{htc}_{ref}$) of 10,000 W m^{-2} K^{-1} is assumed for calculating the refrigerant convective resistance. Although a precise heat transfer coefficient is not calculated for each dataset, the refrigerant resistance is expected to be insignificant compared to the insulation and outer surface resistances; therefore, large uncertainties in this value have nearly no effect on the total thermal resistance.

$$R_{ref} = \frac{1}{\overline{htc}_{ref} A_{preh,in}} = \frac{1}{10000\ W\ m^{-2}K^{-1} * 9.64 \times 10^{-3}\ m^2} \tag{4.9}$$

$$= 0.010\ K\ W^{-1}$$

The conductive resistance through the wall of the heater assembly and the insulation are calculated using Equations 4.10 and 4.11, respectively. The thickness of the insulation is assumed to be 25.4 mm (minimum insulation thickness on the facility).

$$R_{wall} = \frac{\ln\left(\frac{D_{out,wall}}{D_{in,wall}}\right)}{2\pi L_{eff} k_{wall}} = \frac{\ln\left(\frac{38.1\ mm}{17.9\ mm}\right)}{2\pi * 0.172\ m * 14.94\ W\ m^{-1}K^{-1}} \tag{4.10}$$

$$= 0.047\ K\ W^{-1}$$

$$R_{ins} = \frac{\ln\left(\frac{D_{out,wall} + 2th_{ins}}{D_{out,wall}}\right)}{2\pi L_{eff} k_{ins}} = \frac{\ln\left(\frac{38.1\ mm + 2 * 25.4\ mm}{38.1\ mm}\right)}{2\pi * 0.172\ m * 0.043\ W\ m^{-1}K^{-1}} \tag{4.11}$$

$$= 18.29\ K\ W^{-1}$$

The natural convection heat transfer coefficient ($\bar{h}_{nat}$) at the surface of the insulation is calculated using the Raithby and Hollands (1998) correlation for natural convection around a horizontal cylinder. The heat transfer coefficient is a function of the surface temperature, which was calculated with an energy balance between the surface and the ambient after the total heat loss is calculated. The natural convection heat transfer coefficient for the conditions presented in Table 4.6 is 1.97 W m^{-2} K^{-1} and the corresponding thermal resistance is given in equation 4.12.

$$R_{NC} = \frac{1}{\overline{htc}_{nat} A_{ins,out}} = \frac{1}{1.97\ W\ m^{-2}K^{-1} * 4.79 \times 10^{-2}\ m^2} \tag{4.12}$$

$$= 10.6\ K\ W^{-1}$$

Finally, the radiation resistance is calculated using Equation 4.13. This equation is appropriate because the temperature difference between the insulation surface and the surroundings is small (~1°C). In this calculation, the temperature ($\bar{T}_{s/surr}$) is the average temperature of the surface and the surroundings (296.3 K), and the thermal emissivity (ϵ) is assumed to be 0.8.

$$R_{rad} = \frac{1}{4A_{ins,out}\sigma\epsilon\bar{T}_{s/surr}^{\ 3}}$$
$$4.422\ K\ W^{-1} = \frac{1}{4 * 4.79 \times 10^{-2}\ m^2 * \sigma * 0.80 * (296.3\ K)^3} \quad (4.13)$$

The total heat loss to the ambient through the heater assembly is calculated using Equation 4.33. A conservative uncertainty of ±50% is applied to the calculated heat loss. The average refrigerant temperature inside the heater is estimated using a weighted calculation based on the sensible and latent heat transfer rates, as shown in Equation 4.14.

$$\bar{T}_{ref,preh} = \left[\left(\frac{T_{preh.in} + T_{sat}}{2}\right) \times \left(\frac{\dot{Q}_{sens}}{\dot{Q}_{ref,preh}}\right)\right] + \left[T_{sat} \times \left(\frac{\dot{Q}_{lat}}{\dot{Q}_{ref,preh}}\right)\right]$$
$$28.2°C = \left[\left(\frac{12.6°C + 30.2°C}{2}\right) \times \left(\frac{24.4\ W}{107.2\ W}\right)\right] + \left[30.2°C \times \left(\frac{82.8\ W}{107.2\ W}\right)\right] \quad (4.14)$$

$$\dot{Q}_{loss,preh} = \frac{\bar{T}_{ref,preh} - T_{amb}}{R_{ref} + R_{wall} + R_{ins} + \left(\frac{1}{R_{rad}} + \frac{1}{R_{NC}}\right)^{-1}} = 0.25 \pm 0.13\ W \quad (4.15)$$

A similar analysis is also performed for the piping that connects the preheater and the test section. The length and diameter of the inlet piping are 50.8 mm and 4.57 mm, respectively. The details of this analysis are shown in Appendix B.

In addition to the losses described above, there is a conduction heat transfer pathway between the surface of the cartridge heater and the frame of the facility because of the mounting brackets required to secure the component. The magnitude of these losses is difficult to calculate analytically; therefore, it was determined experimentally by fully evaporating the refrigerant through the preheater and directly calculating the exit enthalpy. The difference between the measured heat transfer rate across the heater (accounting for losses to the ambient) and the calculated heat transfer rate from the measured refrigerant inlet and outlet conditions is shown in Figure 4.20. The data were curve fit to estimate the conduction losses to the frame of the facility, which were then assigned a 50% uncertainty. The total conduction heat loss for the sample calculation presented in Table 4.6 is 0.46 ± 0.23 W (0.40% of total heater power).

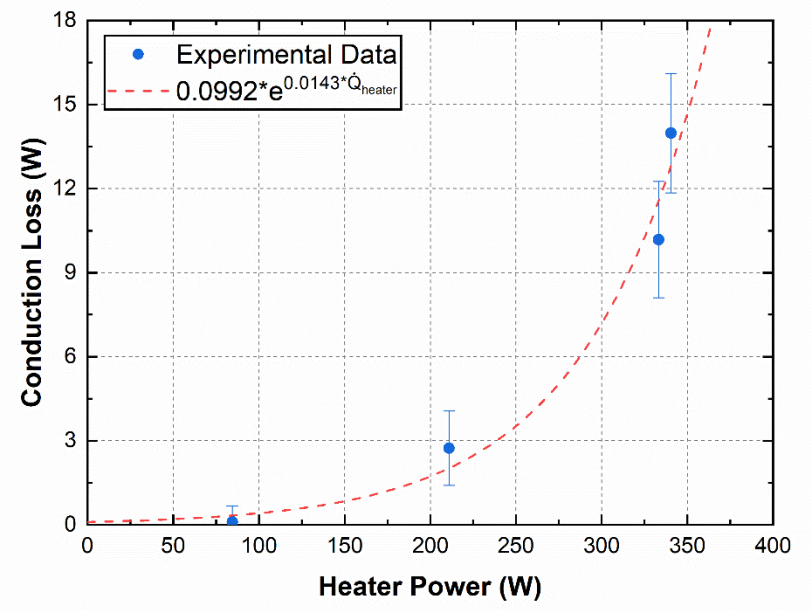

Figure 4.20: Difference between the measured preheater power and heat transfer rate calculated using an energy balance between the inlet and outlet (accounting for ambient losses). These losses are attributed to conduction through the mounting brackets.

Finally, the heat transfer rate into the refrigerant can be calculated with the power drawn by the heater and the total thermal losses described above ($\dot{Q}_{loss,in}$). This information is used in the energy balance shown in Equation 4.16 to calculate the inlet enthalpy into the test section.

$$h_{TS,in} = h_{preh,in} + \frac{\dot{Q}_{preh} - \dot{Q}_{loss,in}}{\dot{m}_{ref,total}}$$
$$178239\,J\,kg^{-1} = 69011\,J\,kg^{-1} + \frac{108\,W - 0.80\,W}{9.81 \times 10^{-4}\,kg\,s^{-1}} \tag{4.16}$$

The inlet quality into the test section is then calculated using the enthalpy and measured pressure, as shown in Equation 4.17.

$$x_{TS,in} = f\left(h_{TS,in}, P_{TS,in}\right) = \boxed{0.488 \pm 0.005} \tag{4.17}$$

The inlet mass flux is calculated from the total refrigerant mass flow rate measured with the Coriolis sensor, as shown in Equation 4.18.

$$G_{TS,in} = \frac{\dot{m}_{ref}}{A_{TS,in}} = \frac{9.81 \times 10^{-4}\,kg\,s^{-1}}{1.64 \times 10^{-5}\,m^2} = \boxed{59.8\,kg\,m^{-2}s^{-1}} \tag{4.18}$$

4.3.2 Channel Measurements

The two-phase flow distribution can be fully specified by the measurement of the mass flow rates of the liquid and vapor phase into each channel. This is accomplished by measuring the inlet quality and the total mass flow rate into the channels. Each refrigerant channel in these experiments is coupled to a coolant stream (liquid water) through a tube-

in-tube heat exchanger. As shown in Figure 4.21, the thermodynamic states of the refrigerant at the outlet, and the water at the inlet and outlet of the heat exchanger are measured. The inlet thermodynamic state of the refrigerant, and thereby the inlet quality, can be calculated from energy balance between the coolant and the refrigerant. Again, to accurately determine the refrigerant inlet state, the energy balance must account for any heat losses or gains.

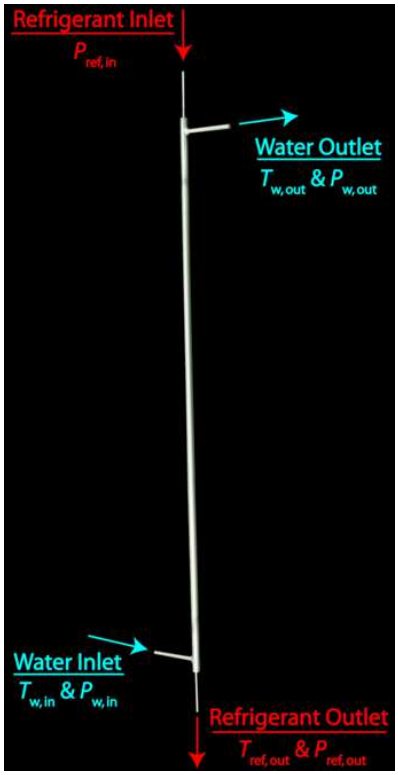

Figure 4.21: Photograph of tube-in-tube heat exchanger with measurement labels

Across a single channel, the water flowing through the annulus can thermally interact with the ambient environment. The ambient temperature is generally greater than 10°C warmer than the coolant, which could cause heat gains large enough to have a significant impact on the calculated refrigerant inlet state. Therefore, thermal gains from the ambient

are considered in the energy balance to calculate the inlet quality and are explained in more detail below.

The thermal gains between the ambient and the chilled water are calculated using a thermal resistance network. The analysis includes the contributions of the coolant convective resistance (R_w), the conductive resistances through the tube wall (R_{wall}) and the insulation (R_{ins}), and the natural convection and radiation surface resistances (R_{NC} and R_{rad}, respectively).

The water-side heat transfer coefficient was calculated using the Rohsenow *et al.* (1998) correlation for flow through an annulus. The heat transfer coefficient for the test case shown in Table 4.6 is 2240 W m^{-2} K^{-1}, which has a corresponding thermal resistance (R_w) of 0.088 K W^{-1}. The thermal resistances due to conduction through the wall and insulation are shown in Equations 4.19 and 4.20, respectively. Although the heat flow through the insulation is two-dimensional, as shown in Figure 4.22, the thermal resistance was estimated using the formulation for a plane wall.

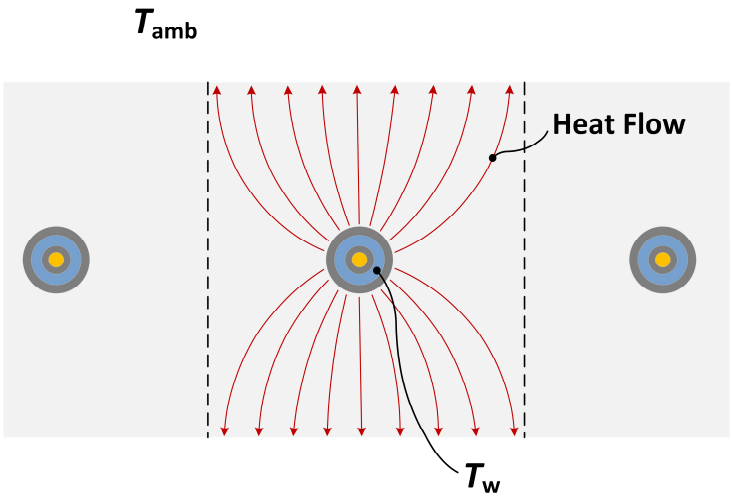

Figure 4.22: Heat flows between outer tube wall and edge of insulation

$$R_{wall} = \frac{\ln\left(\frac{D_{out,wall}}{D_{in,wall}}\right)}{2\pi L_{ch} k_{wall}} = \frac{\ln\left(\frac{6\ mm}{4\ mm}\right)}{2\pi * 0.41\ m * 14.94\ W\ m^{-1}K^{-1}} \tag{4.19}$$

$$= 0.011\ K\ W^{-1}$$

$$R_{ins} = \frac{th_{ins}}{k_{ins}(2 * Pitch_{ch} * L_{ch})}$$

$$48.02\ K\ W^{-1} = \frac{0.025m}{0.043\ W\ m^{-1}K^{-1}(2 * 0.015\ m * 0.41\ m)} \tag{4.20}$$

The natural convection and radiation resistances are calculated using the standard method shown in Equations 4.12 and 4.13. The natural convection heat transfer coefficient was calculated with the Raithby and Hollands (1998) correlation for natural convection at the surface of a vertical plate, with the emissivity of the surface assumed to be 0.8. For the case described in Table 4.6, the natural convection resistance is 29.46 K W^{-1}, while the radiation resistance is 17.93 K W^{-1}.

The thermal gain for the ambient is calculated using the total thermal resistance and the log mean temperature difference, as shown in Equation 4.21. In this equation, *i* denotes the channel number. Again, the heat gain was assigned a 50% uncertainty to account for some of the assumptions and correlations used in the analysis.

$$\dot{Q}_{amb}[i] = \frac{LMTD_{amb}[i]}{R_w[i] + R_{wall} + R_{ins} + \left(\frac{1}{R_{NC}[i]} + \frac{1}{R_{rad}[i]}\right)^{-1}} \tag{4.21}$$

$$0.246\ W \pm 50\% = \frac{14.45\ K}{59.27\ K\ W^{-1}}$$

The inlet refrigerant enthalpy ($h_{ref,in}$) can then be calculated using an energy balance between the water and the refrigerant, accounting for heat gains from the environment. This energy balance is shown in Equation 4.22, where *i* denotes the channel number.

$$h_{ref,in}[i] = \left[\frac{\dot{m}_w[i] * \left(h_{w,out}[i] - h_{w,in}[i]\right) - \dot{Q}_{amb}[i]}{\dot{m}_{ref}[i]}\right] + h_{ref,in}[i] \tag{4.22}$$

With the inlet enthalpy, the thermodynamic state of the fluid is fully defined; therefore, the inlet quality ($x_{ch,in}$) can be calculated, as shown in Equation 4.23.

$$x_{ch,in}[i] = f\left(h_{ref,in}[i], P_{TS,in}\right) = \boxed{0.098 \pm 0.027} \tag{4.23}$$

Finally, the inlet phase flow rates into the channels can be calculated using the refrigerant inlet quality and average fluid velocity ($\bar{u}$) measured with the time of flight sensors. The inlet vapor and liquid flow rates are shown in equations 4.24 and 4.25, respectively.

$$\begin{aligned} \dot{m}_{v,ch}[i] &= x_{ch,in}[i]\left(\rho_{ref,out}[i] * \bar{u}[i] * A_{TOF}\right) \\ &\boxed{1.87 \times 10^{-5} \pm 5.11 \times 10^{-6}\ kg\ s^{-1}} \\ &= 0.098(1262\ kg\ m^{-1} * 0.013\ m\ s^{-1} * 1.14 \times 10^{-5}\ m^2) \end{aligned} \tag{4.24}$$

$$\begin{aligned} \dot{m}_{l,ch}[i] &= \left(\rho_{ref,out}[i] * \bar{u}[i] * A_{TOF}\right) - \dot{m}_{v,ch}[i] \\ &= \boxed{1.17 \times 10^{-4} \pm 9.30 \times 10^{-6}\ kg\ s^{-1}} \end{aligned} \tag{4.25}$$

The phase flow rates are normalized with the perfectly distributed phase flow rate case so that the results for different inlet cases can be easily compared. The normalization is shown in Equation 4.26, where *i* denotes the channel number, *j* specifies the phase (*l* or *v*), $\dot{m}$ is the phase flow rate, and N_{ch} is the total number of channels (= 10).

$$\dot{m}_j^*[i] = \frac{\dot{m}_j[i]}{\left(\sum_{i=1}^{N_{ch}} \dot{m}_j[i]\right)/N_{ch}} \tag{4.26}$$

4.3.3 Distribution Parameter

The normalized standard deviation (*NSTD*) was used to quantify the overall degree of maldistribution for a given inlet condition. This parameter is the ratio of the standard deviation of the channel flow rates to the maximum possible standard deviation. The definition of this variable bounds the degree of maldistribution between 1 (worse possible distribution) and 0 (perfect distribution). The normalized standard deviation is defined in Equation 4.27, where $\dot{m}^*$ is the non-dimensional flow rate in a given channel, *j* represents the fluid phase under consideration (l, v, or total) and N_{ch} is the total number of channels in the heat exchanger.

$$NSTD_j = \sqrt{\frac{\sum_{i=1}^{N_{ch}} \left(\dot{m}_{j,i}^* - 1\right)^2}{(N_{ch} - 1)N_{ch}}} \tag{4.27}$$

The *NSTD* provides useful information when comparing the distribution for different inlet conditions or header geometries and has been used in the literature (Marchitto *et al.*, 2008; Mahvi and Garimella, 2017) to quantify the overall degree of maldistribution in heat exchangers.

4.3.4 Pressure Drop

The overall pressure drops across parallel flow paths in a heat exchanger can have a large impact on two-phase flow distribution. The pressure change across a single circular microchannel can be calculated using correlations from the literature, but two-phase pressure drop in heat exchanger manifolds has not been extensively studied. In this work, the pressure drops between the inlet feeder tube and the inlet of channels 2, 6 and 9 are measured experimentally. Due to spatial limitations, the measurement includes contributions from the pre-heater housing, the feeder tube and a portion of the outlet channels. This also results in a small height difference in the pressure ports (~2.4 mm) which is accounted for by calculating the hydrostatic pressure change in the pressure tap lines. The pressure drop contributions upstream of the test section inlet and at the entrance of the parallel heat exchanger channels are predicted with correlations from the literature and assigned a 25% uncertainty. The inlet losses (ΔP_{inlet}) consist of a frictional loss in the heater assembly, a contraction loss as the cross-sectional area is reduced to the header inlet area, and a frictional loss in the feeder tube. The frictional losses are estimated using the Friedel (1979) correlation, which is commonly used for two-phase flows in macrochannels, while the contraction loss is estimated using the approach proposed by Hewitt *et al.* (1994). The pressure change in the heat exchanger channel upstream of the pressure tap is calculated using the Kim and Mudawar (2012) frictional pressure drop correlation and the Baroczy (1965b) void fraction correlation. The pressure change across the header is then calculated using Equation 4.28. More details about this calculation are included in Appendix B.

$$\Delta P_{header} = \Delta P_{meas} + \left(\rho_{tap,up}\, g L_{tap,up} - \rho_{tap,down} g L_{tap,down}\right) - \Delta P_{inlet} - \phi_v^2 \left(\frac{2 f_v \left(G_{ch} x_{ch,in}\right)^2}{\rho_v D_{ch}}\right) L_{ch,in} + \left[\left(1 - \alpha_{ch,in}\right)\rho_l + \alpha_{ch,in}\rho_v\right] g L_{ch,in} \quad (4.28)$$

The pressure drop across the entire test section is also measured. Again, the measurement includes pressure drop in the inlet and exit tubing and the hydrostatic head between the test section inlet and outlet pressure taps (in the pressure tap lines), as shown in Figure 4.23. The pressure drop in the inlet and exit lines is estimated for using the Friedel (1979) and Churchill (1977b) correlations, respectively, and the hydrostatic head is calculated based on the fluid density and the length of the tap lines. The total pressure drop across the test section is then calculated using Equation 4.29.

$$\Delta P_{TS} = \Delta P_{meas} + \left(\rho_{tap,up}\, g L_{tap,up} - \rho_{tap,down} g L_{tap,down}\right) - \Delta P_{inlet} - \left(\frac{2 f G_{out}^2}{\rho_l D_{feed}}\right) L_{outlet} \quad (4.29)$$

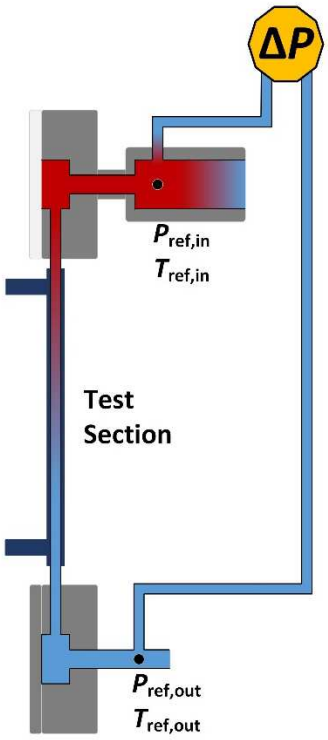

Figure 4.23: Side view of test section showing the pressure transducer (gold), the pressure tap lines, and the location of the taps relative to the test section manifolds and channels

The experimental facility and analysis approach described in this chapter are used to evaluate flow distribution of saturated refrigerants in a plate-type heat exchanger. Chapter 5 presents the experimental results and discusses the observed header flow regimes, measured header and test section pressure drops, and measured distribution characteristics for a range of inlet conditions.

CHAPTER 5. RESULTS AND DISCUSION

This chapter presents an overview of the distribution and pressure drop data collected for saturated refrigerant (R134a) flow in plate-type heat exchanger headers. The heat exchanger considered in this work is a condenser with refrigerant flow through horizontal manifolds supplying vertical-downward flow in minichannels. A summary of the test conditions investigated for the baseline rectangular header is presented in Table 5.1. The flow distribution was measured at a nominal saturation temperature of 30ºC, header inlet qualities between 0 and 1, and header inlet mass fluxes between 23.9 and 95.7 kg m^{-2} s^{-1}. The inlet mass fluxes considered in this work correspond to average channel mass fluxes between 50 and 200 kg m^{-2} s^{-1}.

Table 5.1: Summary of the header inlet qualities and mass fluxes tested in the rectangular header geometry

		Inlet Quality [-]								
		0.1	0.2	0.3	0.4	0.5	0.6	0.7	0.8	0.9
Inlet Mass Flux [kg m^{-2} s^{-1}]	23.9			X		X		X		
	35.9			X		X		X		
	47.8			X		X		X		
	59.8	X	X	X	X	X	X	X	X	X
	71.8			X		X		X		
	83.7			X		X		X		
	95.7			X		X		X		

5.1 Header Flow Regimes

The two-phase flow patterns inside the header can heavily influence the distribution characteristics in a heat exchanger. In these experiments, a transparent window was

installed so that the flow patterns could be recorded and analyzed. The flow regimes were categorized based on visual observation. The two-phase flows in the header were recorded using a Photron FASTCAM SA4 camera with Nikon Micro-NIKKOR 105 mm lens. The high-speed camera was aligned perpendicular to the flow direction and high intensity lights were used to illuminate the two-phase mixture inside the manifold. The Photron FASTCAM viewer software was used to capture the videos and adjust the image resolution, frame rate and shutter speed. All videos are 0.5 seconds in duration and are taken at a frame rate of 3000 fps and a shutter speed of 1/5000.

This section describes the refrigerant flow patterns observed in the header and compares them with the flow patterns seen in the air-water study. The flow patterns are classified into major regimes and the characteristics of each regime are related to the expected liquid and vapor distribution.

5.1.1 Flow Regime Characteristics

Flow patterns often change drastically along the header length because the local phase velocities decrease as fluid progressively exits the manifold. Therefore, it is not possible to define a flow pattern that applies to all locations in the header at a given time. Instead, flow regimes were defined immediately downstream from the inlet port. The observed flows can be broadly categorized into two groups: gravity-dominated and momentum-dominated, as shown in Figure 5.1. In the gravity-dominated regime, the fluid is stratified in the header and a liquid pool is present on the bottom surface near the inlet port. In the momentum-dominated regime, the liquid is mixed with the vapor in the central part of the header near the inlet port. In the air-water study (Chapter 3), the gravity

dominated regime was further discretized into stratified-smooth and stratified-wavy flow, while the momentum-dominated regime was split into smooth-film, wavy-film, and churn-turbulent flow.

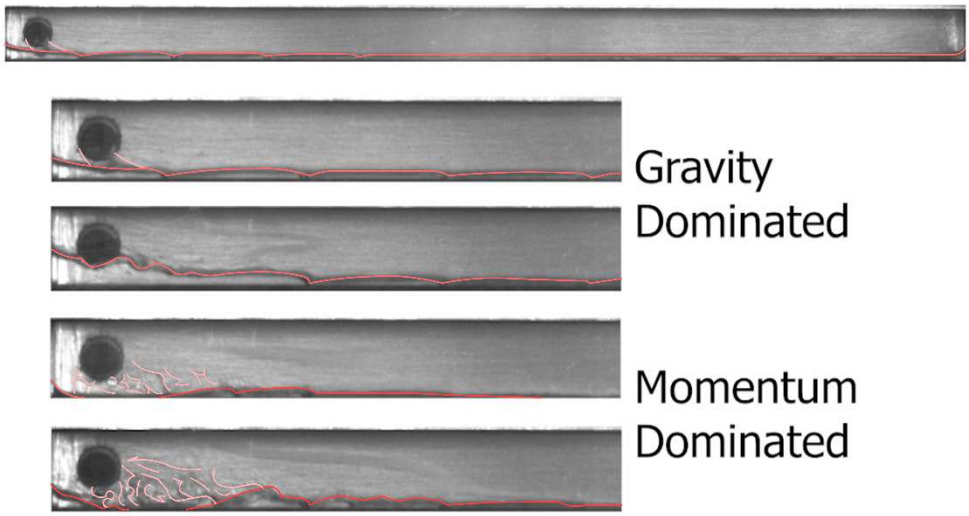

Figure 5.1: A photograph of the full rectangular header (top) and zoomed-in photographs of refrigerant flow regimes observed in the rectangular header. The red lines in the image show the position of the interface.

The flow regimes differ somewhat from those seen in the air-water experiments, which is likely due to the significantly different fluid properties for the conditions tested. Specifically, the average surface tension is about 1 order of magnitude lower ($\sigma_{R134a} \approx 0.0073$ N m^{-1}, $\sigma_{a\text{-}w} \approx 0.073$ N m^{-1}) and the average liquid-gas density ratio is over 20 times smaller ($[\rho_l/\rho_v]_{ref} \approx 31.5$, $[\rho_l/\rho_v]_{a-w} \approx 750$) in the refrigerant experiments. The low surface tension of refrigerants promotes Kelvin-Helmholtz instabilities and results in wavier liquid-vapor interfaces. The low liquid-gas density ratio of refrigerants also promotes Kelvin-Helmholtz instabilities, which will produce wavier interfaces in both the stratified and film flow regimes.

Furthermore, the vapor velocities are much lower for a given inlet condition in the refrigerant experiments due to the higher vapor density ($\rho_{v,a-w} \ll \rho_{v,R134a}$). As discussed in Chapter 3, the stagnation pressure of the vapor as it hits the front wall of the header generates a pressure gradient in the depth direction. When the pressure gradient is sufficiently large, the flow pattern in the header is film flow in which liquid flows along the back surface. Since the vapor velocity, and therefore the stagnation pressure, is lower in the refrigerant experiments, the film-flow regime is not as prevalent. Although film flows were sometimes observed in the saturated refrigerant experiments, the regime often has some characteristics of stratified or churn-turbulent flow.

Despite these differences, the flow patterns seen at the inlet of the header in the refrigerant experiments were categorized into the flow regimes that were most similar to those identified in the air-water experiments. For example, the flow pattern depicted in the bottom photograph in Figure 5.1 shows some similarities to stratified wavy flow; however, the absence of the stratified liquid pool immediately downstream from the inlet port and the mixing of the liquid and vapor in the central area of the header suggest that it could be more appropriately described as churn-turbulent flow.

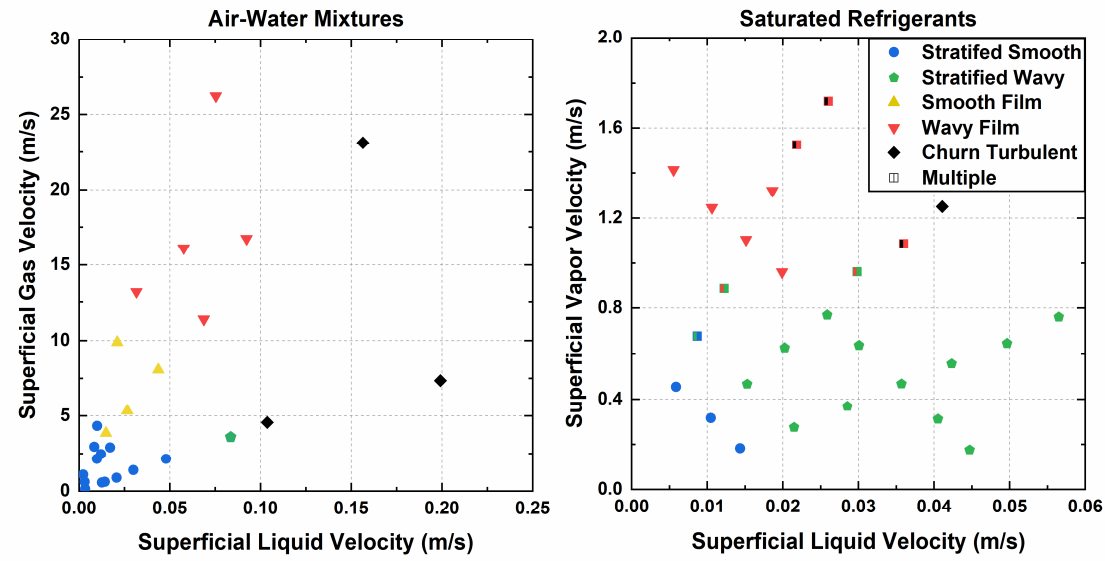

Figure 5.2: Observed flow regimes in rectangular headers as a function of superficial phase velocities for air-water (left) and saturated refrigerant (right) flows. Note: the axis scales are different for the two plots.

The flow regimes in a rectangular header for both the air-water and the refrigerant experiments as a function of the superficial phase velocities are shown in Figure 5.2. Data points that displayed characteristics of multiple flow regimes equally are shown using bicolored symbols with the colors associated with the two patterns they resembles the most. The regions where different flow regimes occur are similar in the two studies. For example, at relatively low superficial liquid and vapor velocities, the flow is stratified-smooth for both fluids. The main differences between the air-water and refrigerant results are the number of data points in different regimes and the magnitudes of the superficial phase velocities where regime transitions occur. A larger percentage of the collected data are in the stratified-wavy and wavy film flow regimes for the saturated refrigerant flows. This is partially due to the differences in the test matrices. In the air-water experiments, the superficial velocities tested were not uniformly spread across the range of interest. More experiments were conducted at low superficial liquid and gas velocities, leading to more

data in the smooth flow regimes. Differences in the observed flow regimes can also be attributed to changes in the fluid properties, as described above. Saturated refrigerant flows are expected to transition to wavy flow regimes faster than air-water mixtures because of the lower surface tension and density ratio.

The other major difference between the air-water and refrigerant results is the phase velocities at which regime transitions occur. Header flow regime maps based on superficial phase velocities far different from those for which they were developed will likely not be applicable in such cases. It is important to be able to predict the flow regime inside a header for a variety of fluids and flow conditions so that the expected distribution can be determined. The transition between gravity-dominated and momentum-dominated flow is particularly important because it causes a significant change in the flow distribution characteristics, which is discussed in more detail in Section 5.3.

The flow regime results can be recast in terms of the Modified Froude number to try to capture the transition from stratified to unstratified flows for a range of fluid properties. The Froude number was chosen because it represents the relative importance of inertia and gravity, which are two of the driving forces governing this transition. The Modified Froude number is the standard Froude number multiplied by a form of the density ratio, as shown in Equation 5.1:

$$\mathrm{Fr}^{*} = \sqrt{\frac{\rho_v}{\rho_l - \rho_v}}\,\frac{j_v}{\sqrt{D_H g}} \tag{5.1}$$

where ρ_l and ρ_v are the liquid and vapor densities, respectively, j_v is the superficial vapor velocity, D_H is the header hydraulic diameter, and g is the gravitational acceleration. Taitel and Dukler (1976) first proposed this parameter when defining the transition between stratified and intermittent or annular-dispersed two-phase flow regimes in a circular horizontal channel. The observed flow patterns in the air-water and refrigerant experiments are shown in Figure 5.3 as a function of the Martinelli and Modified Froude numbers. An estimate of the transition region between stratified and unstratified flows (or gravity-dominated and momentum-dominated flows) is shown in grey. The present study was not designed to precisely identify the transitions between flow regimes; therefore, the grey areas are approximations and are only shown for discussion purposes.

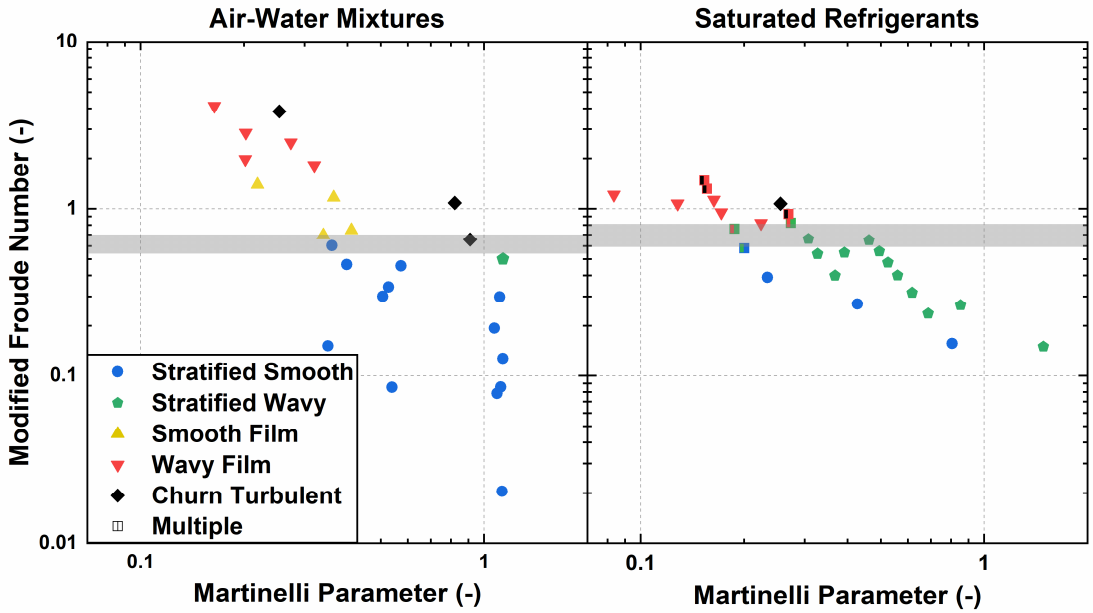

Figure 5.3: Observed flow regimes in rectangular headers as a function of the Martinelli parameter and the Modified Froude number (Equation 5.1) for air-water (left) and saturated refrigerant (right) flows

The results show that the transition between gravity- and momentum-dominated flow regimes occurs near the same Modified Froude numbers for both air-water mixtures and saturated refrigerants. This parameter provides a way to distinguish between these two regimes and is a good candidate for two-phase flow regime maps for plate-type heat exchanger headers.

5.1.2 Distribution Characteristics of Flow Regimes

The flow regime inside the header heavily influences the distribution of liquid and vapor in heat exchanger channels. When the regime is gravity dominated, liquid flows along the bottom surface of the header, as shown in Figure 5.4. When the liquid encounters the first tube, a portion exits the header through the tube, while the remainder flows through the gap between the channel inlet and the front and back walls of the header. The remaining liquid continues downstream to the next channel and splits in a similar fashion. In general, for gravity-dominated flows, the highest liquid flow rates occur in the channel closest to the inlet and taper off in downstream channels. The vapor phase distributes well into channels clear of liquid and is inversely related to the liquid flow in channels near the inlet. The only deviation from this trend occurs when the inlet liquid mass flow rate is significantly higher than the inlet vapor flow rate (low inlet quality). If a large fraction of the total liquid flow exits the header through a single channel, the frictional pressure drop through that path would be very high. There are pressure drop restrictions across each path in the heat exchanger, which are discussed in detail later in this chapter. Due to these pressure drop restrictions, the liquid distributes relatively equally into the first two or three channels in the heat exchanger at low inlet qualities and then tapers off in downstream channels.

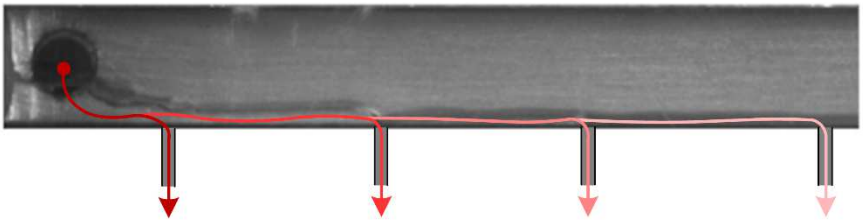

Figure 5.4: Liquid flow paths for gravity-dominated flows (G_{in} = 59.8 kg m^{-2} s^{-1}, x_{in} = 0.29)

In the momentum-dominated regime, the liquid is not confined to the bottom surface of the header, as shown in Figure 5.5. This allows some of the liquid to flow past the entrance to the first channel in the central part of the header. As the flow decelerates, the local flow regime becomes stratified and liquid starts flowing along the bottom surface of the header. Once the gravitational forces become dominant in the header, the flow characteristics are similar to those in the gravity-dominated regime, and the liquid flow rates start to taper off in downstream channels.

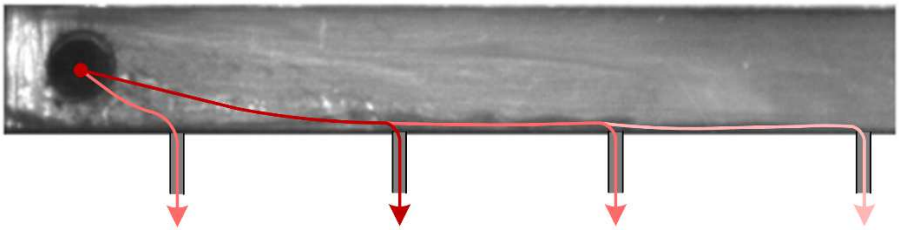

Figure 5.5: Liquid flow paths for momentum-dominated flows (G_{in} = 59.8 kg m^{-2} s^{-1}, x_{in} = 0.70)

5.2 Pressure Drop

Flow distribution in heat exchangers is also constrained by the pressure drop across each flow path. A simple schematic of the flow paths in a three-channel heat exchanger is shown in Figure 5.6. The fluid enters the multi-channel heat exchanger through the inlet

port at a pressure P_{in}. The flow then splits into the three channels in the inlet manifold, exchanges heat with the coupling fluid, and then recombines in the outlet manifold. Finally, the fluid exits the heat exchanger at a pressure P_{out}, which is dependent on the total pressure drop across the component.

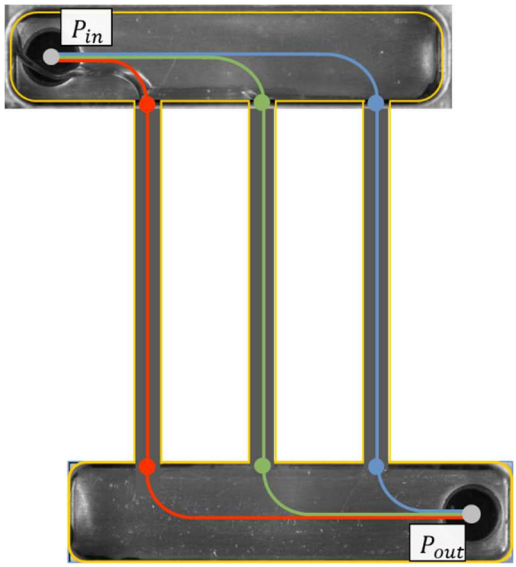

Figure 5.6: Flow paths in a simple three-channel heat exchanger (reproduced from Figure 2.4)

The pressure change through each of the three flow paths must be equal so that the inlet and exit pressure are the same for each path. The path pressure drop is the sum of the pressure drops through the manifolds and the channels. It is important to understand the pressure profiles in each path when considering the flow distribution in a heat exchanger. This section describes the driving factors in the path pressure change for a variety of channel inlet conditions, and then presents the measured pressure changes across the test section and the rectangular inlet header.

5.2.1 Full Test Section

In most cases, the total heat exchanger pressure drop is heavily influenced by the pressure drop characteristics in the channels. The pressure change in the channels is governed by the magnitudes of the frictional and gravitational pressure gradients in the condensing region and the extent of the two-phase region in the channel. In the two-phase region, the frictional pressure drop is relatively high, and the pressure change due to gravity (which is a pressure rise due to the vertical descending flow) is low. The frictional pressure gradient predicted by the Kim and Mudawar (2012) correlation for a variety of local fluid states is shown in Figure 5.7(a), while the gravitational pressure gradient based on the Baroczy (1965a) void fraction correlation is shown in Figure 5.7(b). As the local quality increases, the magnitude of the (negative) frictional pressure gradient increases and the magnitude of the (positive) gravitational pressure gradient decreases, resulting in a higher local pressure drop. When the mass flux increases, the gravitational pressure gradient remains constant because it is not a function of mass flux, but the magnitude of the frictional pressure gradient increases significantly. Therefore, both increasing the mass flux or the local quality increase the local pressure drop.

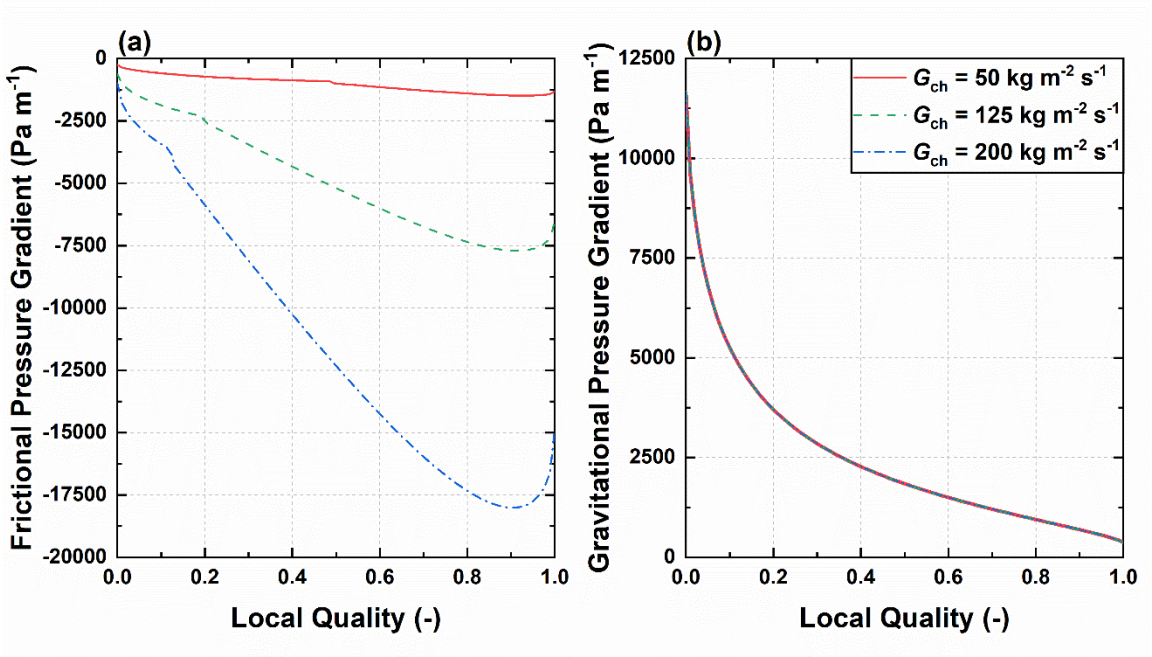

Figure 5.7: The local (a) frictional and (b) gravitational pressure gradients in the heat exchanger channels for a variety of local fluid states

Another factor that substantially influences the pressure change across a heat exchanger channel is the extent of the condensation region (the length of the tube that exhibits two-phase flow). After the fluid fully condenses, the pressure starts to rise rapidly because the magnitude of the frictional pressure gradient is low, and the gravitational gradient is high (see $x_{local} = 0$ in Figure 5.7). The magnitude of the pressure change across the channel is directly proportional to the length of the condensing portion of the tube; therefore, the total pressure drop across the channels will increase as the condensation length increases. The condensation length for a variety of channel mass fluxes and inlet qualities is shown in Figure 5.8. These lengths were calculated using the detailed heat transfer and pressure drop model presented in Chapter 6. The condensation length increases with inlet quality because the fluid must go through a larger enthalpy change to reach a subcooled state. Similarly, the condensation length also increases for higher

channel mass fluxes because of the larger heat duties needed to effect a given quality change at the higher mass fluxes.

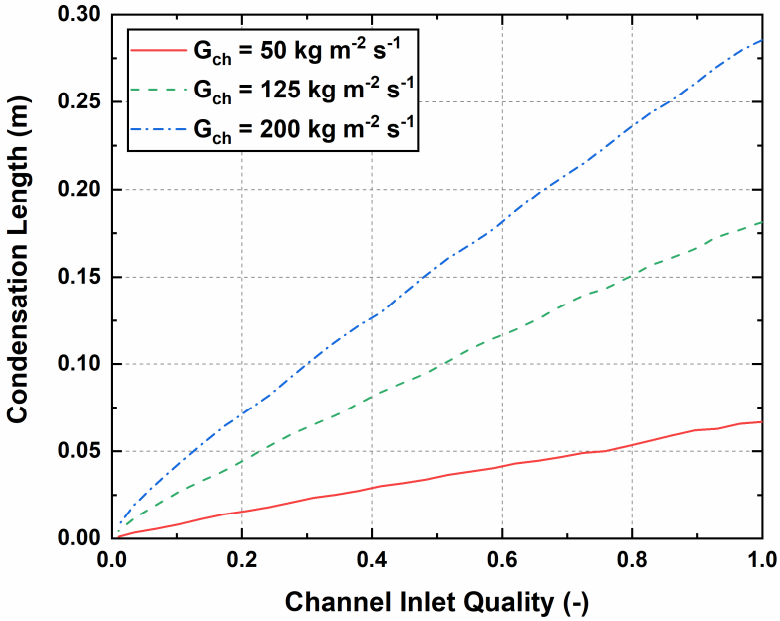

Figure 5.8: Length of the heat exchanger channel that contains two-phase flow for a variety of channel mass flow rates and inlet qualities

The pressure change across the full test section, including the manifolds and parallel channels, is shown in Figure 5.9. The pressure increases from the inlet to the outlet for all cases, indicating that the gravitational pressure rise is larger than the frictional pressure drop for the conditions tested. The variation in pressure rise with inlet quality and mass flux follows the expected trends. As the inlet quality rises, the average inlet qualities into the channels should also rise. This increases the magnitude of the frictional two-phase pressure gradients and increases the condensation length, which both lead to lower pressure gain from the inlet to the outlet of the channel. As the inlet mass flux increases, the average mass flux into the channels should also increase, which has a similar effect on the path pressure rise. Higher mass fluxes will increase the magnitude of the frictional two-phase

pressure gradients and increase the condensation length, leading to lower pressure rise across the test section.

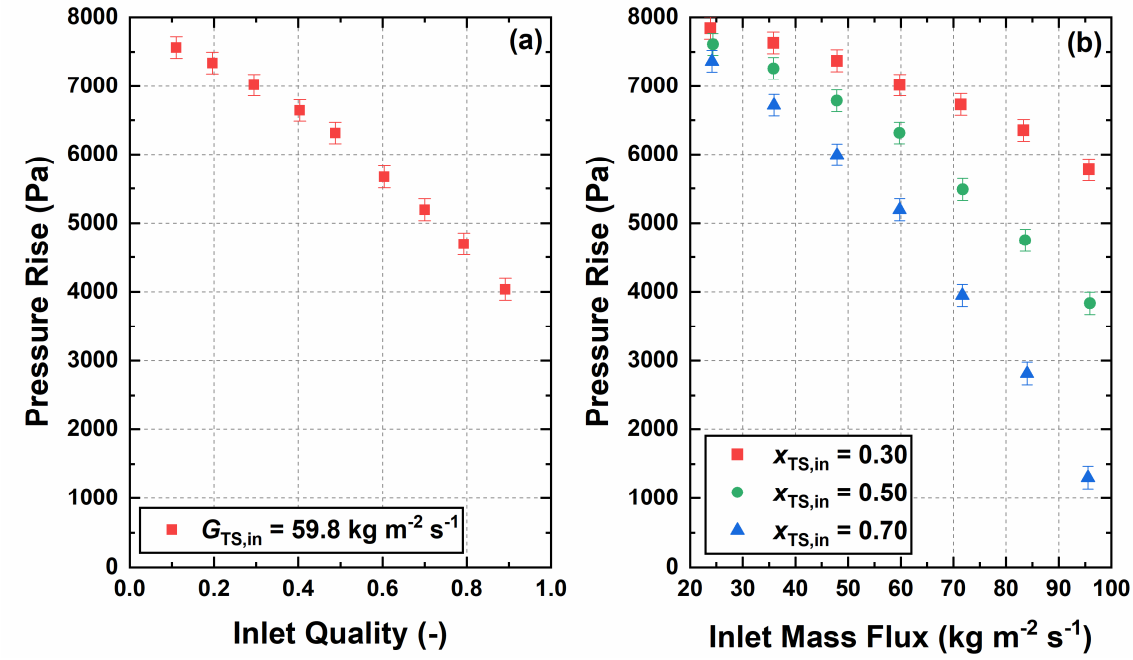

Figure 5.9: Pressure rise through the test section as a function of (a) header inlet quality and (b) header inlet mass flux

5.2.2 Header

Pressure drop in manifolds can also influence two-phase flow distribution if it significantly contributes to the path pressure drop. In the heat exchanger considered in this study, the outlet manifold has the same geometry as the rectangular inlet manifold and always contains liquid refrigerant. The single-phase pressure drop across the rectangular inlet manifold was measured to estimate the magnitude of the pressure loss in the exit header. The single-phase pressure drop in the inlet manifold was on the order of 10 Pa, which is less than about 1% of the total path pressure drop. Since this should not have a

significant influence on the distribution, it was not directly measured and was neglected in the pressure drop model presented in Chapter 6.

However, the pressure drop across a manifold is more significant when it is supplied with a two-phase inlet condition. The measured pressure drop between the header inlet and the inlet to channels 2, 6 and 9 is shown as a function of the inlet quality in Figure 5.10(a). This measurement includes a minor loss associated with the fluid entering and turning 90 degrees into the test section, the frictional pressure loss in the header, the deceleration pressure recovery in the header, and the minor losses associated with the fluid entering each channel. As the quality increases, the pressure drop across the header increases as expected.

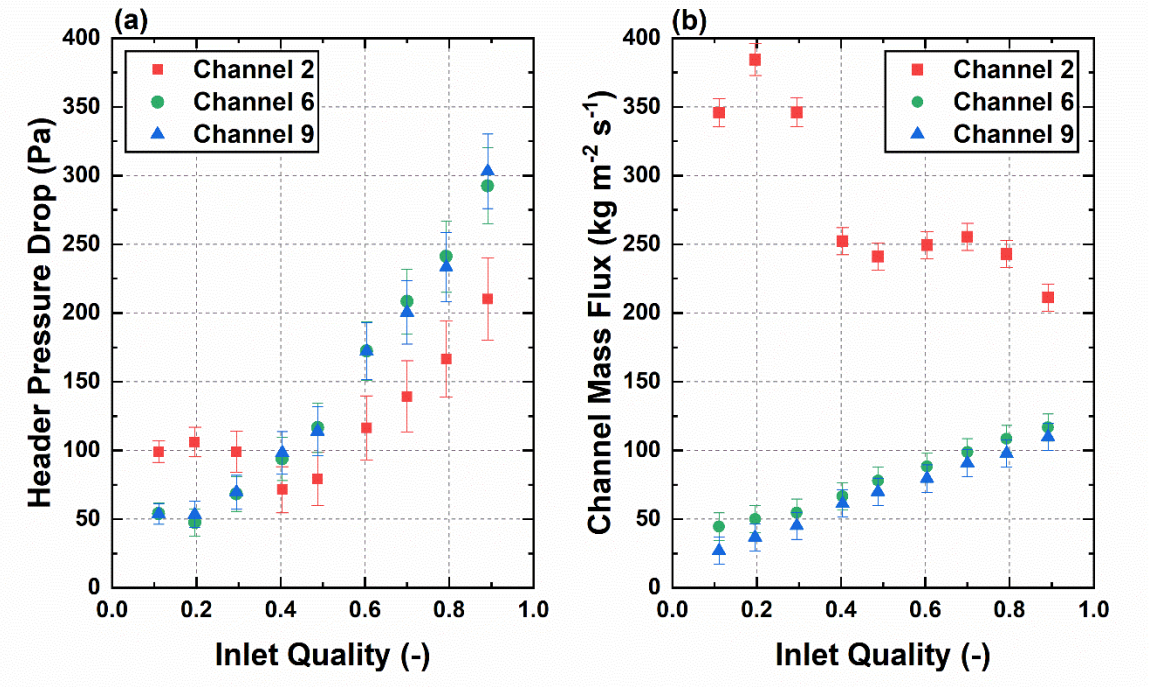

Figure 5.10: The measured (a) pressure drop between the header inlet and the inlet of channels 2, 6, and 9, and (b) the mass flux in channels 2, 6, and 9 for a range of inlet qualities

Additionally, the header pressure drop is affected by the location of the measurement. At low inlet qualities, the pressure drop is highest between the header inlet and the inlet to the second channel. The opposite is true at high qualities, where the pressure drop between the inlet and the second channel is the lowest of those measured. These trends can be explained by considering the minor losses associated with the fluid entering the heat exchanger channels. Two-phase minor losses can be estimated using Equation 5.2, where K_{loss} is the loss coefficient, G_{ch} is the channel mass flux, $x_{ch,in}$ is the quality at the inlet of the channel, and $\phi_{v,ch}$ is the vapor two-phase multiplier (Ghiaasiaan, 2017)

$$\Delta P_{minor} = K_{loss} \times \frac{1}{2}\rho_v\left(G_{ch}A_{ch}x_{ch,in}\right)^2\phi_{v,ch} \tag{5.2}$$

Since the inlet quality entering the second channel is lower than that entering the sixth and ninth channels for all the conditions tested, one might expect the measured header pressure drop to be lower at this location. However, the mass flow rates through the channels closer to the inlet are higher than downstream channels, as shown in Figure 5.10(b). The higher mass flow rates result in higher fluid velocities, increasing the minor loss at the channel inlets. The relationship between the header pressure drop and the channel mass flow rates suggests that the minor losses at the channel inlet play a significant role in the overall pressure drop across the header.

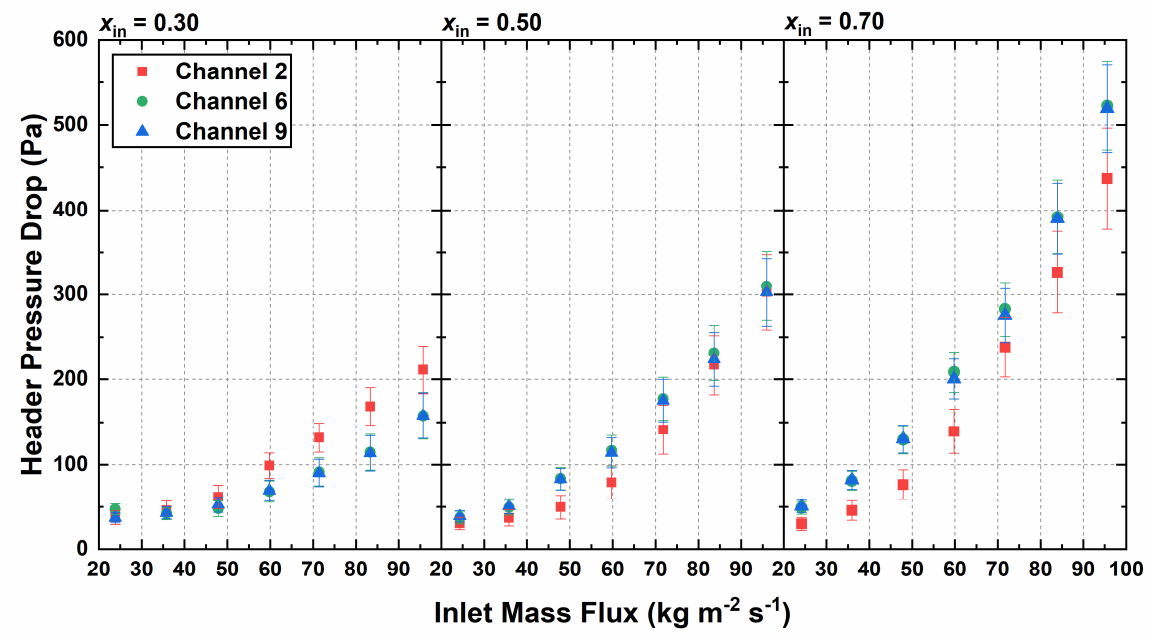

Figure 5.11: Header pressure drop at three different locations as a function of inlet header mass flux at inlet header qualities of 0.30 (left), 0.50 (center) and 0.70 (right)

The pressure drop between the header inlet and the inlets of channels 2, 6, and 9 is shown as a function of mass flux at three different inlet qualities in Figure 5.11. The magnitude of the pressure drop increases with both mass flux and quality, as expected. Again, the variations of the measurement between different locations can be partly explained by the minor losses associated with the fluid entering the heat exchanger channels.

5.3 Two-Phase Flow Distribution

Flow distribution is quantified in this study by measuring the channel mass flow rates and the inlet qualities. This section presents the distribution results and discusses the significance of the header flow regimes and path pressure drops. Additionally, the liquid and vapor distributions in the alternative header geometries are shown and explained.

First, a representative data point is presented, and the distribution characteristics are discussed. The sample case has an inlet mass flux of 59.7 kg m $^{-2}$ s^{-1} and an inlet quality of 0.49 (central conditions in the test matrix). The normalized mass flow rate and inlet quality into each channel for this condition are shown in Figure 5.12. The figure also includes a photograph of the two-phase flow pattern inside the header.

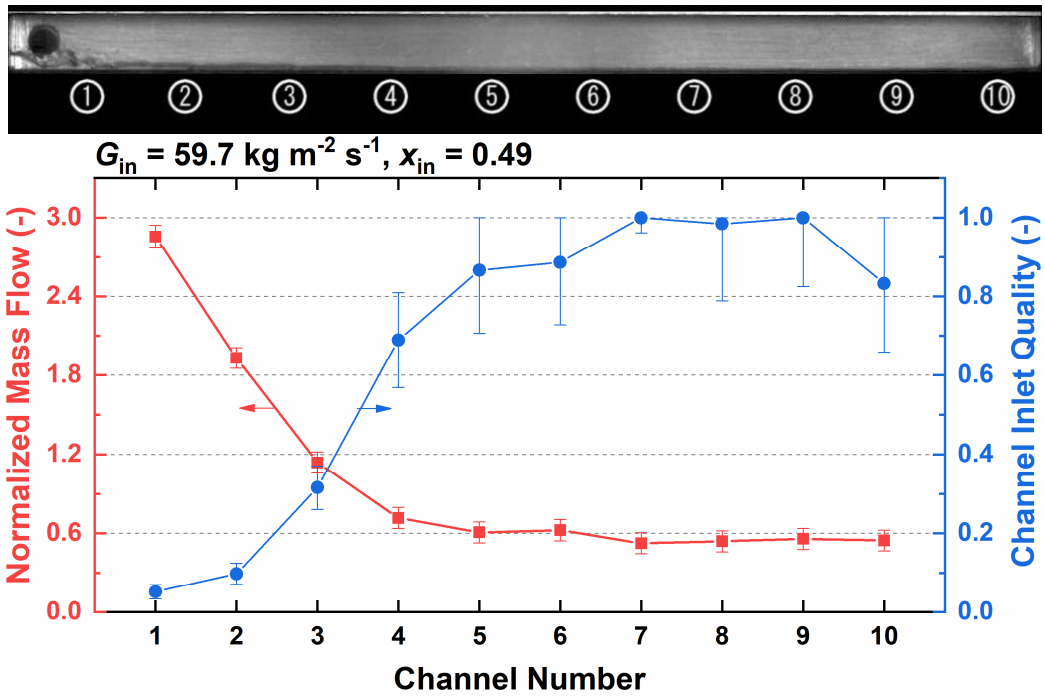

Figure 5.12: Total normalized mass flow rate and the inlet quality into each channel and an image of the header flow patterns for inlet conditions of G_{in} = 59.7 kg m^{-2} s^{-1} and x_{in} = 0.49

The flow regime in the header is gravity-dominated, which forces the liquid to flow down the channels closest to the inlet port. Consequently, most of the fluid entering channels 1 and 2 is in the liquid phase, as indicated by the low inlet qualities in these channels. The channel inlet quality steadily rises in the axial direction until channel 5. At this point, most of the liquid has exited the header, resulting in channel inlet qualities near 1 in the latter half of the manifold. There is a slight drop in the inlet quality into the last

channel, which may be due to edge effects, although the high measurement uncertainty at this location should be noted. The uncertainty bar intersects 1; therefore, it is difficult to say anything definitive about the effect of the far wall on the liquid distribution.

The high liquid flow rates in the channels nearest to the inlet port cause the total mass flow rates through those channels to be the largest because the liquid density is much greater than the vapor density ($\rho_l/\rho_v \approx 31.5$). For this representative case, the normalized mass flow rate is largest in the first channel, and then steadily decreases until channel 5. The total mass flow rate then levels out because most of the fluid entering the channels far from the inlet is in the vapor phase, which tends to distribute well.

The data presented in Figure 5.12 are shown in terms of the phase flow rates (calculated with Equation 4.26) in Figure 5.13 for further discussion. As described above, the liquid enters the channels closest to the inlet and the vapor predominantly distributes into downstream channels. For this condition, about 90% of the liquid exits through the first three channels and the flow is relatively maldistributed.

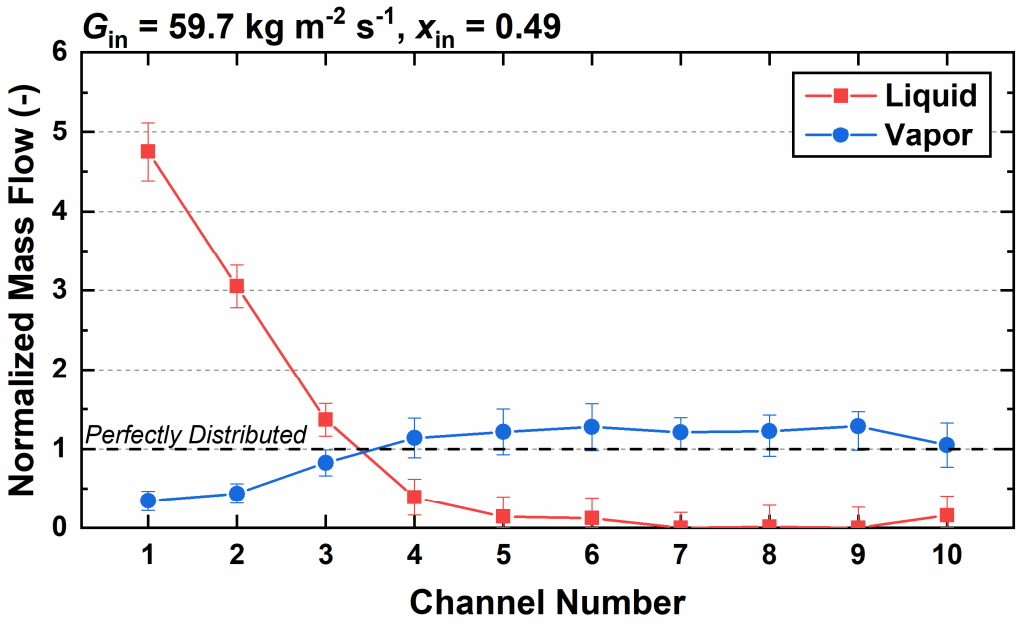

Figure 5.13: Normalized liquid and vapor flow rates at the entrance of each channel for header inlet conditions of G_{in} = 59.7 kg m^{-2} s^{-1} and x_{in} = 0.49

Although the sample case presented above provides insights into typical distribution trends, flow distribution is heavily dependent on the header inlet condition. The remainder of this section presents the flow distribution data collected for a large range of inlet mass fluxes (G_{in} = 23.9 to 95.7 kg m^{-2} s^{-1}) and qualities (x_{in} = 0 to 1). The trends are explained using insights from the header flow patterns and the path pressure drop characteristics, and the overall degree of maldistribution is quantified.

5.3.1 Effect of Inlet Quality on Distribution

The distribution in the rectangular header was measured for inlet qualities between 0.1 and 0.9, subcooled liquid and superheated vapor flows. The normalized liquid and vapor flow rates at the entrance of each channel for a range of header inlet qualities are shown in Figure 5.14.

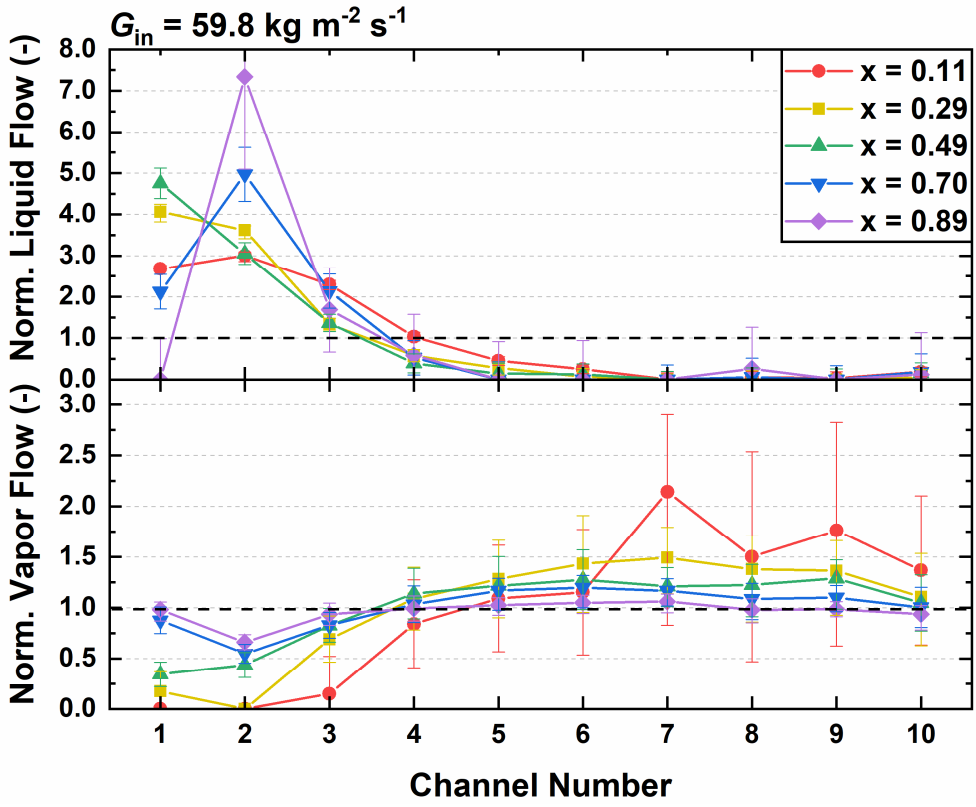

Figure 5.14: Normalized liquid and vapor flow rates at the inlet of each channel when two-phase flow enters the header at a mass flux of 59.8 kg m^{-2} s^{-1} and qualities between 0.11 and 0.89

When the refrigerant enters the header in the gravity-dominated regime (x_{in} = 0.1 to 0.5 for G_{in} = 59.8 kg m^{-2} s^{-1}), the highest liquid flow rate occurs in the first outlet channel. For high inlet qualities within this regime, the liquid mass flow rate monotonically decreases in channel locations farther from the inlet. However, at low inlet qualities the liquid flow rates are nearly equal in the first several channels. For example, when the fluid enters the header at an inlet quality of 0.1, the liquid distributes evenly in the first three channels, and then tapers off in channels farther downstream. The factors causing the observed liquid distribution trends at low inlet qualities were explored with the detailed model described in Chapter 6 that predicts the pressure profiles in each flow path.

When the refrigerant enters the header at a quality of 0.1, most of the fluid is in the liquid phase. If all the liquid enters the first channel and the vapor distributes evenly into the remaining channels, the pressure drops across each flow path would not be equal, as shown in Figure 5.15. In this scenario, the first channel contains single-phase liquid throughout its entire length. This would result in a large gravitational pressure gain but would also cause an extremely high frictional pressure drop because of the high Reynolds number of the flow. All remaining channels in the heat exchanger would contain approximately 11.1% of the inlet vapor flow rate (~1.11% of the total inlet mass flow rate). Although these channels contain two-phase flow, the frictional pressure drop is lower than the single-phase liquid channel because of the sustainably lower mass fluxes. This is offset by a lower gravitational pressure gain, but overall pressure gain in the two-phase channels is higher than the single-phase liquid channel. The pressure difference across each path must be equal; therefore, the case shown in Figure 5.15 is not physically possible. Pressure drop limits the maximum possible liquid flow rate in a single channel, which results in the observed low-quality liquid distribution trends shown in Figure 5.14. The limitations on the liquid distribution that result from requirements on the path pressure drops are discussed in more detail in Chapter 6.

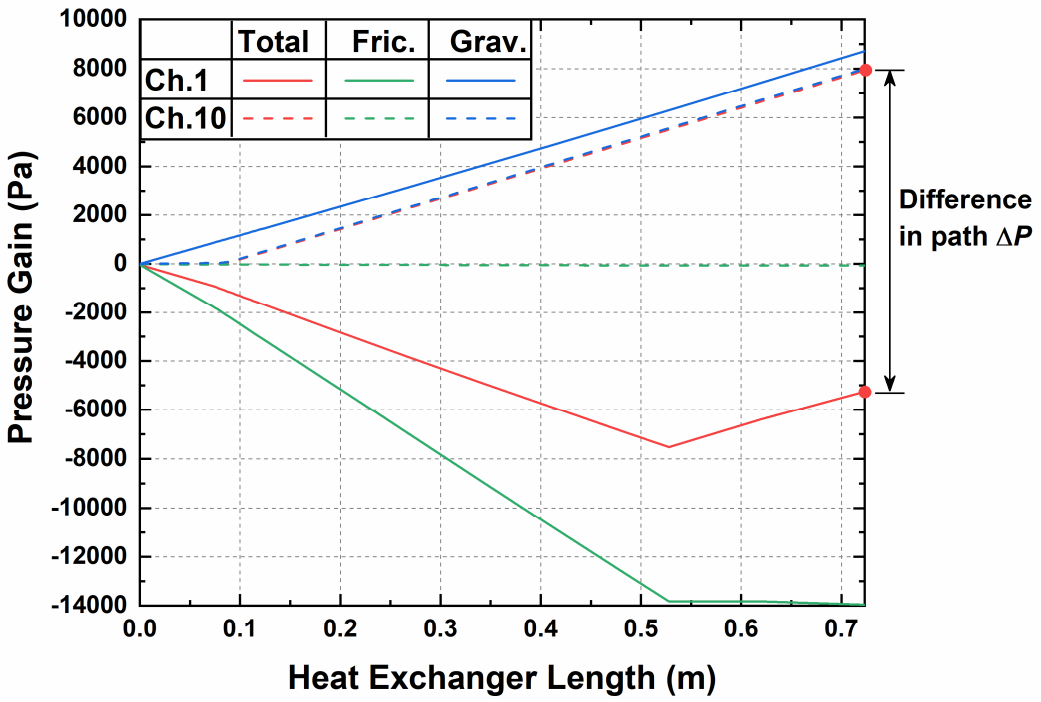

Figure 5.15: Path pressure profiles throughout test section for G_{in} = 59.8 kg m^{-2} s^{-1} and x_{in} = 0.11 assuming all the liquid entering the heat exchanger exits through the first channel.

When the refrigerant enters the header in the momentum-dominated regime (x_{in} = 0.6 to 0.9 for G_{in} = 59.8 kg m^{-2} s^{-1}), the distribution characteristics are different. This regime allows the liquid to flow unstratified through the core of the header past the first channel. For these cases, the peak liquid flow rate is generally in the second channel, as shown in Figure 5.14.

The degree of liquid and vapor maldistribution, defined using the normalized standard deviation (Equation 4.27), is shown as a function of the header inlet quality in Figure 5.16. The distribution is nearly perfect for single-phase liquid and vapor inlet conditions (x_{in} = 0 and 1, respectively). However, the distribution is generally poor when the refrigerant enters the header as a two-phase flow.

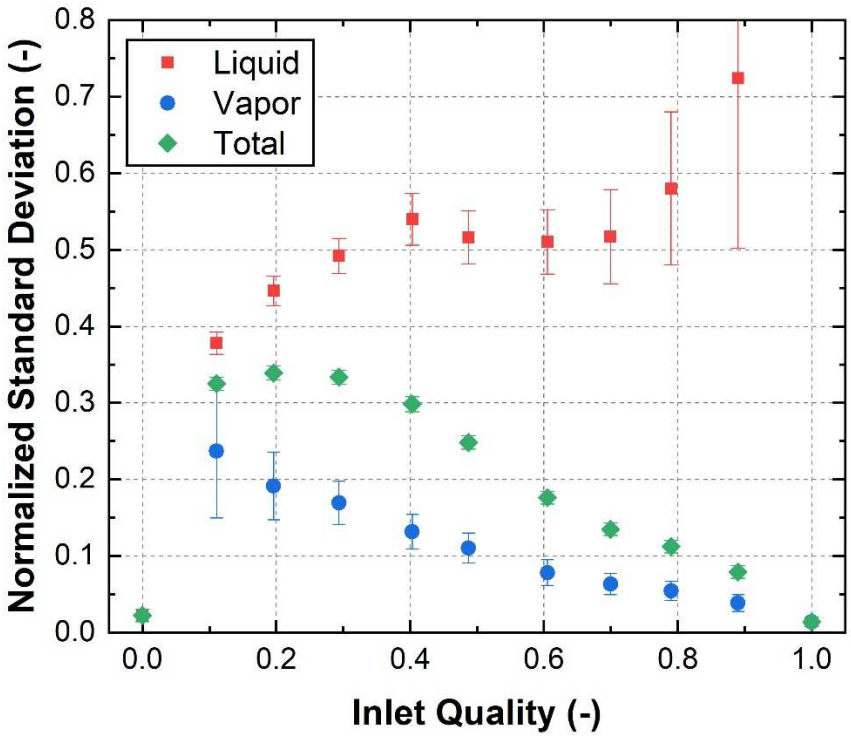

Figure 5.16: Degree of maldistribution of the vapor and liquid phases

At low inlet qualities, the liquid distributes relatively well because the path pressure drop requirements force more liquid into downstream channels. As the quality increases, the pressure drop limitations on the liquid distribution decrease, and the overall distribution worsens. At higher inlet qualities, the flow pattern in the header becomes momentum-dominated. In this regime, more liquid enters channels farther from the test section inlet but the maximum normalized flow rate and the number of channels receiving liquid remain approximately the same, which results in nearly the same degree of maldistribution. Finally, at high inlet qualities, the liquid distribution deteriorates because there is relatively little liquid entering the test section and it is concentrated in just a few channels, as shown in Figure 5.14.

Vapor tends to distribute well among (or across) channels that do not contain a significant amount of liquid. When the liquid mass flow rate in a channel is high, the vapor flow rate is limited because two-phase frictional pressure drop increases sustainably with channel inlet quality, as shown in Figure 5.7(a). As the header inlet quality increases, more of the mass entering the heat exchanger is in the vapor phase and the average liquid flow rates in the channels decreases. The lower liquid flow rates allow the vapor to distribute more evenly throughout the heat exchanger. This phenomenon reduces the degree of vapor maldistribution at higher inlet qualities, as shown in Figure 5.16.

The liquid and vapor distribution trends explain the degree of maldistribution of the total mass flow rate. As the quality increases from zero, the total mass flow distribution worsens because the pressure drop restrictions on the liquid distribution become less severe. As the inlet quality continues to increase, more of the mass entering the component is in the vapor phase, which tends to distribute well. The higher percentage of vapor entering the header results in an overall improvement in the distribution. The distribution continues to improve with quality until near-perfect distribution is achieved at an inlet quality of 1 (single-phase vapor inlet condition).

5.3.2 Effect of Inlet Mass Flux on Distribution

The normalized liquid and vapor flow rates at the entrance of each channel for an inlet quality of 0.50 and a range of inlet mass fluxes are shown in Figure 5.17. As the inlet mass flux increases, the liquid enters the header with a higher momentum. This pushes more of liquid to downstream channels and shifts the liquid distribution profile.

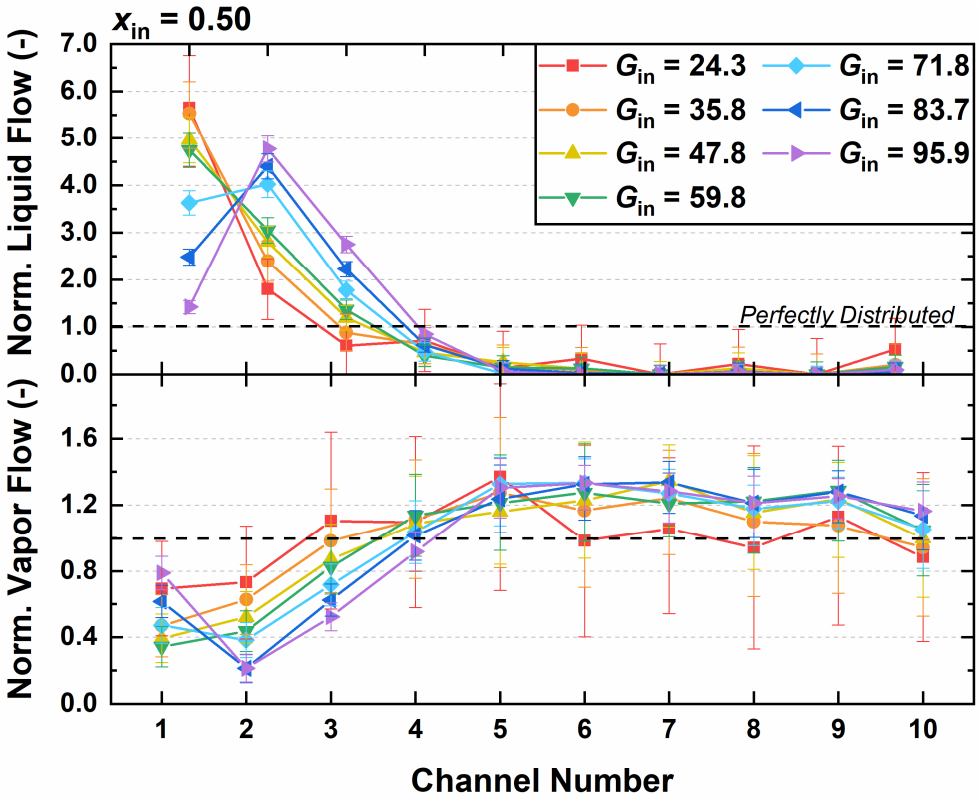

Figure 5.17: Normalized liquid and vapor flow rates at the inlet of each channel when two-phase flow enters the header at a quality of 0.50 and mass fluxes between 24.3 and 95.9 kg m^{-2} s^{-1}

When the flow enters the header in the gravity-dominated regime (G_{in} = 24.3 to 59.8 kg m^{-2} s^{-1} for x_{in} = 0.50), the highest liquid flow rate is in the channel closest to the inlet port. As the inlet mass flux increase, more liquid flows past the first channel in the header and enters the second and third channels. When the flow transitions into the momentum-dominated regime, the liquid has enough momentum to overcome gravity and flow through the central part of the header. This continues to push more of the liquid downstream and shifts the peak liquid flow rate into the second channel.

The vapor is highly mobile in the header and is not restricted by gravitational forces in the same way that the liquid is. This allows the vapor to distribute much more uniformly.

The main factor that determines the vapor distribution is the pressure drop through each flow path. This requires low inlet vapor flow rates in channels with high liquid flow rates to prevent the pressure gain from decreasing below what is achievable in the other channels. This causes the vapor distribution to mirror the liquid distribution. Therefore, as the liquid flow rates increase in downstream channels, the vapor flow rates must decrease, as shown in Figure 5.17.

The degree of liquid and vapor maldistribution is shown as a function of the header inlet mass flux in Figure 5.18. The inlet mass flux causes more liquid to enter downstream channels but does not have a strong influence on the overall distribution in the header. For instance, the normalized liquid flow rates are nearly the same for inlet mass fluxes of 59.8 and 95.9 kg m^{-2} s^{-1}. The only difference between these two cases is in the channels that exhibit the highest flow rates. At the lower inlet mass flux, the highest liquid flow rates occur in channel 1, followed by 2 and 3. At a high inlet mass flux, the highest liquid flow rate occurs in channel 2, followed by channels 3 and 1. Although the distribution profiles differ between these two cases, they are equally maldistributed.

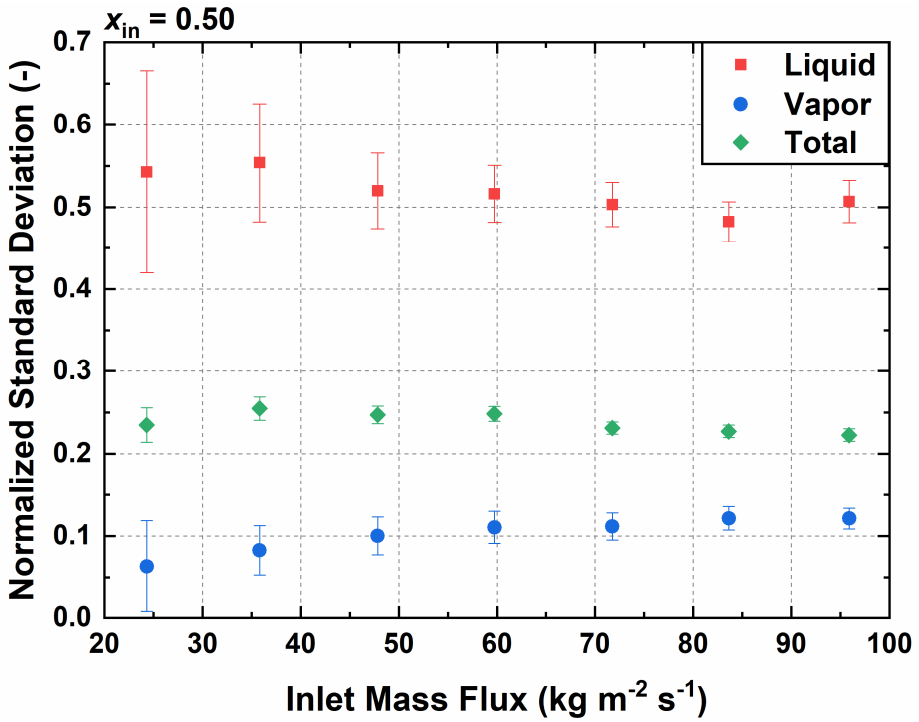

Figure 5.18: Degree of maldistribution of the vapor and liquid phases with inlet quality entering the header = 0.50 and varying inlet mass flux

5.3.3 Alternative Geometries

A triangular shaped header and a header with a guide vane were also experimentally evaluated. The triangular header was selected to maintain higher fluid velocities as the refrigerant flows away from the inlet, which could help transport more liquid to downstream channels. The vane header was designed to restrict flow through the vane and into the initial channels to help transport more liquid away from the inlet. Dimensional details of the vanes are provided in Chapter 4. Photographs of the observed flow regimes in each header are shown in Figure 5.19. The flow patterns inside the rectangular and triangular headers are nearly identical. Both are in the stratified-wavy flow regime, and other characteristics like the height of the stratified pool are similar in the two headers. The refrigerant in the vane header is still in the stratified-wavy flow regime, but the liquid pool

extends farther from the inlet. The differences in the liquid flow patterns are likely due to a combination of the extra resistance in the vane flow passages and the smaller effective header cross-sectional area.

There are also some interesting flow phenomena in the small gap between the vane and the bottom surface of the header. Near the entrances to the third and fourth channels, liquid slugs span the entire area. This restricts the mobility of the vapor in the header. The distance between the vane and the bottom surface was set based on the size of the rectangular header. The distribution properties of the vane header design may improve if this area is enlarged.

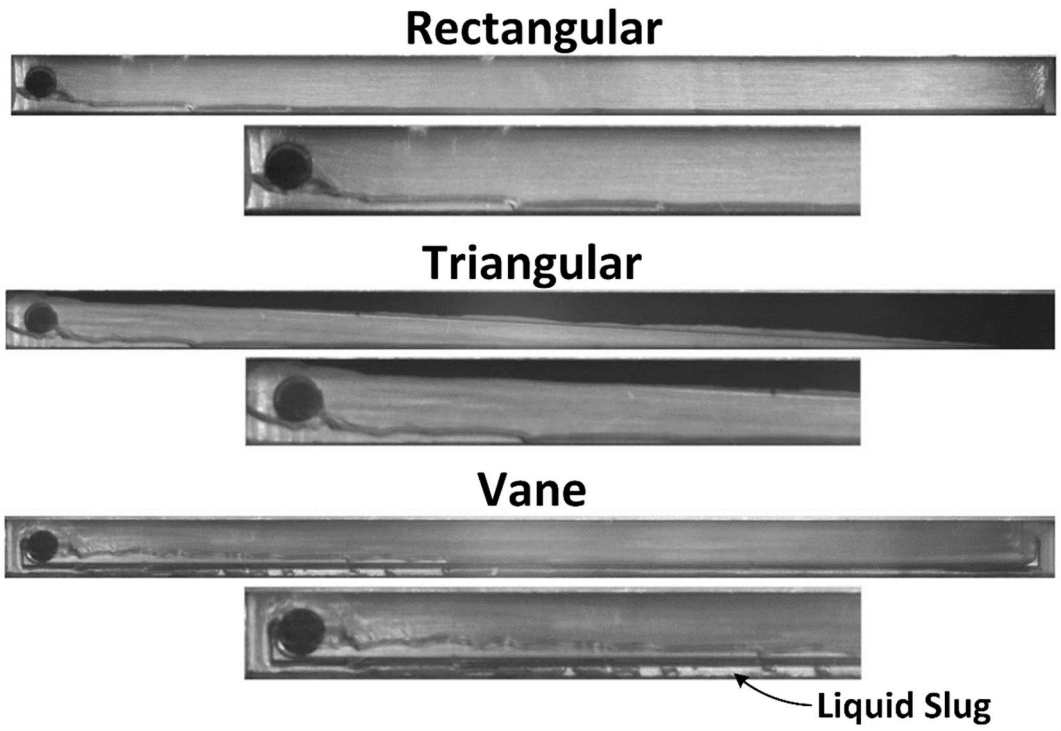

Figure 5.19: Photographs of the flow patterns in the rectangular (top), triangular (middle) and vane (bottom) headers with an inlet condition of G_{in} = 59.9 kg m^{-2} s^{-1} and x_{in} = 0.30

The liquid and vapor normalized flow rates throughout each heat exchanger are shown in Figure 5.20 when the inlets are supplied with a mass flux of 59.8 kg m^{-2} s^{-1} and a quality of 0.30. There is no significant difference between the distribution profiles in the rectangular and triangular headers. In this case, the area restriction is not severe enough near the inlet to increase the momentum of the liquid phase, resulting in a similar distribution. The vane header can transport more liquid downstream, but it is still not uniform. The vane restricts the liquid flow into the first two channels, but this affect diminishes partway down the header. Once a liquid slug forms in the gap between the vane and the bottom surface of the header, the channels underneath the slug contain high liquid flow rates.

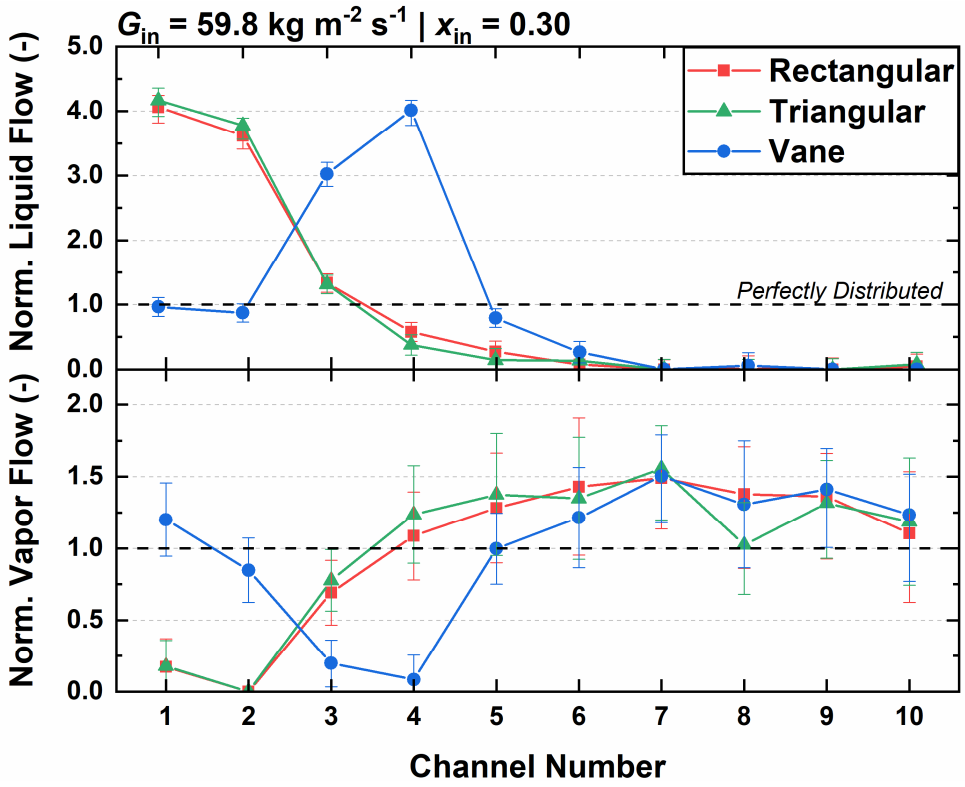

Figure 5.20: Normalized liquid and vapor flow rates entering each channel when the heat exchangers are supplied with refrigerant at a mass fluxes of 59.8 kg m^{-2} s^{-1} and a quality of 0.30

Despite the higher liquid flow rates in channels 3 and 4, the liquid distribution in the vane header is still better than that in the rectangular and triangular headers for the case shown above. This is shown more clearly in Figure 5.21. For an inlet quality of 0.30, the vane header reduces the normalized standard deviation of the total channel flow rates by about 15%. The vaned header has the largest impact on the distribution when the flow regime at the header inlet is gravity-dominated. This allows for a liquid pool to form that extends farther from the inlet port. The triangular header did not significantly impact the distribution for any of the conditions tested with an inlet mass flux of 59.8 kg m^{-2} s^{-1}.

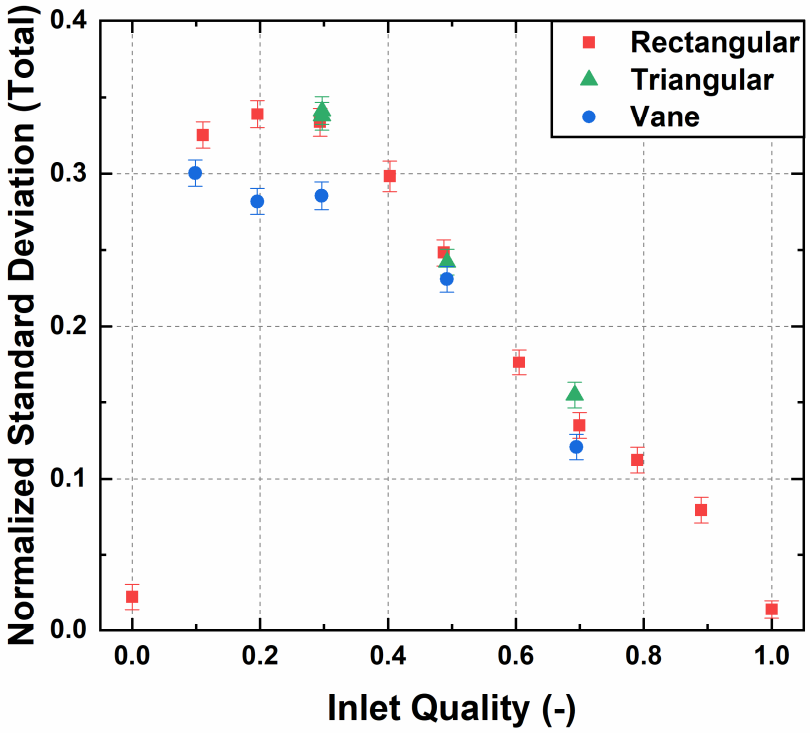

Figure 5.21: Degree of maldistribution (NSTD) of the total flow rate in three header geometries for a range of inlet qualities

The degree of maldistribution is shown as a function of inlet mass flux in Figure 5.22. Again, the vaned header has the largest benefit when the flow regime inside the

header is gravity dominated, which occurs at low inlet qualities and mass fluxes. These results show that there are some cases where the vane header improves the distribution, but the design is not an ideal solution for all situations. Additionally, the maximum observed decrease in the normalized standard deviation was only around 37%, which occurred for a condition that already had relatively good distribution characteristics (G_{in} = 35.9 kg m^{-2} s^{-1}, x_{in} = 0.70). Although this header geometry has potential, further design iterations are needed to achieve a more significant improvement in distribution. Specifically, the distances between the vane and the edges of the header, and the size of the vane slots should be further studied to optimize the design for different inlet cases.

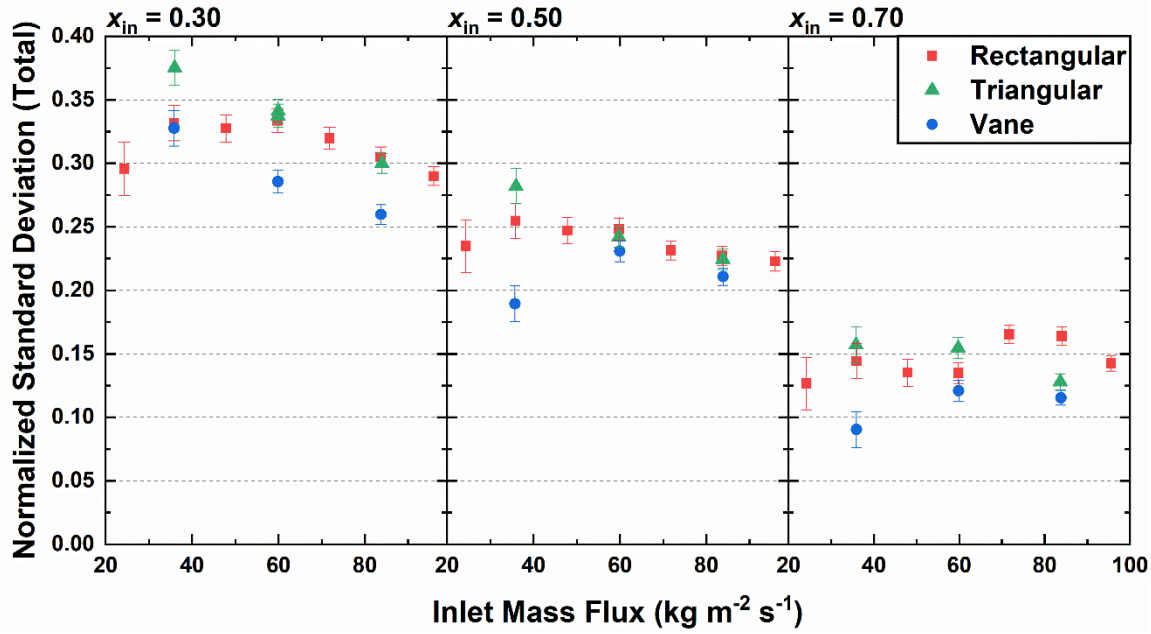

Figure 5.22: Degree of maldistribution (NSTD) of the total flow rate in three header geometries for inlet qualities of 0.30 (left), 0.50 (center), and 0.70 (right) and a range of inlet mass fluxes

Another important consideration in manifold design is pressure drop. Reducing the cross-sectional area or introducing features into the header will inevitably increase the

pressure drop. The measured pressure drops across the header for a range of inlet qualities and mass fluxes are shown in Figure 5.23 and Figure 5.24, respectively. The triangular header increases the velocities as the fluid flows downstream from the inlet port. This results in higher frictional pressure losses, particularly at the far end of the header. This is seen in the results, where larger differences between the rectangular and triangular header pressure drop occur in the flow paths farther downstream from the inlet (channels 6 and 9).

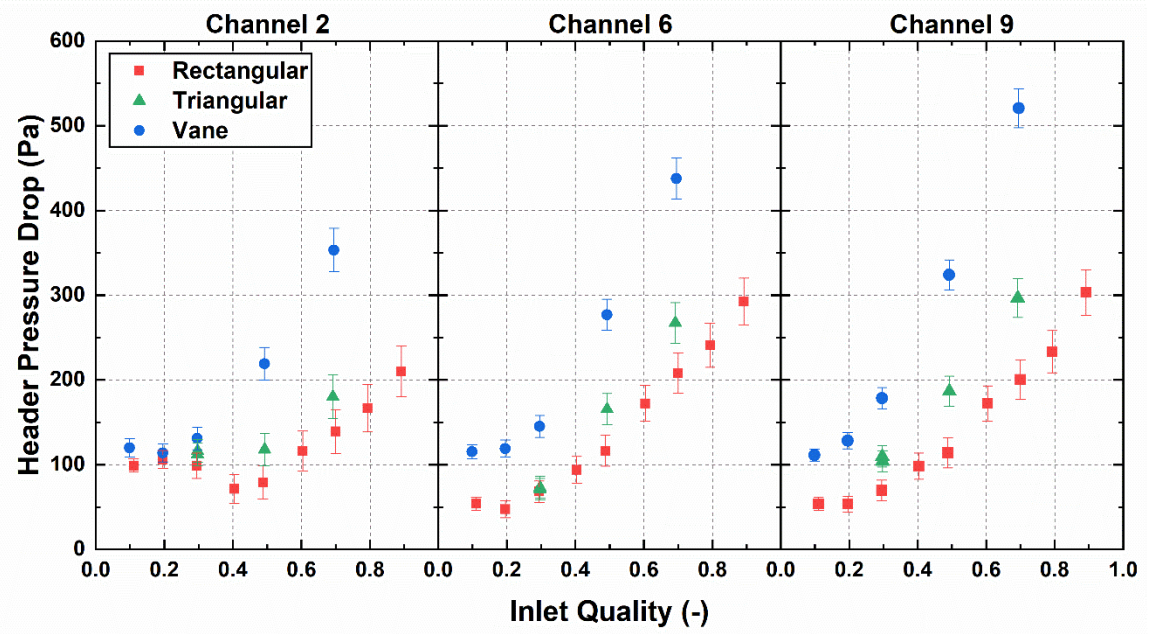

Figure 5.23: Measured pressure drop between the header inlet and the inlets of channel 2 (left), channel 6 (middle) and channel 9 (right) for an inlet mass flux is 59.8 kg m^{-2} s^{-1}

The vane header also increases the header pressure drop compared to the baseline rectangular case. The vane acts as a flow obstruction, which forces the fluid to pass through small slits in the vane or bypass the vane on the left or right sides. This results in a large minor loss, which ultimately increases the pressure drop across the manifold. Fortunately, the header pressure drop does not increase significantly at low inlet qualities and mass

fluxes, where the vane header performs the best. However, these results show that this geometry may not be well suited for cases that have high mass flow rates or qualities inside the header.

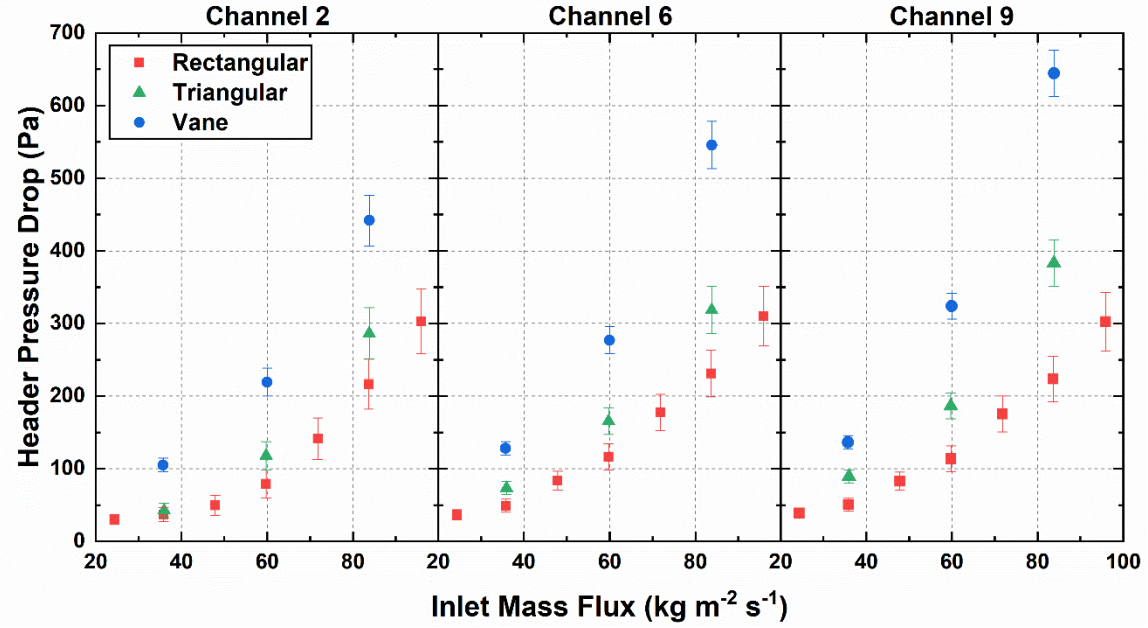

Figure 5.24: Measured pressure drop between the header inlet and the inlets of channel 2 (left), channel 6 (middle) and channel 9 (right) for an inlet quality is 0.50

5.4 Conclusions from Refrigerant Study

Two-phase flow distribution is heavily dependent on the flow regimes inside the heat exchanger header and the pressure drop through each flow path in the component. This study quantified the flow distribution and related the findings to these two parameters.

Distribution data were collected over a wide range of header inlet qualities and mass fluxes. The most significant changes in the overall degree of maldistribution occurred while varying the inlet quality into the test section. As the inlet quality increases, the liquid distribution remains approximately the same, but the vapor distribution improves. This

results in good distribution characteristics at high qualities when most of the fluid entering the heat exchanger is in the vapor phase. The only deviation from this general trend occurs at low qualities. For these conditions, pressure drop restrictions across each flow path requires the liquid to distribute more evenly and improves the overall distribution.

In contrast, the header inlet mass flux does not have a significant impact on the distribution. Increasing the momentum of the liquid phase in the header transports more liquid to downstream channels but results in low liquid flow rates in the channels closest to the inlet port. The global effect is a shift in the flow distribution profile with nearly the same degree of maldistribution (defined using the normalized standard deviation). This result is partially due to the overall length of the header. In all the cases tested, the liquid did not have enough momentum to interact with the far surface of the header. A larger influence may exist for much higher inlet mass fluxes, which would allow the liquid to flow through the entire length of the header and interact with the surfaces farthest from the inlet.

CHAPTER 6. DISTRIBUTION MODELING

Many investigators have studied two-phase flow distribution in different types of heat exchanger headers. These studies have demonstrated that many parameters affect distribution in heat exchangers, including inlet conditions (quality, mass flux, and fluid properties), geometry of the header and channels, and orientation of the heat exchanger. However, modeling approaches to predict the liquid and vapor flow rates entering each channel are lagging behind. Some researchers have developed empirical models based on their experimental work (Watanabe *et al.*, 1995; Kim *et al.*, 2011; Wijayanta *et al.*, 2017), and others have developed more complex segmented models that treat the manifold as a series of T-junctions (Ablanque *et al.*, 2010). The empirical models in the literature usually incorporate relevant non-dimensional parameters such as the liquid and vapor Reynolds numbers (inertial vs. viscous forces), the Froude number (inertial vs. gravitational forces), and the Weber number (surface tension vs. gravitational forces) to capture the flow phenomena. Although these models sometimes work well for the experimental data for which they were developed, they generally have poor predictive capabilities for other heat exchangers. For example, the Wijayanta *et al.* (2017), and Watanabe *et al.* (1995) models were used to predict the liquid flow distribution in the heat exchanger described in Chapter 4. The predictions are compared with the experimental data in Figure 6.1. The accuracy of these models was then evaluated using the absolute average deviation (*AAD*), defined in Equation 6.1. This calculation excludes cases with measured normalized liquid flow rates below 0.05 to prevent the percent error from approaching infinity. The Watanabe *et al.*

(1995) model has the best predictive capabilities, but the absolute average deviation is still high, with an AAD_l = 131.0%.

$$AAD_l = \frac{100\%}{n}\sum_{i=1}^{n}\left|\frac{\gamma_{pred} - \gamma_{meas}}{\gamma_{meas}}\right| \tag{6.1}$$

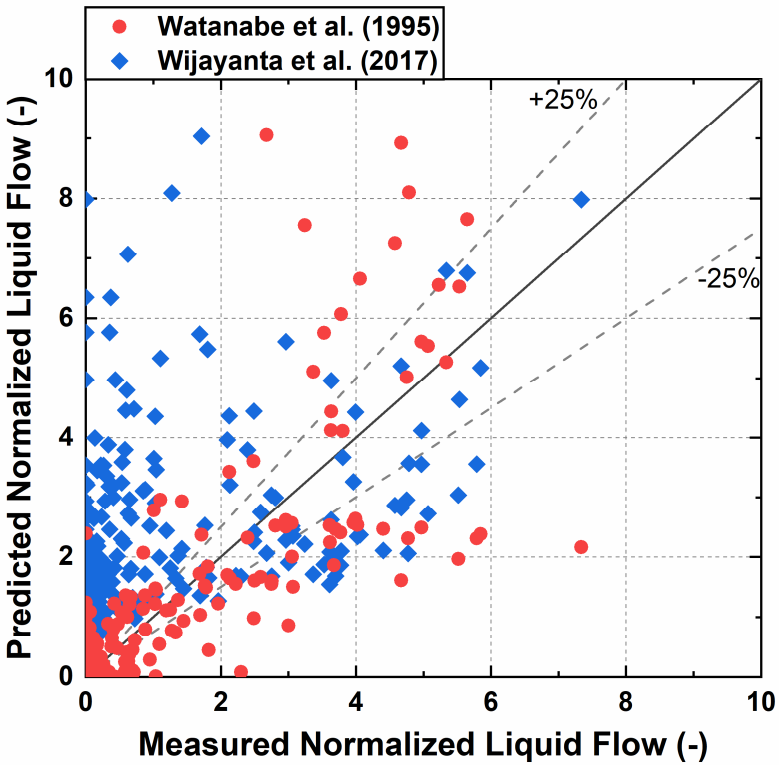

Figure 6.1: Comparison between empirical two-phase flow distribution models and the refrigerant experimental results

Another more complex modeling approach takes the pressure drop across each flow path into account by segmenting the header and channels, as shown in Figure 6.2. The inlet quality into each channel is determined using a T-junction phase-splitting model and the mass flux is determined by equating the pressure drop across each flow path. These types of models capture more of the physics inside the heat exchanger, but are highly

dependent on the correlations chosen to predict the header and channel pressure drops, the channel heat transfer coefficients, and the phase-splitting characteristics in the header.

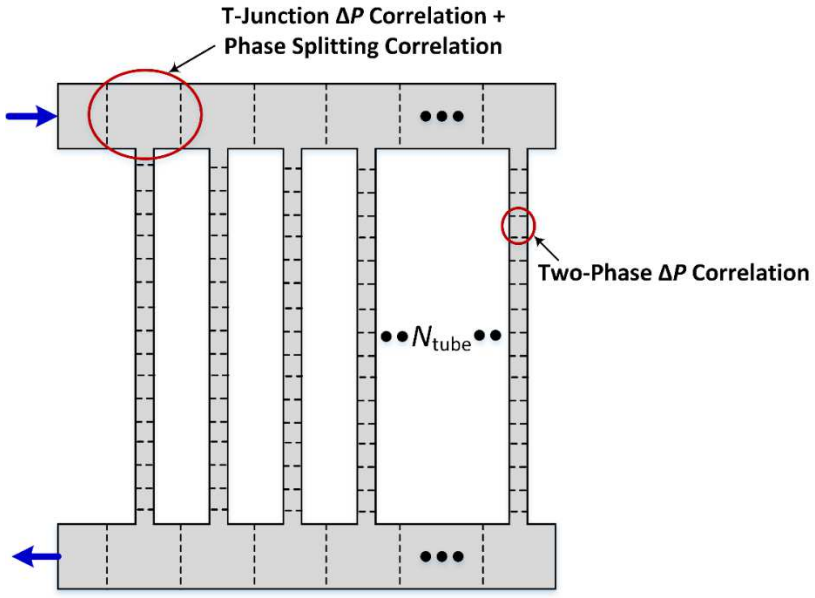

Figure 6.2: Detailed model to predict flow distribution that segments the header and channels to obtain detailed information about the pressure drop across the component (reproduced from Figure 2.5)

One potential deficiency in this approach is the use of T-junction models to describe the flow in the header. These models are usually developed from experiments where the flow enters a T-junction through a long straight channel. This allows the flow to fully develop before it is split into the two perpendicular paths. Although a header can be viewed as a series of T-junctions, the flow conditions entering each one is far from this idealized case. The differences can be seen when the phase splitting model developed by Tae and Cho (2006) for saturated refrigerants flowing through T-junctions is used to predict the inlet quality into each channel of the refrigerant heat exchanger described in Chapter 4.

The results confirm that this type of phase-splitting model cannot accurately describe the complex flow mechanisms in a heat exchanger header.

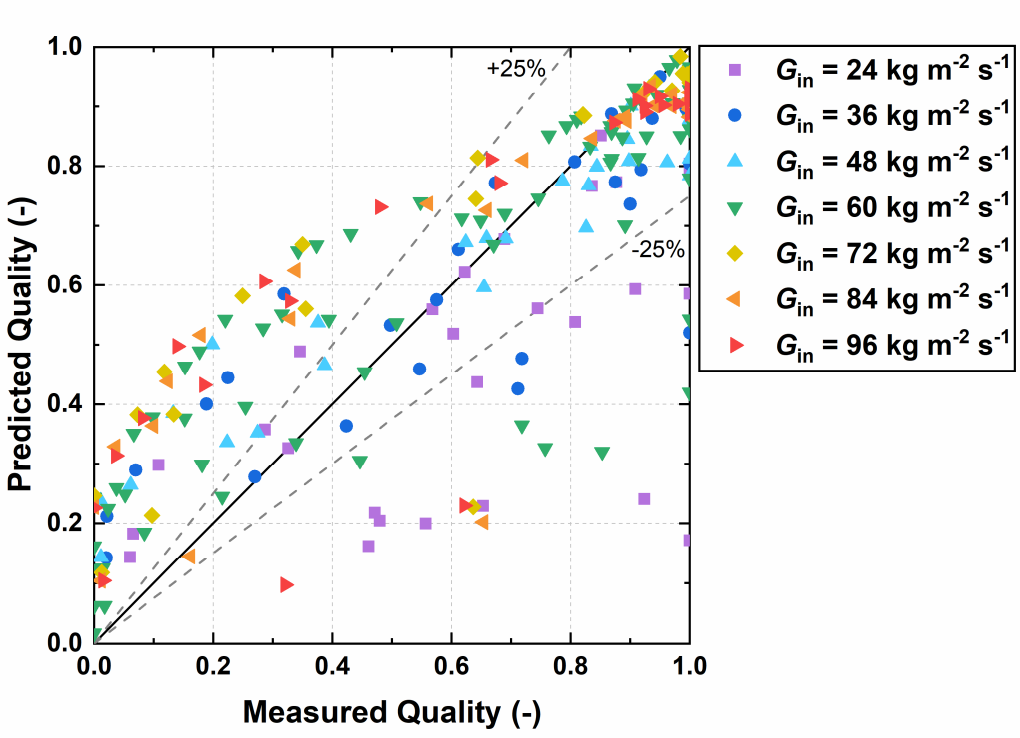

Figure 6.3: Comparison between the inlet qualities predicted using a T-junction phase splitting correlation (Tae and Cho, 2006) and the measured inlet qualities for the refrigerant experiments

This chapter presents a modeling approach that combines aspects of the empirical methods that focus on two-phase flow characteristics in headers and the detailed pressure drop models that account for pressure drop requirements in heat exchangers. The proposed pressure drop model ensures that the predicted flow distribution is physically possible but removes the use of T-junction correlations, which are not very applicable to the complex flow patterns in headers. The details of the model are discussed below, and the results are compared with the experimental data presented in the previous chapter.

6.1 Pressure Drop Model

A detailed model of the test section was developed to predict the pressure change between the inlet and outlet of each flow path. This section describes the structure of the pressure drop model, while the following sections use the model to predict the two-phase flow distribution in horizontal plate-type heat exchanger headers.

6.1.1 Header Pressure Drop

The pressure change across a flow path in a multi-channel heat exchanger includes the pressure drop across the inlet header, the pressure change across the channels (including the effects of friction, gravity and deceleration), and the pressure drop across the outlet header, as shown in Figure 6.4. The pressure drop across the outlet header does not significantly contribute to the total pressure change because the flow is single-phase. It is therefore neglected in this analysis. The pressure drop in the inlet header has a larger effect on the total pressure change and is included in the calculations.

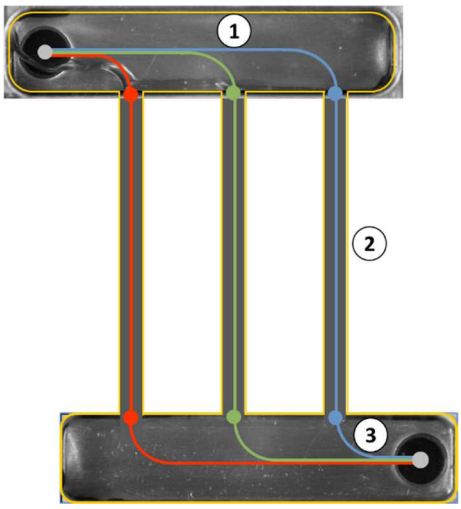

Figure 6.4: Contributions to the total path pressure drop (1 – inlet manifold, 2 – channel, and 3 – outlet manifold)

A common way to estimate the pressure drop across a heat exchanger header is to apply T-junction pressure drop models. These models account for both the reversible pressure change associated with flow deceleration and the irreversible pressure drop associated with minor and friction losses. However, as discussed above, T-junction models may not accurately represent the flow characteristics in heat exchanger headers. The Tae and Cho (2006) T-junction pressure drop model was applied to the conditions present in the refrigerant header and the results were compared with the measured data (Figure 6.5). The T-junction model tends to underpredict the data for low inlet flow rates and qualities and over predict the data at higher inlet flow rates and qualities. The absolute average deviation between the predicted and measured pressure drop is 43.5%, showing that it is not an ideal modeling approach for this header configuration.

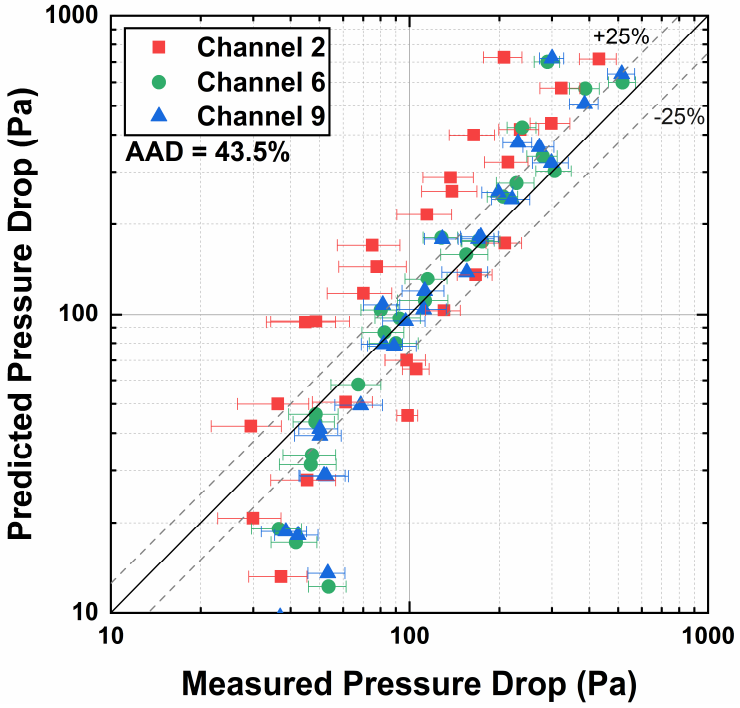

Figure 6.5: Comparison between the header pressure drop predicted using a T-junction correlation (Tae and Cho, 2006) and the measured pressure drop for the refrigerant experiments

Although T-junction models are not very accurate, the general approach of treating a header as a series of minor losses can be a useful way to describe the pressure drop. For the headers considered in this work, the pressure losses result from the flow entering the heat exchanger and turning 90 degrees, flowing through the header, and then turning 90 degrees and entering the heat exchanger channels. Considering these different contributions, a new correlation for predicting pressure drop in rectangular plate-type heat exchanger headers was developed. The correlation includes pressure drop terms associated with flow entering and exiting the header based on the standard approach for calculating minor losses in two-phase flows (Ghiaasiaan, 2017), which takes the form of a loss coefficient multiplied by the dynamic pressure and a two-phase multiplier. The pressure drop through the central part of the header is estimated using a minor loss term calculated with the average flow rate in the portion of the header under consideration. This approximation does not capture the intricacies of the pressure losses and recoveries in the manifold but was found to work well for this simplified correlation approach.

The proposed correlation is shown in Equation 6.2 where ω^* is the ratio of the average flow rate in the area between the header inlet and the channel inlet to the total inlet mass flow rate (Equation 6.3), $u_{lo,in}$ is the velocity of the entire incoming mixture entering the header if it were flowing alone as a liquid in the feeder tube ($= G_{inlet}/\rho_l$), $u_{v,ch}$ is the velocity of the vapor in the channels ($= G_{ch}x_{ch,in}/\rho_v$), and the ϕ terms are two-phase multipliers. The inlet two-phase multiplier is calculated using the Friedel (1979) correlation, which is a popular pressure drop model for macro-channels, while the channel two-phase multiplier is calculated using the Kim and Mudawar (2012) correlation, which is applicable to mini- and microchannels.

$$\Delta P_{header} = \left(K_{in,1} + K_{in,2}\omega^*\right)\frac{1}{2}\rho_l u_{lo,in}^2 \phi_{lo,in} + K_{ch}\frac{1}{2}\rho_v u_{v,ch}^2 \phi_v \tag{6.2}$$

$$\omega^*[i] = \frac{\sum_{j=1}^{i} \dot{m}_{header}[j]}{N_{ch}[i] * \dot{m}_{ref,in}} \tag{6.3}$$

The loss coefficients were determined using a regression analysis on the data. The resulting inlet loss coefficients in Equation 6.3 are $K_{in,1}$ = 1.651 and $K_{in,2}$ = 6.761 and the channel loss coefficient is K_{ch} = 1.123.

The proposed correlation was used to predict the header pressure drop for all inlet conditions investigated in Chapter 5. The predicted values are compared with the measured data in Figure 6.6(a). The absolute average deviation (*AAD*) is 19.0%, but the correlation shows better agreement for cases with inlet superficial vapor velocities greater than 0.4 m s^{-1} (*AAD* = 14.2%). The header pressure drop model is needed to calculate the total pressure change across each flow path, but the header pressure drop only has a large influence on the flow distribution if it significantly contributes to the total path pressure change. To gain some insight into the effect of the prediction errors at low inlet superficial vapor velocities, the predicted header pressure drop ($\Delta P_{header,pred}$) was divided by the total measured test section pressure drop ($\Delta P_{TS,meas}$), as shown in Equation 6.4.

$$F_{\Delta P,header} = \left|\frac{\Delta P_{header,pred}}{\Delta P_{TS,meas}}\right| * 100\% \tag{6.4}$$

In cases where the predicted value falls below 75% of the measured value (low inlet superficial vapor velocities), the header pressure drop accounts for less than 1% of the total

path pressure change. Even large errors in the header pressure drop for these conditions will not have a significant impact on the flow distribution. Therefore, the simple model presented in Equation 6.2 is sufficient for modeling the heat exchanger considered in this work.

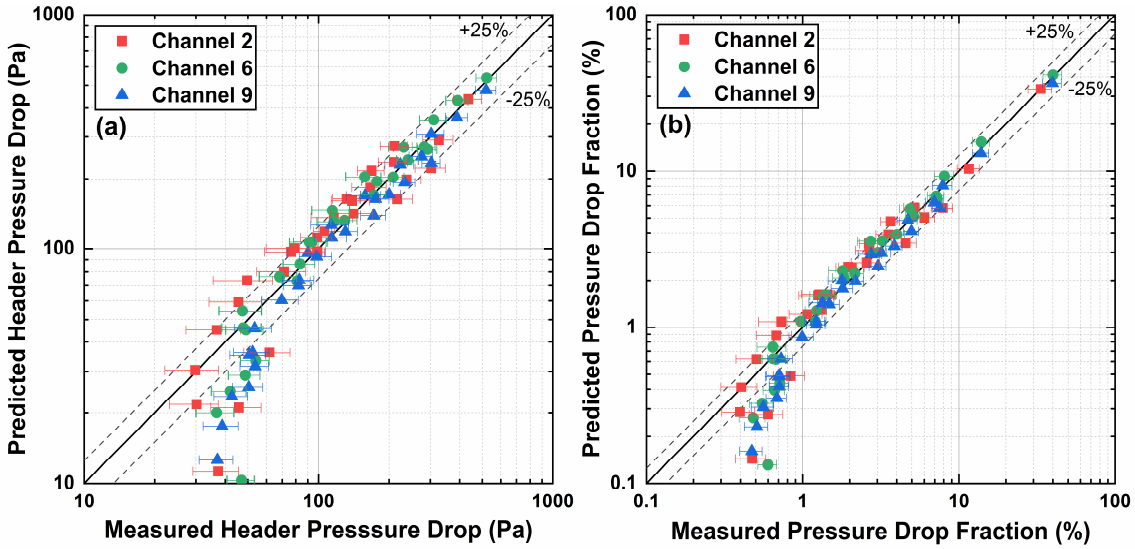

Figure 6.6: A comparison between (a) the predicted and measured header pressure drop and (b) the predicted and measured header pressure drop divided by the total test section pressure drop

6.1.2 Channel Pressure Drop

The pressure change across each channel must also be determined to calculate the total pressure difference between the inlet and the outlet of a heat exchanger. As discussed in Chapter 5, the pressure change across the channels in the refrigerant test section is dependent on the frictional pressure losses, gravitational pressure gains, deceleration pressure gains, and the condensation length. These parameters were calculated using a segmented, coupled heat transfer and fluid dynamic model of the test section developed on

the *Engineering Equation Solver* (Klein, 2018) platform. The segmentation accounts for the changing fluid properties in the refrigerant and coolant channels.

The goal of the channel pressure drop model is to accurately predict the refrigerant-side pressure change between the inlet and outlet manifolds, including contributions for the refrigerant channel, measurement components and auxiliary tubing. A schematic of a single heat exchanger channel attached to a TOF flow sensor and exit tubing is shown in Figure 6.7. The refrigerant exits the inlet manifold and enters a short section of tubing milled out of the manifold assembly block ($D_{ch,assb} = 1.0\ mm, L_{ch,assb} = 27.8\ mm$). This section of the channel was included in the design to allow space for pressure taps, connection fittings, and for gaskets to seal the inlet header. The fluid then enters the tube-in-tube heat exchanger (location 1 in Figure 6.7) where the refrigerant is condensed by cold water that flows in a counterflow orientation through an outer annulus. The refrigerant channel is 0.5 m long, but has a heat transfer length of only 0.41 m so that fittings can be used to connect the heat exchanger with the inlet manifold and the flow rate sensor. The tubing segments upstream and downstream of the heat transfer section are adiabatic ($L_{adi} = 0.045\ m$). After the fluid is fully condensed and subcooled in the heat transfer portion of the test section, the refrigerant enters a time-of-flight flow rate sensor (location 2 in Figure 6.7). Although thermocouples and a small heater are inserted into the flow in the sensor, the pressure drop is estimated for single-phase flow through a pipe. Finally, the refrigerant exits the heat exchanger channel through a short section of tubing (location 2 in Figure 6.7) that is attached to the exit manifold.

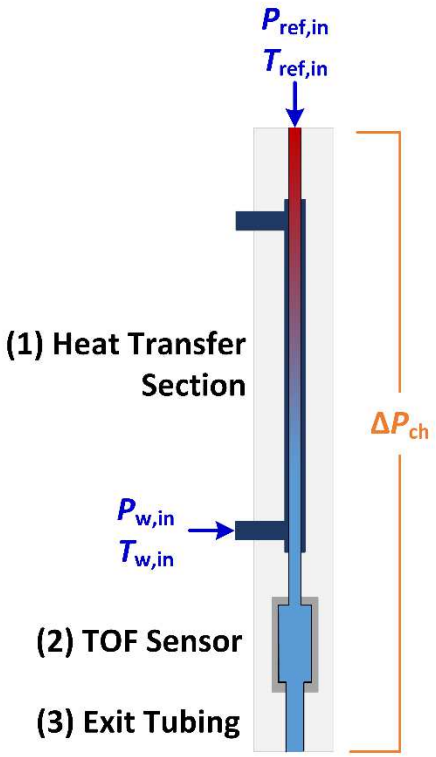

Important Geometric Parameters	
$D_{ref,ch}$	1.00 mm
$D_{w,in}$	2.00 mm
$D_{w,out}$	4.00 mm
D_{TOF}	3.81 mm
D_{exit}	1.75 mm
$L_{ref,ch}$	0.50 m
$L_{w,ch}$	0.41 m
L_{TOF}	0.09 m
L_{exit}	0.10 m

Figure 6.7: Schematic of a single heat exchanger channel with values for some of the important geometric parameters

Fluid properties influence the pressure change across a pipe, particularly for two-phase flow (see Figure 5.7). To capture these affects, all ten heat exchanger channels are segmented, and the fluid states are solved at each node. To decrease the computational time requirements, each channel is divided so that areas with large changes in fluid properties contained short segments, while other areas contain longer segments. The first segment includes the channel section in the inlet header assembly block and the adiabatic section. The refrigerant experiences a small change in fluid properties in this segment mainly due to thermal losses to the environment. The quality change between the inlet and the outlet of the first segment is always less than 0.01; therefore, the local pressure gradients should not change significantly throughout its length. As a result, the first

section of the heat exchanger channel is treated as a single segment and is not further subdivided. The section of the refrigerant channel that is actively cooled by the water stream is divided into 30 segments to capture the large changes in fluid properties. Fluid properties have a larger effect on the pressure drop for two-phase flows than single-phase flows; therefore, the condensing portion of the channel is divided into 25 segments, while the remaining length is divided into five segments. Finally, the remaining parts of the test section channels are treated as single segments because the flow is single phase and the fluid properties do not change significantly. A summary of the different nodes is provided in Table 6.1.

Table 6.1: Description of the different nodes used to model the heat exchanger channels

Segment Number	Description	Length
0	Portion of channel in inlet header assembly block and inlet adiabatic section	0.072 m
1-25	Condensing length (L_{cond})	Varies
25-30	$L_{HT} - L_{cond}$	Varies
31	Outlet adiabatic section	0.045 m
32	Time of flight sensor	0.093 m
33	Exit tubing	0.103 m

The fluid properties at the inlet of each node are calculated using the pressure drop and an energy balance across the previous node, as shown in Equations 6.5 and 6.6, respectively. In these equations, ΔP_{seg} is defined as the pressure decrease between the inlet and the outlet of the segment. If the pressure drop is negative, the pressure gradient is

positive, and the downstream pressure will be higher than the upstream pressure (due to gravitational and deceleration effects).

$$P_{in}[i] = P_{in}[i-1] - \Delta P_{seg}[i-1] \tag{6.5}$$

$$h_{in}[i] = h_{in}[i-1] - \frac{\dot{Q}_{seg}[i-1]}{\dot{m}_{ch}} \tag{6.6}$$

To close the model, the pressure drop and heat transfer rate across each segment must be determined. The pressure drop in any two-phase segment is calculated using Equation 6.7.

$$-dP = \underbrace{\int_{in}^{out} \left(\frac{dP}{dz}\right)_{fric} dz}_{frictional} + \underbrace{\int_{in}^{out} [(1-\alpha)\rho_l + \alpha\rho_v] g \, dz}_{gravitational} + \underbrace{\int_{in}^{out} \frac{d}{dz}\left[\frac{G^2x^2}{\rho_v\alpha} + \frac{G^2(1-x)^2}{\rho_l(1-\alpha)}\right] dz}_{deceleration} \tag{6.7}$$

The integrals in the two-phase pressure drop equation are estimated using the trapezoidal rule, defined in Equation 6.8, where γ is an arbitrary variable.

$$\int_{\gamma_1}^{\gamma_2} f(\gamma) da = (\gamma_2 - \gamma_1) \times \frac{f(\gamma_2) + f(\gamma_1)}{2} \tag{6.8}$$

Applying the trapezoidal rule, the frictional, gravitational and deceleration pressure drop contributions are shown in Equations 6.9 - 6.11. In these equations, *in* represents the value of the parameter at the segment inlet, while *out* represents the value at the segment outlet.

The two-phase multipliers in the frictional pressure drop equation (Equation 6.9) are calculated using a correlation from the literature. The next section evaluates several different correlations to determine the most appropriate one for this model. The void fraction in the gravitational pressure drop equation (Equation 6.10) is calculated using the Baroczy (1965b) correlation.

$$dP_{fric} = L_{seg} \times \left[\frac{(G_{ch} x_{out})^2}{D_{ch} \rho_v} \phi_{v,out}^2 f_{v,out} + \frac{(G_{ch} x_{in})^2}{D_{ch} \rho_v} \phi_{v,in}^2 f_{v,in} \right] \tag{6.9}$$

$$dP_{grav} = \frac{L_{seg} g}{2} \{ [(1 - \alpha_{out}) \rho_l + \alpha_{out} \rho_v] + [(1 - \alpha_{in}) \rho_l + \alpha_{in} \rho_v] \} \tag{6.10}$$

$$dP_{decel} = \left[\frac{G_{ch}^2 x_{out}^2}{\rho_v \alpha_{out}} + \frac{G_{ch}^2 (1 - x_{out})^2}{\rho_l (1 - \alpha_{out})} \right] - \left[\frac{G_{ch}^2 x_{in}^2}{\rho_v \alpha_{in}} + \frac{G_{ch}^2 (1 - x_{in})^2}{\rho_l (1 - \alpha_{in})} \right] \tag{6.11}$$

When the fluid enters a segment below the saturated liquid enthalpy (a location downstream from where the fluid fully condenses), the pressure drop calculation simplifies to Equation 6.12. The fluid density is approximately constant across each segment in the subcooled liquid region; therefore, the average density is used in the calculation and any pressure change resulting from flow deceleration is neglected.

$$dP = \underbrace{\frac{G^2 L_{seg}}{2 \rho D_{ch}} \times \frac{f_{out} + f_{in}}{2}}_{frictional} - \underbrace{\rho g L_{seg}}_{gravitational} \tag{6.12}$$

The friction factor (f) in subcooled liquid segment is evaluated using the Churchill (1977b) correlation.

As shown above, the total pressure drop across a segment is a function of several fluid properties including quality, void fraction, and the phase densities. Two fluid properties are required to establish the state in each node; therefore, a heat transfer analysis must be performed to calculate the enthalpy variation through the channel. The heat transfer rate leaving the refrigerant in each node is calculated using the thermal resistance approach. A schematic of a single segment with the relevant thermal resistances is shown in Figure 6.8. Each thermal resistance is determined using the standard equations presented in Chapter 4 (Nellis and Klein, 2009).

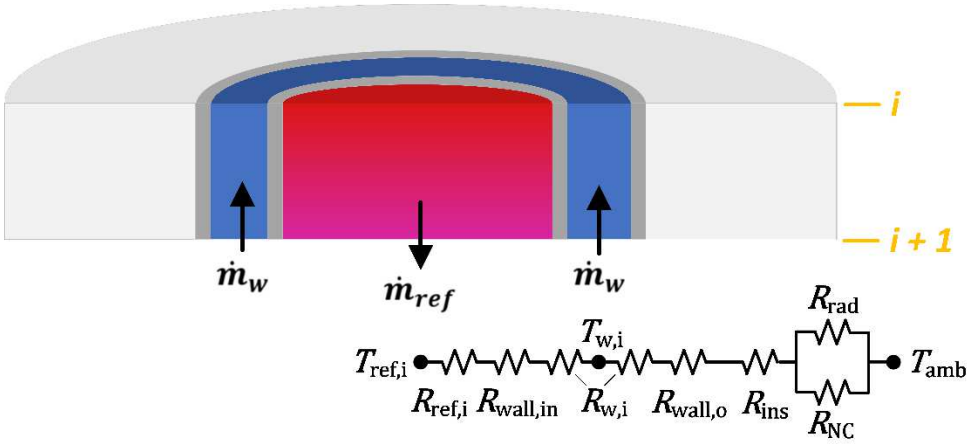

Figure 6.8: Schematic of a segment in the actively cooled portion of the refrigerant channel with all relevant thermal resistances

The convective thermal resistances ($R_{ref,i}$, $R_{w,i}$, and R_{NC}) all depend the magnitude of the convective heat transfer coefficient for each fluid stream. The refrigerant heat transfer coefficient in the single-phase segments was calculated using the Churchill (1977a) correlation, while the condensing heat transfer coefficient was evaluated using a correlation from the literature. Several condensation heat transfer correlations are evaluated in the next section to determine the most appropriate one for these conditions. The water-side

heat transfer coefficient was calculated using the Rohsenow *et al.* (1998) correlation for flow through an annulus, and the spatially averaged natural convection heat transfer coefficient was evaluated with the Raithby and Hollands (1998) correlation.

The UA-LMTD approach is used to calculate the heat transfer rate between the refrigerant and the water, and the thermal losses (or gains) to the ambient. For the segments that are actively cooled, Equations 6.13 through 6.15 are used to calculate the heat leaving the refrigerant in segment *i* ($\dot{Q}_{ref-w}[i]$). In these equations, the outlet fluid properties from the segment (for example $T_{ref}[i+1]$ and $T_w[i]$) are calculated iteratively using an energy balance across each fluid stream.

$$UA_{ref-w}[i] = \frac{1}{R_{ref}[i] + R_{wall,in} + R_{w,in}[i]} \tag{6.13}$$

$$LMTD_{ref-w}[i] = \frac{\left(T_{ref}[i] - T_w[i]\right) - \left(T_{ref}[i+1] - T_w[i+1]\right)}{\ln\left(\frac{T_{ref}[i] - T_w[i]}{T_{ref}[i+1] - T_w[i+1]}\right)} \tag{6.14}$$

$$\dot{Q}_{ref-w}[i] = UA_{ref-w}[i] \times LMTD_{ref-w}[i] \tag{6.15}$$

The heat gain from the ambient is similarly calculated using Equations 6.16 through 6.18. The water gains heat from the ambient in all segments because the annulus outlet temperature never exceeds the ambient temperature ($\bar{T}_{amb} \sim 22$°C). Again, the outlet fluid states are solved iteratively using an energy balance for both the refrigerant and water streams.

$$UA_{amb-w}[i] = \frac{1}{R_{w,out}[i] + R_{wall,out} + R_{ins} + \left(\frac{1}{R_{rad}} + \frac{1}{R_{NC}}\right)^{-1}} \tag{6.16}$$

$$LMTD_{amb-w}[i] = \frac{(T_{amb} - T_w[i]) - (T_{amb} - T_w[i+1])}{\ln\left(\frac{T_{amb} - T_w[i]}{T_{amb} - T_w[i+1]}\right)} \tag{6.17}$$

$$\dot{Q}_{amb-w}[i] = UA_{amb-w}[i] \times LMTD_{amb-w}[i] \tag{6.18}$$

The thermal losses and gains in the segments that are not actively cooled are evaluated using the same approach with a slightly different resistance network. The total thermal resistance between the refrigerant and ambient for these nodes include contributions from the refrigerant convective resistance, the conduction resistance through the wall and insulation, and radiation and natural convection resistances at the surface. Evaluating the heat transfer rates into and out of these segments closes the systems of equations and allows for the iterative solution of the segmental pressure drops. The pressure change between the inlet and outlet of the channel can then be determined using the calculated pressure difference across each segment, as shown in equation 6.19.

$$P_{ch,in} - P_{ch,out} = \sum_{i=0}^{N_{seg}} dP[i] \tag{6.19}$$

6.1.3 Assessment of Correlations

The results from the model described in Section 6.1.2 are highly dependent on the two-phase frictional pressure drop and heat transfer correlations used. Prediction of these parameters is difficult in this case because of the large range of local qualities (x_{seg} = 0 to

1) and mass fluxes (G_{ch} = 15.8 to 543 kg m^{-2} s^{-1}) present in the test section channels. Correlations must be chosen based on their applicability for the conditions of interest.

The measured channel pressure change ($\Delta P_{ch}[j] = \Delta P_{TS} - \Delta P_{header}[j]$) was compared to the model results using several different correlations from the literature. The measured and predicted values were specifically compared for channels 2, 6 and 9, where the header pressure drop was directly measured. Initially, the refrigerant heat transfer coefficients in the two-phase segments were calculated using the Kim and Mudawar (2013) correlation, which was developed for condensing flow in mini- and microchannels from a large experimental database. Six different two-phase frictional pressure drop correlations (Friedel, 1979; Mishima and Hibiki, 1996; Garimella *et al.*, 2005; Li and Wu, 2010; Kim and Mudawar, 2012; Andresen *et al.*, 2015) were then evaluated to determine those that could most accurately predict the overall channel pressure change. A comparison between the measured and predicted pressure gain across the heat exchanger channels is shown in Figure 6.9. As discussed in Chapter 5, the gravitational pressure rise across the test section causes the pressure to increase from the inlet to the outlet of the channels, which is why the results are presented as pressure gains instead of losses. The Garimella *et al.* (2005) correlation performed the best with an absolute average deviation of 10.9%.

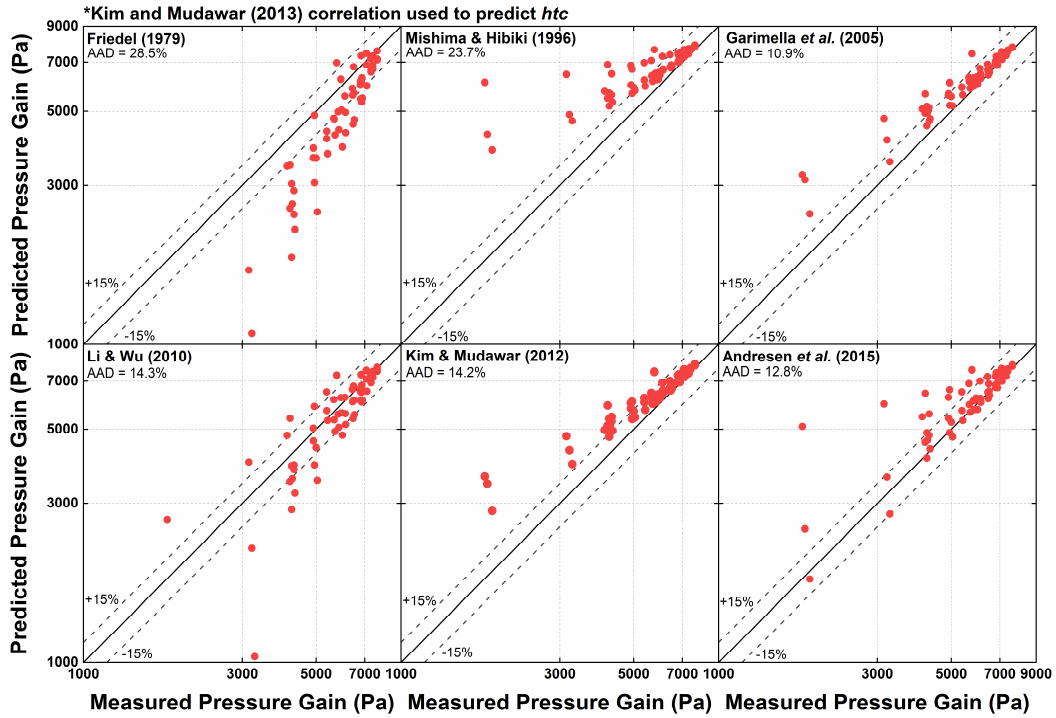

Figure 6.9: Comparison of overall channel pressure gain data with proposed model using different frictional pressure drop correlations from the literature

The Garimella *et al.* (2005) correlation was then used to calculate the frictional pressure gradient in each two-phase segment, and six different heat transfer coefficient correlations (Shah, 1979; Moser *et al.*, 1998; Shah, 2009; Kim and Mudawar, 2013; Murphy, 2014; Keinath and Garimella, 2018) were evaluated for use in the proposed model. Although the Shah (2009) correlation showed the best overall performance with an *AAD* of 10.8%, the results for different channels at the same condition were relatively scattered at low inlet flow rates. For this model, it is important that the predicted pressure change through each flow path is nearly equal for a given inlet condition. Therefore, the Kim and Mudawar (2013) correlation was selected for this model because it is nearly as accurate as the Shah (2009) correlation (*AAD* = 10.9%) and has less scatter at low inlet flow rates.

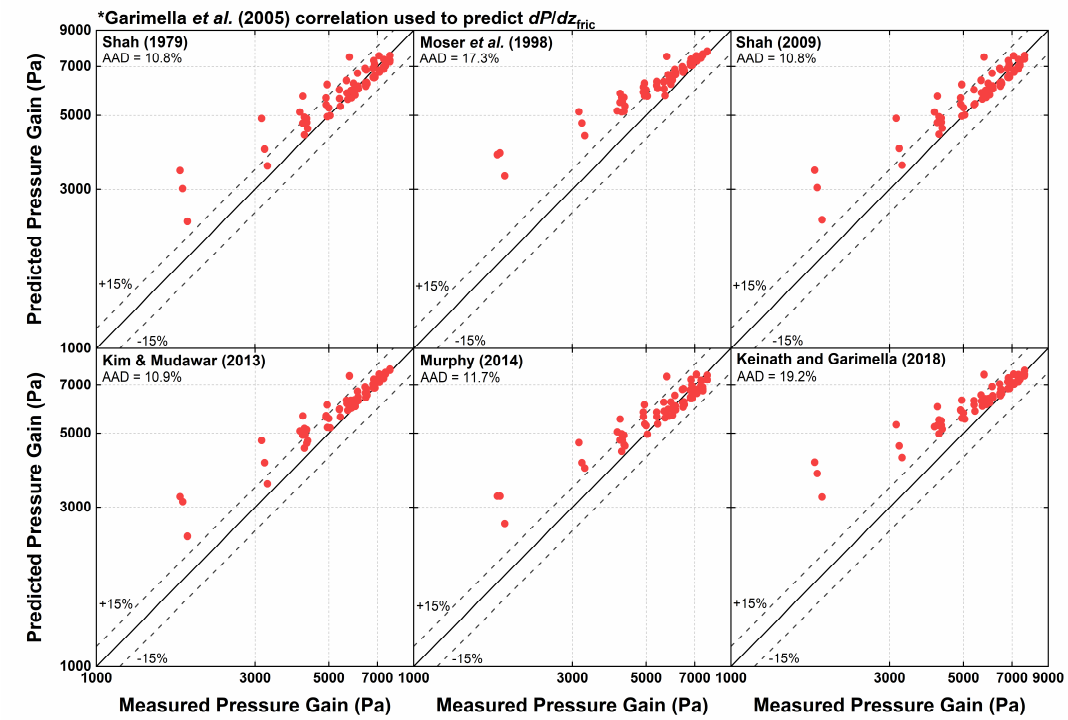

Figure 6.10: Comparison of overall channel pressure gain data with proposed model using different heat transfer coefficient correlations from the literature

6.1.4 Comparison with Representative Experimental Results

The proposed model was used to predict the temperature and pressure profiles across the heat exchanger both to validate the model and to gain additional insight into the parameters affecting pressure drop. The predicted local temperature and pressure profiles are presented for a sample inlet condition (G_{in} = 59.8 kg m^{-2} s^{-1} and x_{in} = 0.49 - central condition in test matrix). The model inputs are the measured channel flow rates and the measured inlet states to the refrigerant and coolant channels.

The refrigerant and water temperatures are shown along the length of the heat exchanger channel in Figure 6.11. The temperature of the refrigerant remains approximately constant in the condensing region near the channel inlet, but then decreases

rapidly once the flow becomes subcooled. The refrigerant temperature gradient is greater than the water gradient because the refrigerant has a significantly lower thermal capacitance rate ($\dot{C}_{ref} \approx 0.085\ W\ K^{-1}$ and $\dot{C}_{w} \approx 2.120\ W\ K^{-1}$). Finally, after the refrigerant exits the actively cooled region of the test section, the temperature starts to rise due to thermal gains from the environment. The figure also shows the measured refrigerant and water temperatures at the outlets of the heat exchanger. The model accurately predicts these outlet temperatures, suggesting that the chosen correlations are appropriate for this case.

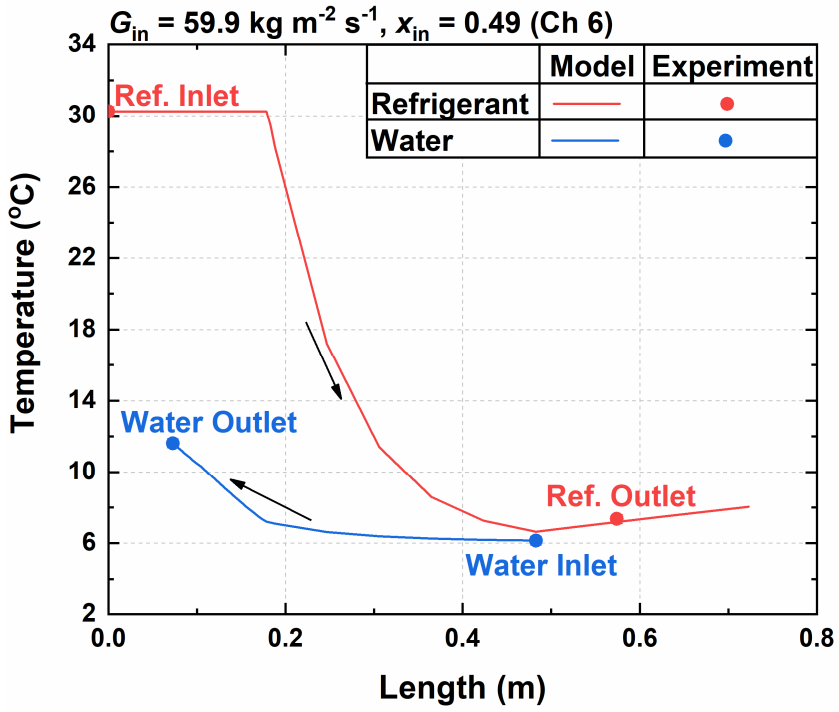

Figure 6.11: Predicted local refrigerant and water temperatures throughout the heat exchanger channel (channel 6) for the sample condition

The difference between the inlet and local pressure along the length of the heat exchanger channel is shown in Figure 6.12. The total pressure difference is slightly positive at the channel entrance (L = 0) due to the pressure losses in the header (predicted

using Equation 6.2). In the two-phase region of the channel (L = 0 to 0.183 m), the frictional pressure gradient is relatively high and the gravitational and deceleration contributions to the total pressure change are low. This results in a pressure drop in this portion of the channel ($P_{ref,in} > P_{ref,local}$). After the fluid fully condenses, the channel frictional pressure gradient decreases, and the gravitational pressure gain increases due to the substantial increase in fluid density. This causes the pressure to increase in the single-phase region of the channel (L = 0.183 to 0.723 m). The gravitational effects are dominant in this heat exchanger design; therefore, the pressure rises between the inlet and the outlet for all conditions tested ($P_{ref,in} < P_{ref,out}$).

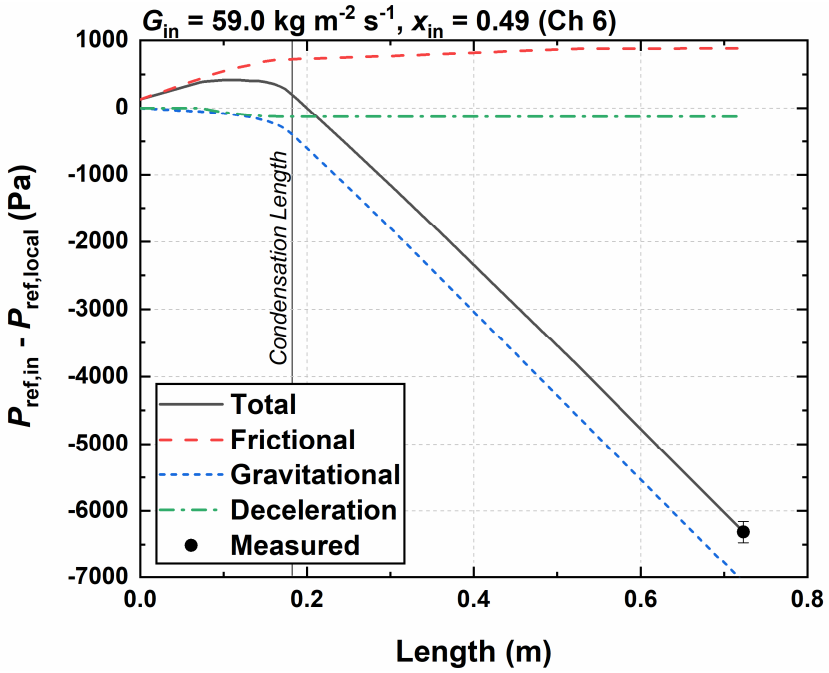

Figure 6.12: Predicted refrigerant pressure profile along the length of the heat exchanger channel (channel 6) for the sample condition

Unlike in single-phase channel flows, there are many combinations of channel inlet conditions that can result in the same overall pressure drop. This can be seen by comparing

the pressure profiles in the channels with the lowest and highest inlet qualities for the sample condition (G_{in} = 59.8 kg m^{-2} s^{-1} and x_{in} = 0.49). Channel 1 has a low inlet quality (x_{ch1} = 0.05), but since the liquid is much denser than the vapor, the channel mass flux is relatively high (G_{ch1} = 357 kg m^{-2} s^{-1}). The low inlet quality results in a short two-phase region because only a small amount of heat needs to be removed to fully condense the flow. This would normally lead to a low frictional pressure drop, but in this case the frictional pressure gradient is high in both the single- and two-phase regions because of the high mass flux in the channel. The flow enters the ninth channel in the test section at a higher quality and a lower channel mass flux (x_{ch9} = 1.00, G_{ch9} = 69.8 kg m^{-2} s^{-1}). The two-phase length in this case is larger, but the mass flux is significantly lower, resulting in a reduction in the total frictional pressure drop. This is offset by a nearly equal decrease in the gravitational pressure gain across the channel, ultimately resulting in the same total pressure change across these different flow paths. This analysis shows how different liquid and vapor flow rates can result in the same total pressure change, which allows for many possible distribution profiles for a given set of inlet conditions and geometric characteristics.

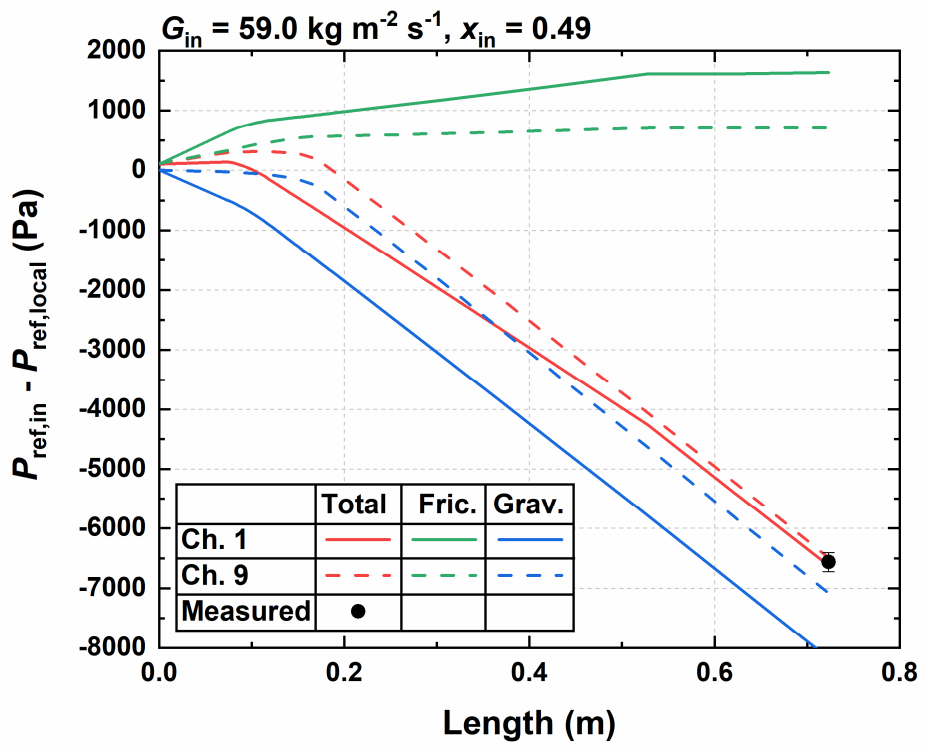

Figure 6.13: Predicted refrigerant total, frictional and gravitational pressure profiles along the flow paths with the lowest (channel 1) and highest (channel 9) inlet qualities for the sample case

6.2 Limits to Degree of Liquid Maldistribution

The pressure drop through each flow path in a multi-channel heat exchanger must be equal. This requirement limits the possible flow rates into each channel, which can have a large effect on the distribution. For example, the experimental data show several cases were the liquid flow rates into channels far from the inlet port are nearly zero (Figure 5.13). Two-phase pressure drop in the heat exchanger channels is dependent on the inlet quality and total mass flow rate. As shown above, it is possible to achieve the same path pressure drop at different channel inlet qualities by adjusting the mass flux. However, the only way to adhere to the path pressure drop requirements when the fluid enters several channels at a quality of one (no liquid flow at the inlet) is to have equal mass fluxes in each (assuming

negligible differences in the header pressure drop between these channels). This result is consistent with the experimental data shown in Chapter 5.

The path pressure drop requirements can also have a significant effect on the liquid distribution in a heat exchanger, especially when the flow enters at a low inlet quality. For example, if the fluid enters the header at an inlet quality of 0.10, ninety percent of the inlet mass is in the liquid phase. If all the liquid enters a single channel (most maldistributed case), the channel mass flux would be extremely high. The frictional pressure drop in this channel would be excessive compared to channels with a vapor inlet condition because the mass flow rate would be 81 times higher (vapor would be required to distribute evenly in remaining 9 channels, neglecting any pressure drop in the header). In this case, the path pressure drop requirements would restrict the liquid flow rate in a single channel to match the pressure change across the channels with an inlet quality of one.

The vapor is highly mobile in the header and will distribute into the heat exchanger channels in a way that achieves equal path pressure drops. The liquid can generally only distribute into channels near the inlet port because it does not contain sufficient momentum to move farther downstream. However, in some cases, the liquid is forced downstream by the requirement that each flow path must have an equal pressure drop. This allows for the distribution to improve as the inlet quality approaches zero. To understand the manner in which the pressure drop requirements affect the liquid flow rates entering each channel, the model described in the previous section was used to determine the worst possible liquid distribution for each inlet case. The overall degree of liquid maldistribution is described using the normalized standard deviation, which is defined as the standard deviation of the

inlet liquid flow rates into each channel divided by the highest possible standard deviation (Equation 6.20).

$$NSTD_l = \sqrt{\frac{\sum_{i=1}^{N_{ch}} \left(\dot{m}_{l,i}^* - 1\right)^2}{(N_{ch} - 1)N_{ch}}} \tag{6.20}$$

The highest standard deviation occurs when all the liquid exiting the header is concentrated in a single channel. This situation is only achievable when the liquid flow is not pressure drop limited. In many cases, the highest possible degree of maldistribution requires the liquid to flow down more than one channel because of these limits ($NSTD_l < 1$).

The worst physically possible liquid distribution is determined by assuming the liquid exits the header down channels closest to the inlet and the vapor distributes through the remainder of the heat exchanger. First, the pressure drop across each flow path is calculated assuming that only liquid enters the first channel and only vapor enters the remaining nine channels. If the pressure drop across the liquid channel is lower than that in the vapor channels, then there are no restrictions on the inlet liquid flow rates. If the pressure drop across the liquid channel is greater than that in the vapor channels, some of the liquid must continue downstream. The pressure drop is then calculated assuming the liquid distributes evenly into two channels and the vapor distributes into the remaining eight. This procedure is continued until the pressure drop in the liquid channels is less than the pressure drop in the vapor channels. The location where this criterion is met is called the transition channel, which has both liquid and vapor flow. Only liquid is permitted to enter locations upstream from the transition channel and only vapor is allowed downstream. The flow rates in each channel are then determined by equating the pressure

drops across each flow path. The procedure is shown for a sample case (G_{in} = 59.8 kg m^{-2} s^{-1}, x_{in} = 0.49) in Figure 6.14, where the normalized phase flow rates are shown on the top plots and the total path pressure drop (the path pressure drop is negative in this case because of the large gravitational pressure gains across the component) is shown in the bottom plots. The first, second and third iterations are shown in 6.14(a), 6.14(b), and 6.14(c), respectively. The transition channel in this case is channel 2, and the worst possible liquid distribution has a normalized standard deviation below one.

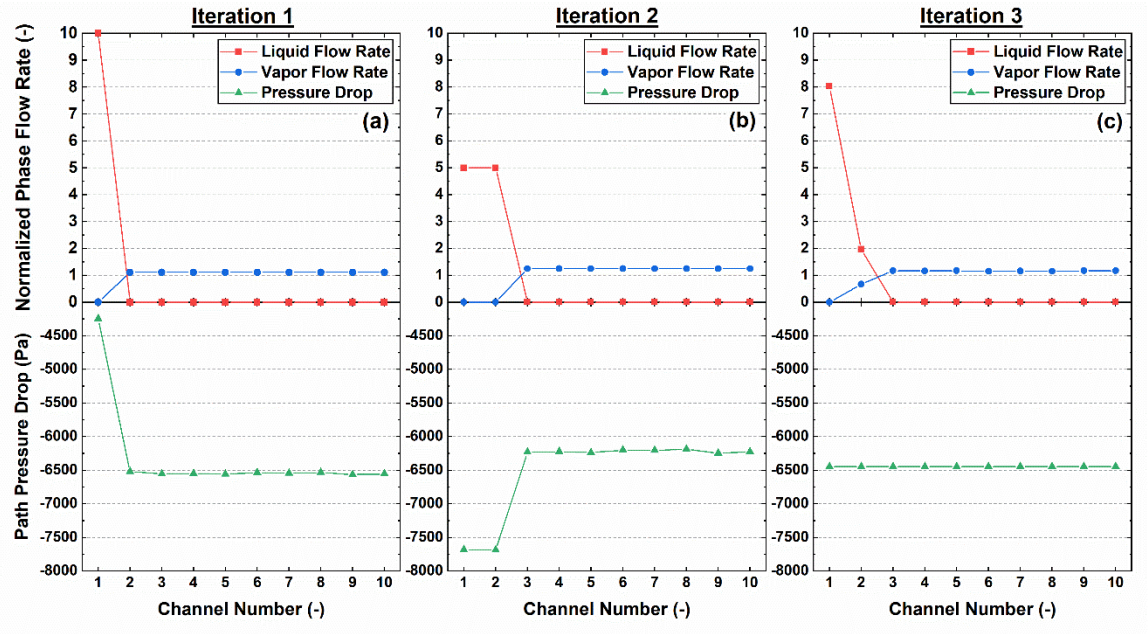

Figure 6.14: Normalized phase flow rates and path pressure drops in each channel for model iterations one (a), two (b), and three (c) used to find worst possible liquid distribution

The worst possible liquid distribution was determined for a wide range of qualities (0.1 to 0.9) and mass fluxes (23.9 and 95.7 kg m^{-2} s^{-1}) entering the heat exchanger. The minimum number of channels containing liquid at the inlet is shown in Figure 6.15 by the different symbols. At high inlet qualities, the liquid is not restricted, and it can potentially

exit the header through a single channel. At lower inlet qualities and/or higher inlet mass fluxes, only a fraction of the inlet liquid can enter a single channel, requiring the remaining liquid to continue downstream. This effect was most extreme at the lowest inlet qualities tested, where the pressure drop requirements forced the liquid to enter a minimum of four outlet channels.

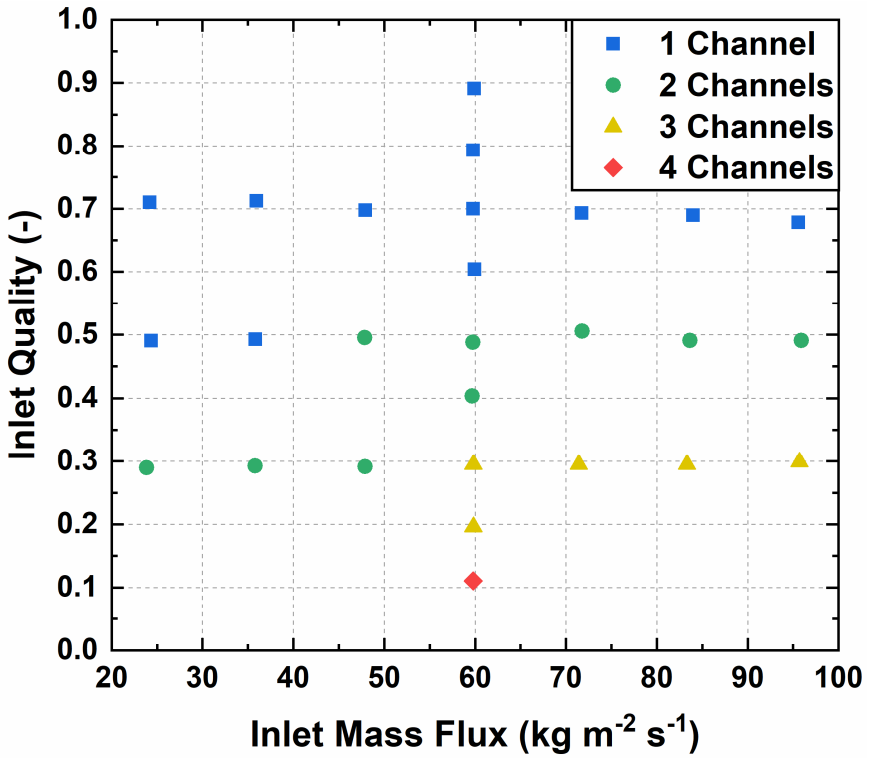

Figure 6.15: Minimum number of channels containing liquid at the inlet to achieve equal pressure drop across each flow path

The limitations on the liquid flow rate through a single channel has a large impact on the maximum possible degree of maldistribution in cases where the flow is forced to enter several different flow paths. The maximum liquid normalized standard deviation for a range of inlet conditions is shown Figure 6.16. As the inlet quality decreases and the inlet mass flux increases, the potential degree of liquid maldistribution decreases.

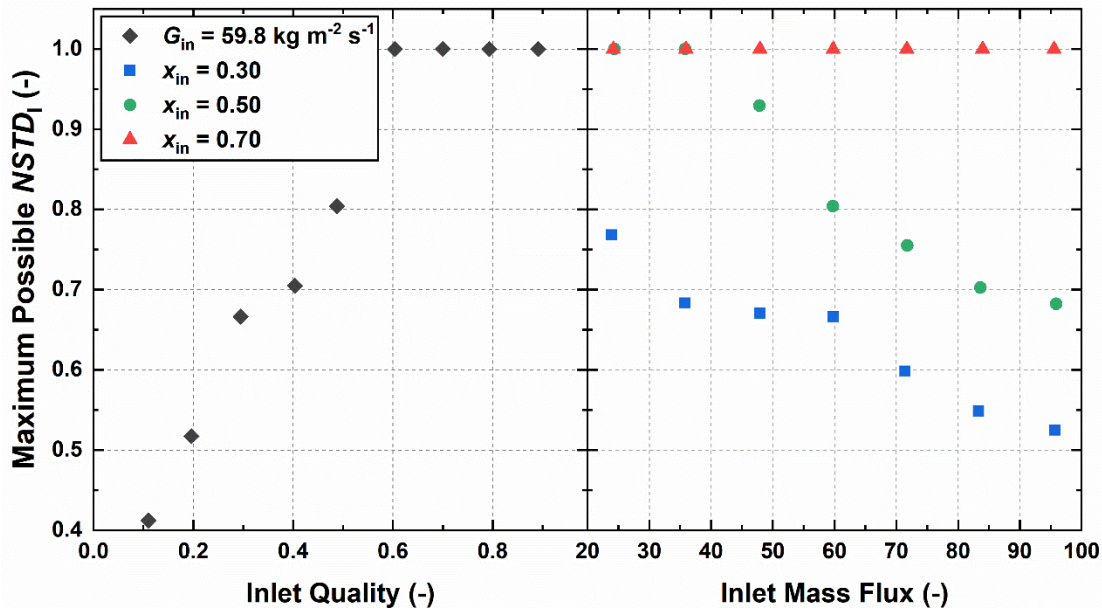

Figure 6.16: Maximum possible normalized standard deviation for a range of inlet qualities and mass fluxes considering the pressure drop requirements across the heat exchanger

The normalized standard deviation trends shown in Figure 6.16 are discontinuous. If the distribution is not limited by the pressure drop constraints, all the liquid will flow down the first channel and the worst case $NSTD_l$ is 1. When liquid is forced into the second channel, the normalized flow rate in the first channel drops from 10 to 5 as the flow rate in the second channel increases from 0 to 5. This is accompanied by a drastic decrease in the degree of maldistribution as the liquid starts to enter the second channel, but a more modest decrease as the flow rate in the second channel approaches the first. Forcing some of the liquid into the third channel ($\dot{m}^*_{l,ch1} = \dot{m}^*_{l,ch2} = 0.50 \rightarrow 0.33$ and $\dot{m}^*_{l,ch3} = 0 \rightarrow 0.33$) has the same effect on the degree of maldistribution, sharply decreasing the $NSTD_l$ as liquid start to enter the third channel, which diminishes as it approaches the flow rate of the first two channels. This trend is shown more clearly in Figure 6.17, which shows the relationship between the normalized liquid flow rate limit in the first channel and the worst

possible degree of liquid maldistribution ($NSTD_l$). The discontinuities in this trend correspond to the changes in $NSTD_l$ slope seen in the modeling results.

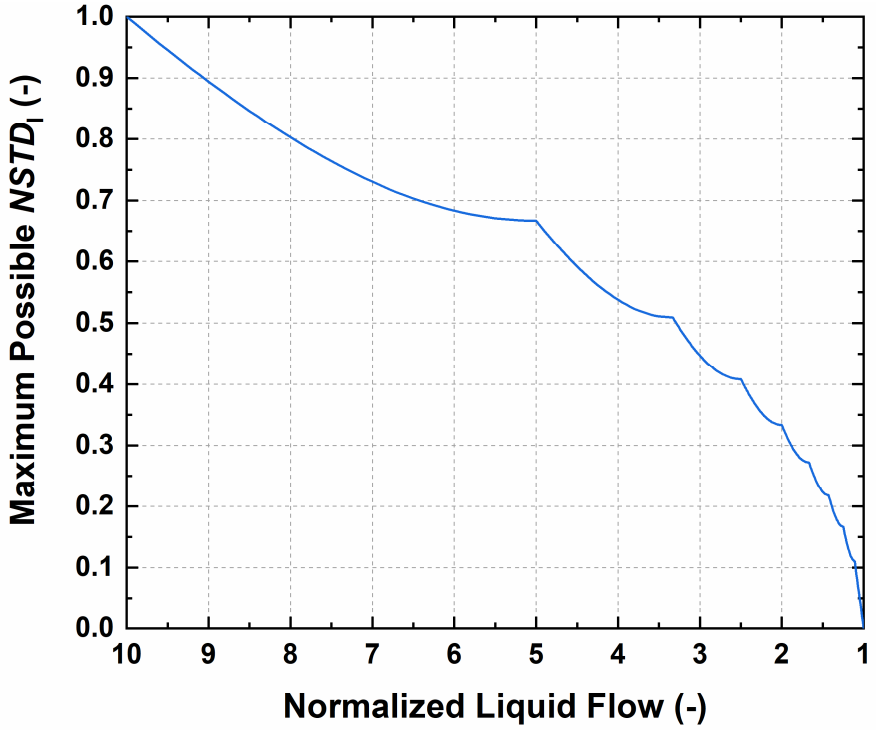

Figure 6.17: Normalized standard deviation as a function of the normalized liquid flow rate in the first channel (as $\dot{m}^*_{l.ch1}$ decreases, more liquid is distributed to downstream channels)

6.3 Liquid Distribution Prediction Approach

The worst possible distribution case bounds the achievable liquid flow rate in a given channel but does not accurately predict the measured distribution. The two-phase flow patterns in the header have a strong influence on the liquid distribution and must be considered for any modeling efforts. A new model was developed for refrigerant flow distribution that considers the effects of momentum, viscosity, and gravitational forces in the header. Although surface tension will also impact the liquid distribution, it was not varied in the experimental study and was therefore not considered in the proposed model.

The model first calculates the expected flow rate in a given channel, and then modifies the results based on the flow conditions entering the header. A new parameter, $\delta_{baseline}$, represents the expected ratio of the liquid flow rates in the channel to the flow rate in the header immediately before the channel inlet when the liquid momentum is neglected. The effects of liquid momentum and the header flow regime are discussed later in this section. Based on observations from the experiments, the expected value of $\delta_{baseline}$ for cases that are not pressure drop limited is equal to the projected area of the channel perpendicular to the flow direction divided by the cross-sectional area of the header. In cases were the path pressure drop restrictions limit the possible liquid flow rates in a single channel, $\delta_{baseline}$ is calculated using the maximum possible flow rate (see Section 6.2):

$$\delta_{baseline}[i] = min\begin{cases} \dfrac{D_{ch}}{W_{header}} \\ \dfrac{\dot{m}_{max}[i]}{\dot{m}_{header}[i]} \end{cases} \tag{6.21}$$

For high header inlet velocities, the liquid flow distribution can change drastically from the predictions of $\delta_{baseline}$. An example of this is shown in Figure 6.18. In this case, the flow enters the header in the momentum-dominated regime, meaning that the fluid velocities are high enough to overcome to gravitational forces near the inlet. The fluid momentum allows more of the liquid to skip over the first channel than $\delta_{baseline}$ would predict. Also, the conditions at the inlet can create a two-phase jet in the header. This results in higher liquid flow rates in channel locations near the jet impact point.

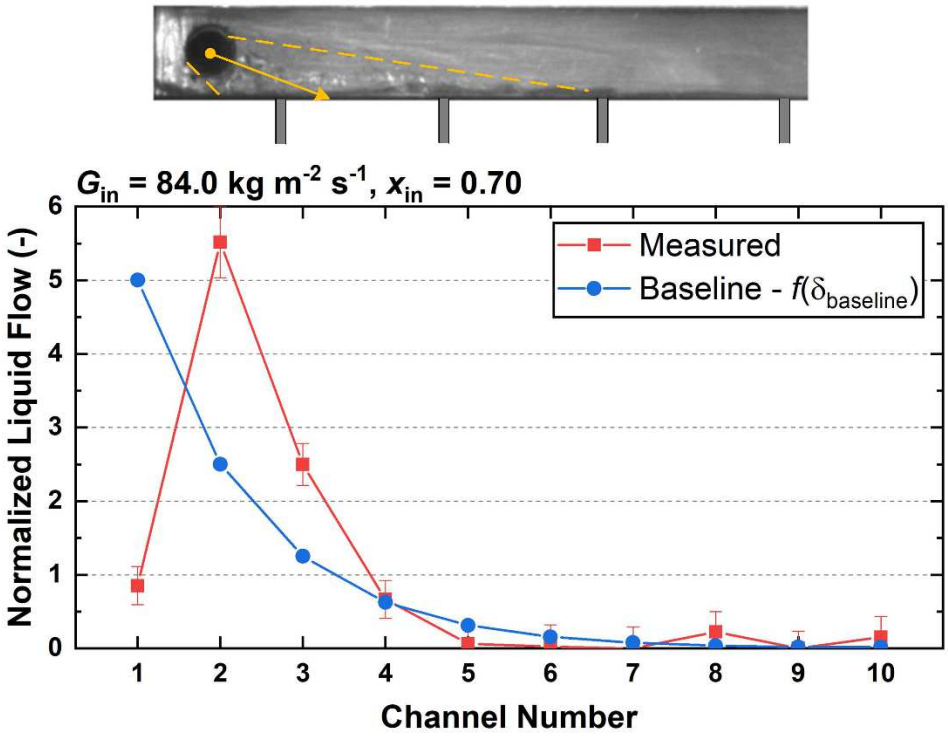

Figure 6.18: Comparison between the measured liquid distribution and the baseline prediction (only a function of $\delta_{baseline}$)

The proposed model captures the behavior of the flow in the header by correcting the baseline prediction. The model contains two terms: the first describes the tendency for more liquid to flow past channels near the inlet as the momentum increases, while the second captures the behavior of the jet. The model is formulated as a correction to $\delta_{baseline}$ in the form

$$\delta_l[i] = \delta_{baseline}[MC + JC] \tag{6.22}$$

where MC is a momentum-correction term, JC is a jet-correction term, and δ_l is the fraction of the liquid in the header that enters the channel (Equation 6.23).

$$\delta_l[i] = \frac{\dot{m}_{l,ch}[i]}{\dot{m}_{l,header}[i]} \tag{6.23}$$

Many different functions were considered for MC and JC, and the final form was selected based on the observed physical behavior. Experimental data showed that for high inlet momentum fluxes, $\delta_l[i]$ is close to zero in the first channel due to liquid flowing past it through the central part of the header (MC term), then peaks near the jet impact location, usually in channel 2 or 3 (JC term), and then returns to $\delta_{baseline}$. The momentum-correction term must reduce the flow in channels near the header inlet and approach 1 so that the function can return to the baseline case for downstream channels. The hyperbolic tangent is appropriate to capture these physical effects.

The jet-correction term must increase the flow rates in the channels near the jet impact location, but not significantly affect $\delta_l[i]$ outside the area of influence of the jets. A Gaussian distribution can describe this behavior, with good control over the position and area of influence of the jet, as well as the magnitude of the increase in liquid flow rates (the height of the Gaussian peak). With these functions, the correction terms can now be described using Equations 6.24 and 6.25

$$MC = \tanh(\varphi * l^*[i]) \tag{6.24}$$

$$JC = \chi * \exp\left[-\frac{(l^*[i] - \lambda)^2}{(\omega)^2}\right] \tag{6.25}$$

where φ is a function that specifies the behavior of the momentum-correction term for different inlet conditions, l^* is the normalized channel position ($l^* = pos_{ch}/L_{header}$), and λ, χ, and ω represent the position, height, and width of the Gaussian peak.

The functions describing the flow behavior in the header should capture the important forces present, including inertia, gravity, viscosity, and surface tension. The non-dimensional parameters considered include different forms of the Froude number (relative importance of inertia and gravity) and the Reynolds number (relative importance of inertia and viscosity). The Weber number (relative importance of inertia and surface tension) and Bond numbers (relative importance of gravity and surface tension) are also likely important, but the surface tension was not varied in the experimental work, which precluded obtaining any insights on the effects of surface tension in the present study. Future work in this area should focus on the effects of surface tension on flow distribution in plate-type heat exchangers.

The momentum correction term decreases the flow rates in channels near the inlet. This term should have a larger effect as the momentum entering the header increases, which allows more fluid to flow past the first channel. This behavior is best described using the inlet Froude number. The jet-correction term is controlled by several parameters. The experimental results show that the peak location can be described as a function of the liquid Reynolds number, the peak height is a function of the mixture Froude number, and the peak width remains relatively constant.

The final form of the proposed model is shown in Equation 6.26. The variations in these effects with inlet flow conditions are captured with the mixture Froude number

$\left(Fr_{mix} = G_{in}^2/(\rho_{mix,in}^2 D_{in} g)\right)$ and the liquid Reynolds number $\left(Re_l = G_{in}(1 - x_{in})D_{in}/\mu_{l,in}\right)$, where the mixture density is defined using the void fraction predicted with the Baroczy (1965b) correlation $\left(\rho_{mix,in} = \alpha_{in}\rho_{v,in} + (1 - \alpha_{in})\rho_{l,in}\right)$. All the constants were determined from the refrigerant experimental data using a regression analysis.

$$\delta_l[i] = \delta_{baseline}[i]\left\{\tanh\left[AFr_{mix}^B l^*[i]\right] + \frac{Fr_{mix}^{0.769}}{5.37} exp\left[-\left(10.1 * l^*[i] - \frac{Re_l^{0.695}}{210}\right)^2\right]\right\} \tag{6.26}$$

Constants A and B in Equation 6.26 are flow regime dependent, or in other words, the amount of liquid that can skip past the channels closest to the inlet depends on whether the flow is gravity-dominated or momentum-dominated. The values of these constants are shown in Table 6.2. The flow transitions from the gravity-dominated to the momentum-dominated regime when the density-modified Froude number increases above 0.72. The density-modified Froude number (shown in Equation 6.27) was introduced by Taitel and Dukler (1976) to describe two-phase flow regimes in circular channels and was found to accurately predict the transition between the two flow regime categories seen in plate-type heat exchanger headers (Section 5.1.1).

$$\mathrm{Fr}^* = \sqrt{\frac{\rho_v}{\rho_l - \rho_v}} \frac{j_v}{\sqrt{D_H g}} \tag{6.27}$$

Table 6.2: Empirical constants used to predict liquid distribution in headers with a two-phase inlet condition

Header Flow Regime	A	B
Gravity-Dominated	28.43	-0.43
Momentum-Dominated	73.85	-1.40

6.3.1 Comparison with Experiments

The liquid flow distribution model presented in Equation 6.26 is compared with the measured data in Figure 6.19 for low, intermediate, and high inlet qualities. At low inlet qualities, the liquid flow rates in the channels near the inlet are limited by the path pressure drop requirements. The proposed model accurately captures this effect by predicting the maximum possible liquid flow rate into each channel using the approach outlined in Section 6.2. The model also predicts the liquid distribution relatively well at intermediate inlet qualities; however, the shift in liquid flow to downstream channels starts to occur at slightly lower qualities in the model than was seen experimentally. Finally, at high inlet qualities, the model predicts the general trends well but over-predicts the flow rate in the first channel.

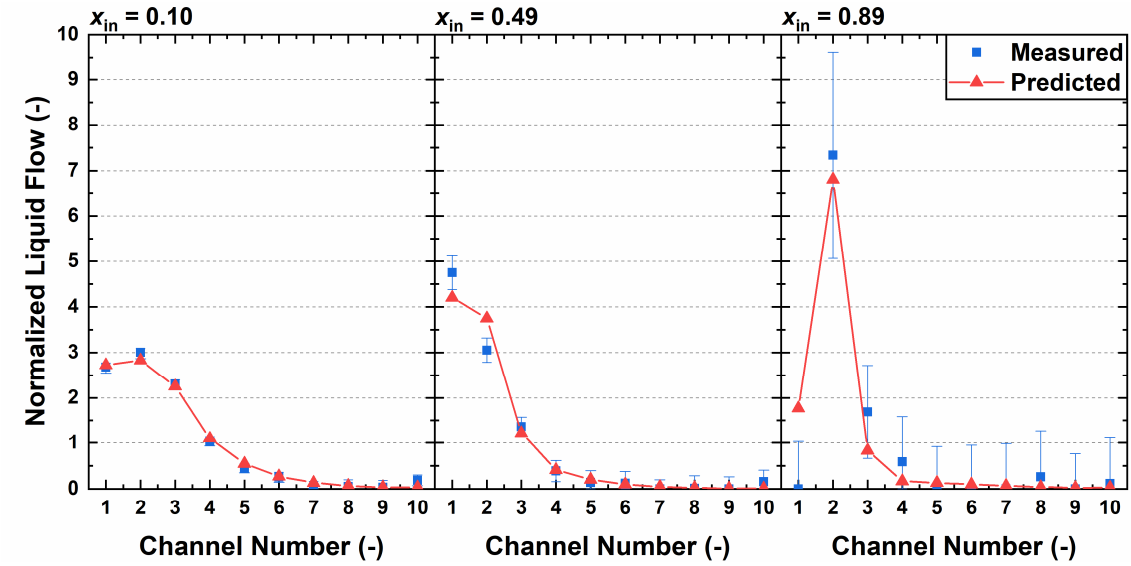

Figure 6.19: Measured and predicted liquid flow rates in each heat exchanger channel when fluid enters the header at a mass flux of 59.8 kg m^{-2} s^{-1} and qualities of 0.10 (left), 0.49 (center) and 0.89 (right)

The model predictions are compared with the experimental results for low and high inlet mass flux conditions in Figure 6.20 (x_{in} = 0.50). Again, the model accurately captures both the trends and the magnitudes of the liquid flow rates into each channel across the range of conditions tested.

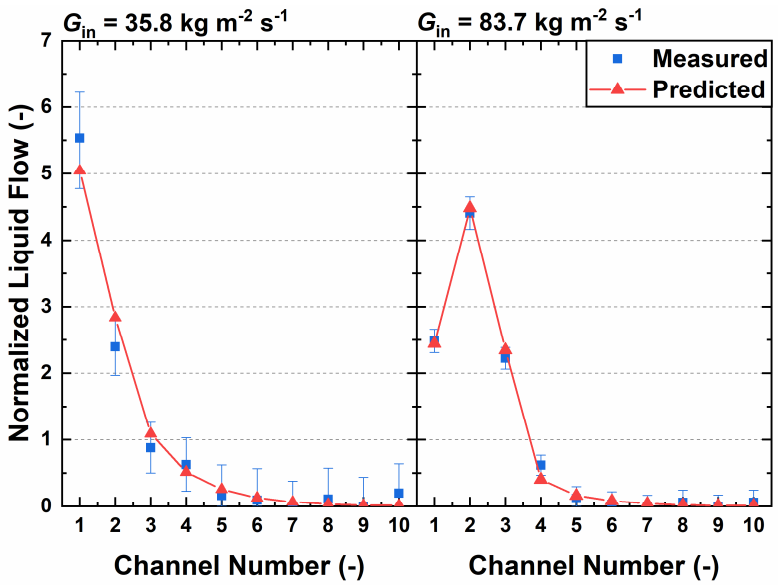

Figure 6.20: Measured and predicted liquid flow rates in each heat exchanger channel when fluid enters the header at a quality of 0.50 and mass fluxes of 35.8 kg m^{-2} s^{-1} (left) and 83.7 kg m^{-2} s^{-1} (right)

The model was used to predict the liquid flow rates in each channel for all the inlet conditions that were experimentally evaluated. The results are compared with the data in Figure 6.21. The model results match the data well for nearly all cases, with an absolute average deviation of 39.0%. Again, only channels with measured normalized liquid flow rates above 0.05 were included in this calculation to eliminate any errors approaching infinity. The model performs better in the gravity-dominated flow regime (AAD = 35.1%) than in the momentum-dominated regime (AAD = 45.7%), likely because the flow pattern characteristics are simpler and easier to mathematically describe. The largest errors occur at very low measured flow rates. As the measured liquid flow rate approaches zero, the percent error tends to infinity; therefore, this trend is expected. However, the percent uncertainty of these data points is also high, and in many cases, the uncertainty bars intersect the predicted values.

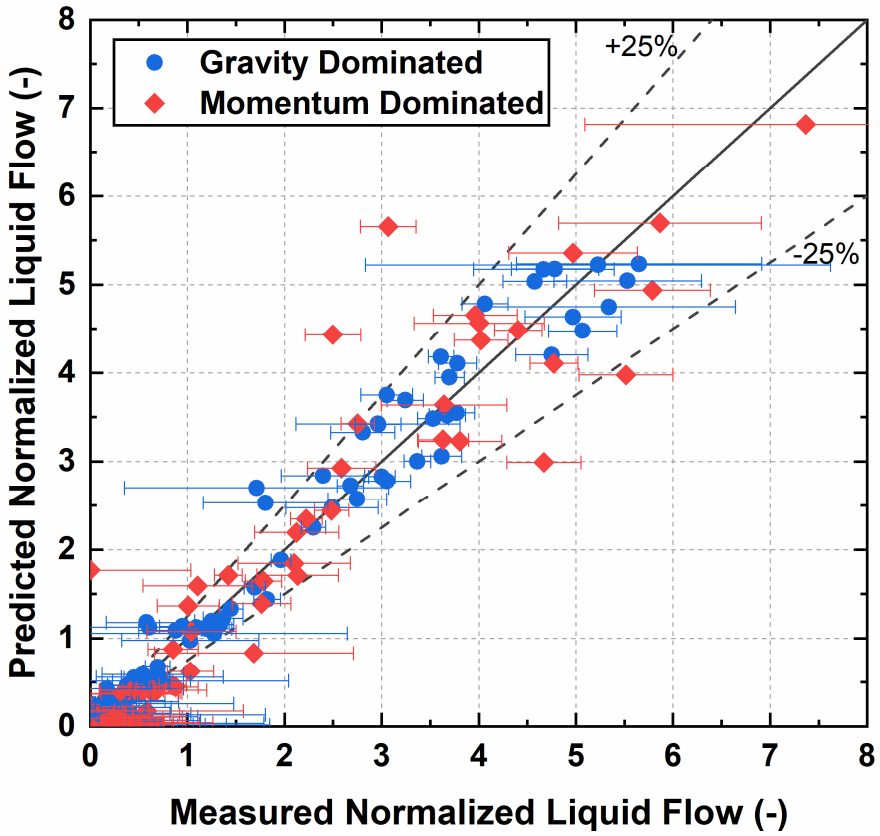

Figure 6.21: Comparison between the measured and predicted liquid flow rates in each heat exchanger channel

6.4 Vapor Distribution Prediction Approach

The vapor distribution in a heat exchanger with a two-phase inlet condition can be calculated with knowledge of the pressure drop and the liquid distribution. This approach guarantees that the resulting flow rate profiles are physically consistent with the path pressure drop requirements across the component. Other authors have developed empirical correlations to predict both the liquid and vapor flow rates in each channel (Kim *et al.*, 2011; Wijayanta *et al.*, 2017), but these models potentially introduce errors that will result in a predicted distribution that is not physically attainable, e.g., by not conserving mass.

The model presented in Section 6.1 was developed to calculate the pressure profiles in each flow path given the liquid and vapor flow rates down each channel. The same model was used to predict the vapor channel flow rates using the predicted liquid flow rates by equating the total pressure change across the ten flow paths and applying a mass balance to the vapor phase (assuming no phase change occurs in the header). Although this modeling approach is heavily dependent on the quality of the correlations used to predict the liquid distribution, two-phase pressure drops and condensation heat transfer coefficients, it calculates flow rates based on the parameter that truly dictates the vapor distribution.

The model was initially developed to calculate the pressure drop for a given channel inlet condition. Although it works well and predicts the path flow rates with a reasonable level of accuracy (see Section 6.1.4), it is computationally expensive because it involves the iterative solution of 8380 equations. Additionally, the code is robust when it is supplied with the inlet liquid and vapor flow rates, but it requires good guess values to solve for phase flow rates using pressure drop information. The model in its present form is not ideal for predicting the vapor flow distribution because of its rigid nature when attempting to solve for phase flow rates. As a result, the vapor flow rates were not calculated for every inlet condition that was experimentally evaluated. Instead, the vapor distribution was determined for a subset of the data to show the validity of the approach. The predicted flow rates are compared with the experimental data in the next section. Future work should focus on expanding the practicality of this approach by developing a simplified, more flexible pressure drop model that can reliably predict vapor flow rates in heat exchangers.

6.4.1 Comparison with Experiments

The vapor flow distribution predicted using the pressure drop model is compared with the experimental results for low, intermediate, and high inlet quality conditions in Figure 6.22 (G_{in} = 59.8 kg m^{-2} s^{-1}). The model correctly captures the vapor distribution trends, and predicts most of the vapor flow rates within the experimental error.

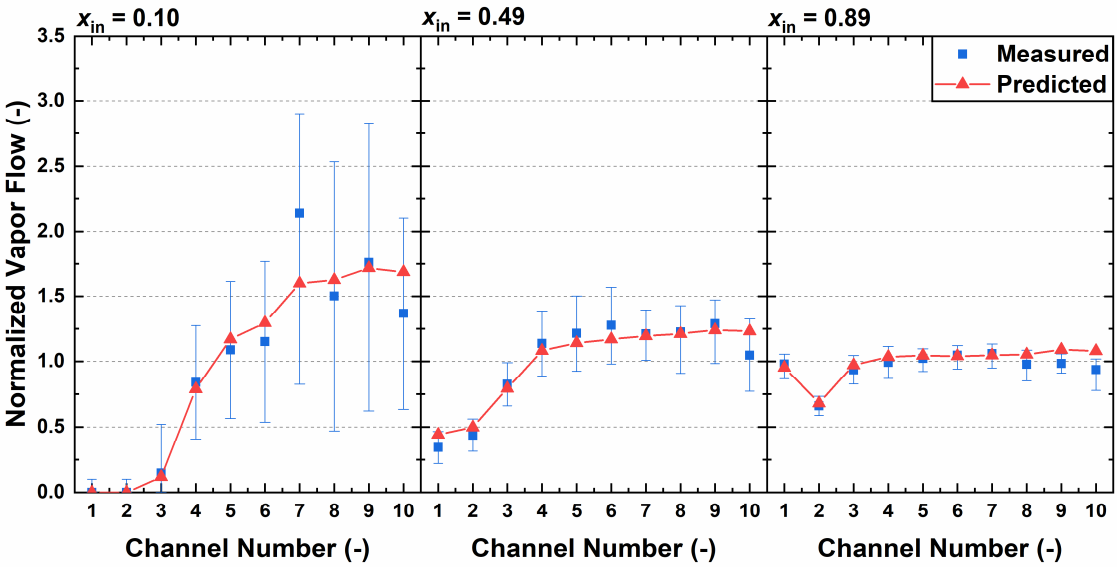

Figure 6.22: Measured and predicted vapor flow rates in each heat exchanger channel when fluid enters the header at a mass flux of 59.8 kg m^{-2} s^{-1} and qualities of 0.10 (left), 0.49 (center) and 0.89 (right)

The vapor flow distribution was also calculated for a low and high inlet mass flux condition (x_{in} = 0.50). The results are compared with the experimental data in Figure 6.23. Again, the model accurately predicts both the trends and magnitude of the vapor distribution for these conditions.

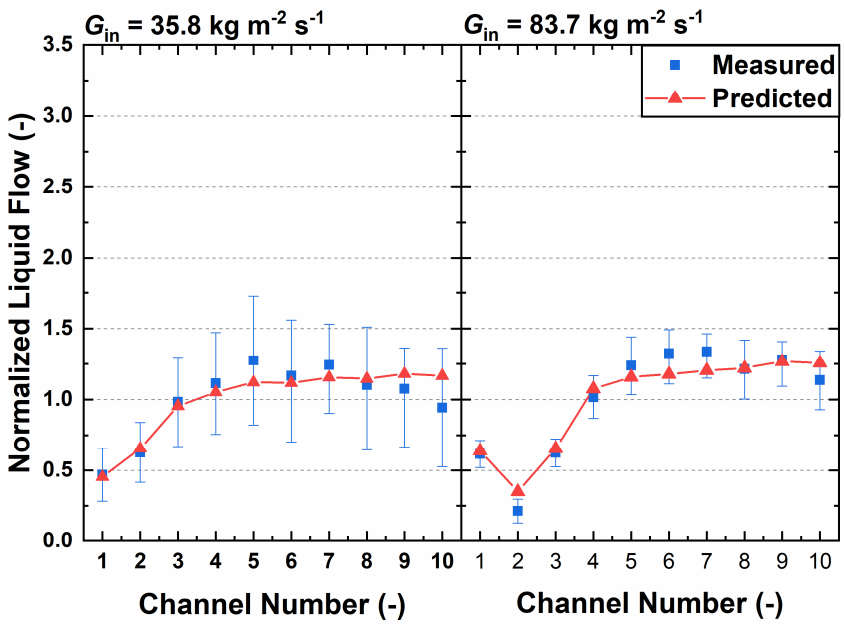

Figure 6.23: Measured and predicted vapor flow rates in each heat exchanger channel when fluid enters the header at a quality of 0.5 and mass fluxes of 35.8 kg m^{-2} s^{-1} (left) and 83.7 kg m^{-2} s^{-1} (right)

6.5 Conclusions on Flow Distribution Modeling

This study proposes a new approach to predicting two-phase flow distribution in multi-channel heat exchangers that combines information about the header flow patterns and component pressure drop. A detailed model of the heat exchanger presented in Chapter 4 was developed to understand the relationship between flow distribution and the pressure change across each flow path. This model was used to find the worst possible liquid distribution for a range of header inlet qualities and flow rates, which set limits on the liquid flow rates in a single channel. Using this information and observations from the experimental study, a liquid distribution model was developed for refrigerant flows in plate-type heat exchanger headers. The model can predict the trends and magnitudes of the liquid flow rates in each heat exchanger channel with an absolute average deviation of 39.0%, which is a substantial improvement over other empirical models in the literature.

The liquid flow rates were then used to predict the vapor distribution using the detailed pressure drop model. A schematic representation of the modeling approach is shown in Figure 6.24. The results shown that the approach is an appropriate method for predicting the vapor distribution characteristics in heat exchangers. Future work should focus on developing a simplified pressure drop model that reduces the computational time required to predict the vapor flow rates.

This proposed modeling approach enables the prediction of the liquid and vapor flow rates in each channel for microchannel refrigerant heat exchangers, but it also provides a broader understanding of the parameters that affect flow distribution. Many previous researchers explain two-phase flow distribution based solely on the flow patterns in the header. This modeling work shows that the flow patterns are an important consideration, but the pressure drop across each flow path must also be considered to fully understand liquid and vapor distribution in a multi-channel heat exchanger.

Furthermore, this modeling approach is an effective framework for predicting flow distribution in a broad range of heat exchangers. The path pressure drops in all multi-channel heat exchangers restrict the possible liquid and vapor flow rates and can have a profound influence on distribution. Accounting for the effects of pressure drop make the results physically consistent and allow for accurate predictions of both the liquid flow rates (especially at low inlet qualities,) and vapor flow rates.

Distribution is also heavily dependent on the header flow regime. A liquid distribution model was developed from insights on the fluid dynamics inside the header and accounts for the important driving forces. Specifically, the relative effects of gravity,

inertia, and viscosity were considered using the Froude and Reynolds numbers. These parameters are important for all heat exchangers with the orientation studied here (horizontal header with vertical channels), which extends the range of applicability of the model. The results should be valid for horizontal plate-type heat exchanger headers, although the correlation should be further validated and refined for different geometries (L_{header}, A_{inlet}, A_{header}, etc.) and fluids. This work could be extended to cross flow heat exchangers with some consideration for the effects of geometry variations between plate-type and cross flow headers, and expansion as the flow enters the header.

The liquid distribution model would not be directly applicable cases where the flow patterns in the header differ substantially from those seen in the rectangular header for which it was developed. This can occur when features are added to the header to improve distribution (protruding channels, guide vanes, etc.) or when the orientation is changed. In these cases, a new liquid distribution model must be developed to account

for the changing flow regimes, but the overall model framework can still be applied.

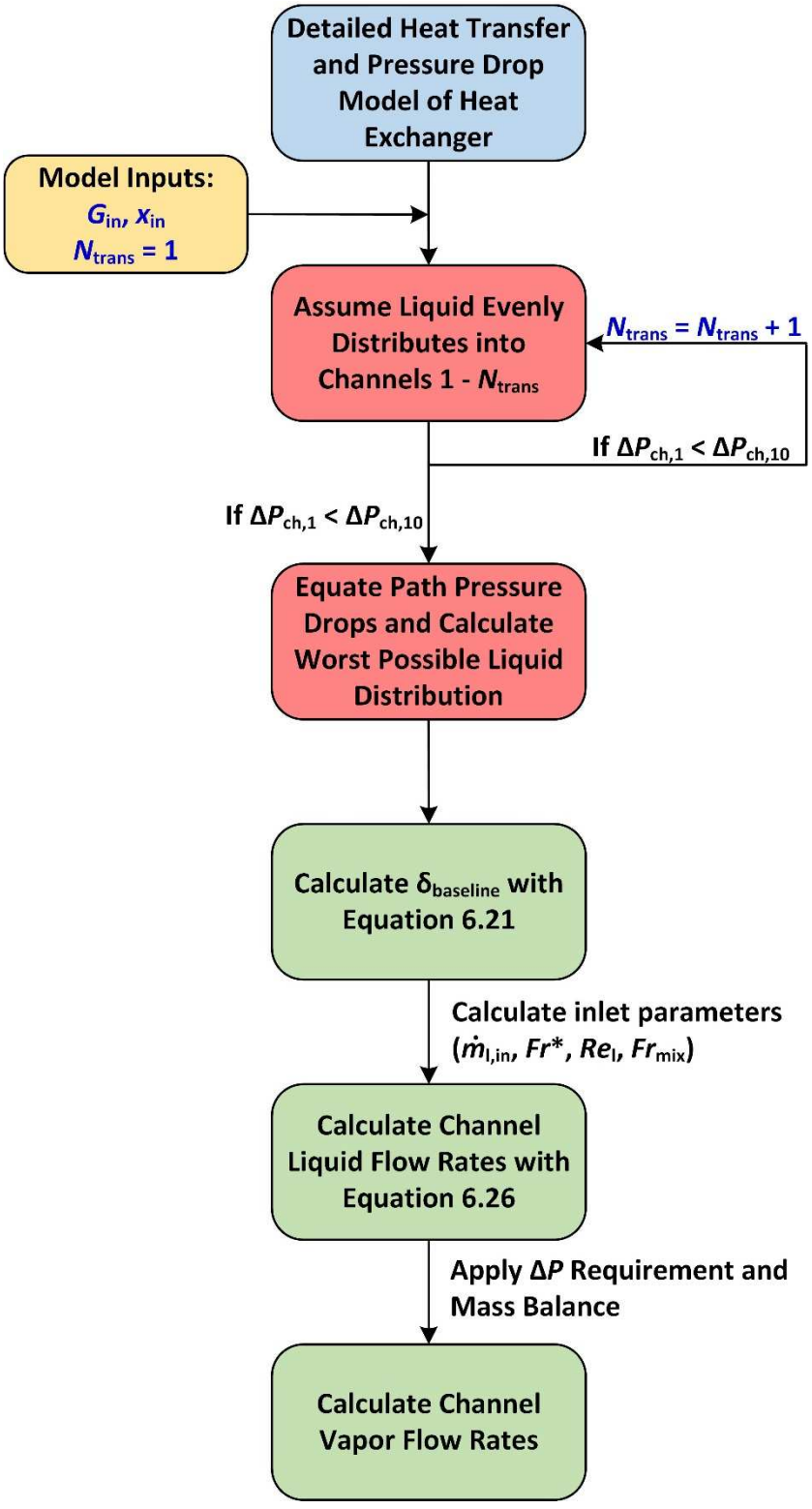

Figure 6.24: Procedure for proposed model

CHAPTER 7. CONCLUSIONS AND RECOMMENDATIONS

A comprehensive study on the distribution of air-water mixtures and saturated refrigerants in multi-channel heat exchangers was conducted. The heat exchangers considered here contain vertical parallel minichannels connected to a common horizontal header with a rectangular cross section. The header geometries are based on those commonly seen in plate-type heat exchangers. In this study, fluid flowed through the parallel channels in the direction of gravity (downward). Distribution experiments were conducted on air-water mixtures with varying inlet mass fluxes ($2.60 < G_{in} < 200$ kg m^{-2} s^{-1}), inlet qualities ($0.05 < x_{in} < 0.35$), outlet channel diameters ($1 < D_{ch} < 3$ mm), and header geometries (rectangular and triangular). Experiments on the distribution of saturated refrigerants were conducted for multiple inlet mass fluxes ($23.9 < G_{in} < 95.7$ kg m^{-2} s^{-1}), inlet qualities ($0.10 < x_{in} < 0.90$), and header geometries (rectangular, triangular, and vane) for ten parallel 1-mm diameter channels functioning as a counterflow water-cooled heat exchanger.

An experimental approach and data analysis procedure were developed for identifying header flow patterns and evaluating the liquid and vapor flow rates into each heat exchanger channel for a give set of inlet conditions. The overall degree of maldistribution was also determined so that different cases could be directly compared. In both the air-water and refrigerant distribution experiments, the header flow regimes were categorized into five major groups: stratified smooth, stratified wavy, smooth film, wavy film, and churn-turbulent. Flow regime maps were developed for both fluids based on the saturated liquid and vapor velocities. The flow patterns were then more broadly

categorized into gravity-dominated (stratified-smooth and stratified-wavy) and momentum-dominated (smooth film, wavy film and churn-turbulent) regimes, which have distinctly different distribution characteristics. The transition between these flow regimes was defined using the density-modified Froude number, which was later used to develop a regime-specific liquid distribution model.

Header flow regimes have a strong influence on liquid and vapor distribution. In the air-water experiments, the worst liquid distribution occurred in the gravity dominated regime. In many of these cases, all the liquid enters a single channel resulting in the worst possible distribution ($NSTD_l = 1$). At higher inlet mass fluxes and/or qualities, the flow transitioned to more favorable flow regimes (momentum-dominated), transporting a larger portion of the liquid to downstream channels. In general, the liquid and gas distribution improved with increasing inlet mass fluxes and qualities.

In the refrigerant experiments, the most significant changes in the overall degree of maldistribution occurred while varying the inlet quality into the test section. As the inlet quality increased, the liquid distribution remained approximately the same, but the vapor distribution improved. This resulted in good distribution characteristics at high qualities when most of the fluid entering the heat exchanger was in the vapor phase. The only deviation from this general trend occurred at low qualities. For these conditions, pressure drop restrictions across each flow path required the liquid to distribute more evenly.

In contrast, the header inlet mass flux did not have a significant impact on the distribution in the refrigerant experiments. Increasing the momentum of the liquid phase in the header transported more liquid to downstream channels but resulted in low liquid

flow rates in the channels closest to the inlet port. The global effect was a shift in the flow distribution profile with nearly the same degree of maldistribution. This result is partially due to the overall length of the header and the limited range of mass fluxes tested.

This study also investigated the effect of header geometry on distribution. In the air-water experiments, a triangular header was evaluated and compared with the baseline rectangular one. The triangular header performed slightly better, reducing the average liquid and gas normalized standard deviation by 0.06 and 0.04, respectively. The largest improvements in distribution occurred when the inlet conditions were near a flow regime transition. Conversely, in the refrigerant experiments, the triangular header did not significantly impact the distribution. This is likely a consequence of the overall length of the refrigerant header, which is longer than the air-water manifold ($L_{\text{header,a-w}}$ = 52.8 mm vs. $L_{\text{header,ref}}$ = 155 mm), because it feeds more heat exchanger channels ($N_{\text{ch,a-w}}$ = 3 and $N_{\text{ch,ref}}$ = 10). This results in a more gradual reduction in cross sectional area along the header length, which does not considerably affect the liquid velocities near the inlet. Therefore, the distribution characteristics of the rectangular and triangular headers were similar for these cases. A header with a guide vane was also evaluated in the refrigerant heat exchanger. The vane header improved the distribution, especially in the gravity-dominated flow regime. The maximum observed decrease in the overall normalized standard deviation was 37%. Further work is needed to improve and optimize the geometry of vaned headers for use in plate-type heat exchangers.

Additionally, a distribution model was developed for horizontal plate-type heat exchanger headers containing saturated refrigerants. The liquid distribution model considers the limitations imposed by the pressure drop requirements across each flow path,

and the two-phase flow characteristics in the header. The vapor flow rates were calculated by equating the pressure drop across each flow path using a detailed hydrodynamic and heat transfer model of the component. The final model was validated with the experimental data and showed significant improvement over existing liquid distribution models (AAD_l = 39.0%).

The findings of this study advance the understanding of two-phase flow distribution in heat exchangers. This understanding will facilitate future development of low pressure drop methods to evenly distribute both the liquid and vapor in manifolds. Mitigating flow maldistribution in mini and microchannel heat exchangers can help enable the development of extremely compact, cost effective heat exchangers for a variety of power production, heating, and/or cooling system.

7.1 Recommendations for Future Work

There are several opportunities for continued work in the area of two-phase flow distribution in heat exchangers. A summary of some of the most important avenues for further research is provided below.

- It is important to understand the effects of fluid properties on flow distribution, particularly surface tension, density ratio and viscosity ratio. This study focused on the distribution characteristics of air-water mixtures and saturated refrigerants, which have vastly different fluid properties. Additional systematic studies are needed on saturated fluids with properties commonly seen in mini and microchannel heat exchangers to further explore the relationship between header flow regimes and fluid properties.

- Although there have been many previous experimental studies on flow distribution, the effect of geometry (for example: the header length, channel pitch, cross sectional areas of the feeder tube, header, and outlet channels, etc.) on distribution are still not fully understood. Future work should focus on characterizing two-phase flow distribution for a variety of distributor geometries relevant to cross-flow, plate-type, and shell-and-tube heat exchangers.
- The experimental approach used in this work provides detailed information about the flow distribution characteristics in heat exchangers, but the facility was labor-intensive to build and calibrate. Future work could develop different approaches to evaluate the degree of maldistribution for different header designs using infrared imaging or global performance parameters, which could simplify the experimental setup.
- The present study designed and experimentally evaluated alternative header geometries to improve distribution in plate-type heat exchanger. The vane header showed some promise, but further work is needed to optimize the design and to evaluate the performance of a larger range of possible geometries that can be integrated into plate-type heat exchangers. One optimization approach for headers that aim to restrict the maximum channel flow rates that warrants further study is restrictions that are based on the flow regime. For example, in the gravity-dominated regime, the slots in the vane could be small near the inlet and increase in area further downstream.
- The surface properties of the header could also be modified to improve flow distribution. Additional research is needed to develop surfaces capable of wicking

liquid refrigerants in specified directions and integrating these surfaces into heat exchanger headers.

- A two-phase flow distribution model was developed in this study to predict the liquid and vapor flow rates in each channel in a heat exchanger. The model was specifically developed for saturated refrigerant (R134a) flows into the heat exchanger described in Chapter 4. Further study is needed to determine the applicability of this modeling approach for other refrigerants and horizontal header geometries.
- It was not possible in this study to measure the local velocity and pressure profiles in the header. This type of information could improve the understanding of two-phase flow distribution but is difficult to obtain experimentally. The development of validated computational fluid dynamic (CFD) models could provide local velocity and pressure information in the header and answer some of the outstanding questions in this field.

APPENDIX A. ANALYTICAL MODEL FOR TIME OF FLIGHT SENSOR

This appendix introduces a simplified analytical solution for a thermal time of flight sensor subject to a time dependent heat flux at the inlet boundary (Neumann boundary condition). A general solution for the problem is derived and the solution for a step heat flux boundary condition is presented to predict the operation of the thermal TOF sensor.

A.1 Governing Equations

Heat transport in the sensor can be described by the two-dimensional unsteady advection diffusion equation subject to a time-dependent inlet boundary condition. This analysis focuses on laminar flow because the Reynolds numbers are below 2000 for all the conditions tested. Therefore, the governing equation for this problem can be expressed as:

$$\rho c_p \frac{\partial T}{\partial t} + \rho c_p u_r \frac{\partial T}{\partial x} = \frac{k}{r}\frac{\partial}{\partial r}\left(r\frac{\partial T}{\partial r}\right) + k\frac{\partial^2 T}{\partial x^2} + 2\mu\left(\frac{\partial u_r}{\partial r}\right)^2 \qquad \text{(A.1)}$$

Chen *et al.* (2011) developed an analytical solution for the 2-D advection diffusion equation for a Robin (third-type) inlet boundary condition, neglecting viscous dissipation. They compared their 2-D solution with the results of a 1-D axial model and found that the results were nearly identical. Additionally, Berthet *et al.* (2011) developed a 1-D analytical model for a thermal TOF sensor assuming a constant temperature inlet boundary condition. The time-of-flight predictions from the model agreed well with both numerical and experimental results. Additionally, viscous dissipation can be neglected in the devices because the temperature gradients are relatively small (Br <<< 1). Based on these

observations, the governing equation can be reduced to the one-dimensional time dependent advection diffusion equation shown in Equation A.2. For convenience, this equation is non-dimensionalized using the transform $\Delta T = T(x,t) - T_\infty$ and normalized using the scales $x^* = x/L$, $t^* = \bar{u}t/L$ and $\theta^* = k\Delta T/Q_0'' L$ as follows:

$$\frac{1}{Pe}\frac{\partial^2 \theta^*}{\partial x^{*2}} - \frac{\partial \theta^*}{\partial x^*} = \frac{\partial \theta^*}{\partial t^*} \tag{A.2}$$

This equation is subject to several restrictions. The underlying assumptions are listed below:

(a) Unsteady one-dimensional flow

(b) Laminar flow with negligible viscous dissipation

(c) Negligible radial conduction

(d) Constant fluid properties

Although Equation A.2 provides a starting point for a simplified analytical model, it does not account for the parabolic velocity profile or any radial diffusion effects present in the sensor. Aris (1956) first investigated correcting the dispersion coefficient when predicting mass transfer phenomena in straight pipes using a one-dimensional model. Ajdari *et al.* (2006) extended this work by developing a method to correct for 2-D thermal diffusion effects using the mass transfer analogy. For laminar flow in circular pipes, they suggested using an effective thermal diffusivity of $\kappa(1 + 0.0031Pe_D^2)$ in the governing equation. This effective thermal diffusivity was used in place of the actual thermal diffusivity for this analysis.

Boundary conditions applicable to the thermal TOF sensor described above include a periodic heat flux at the inlet (x = 0), specified as $f(t)$, and a temperature gradient equal to zero at the outlet (x = L). The initial temperature distribution in the devices is assumed to be uniform and is specified as T_∞. The initial and boundary conditions are mathematically summarized below.

$$-\frac{\partial\theta^*(x^*=0,t^*)}{\partial x^*}=\frac{f\left(\frac{L}{\overline{\overline{u}}}t^*\right)}{Q_0''}=F\left(\frac{L}{\overline{\overline{u}}}t^*\right)\qquad\forall\ t^*>0 \tag{A.3}$$

$$\frac{\partial\theta^*(x^*=1,t^*)}{\partial x^*}=0\qquad\forall\ t^*>0 \tag{A.4}$$

$$\theta^*(x^*,t^*=0)=0\qquad 0\le x^*\le 1 \tag{A.5}$$

A.2 Derivation of Analytical Solution for Arbitrary *f*(t)

The analytical solution is derived using a Laplace transform with respect to the dimensionless time t^*, where $\tilde{\theta}(x^*,s)=\mathcal{L}[\theta^*(x^*,t^*)]=\int_0^\infty\theta^*(x^*,t^*)e^{-st^*}dt^*$ and $F(s)=\mathcal{L}\left[f\left(\frac{L}{\overline{\overline{u}}}t^*\right)\right]=\int_0^\infty f\left(\frac{L}{\overline{\overline{u}}}t^*\right)e^{-st^*}dt^*$. The Laplace transform is then modified using the approach developed by Guerrero *et al.* (2009), as shown in Equation A.6.

$$\vartheta(x^*,s)=\left[\tilde{\theta}(x^*,s)-F(s)\right]\exp\left(-\frac{Pe}{2}x^*\right) \tag{A.6}$$

This transformation converts the governing equation into a purely diffusive problem, which allows for a more straight-forward analysis. The final forms of the governing equation and boundary conditions are shown in Equations A.7 to A.9, respectively.

$$\frac{1}{Pe}\frac{\partial^2\vartheta}{\partial x^{*2}} - \left(\frac{Pe}{4} + s\right)\vartheta = sF(s)\exp\left(-\frac{Pe}{2}x^*\right) \tag{A.7}$$

$$\frac{\partial\vartheta(x^* = 0, s)}{\partial x^*} - \frac{Pe}{2}\vartheta(x^* = 0, s) = 0 \tag{A.8}$$

$$\frac{\partial\vartheta(x^* = 1, s)}{\partial x^*} + \frac{Pe}{2}\vartheta(x^* = 1, s) = 0 \tag{A.9}$$

These equations are then solved using the general integral transform technique (Hahn and Ozisik, 2012). A normalized eigenfunction $X(\beta_m, x^*)$ is chosen so that the governing equation is in the form of the Sturm-Liouville problem subject to the same boundary conditions shown above (Equations A.8 and A.9).

$$\frac{d^2X(x^*)}{dx^{*2}} + \beta^2 X(x^*) = 0 \tag{A.10}$$

Evaluating Equation A.10, the eigenfunction and eigenvalue (β_m) can be expressed as:

$$X(\beta_m, x^*) = \sqrt{2}\,\frac{\beta_m\cos(\beta_m x^*) + \frac{\mathrm{Pe}}{2}\sin(\beta_m x^*)}{\sqrt{\lambda^2 + \frac{Pe}{2}}} \tag{A.11}$$

$$\frac{\beta_m^2}{Pe} - \beta_m cot\beta_m = \frac{Pe}{4} \tag{A.12}$$

Therefore, the generalized integral transform pair for this problem is:

$$\overline{\vartheta}(x^*, s) = \int_0^1 X(\beta_m, x^*)\vartheta(x^*, s)dx^* \tag{A.13}$$

$$\vartheta(x^*, s) = \sum_{m=1}^{\infty} X(\beta_m, x^*)\overline{\vartheta}(x^*, s) \tag{A.14}$$

Finally, completing the integral transformation given by Equations A.13 and A.14, one can obtain the following result for $\overline{\vartheta}(x^*, s)$:

$$\overline{\vartheta}(x^*, s) = \frac{s\beta_m Pe}{\lambda^2\sqrt{\lambda^2 + \frac{Pe}{2}}} \frac{-\sqrt{2}F(s)}{\lambda^2 + 2s} \tag{A.15}$$

where $\lambda^2 = \beta_m^2 + \frac{Pe^2}{4}$. The analytical solution in the time domain can be easily retrieved by reversing all the variable transformations and taking the inverse Laplace transform of the expression. The inverse Laplace transform can be obtained using the convolution method. The dimensionless temperature distribution in the time domain can then be expressed by Equation A.16:

$$\theta^*(x^*, t^*) = F\left(\frac{L}{\overline{\overline{U}}}t^*\right) - \sum_{m=1}^{\infty} M(\beta_m, x^*)N(\beta_m, t^*) \tag{A.16}$$

In the above equation, the functions M and N are expressed as:

$$M(\beta_m, x^*) = \frac{2Pe\beta_m\left[\beta_m\cos(\beta_m x^*) + \frac{\mathrm{Pe}}{2}\sin(\beta_m x^*)\right]}{\lambda^2\left(\lambda^2 + \frac{Pe}{2}\right)}\exp\left(\frac{Pe}{2}x^*\right) \tag{A.17}$$

$$N(\beta_m, t^*) = F\left(\frac{L}{\overline{\overline{u}}}t^*\right) - \gamma e^{-\gamma t^*}\int_{\tau=0}^{t^*} F\left(\frac{L}{\overline{\overline{u}}}\tau\right)e^{\gamma\tau}d\tau \tag{A.18}$$

where $\gamma = \frac{\beta_m^2}{Pe} + \frac{Pe}{4}$.

A.3 Model for TOF Flow Meter

Finally, a closed-form solution for boundary conditions relevant to the thermal time of flight sensor is developed. The sensor is initiated by supplying a voltage to the heater for 1 second, or mathematically:

$$f(t) = Q_0''[H(t) - H(t-1)] \tag{A.19}$$

Using the general solution given in Equation A.16, the temperature at a given time and position can be expressed using Equation A.20:

$$\theta^*(x^*, t^*) = \left[1 - H\left(\frac{L}{\overline{u}}(t^* - 1)\right)\right] - \sum_{m=1}^{\infty} M(\beta_m, x^*)N(\beta_m, t^*) \tag{A.20}$$

In this solution, the functions $M(\beta_m, x^*)$ and $N(\beta_m, t^*)$ are given in Equations A.17 and A.21, respectively.

$$N(t^*) = \left[1 - H\left(\frac{L}{\overline{u}}(t^* - 1)\right)\right] - \gamma e^{-\gamma t^*} I \tag{A.21}$$

where $I = \int_{\tau=0}^{t^*} \left(1 - H\left(\frac{L}{\overline{u}}(t^* - 1)\right)\right) e^{\gamma\tau} d\tau = \frac{1}{\gamma}\exp\left(\frac{\gamma\overline{u}}{L}\right) - 1$.

A.4 Comparison with Experimental Data

The predictions of the analytical model are compared with the experimental data here. One major limitation of the model is the one-dimensional assumption. As discussed

in the previous section, radial diffusion may significantly affect the measured time of flight, especially at low velocities. This effect cannot be captured by the proposed model; therefore, it was initially compared with experimental cases where radial diffusion effects are minimal, e.g., when the temperature difference between the wall and the centerline is the largest.

Two representative velocities were chosen for model validation: one velocity in the lower range and another in the upper range. The temperature profiles calculated using the analytical model and the experimental data for average refrigerant velocities of 6 mm s^{-1} and 15 mm s^{-1}, respectively, are compared in Fig. 10 (a) and (b). The results show good qualitative agreement; however, there is a phase lag between the results. As discussed previously, this lag can be attributed to off-center placement of the heater or thermocouples, mixing induced by components in the flow stream, thermal capacitances, and diffusion effects. However, despite the relative simplicity of the model, it was able to provide a good estimate for time of flight and therefore can give some insight into the design of TOF sensors for different operating conditions.

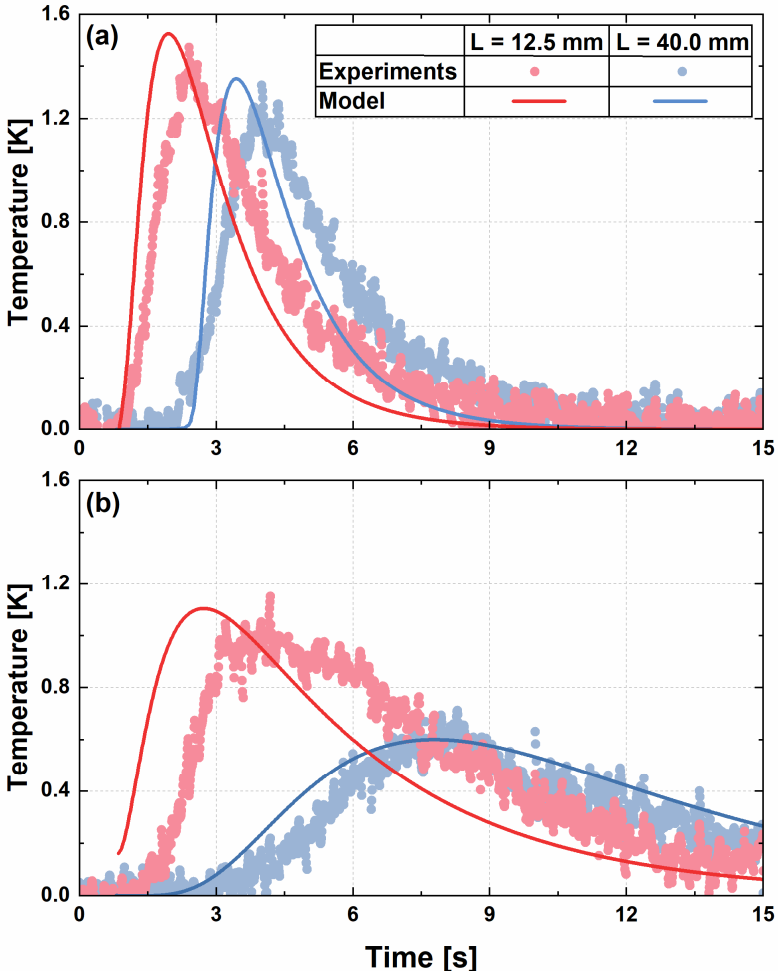

Figure A.1: Comparison of analytical model and experimental data for (a) $\bar{u} = 6$ mm s^{-1} and (b) 15 mm s^{-1}. Experimental results correspond to cases with the highest radial temperature gradient.

In addition to comparing the temperature profiles for low and high velocity cases, the time of flight predicted by the analytical model was compared with the measured values over the entire velocity range. These results are shown in Fig. 11. This plot presents the analytically derived time of flight at the first and second thermocouple locations as squares and diamonds, respectively. Additionally, all of the collected experimental data for velocities ranging from 1 to 20 mm s^{-1} and radial temperature differences $(T_{wall} - T_{base})$ between about 0 and 3.5 K are shown in the shaded regions.

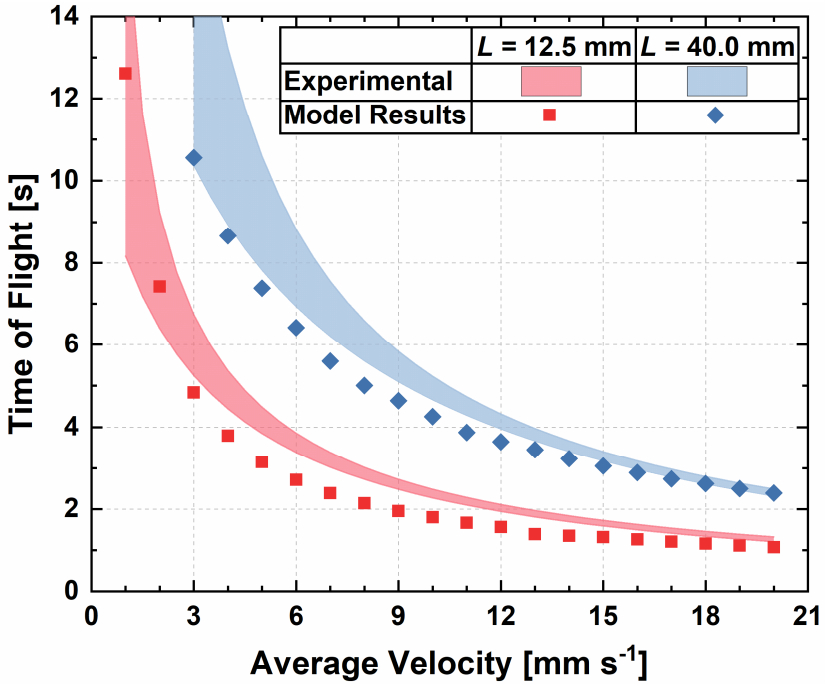

Figure A.2: Comparison between the measured time of flight and the analytical results over the full sensor range

The lower bound of these regions corresponds to the cases with the highest temperature difference between the sensor wall and the bulk fluid and therefore the lowest rates of radial diffusion away from the centerline. The analytical model is able to predict the trend and the magnitude of the time of flight well for these conditions, with an average error of about 8.5%. Most of the predicted values are lower than the experimental data, as discussed above. However, at a velocity of 1 mm s^{-1}, the analytical model over-predicts the data by about 50%. The model is unstable when calculating temperatures at times near zero, especially at low flow rates. At a velocity of 1 mm s^{-1}, the temperatures predicted by the model are erroneous and do not follow the correct trends below times of about 5 seconds. This instability is likely leading to the large errors at low flow rates.

APPENDIX B. SAMPLE CALCULATION

This appendix presents the data analysis approach for a representative data point used to calculate the flow distribution in the refrigerant experiments. The methods to calculate the inlet ambient losses (section B.1), the mass flux and quality entering the test section (section B.2), the channel ambient gains (section B.3), the mass flux and quality entering the heat exchanger channels (section B.4) and the degree of maldistribution in the heat exchanger (section B.5) are presented in the tables below. The calculations are shown for the data collected using the rectangular header for the central condition in the test matrix (G_{in} = 59.7 kg m^{-2} s^{-1}, x_{in} = 0.50). For all channel-specific calculations, the measured values for channel 2 are used. All relevant data collected for this case are shown in Table 4.6.

B.1 Inlet Ambient Losses

The fluid state at the test section inlet is calculated from an energy balance across the preheater. The refrigerant enters the preheater as a subcooled liquid and the fluid state is established using the temperature and pressure. A cartridge heater then adds enough heat to the fluid to reach the specified inlet quality for the experiment. The heater power is measured using a wattmeter, but the thermal losses to the environment must also be considered to accurately calculate the fluid state at the test section inlet. The losses were calculated in the section of the heater assembly that contains the cartridge heater, the section that does not contain the cartridge heater, and the inlet piping. Important geometric characteristics of the heater assembly are shown in Table B.1 and a schematic of the preheater and the inlet piping is shown in Figure B.1.

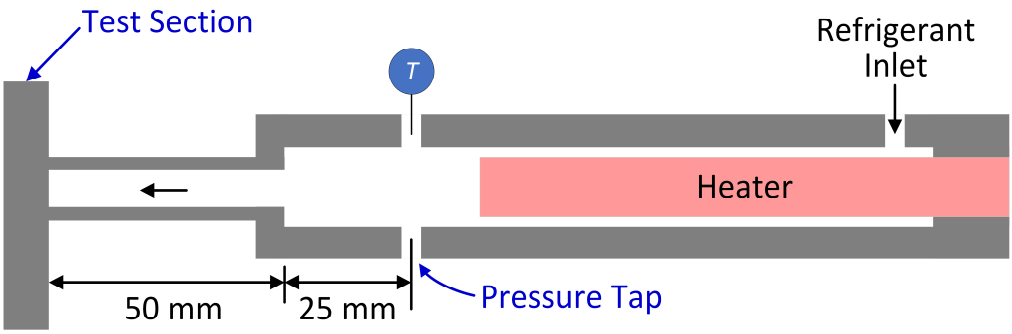

Figure B.1: Schematic of the preheater assembly and the tubing connecting it to the test section.

Table B.1: Geometric specifications of the preheater and the preheater housing assembly

Dimension	Symbol	Value
Heater Length	L_h	172 mm
Heater Diameter	D_h	12.7 mm
Assembly Length	L_{assb}	197 mm
Assembly Inner Diameter	$D_{assb,in}$	17.9 mm
Assembly Outer Diameter	$D_{assb,out}$	38.1 mm
Minimum Insulation Thickness	th_{ins}	25.4 mm

The method used to calculate the losses in the preheater and inlet piping is shown in Table B.2 for the sample case. All measured variables are shown in blue, and values that were calculated iteratively are shown in red. The calculation approach is described in more detail in Chapter 4.

Table B.2: Inlet heat loss – sample calculation

Inputs	Equations	Results
Calculation of Ambient Losses in the Portion of Assembly Containing the Preheater		
$T_{preh,in} = 12.6℃$ $P_{preh,in} = 774\ kPa$ $P_{preh,out} = 777\ kPa$	$\bar{P}_{preh} = \frac{P_{preh,in} + P_{preh,out}}{2}$ $T_{sat} = f(\bar{P}_{preh})$ $h_{preh,in} = f(T_{preh,in}, P_{preh,in})$ $h_{sat,l} = f(x = 0, \bar{P}_{preh})$	$\bar{P}_{preh} = 775.5\ kPa$ $T_{sat} = 30.2℃$ $h_{preh,in} = 69011\ J\ kg^{-1}$ $h_{sat,l} = 93872\ J\ kg^{-1}$
$\dot{m}_{ref} = 9.81 \times 10^{-4}\ kg\ s^{-1}$ $h_{preh,in} = 69011\ J\ kg^{-1}$ $h_{sat,l} = 93872\ J\ kg^{-1}$ $\dot{Q}_{ref,preh} = 107.2\ W$	$\dot{Q}_{sens} = \dot{m}_{ref} * [h_{sat,l} - h_{preh,in}]$ $\dot{Q}_{lat} = \dot{Q}_{ref,preh} - \dot{Q}_{sens}$	$\dot{Q}_{sens} = 24.4\ W$ $\dot{Q}_{lat} = 82.8\ W$
$T_{preh,in} = 12.6℃$ $T_{sat} = 30.2℃$ $\dot{Q}_{sens} = 24.4\ W$ $\dot{Q}_{lat} = 82.8\ W$ $\dot{Q}_{ref,preh} = 107.2\ W$	$\bar{T}_{preh} = \left(\frac{T_{preh.in} + T_{sat}}{2}\right)\left(\frac{\dot{Q}_{sens}}{\dot{Q}_{ref,preh}}\right) + T_{sat}\left(\frac{\dot{Q}_{lat}}{\dot{Q}_{ref,preh}}\right)$	$\bar{T}_{preh} = 28.2℃$
$htc_h = 10000\ W\ m^{-2}K^{-1}$ (assumed) $D_{assb,in} = 0.018\ m$ $L_h = 0.172\ m$	$R_{h,ref} = \frac{1}{htc_h \times \pi D_{assb,in} L_h}$	$R_{ref,h} = 0.010\ K\ W^{-1}$
Material = Stainless AISI304 $\bar{T}_{preh} = 28.2℃$ $D_{assb,in} = 0.018\ m$ $D_{assb,out} = 0.038\ m$ $L_h = 0.172\ m$	$\bar{T}_{assb} = \bar{T}_{preh}$ (assumed) $k_{assb} = f(Material, \bar{T}_{assb})$ $R_{wall,h} = \frac{\ln\left(\frac{D_{assb,out}}{D_{assb,in}}\right)}{2\pi L_h k_{assb}}$	$\bar{T}_{assb} = 28.2℃$ $k_{assb} = 14.9\ W\ m^{-1}K^{-1}$ $R_{wall,h} = 0.047\ K\ W^{-1}$
$D_{assb,in} = 0.018\ m$ $D_{assb,out} = 0.038\ m$ $L_h = 0.172\ m$ $th_{ins} = 0.025\ m$ $k_{ins} = 0.043\ W\ m^{-1}K^{-1}$	$R_{ins,h} = \frac{ln\left(\frac{D_{assb,out} + 2th_{ins}}{D_{assb,out}}\right)}{2\pi L_h k_{ins}}$	$R_{ins,h} = 18.29\ K\ W^{-1}$
$T_{amb} = 22.8℃$ $T_{ins,out} = 23.6℃$ $D_{assb,out} = 0.038\ m$ $th_{ins} = 0.025\ m$ $L_h = 0.172\ m$ $\epsilon = 0.8$ (assumed)	$\bar{T}_{out} = \frac{T_{amb} + T_{ins,out}}{2}$ $D_{ins,out} = D_{assb,out} + 2th_{ins}$ $R_{rad,h} = \frac{1}{4(\pi D_{ins,out} L_{assb})\sigma\epsilon\bar{T}^3}$	$\bar{T}_{out} = 23.2℃ = 296.3\ K$ $D_{ins,out} = 0.089\ m$ $R_{rad,h} = 4.422\ K\ W^{-1}$
$\bar{T}_{out} = 23.2℃$ $P_{amb} = 101\ kPa$	Air Properties = $f(\bar{T}_{out}, P_{amb})$	$\beta_a = 0.00338\ K^{-1}$ $\nu_a = 1.55 \times 10^{-5}\ m^2\ s^{-1}$ $\alpha_a = 2.12 \times 10^{-5}\ m^2 s^{-1}$

Table B.2: Inlet heat loss – sample calculation (cont'd)

Inputs	Equations	Results
$T_{amb} = 22.8℃$ $T_{ins,out} = 23.6℃$ $D_{ins,out} = 0.089\ m$ $L_h = 0.172\ m$ $\beta_a = 0.00338\ K^{-1}$ $\nu_a = 1.55 \times 10^{-5}\ m^2\ s^{-1}$ $\alpha_a = 2.12 \times 10^{-5}\ m^2 s^{-1}$	$Ra_{air} = \frac{g D_{ins,out}^3 \beta_a (T_{ins,out} - T_{amb})}{\nu_a \alpha_a}$ $Nu_{NC} = f(Ra_{air}, Pr_{air})$ Calculated w/ Churchill & Chu (1975) $htc_{NC} = \frac{Nu_{NC} k}{D_{ins,out}}$ $R_{NC,h} = \frac{1}{\pi D_{ins,out} L_h htc_{NC}}$	$Ra_{air} = 55780$ $Nu_{NC} = 6.90$ $htc_{NC} = 1.97\ W\ m^{-2} K^{-1}$ $R_{NC,h} = 10.6\ K\ W^{-1}$
$R_{ref,h} = 0.010\ K\ W^{-1}$ $R_{wall,h} = 0.047\ K\ W^{-1}$ $R_{ins,h} = 18.3\ K\ W^{-1}$ $R_{rad,h} = 4.42\ K\ W^{-1}$ $R_{NC,h} = 10.6\ K\ W^{-1}$	$R_{total,h} = R_{ref,h} + R_{wall,h} + R_{ins,h} + \left(\frac{1}{R_{rad,h}} + \frac{1}{R_{NC,h}}\right)^{-1}$	$R_{total,h} = 21.5\ K\ W^{-1}$
$T_{amb} = 22.8℃$ $\bar{T}_{preh} = 28.2℃$ $R_{total} = 21.5\ K\ W^{-1}$	$\dot{Q}_{loss,h} = \frac{\bar{T}_{heater} - T_{amb}}{R_{total}}$	$\boxed{\dot{Q}_{loss,h} = 0.25\ W}$
$T_{amb} = 22.8℃$ $R_{rad,h} = 4.42\ K\ W^{-1}$ $R_{NC,h} = 10.6\ K\ W^{-1}$ $\dot{Q}_{loss,h} = 0.25\ W$	$T_{ins,out} = \dot{Q}_{loss,h} \left(\frac{1}{R_{rad,h}} + \frac{1}{R_{NC,h}}\right)^{-1} + T_{amb}$	$T_{ins,out} = 23.6℃$
Calculation of ambient losses in portion of assembly that does not contain the preheater		
$htc_h = 10000\ W\ m^{-2} K^{-1}$ (assumed) $D_{assb,in} = 0.018\ m$ $L_{assb,e} = 0.025\ m$	$R_{ref,assb,e} = \frac{1}{htc_h \times \pi D_{assb,in} L_{assb,e}}$	$R_{ref,assb,e} = 0.070\ K\ W^{-1}$
$k_{assb} = 14.9\ W\ m^{-1} K^{-1}$ $D_{assb,in} = 0.018\ m$ $D_{assb,out} = 0.038\ m$ $L_{assb,e} = 0.025\ m$	$R_{wall,assb,e} = \frac{\ln\left(\frac{D_{assb,out}}{D_{assb,in}}\right)}{2\pi L_{assb,e} k_{assb}}$	$R_{wall,assb,e} = 0.318\ K\ W^{-1}$
$D_{assb,out} = 0.038\ m$ $D_{ins,out} = 0.089\ m$ $L_{assb,e} = 0.025\ m$ $k_{ins} = 0.043\ W\ m^{-1} K^{-1}$	$R_{ins,assb,e} = \frac{ln\left(\frac{D_{ins,out}}{D_{assb,out}}\right)}{2\pi L_{assb,e} k_{ins}}$	$R_{ins,assb,e} = 123.5\ K\ W^{-1}$
$\bar{T}_{out} = 296.3\ K$ $D_{ins,out} = 0.089\ m$ $L_{assb,e} = 0.025\ m$ $\epsilon = 0.8$ (assumed)	$R_{rad,assb,e} = \frac{1}{4\left(\pi D_{ins,out} L_{assb,e}\right) \sigma \epsilon \bar{T}_{out}^{\ 3}}$	$R_{rad,assb,e} = 29.85\ K\ W^{-1}$

Table B.2: Inlet heat loss – sample calculation (cont'd)

Inputs	Equations	Results
$htc_{NC} = 1.97\ W\ m^{-2}K^{-1}$ $D_{ins,out} = 0.089\ m$ $L_{assb,e} = 0.025\ m$	$R_{NC,assb,e} = \frac{1}{\pi D_{ins,out} L_{assb,e} htc_{NC}}$	$R_{NC,assb,e} = 71.58\ K\ W^{-1}$
$R_{ref,assb,e} = 0.07\ K\ W^{-1}$ $R_{wall,assb,e} = 0.318\ K\ W^{-1}$ $R_{ins,assb,e} = 124\ K\ W^{-1}$ $R_{rad,assb,e} = 29.9\ K\ W^{-1}$ $R_{NC,assb,e} = 71.6\ K\ W^{-1}$	$R_{tot,assb,e} = R_{ref,assb,e} + R_{wall,assb,e} + R_{ins,assb,e} + \left(\frac{1}{R_{rad,assb,e}} + \frac{1}{R_{NC,assb,e}}\right)^{-1}$	$R_{tot,assb,e} = 144.9\ K\ W^{-1}$
$P_{preh,out} = 777\ kPa$ $T_{amb} = 22.8℃$ $R_{tot,assb,e} = 145\ K\ W^{-1}$	$T_{preh,out} = f(P_{preh,out})$ $\dot{Q}_{loss,assb,e} = \frac{T_{preh,out} - T_{amb}}{R_{tot,assb,e}}$	$T_{preh,out} = 30.3℃$ $\dot{Q}_{loss,assb,e} = 0.05\ W$
$\dot{Q}_{loss,h} = 0.25\ W$ $\dot{Q}_{loss,assb,e} = 0.05\ W$	$\dot{Q}_{loss,assb} = \dot{Q}_{loss,h} + \dot{Q}_{loss,assb,e}$	$\boxed{\dot{Q}_{loss,assb} = 0.30\ W}$
Calculation of Ambient Losses in Feeder Tube		
$\dot{m}_{ref} = 9.81 \times 10^{-4}\ kg\ s^{-1}$ $P_{preh,out} = 777\ kPa$ $x_{preh,out} = 0.488$ $D_{inlet} = 4.57 \times 10^{-3}\ m$	$htc_{feed} = f(\dot{m}_{ref}, P_{preh,out}, x_{preh,out}, D_{feed})$ Calculated with Shah (2009)	$htc_{feed} = 1051\ W\ m^{-2}K^{-1}$
$htc_{feed} = 1051\ W\ m^{-2}K^{-1}$ $D_{inlet} = 4.57 \times 10^{-3}\ m$ $L_{feed} = 0.076\ m$	$R_{ref,feed} = \frac{1}{htc_{feed} \times \pi D_{inlet} L_{feed}}$	$R_{ref,feed} = 0.914\ K\ W^{-1}$
$k_{feed} = 14.9\ W\ m^{-1}K^{-1}$ $D_{feed,out} = 6.35 \times 10^{-3}\ m$ $D_{inlet} = 4.57 \times 10^{-3}\ m$ $L_{feed} = 0.076\ m$	$R_{wall,feed} = \frac{\ln\left(\frac{D_{feed,out}}{D_{inlet}}\right)}{2\pi L_{feed} k_{feed}}$	$R_{wall,feed} = 0.046\ K\ W^{-1}$
$D_{feed,out} = 6.35 \times 10^{-3}\ m$ $th_{ins} = 0.025\ m$ $L_{feed} = 0.076\ m$ $k_{ins} = 0.043\ W\ m^{-1}K^{-1}$	$R_{ins,feed} = \frac{ln\left(\frac{D_{feed,out} + 2th_{ins}}{D_{feed,out}}\right)}{2\pi L_{feed} k_{ins}}$	$R_{ins,feed} = 106.7\ K\ W^{-1}$
$\bar{T}_{out} = 296.3\ K$ $D_{feed,out} = 6.35 \times 10^{-3}\ m$ $th_{ins} = 0.025\ m$ $L_{feed} = 0.076\ m$ $\epsilon = 0.8$ (assumed)	$R_{rad,feed} = \frac{1}{4\pi\left(D_{feed,out} + 2th_{ins}\right) L_{feed} \sigma \epsilon \bar{T}_{out}^{\ 3}}$	$R_{rad,feed} = 15.48\ K\ W^{-1}$

Table B.2: Inlet heat loss – sample calculation (cont'd)

Inputs	Equations	Results
$htc_{NC} = 1.97\ W\ m^{-2}K^{-1}$ $D_{feed,out} = 6.35 \times 10^{-3}\ m$ $th_{ins} = 0.025\ m$ $L_{feed} = 0.076\ m$	$R_{NC,feed} = \frac{1}{\pi(D_{feed,out} + 2th_{ins})L_{feed}htc_{NC}}$	$R_{NC,feed} = 31.91\ K\ W^{-1}$
$R_{ref,feed} = 0.914\ K\ W^{-1}$ $R_{wall,feed} = 0.046\ K\ W^{-1}$ $R_{ins,feed} = 106.7\ K\ W^{-1}$ $R_{rad,feed} = 15.48\ K\ W^{-1}$ $R_{NC,feed} = 31.91\ K\ W^{-1}$	$R_{tot,feed} = R_{ref,feed} + R_{wall,feed} + R_{ins,feed} + \left(\frac{1}{R_{rad,feed}} + \frac{1}{R_{NC,feed}}\right)^{-1}$	$R_{tot,feed} = 118.1\ K\ W^{-1}$
$T_{preh,out} = 30.3℃$ $T_{amb} = 22.8℃$ $R_{tot,feed} = 118.1\ K\ W^{-1}$	$\dot{Q}_{loss,feed} = \frac{T_{preh,out} - T_{amb}}{R_{tot,feed}}$	$\boxed{\dot{Q}_{loss,feed} = 0.06\ W}$
Calculation of Conduction Losses through Frame		
$\dot{Q}_{heater} = 108.0\ W$	$\dot{Q}_{loss,cond} = 0.0992 \times \exp(0.0143\ \dot{Q}_{heater})$	$\boxed{\dot{Q}_{loss,cond} = 0.464\ W}$

B.2 Test Section Inlet Conditions

Two-phase flow distribution is significantly affected by the header inlet conditions. In this study, the distribution was quantified as a function of the inlet mass flux and quality. The equations used to calculate the inlet mass flux (G_{in}) and quality (x_{in}) are shown in Table B.3 for the sample case. All measured variables are shown in blue, while all values either calculated or specified by the manufacturer are shown in black. The calculation approach is also described in detail in Chapter 4.

Table B.3: Test section inlet conditions – sample calculation

Inputs	Equations	Results
$\dot{m}_{ref} = 9.81 \times 10^{-4}\ kg\ s^{-1}$ $D_{inlet} = 4.57 \times 10^{-3}\ m$	$G_{in} = \frac{4\dot{m}_{ref}}{\pi D_{inlet}^2}$	$\boxed{G_{in} = 59.76\ kg\ m^{-2}s^{-1}}$
$\dot{Q}_{loss,h} = 0.25\ W$ $\dot{Q}_{loss,assb,e} = 0.05\ W$ $\dot{Q}_{loss,feed} = 0.06\ W$ $\dot{Q}_{loss,cond} = 0.46\ W$	$\dot{Q}_{loss} = \dot{Q}_{loss,h} + \dot{Q}_{loss,assb,e} + \dot{Q}_{loss,feed} + \dot{Q}_{loss,cond}$	$\dot{Q}_{loss} = 0.82\ W$
$\dot{m}_{ref} = 9.81 \times 10^{-4}\ kg\ s^{-1}$ $h_{preh,in} = 69011\ J\ kg^{-1}$ $\dot{Q}_{heater} = 108\ W$ $\dot{Q}_{loss} = 0.82\ W$	$h_{TS,in} = h_{preh,in} + \frac{\dot{Q}_{heater} - \dot{Q}_{loss}}{\dot{m}_{ref}}$	$h_{TS,in} = 178264\ J\ kg^{-1}$
$h_{TS,in} = 178264\ J\ kg^{-1}$ $P_{preh,out} = 777\ kPa$	$x_{in} = f(P_{preh,out}, h_{TS,in})$	$\boxed{x_{in} = 0.488}$

B.3 Channel Ambient Gains

The inlet quality into each heat exchanger channel is calculated from an energy balance across the coolant stream. Although most of the energy into the coolant stream comes from the condensing refrigerant, the fluid also gains some heat from the warmer ambient environment. The thermal gains between the ambient and the chilled water are calculated using a thermal resistance network. The analysis includes the contributions of the coolant convective resistance, the conductive resistance through the tube wall and the insulation, and the natural convection and radiation resistances. The calculations of these resistances and the ambient thermal gains are shown in Table B.4. All measured variables are shown in blue, all values either calculated or specified by the manufacturer are shown in black, and variables that were calculated iteratively are shown in red. More information about these calculations is provided in Section 4.3.2.

Table B.4: Ambient gains from environment– sample calculation

Inputs	Equations	Results
$T_{w,in}[2] = 6.04℃$ $T_{w,out}[2] = 10.43℃$ $P_{w,in} = 195.4\ kPa$ $P_{w,out} = 172\ kPa$	$\bar{T}_w[2] = \frac{(T_{w,in}[2] + T_{w,out}[2])}{2}$ $\bar{P}_w = \frac{P_{w,in} + P_{w,out}}{2}$	$\bar{T}_w[2] = 8.24℃$ $\bar{P}_w = 183.6\ kPa$
$\dot{m}_w[2]$ $= 4.85 \times 10^{-4}\ kg\ s^{-1}$ $\bar{T}_w[2] = 8.24℃$ $\bar{P}_w = 183.6\ kPa$ $D_{ann,in} = 0.002\ m$ $D_{ann,out} = 0.004\ m$ $L_{HT} = 0.41\ m$	$htc_w[2] = f(\dot{m}_w[2], \bar{T}_w[2],$ $\bar{P}_w, D_{ann,in}, D_{ann,out}\ L_{HT})$ Calculated w/ Rohsenow *et al.* (1998)	$htc_w[2]$ $= 2240\ W\ m^{-2}K^{-1}$
$htc_w[2]$ $= 2240\ W\ m^{-2}K^{-1}$ $D_{ann,out} = 0.004\ m$ $L_{HT} = 0.41\ m$	$R_{water}[2] = \frac{1}{htc_w[2]\pi D_{ann,out} L_{ch}}$	$R_w[2] = 0.088\ K\ W^{-1}$
$D_{ann,out} = 0.004\ m$ $D_{wall,out} = 0.006\ m$ $L_{HT} = 0.41\ m$ $k_{wall} = 14.94\ W\ m^{-1}K^{-1}$	$R_{wall} = \frac{\ln\left(\frac{D_{wall,out}}{D_{ann,out}}\right)}{2\pi L_{HT} k_{wall}}$	$R_{wall} = 0.011\ K\ W^{-1}$
$th_{ins} = 0.025\ m$ $k_{ins} = 0.043\ W\ m^{-1}K^{-1}$ $Pitch_{ch} = 0.015\ m$ $L_{HT} = 0.41\ m$	$R_{ins} = \frac{th_{ins}}{k_{ins}(2Pitch_{ch}L_{HT})}$	$R_{ins} = 48.02\ K\ W^{-1}$
$\bar{T}_{ins,out} = 19.93℃$ $T_{amb} = 22.79℃$ $P_{amb} = 101.3\ kPa$ $L_{HT} = 0.41\ m$	$htc_{NC}[2] = f(\bar{T}_{ins,out}, T_{amb}, P_{amb}, L_{HT})$ Calculated w/ Raithby and Hollands (1998)	$htc_{NC}[2]$ $= 2.20\ W\ m^{-2}K^{-1}$
$htc_{NC}[2]$ $= 2.75\ W\ m^{-2}K^{-1}$ $Pitch_{ch} = 0.015\ m$ $L_{HT} = 0.41\ m$	$R_{NC}[2] = \frac{1}{htc_{NC}[2]2Pitch_{ch}L_{HT}}$	$R_{NC}[2] = 36.94\ K\ W^{-1}$
$\bar{T}_{ins,out} = 293.1\ K$ $T_{amb} = 295.9\ K$ $Pitch_{ch} = 0.015\ m$ $L_{HT} = 0.41\ m$ $\epsilon = 0.8$ (assumed)	$\bar{T}_{rad,out} = \frac{\bar{T}_{ins,out} + T_{amb}}{2}$ $R_{rad}[2] = \frac{1}{(2Pitch_{ch}L_{HT})\sigma\epsilon 4\bar{T}_{rad,out}^{\ 3}}$	$R_{rad}[2] = 17.54\ K\ W^{-1}$
$R_w[2] = 0.088\ K\ W^{-1}$ $R_{wall} = 0.011\ K\ W^{-1}$ $R_{ins} = 48.02\ K\ W^{-1}$ $R_{NC}[2] = 36.94\ K\ W^{-1}$ $R_{rad}[2] = 17.54\ K\ W^{-1}$	$R_{tot,amb}[2] = R_w[2] + R_{wall} + R_{ins}$ $+\left(\frac{1}{R_{NC}[2]} + \frac{1}{R_{rad}[2]}\right)^{-1}$	$R_{tot,amb}[2]$ $= 60.02\ K\ W^{-1}$

Table B.4: Ambient gains from environment– sample calculation (cont'd)

Inputs	Equations	Results
$T_{w,in}[2] = 6.04℃$ $T_{w,out}[2] = 10.43℃$ $T_{amb} = 295.9\ K$	$LMTD_{amb}[2] = \frac{(T_{amb} - T_{w,in}[2]) - (T_{amb} - T_{w,out}[2])}{\ln\left(\frac{T_{amb} - T_{w,in}[2]}{T_{amb} - T_{w,out}[2]}\right)}$	$LMTD_{amb}[2] = 14.45℃$
$LMTD_{amb}[2] = 14.45℃$ $R_{tot,amb}[2] = 60.02\ K\ W^{-1}$	$\dot{Q}_{amb}[2] = \frac{LMTD_{amb}[2]}{R_{tot,amb}[2]}$	$\boxed{\dot{Q}_{amb}[2] = 0.241\ W}$
$T_{amb} = 295.9\ K$ $\dot{Q}_{amb}[2] = 0.241\ W$ $R_{NC}[2] = 36.94\ K\ W^{-1}$ $R_{rad}[2] = 17.54\ K\ W^{-1}$	$\bar{T}_{ins,out}[2] = T_{amb} - \dot{Q}_{amb}[2]\left(\frac{1}{R_{NC}[2]} + \frac{1}{R_{rad}[2]}\right)^{-1}$	$\bar{T}_{ins,out}[2] = 19.93℃$

B.4 Channel Inlet Conditions

Flow distribution in a heat exchanger is fully defined by the mass fluxes and the inlet qualities (or the inlet liquid and vapor flow rates) into each channel. This section outlines the approach used to calculate these values (Table B.5). All measured variables are shown in blue and all values either calculated or specified by the manufacturer are shown in black. Some variables are also shown with multiple unit systems. Any variable that is presented in non-SI units is shown in green. More information about these calculations is provided in Section 4.3.2.

Table B.5: Phase flow rates into heat exchanger channels – sample calculation

Inputs	Equations	Results
$\bar{T}_{TOF}[2] = 10.24℃$ $P_{ref,out} = 770.4\ kPa$	$\rho_{ref,TOF}[2] = f(\bar{T}_{TOF}[2], P_{ref,out})$	$\rho_{ref,TOF}[2] = 1262\ kg\ m^{-3}$
$D_{TOF} = 0.0038\ m$	$A_{TOF} = \pi\left(\frac{D_{TOF}}{2}\right)^2$	$A_{TOF} = 1.14 \times 10^{-5}\ m^2$
$\bar{u}_{ref}[2] = 13.16\ mm\ s^{-1}$	$\dot{m}_{ref}[2] = \rho_{ref,TOF}[2]\bar{u}_{ref}[2]A_{TOF}$ $G_{ref}[2] = \rho_{ref,TOF}[2]\bar{u}_{ref}[2]$	$\dot{m}_{ref}[2] = 1.89 \times 10^{-4}\ kg\ s^{-1}$ $\dot{m}_{ref}[2] = 11.36\ g\ min^{-1}$ $\boxed{G_{ref}[2] = 241\ kg\ m^{-2}s^{-1}}$

Table B.5: Phase flow rates into heat exchanger channels – sample calculation (cont'd)

Inputs	Equations	Results
$T_{ref,out}[2] = 9.76℃$ $P_{ref,out} = 770.4\ kPa$	$h_{ref,out}[2] = f(T_{ref,out}[2], P_{ref,out})$	$h_{ref,out} = 65170\ J\ kg^{-1}$
$T_{w,in}[2] = 6.04℃$ $T_{w,out}[2] = 10.43℃$ $P_{w,in} = 195.4\ kPa$ $P_{w,out} = 172\ kPa$	$h_{w,in}[2] = f(T_{w,in}[2], P_{w,in})$ $h_{w,out}[2] = f(T_{w,out}[2], P_{w,out})$	$h_{w,in}[2] = 25560\ J\ kg^{-1}$ $h_{w,out}[2] = 43940\ J\ kg^{-1}$
$\dot{m}_w[2] = 4.85 \times 10^{-4}\ kg\ s^{-1}$ $h_{w,in}[2] = 25560\ J\ kg^{-1}$ $h_{w,out}[2] = 43940\ J\ kg^{-1}$	$\dot{Q}_w[2] = \dot{m}_w[2](h_{w,out}[2] - h_{w,in}[2])$	$\dot{Q}_w[2] = 8.92\ W$
$\dot{m}_{ref}[2] = 1.89 \times 10^{-4}\ kg\ s^{-1}$ $h_{ref,out} = 65170\ J\ kg^{-1}$ $\dot{Q}_w[2] = 8.92\ W$ $\dot{Q}_{amb}[2] = 0.241\ W$	$h_{ref,in}[2] = h_{ref,out}[2] + \frac{\dot{Q}_w[2] - \dot{Q}_{amb}[2]}{\dot{m}_{ref}[2]}$	$h_{ref,in}[2] = 110980\ J\ kg^{-1}$
$h_{ref,in}[2] = 110980\ J\ kg^{-1}$ $P_{ref,in} = 776\ kPa$	$x_{ref,in}[2] = f(P_{ref,in}, h_{ref,in}[2])$	$\boxed{x_{ref,in}[2] = 0.098}$
$\dot{m}_{ref}[2] = 1.89 \times 10^{-4}\ kg\ s^{-1}$ $x_{ref,in}[2] = 0.098$	$\dot{m}_{v,ref}[2] = x_{ref,in}[2]\dot{m}_{ref}[2]$	$\dot{m}_{v,ref}[2] = 1.87 \times 10^{-5}\ kg\ s^{-1}$ $\dot{m}_{v,ref}[2] = 1.12\ g\ min^{-1}$
$\dot{m}_{ref}[2] = 1.89 \times 10^{-4}\ kg\ s^{-1}$ $\dot{m}_{v,ref}[2] = 1.87 \times 10^{-5}\ kg\ s^{-1}$	$\dot{m}_{l,ref}[2] = \dot{m}_{ref}[2] - \dot{m}_{v,ref}[2]$	$\dot{m}_{l,ref}[2] = 1.71 \times 10^{-4}\ kg\ s^{-1}$ $\dot{m}_{l,ref}[2] = 10.2\ g\ min^{-1}$
$\dot{m}_{ref}[1..N_{ch}]$ $\dot{m}_{v,ref}[1..N_{ch}]$ $\dot{m}_{l,ref}[1..N_{ch}]$	$\dot{m}_{ref,tot} = \sum_{i=1}^{N_{ch}} \dot{m}_{ref}[i]$ $\dot{m}_{l,ref,tot} = \sum_{i=1}^{N_{ch}} \dot{m}_{ref}[i]$ $\dot{m}_{v,ref,tot} = \sum_{i=1}^{N_{ch}} \dot{m}_{ref}[i]$	$\dot{m}_{ref,tot} = 9.86 \times 10^{-4}\ kg\ s^{-1}$ $\dot{m}_{ref,tot} = 59.1\ g\ min^{-1}$ $\dot{m}_{v,ref,tot} = 4.26 \times 10^{-4}\ kg\ s^{-1}$ $\dot{m}_{v,ref,tot} = 25.6\ g\ min^{-1}$ $\dot{m}_{l,ref,tot} = 5.59 \times 10^{-4}\ kg\ s^{-1}$ $\dot{m}_{l.ref,tot} = 33.6\ g\ min^{-1}$
$\dot{m}_{v,ref}[2] = 1.12\ g\ min^{-1}$ $\dot{m}_{l,ref}[2] = 10.2\ g\ min^{-1}$ $\dot{m}_{v,ref,tot} = 25.6\ g\ min^{-1}$ $\dot{m}_{l.ref,tot} = 33.6\ g\ min^{-1}$	$\dot{m}^*_{v,ref}[2] = \frac{\dot{m}_{v,ref}[2]}{\dot{m}_{v,ref,tot}}$ $\dot{m}^*_{l,ref}[2] = \frac{\dot{m}_{l,ref}[2]}{\dot{m}_{l,ref,tot}}$	$\boxed{\dot{m}^*_{v,ref}[2] = 0.438}$ $\boxed{\dot{m}^*_{l,ref}[2] = 3.053}$

B.5 Degree of Maldistribution

The normalized standard deviation (*NSTD*) was used to quantify the overall degree of maldistribution for a given inlet condition. This parameter is the ratio of the standard deviation of the channel flow rates to the maximum possible standard deviation. The definition of this variable bounds the degree of maldistribution between 1 (worst possible distribution) and 0 (perfect distribution). The method used to calculate the *NSTD* for the liquid phase, vapor phase, and total flow is shown in Table B.6. More information about the calculation is included in Section 4.3.3.

Table B.6: Degree of maldistribution (*NSTD*) – sample calculation

Inputs	Equations	Results
$\dot{m}^*_{v,ref}[1..N_{ch}]$	$NSTD_v = \sqrt{\frac{\sum_{i=1}^{N_{ch}}\left(\dot{m}^*_{v,ref}[i]-1\right)^2}{(N_{ch}-1)N_{ch}}}$	$NSTD_v = 0.110$
$\dot{m}^*_{l,ref}[1..N_{ch}]$	$NSTD_l = \sqrt{\frac{\sum_{i=1}^{N_{ch}}\left(\dot{m}^*_{l,ref}[i]-1\right)^2}{(N_{ch}-1)N_{ch}}}$	$NSTD_l = 0.516$
$\dot{m}^*_{ref}[1..N_{ch}]$	$NSTD_{tot} = \sqrt{\frac{\sum_{i=1}^{N_{ch}}\left(\dot{m}^*_{ref}[i]-1\right)^2}{(N_{ch}-1)N_{ch}}}$	$NSTD_{tot} = 0.248$

APPENDIX C. REFRIGERANT FACILITY VALIDATION

C.1 Mass Balance

In this study, a time of flight sensor was developed to measure the average refrigerant velocity in each heat exchanger channel. These sensors were calibrated with refrigerants at conditions similar to those seen in the distribution experiments. The measured flow rates were further verified by comparing the total mass flow rate entering the test section (measured with a Coriolis flow meter) with the sum of the time of flight measurements. The results are shown in Figure C.1. The mass flow rates through the inlet port and the channels balance to within ±5% except for the lowest inlet flow rates. Some of the measured channel flow rates at very low inlet mass fluxes were outside the TOF calibration range, which is likely contributing to these errors.

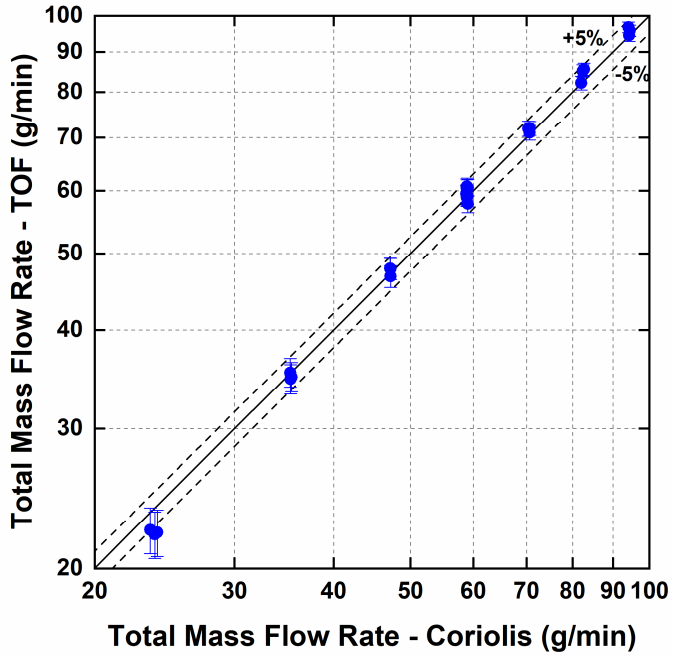

Figure C.1: Mass balance between the header inlet and channels in the rectangular header distribution experiments

C.2 Flow Instabilities

Flow instabilities can occur in multi-channel heat exchangers, which can result in temporally changing flow distribution characteristics (Ruspini *et al.*, 2014). Flow oscillations between different flow paths can degrade system control and performance and lead to thermal oscillations in the component. O'Neill *et al.* (2018) found that oscillations can occur in condensing flows with a range of qualities and mass fluxes that were similar to those investigated in the present maldistribution experiments. Therefore, the data were examined to determine the occurrence of flow oscillations occur and their effect on header flow regimes and distribution.

Flow instabilities can be directly measured by monitoring variations in the channel flow rates; however, time of flight sensors have a low sampling rate and are not well suited for unsteady flows. The liquid and vapor flow rates through each channel describe two-phase flow distribution, but also set the pressure drop across the component. If the flow rates through different channels are oscillating, the total or header pressure drops should also vary with time. The differential pressure transducers connected to the facility have high sampling rates (1000 samples/second) and can be used to identify conditions that result in unstable flows. The pressure drop was monitored over a 30 second period for all the conditions tested and inspected for evidence of flow instabilities. An example of the collected pressure drop data is shown in Figure C.2 (G_{in} = 59.8 kg m^{-2} s^{-1} and x_{in} = 0.30). Most of the heat exchanger pressure drop data are within ±15 Pa of the average value (<1% deviation from the average), while most of the header pressure drop data are within ±3 Pa of the average value (<2.5% deviation from the average). Although there are some oscillations in these measurements, the amplitude of the oscillations is on the same order

of magnitude as the transducer uncertainty. The very low amplitude of the oscillation behavior suggests that significant flow instabilities are not present in the heat exchanger for these inlet conditions.

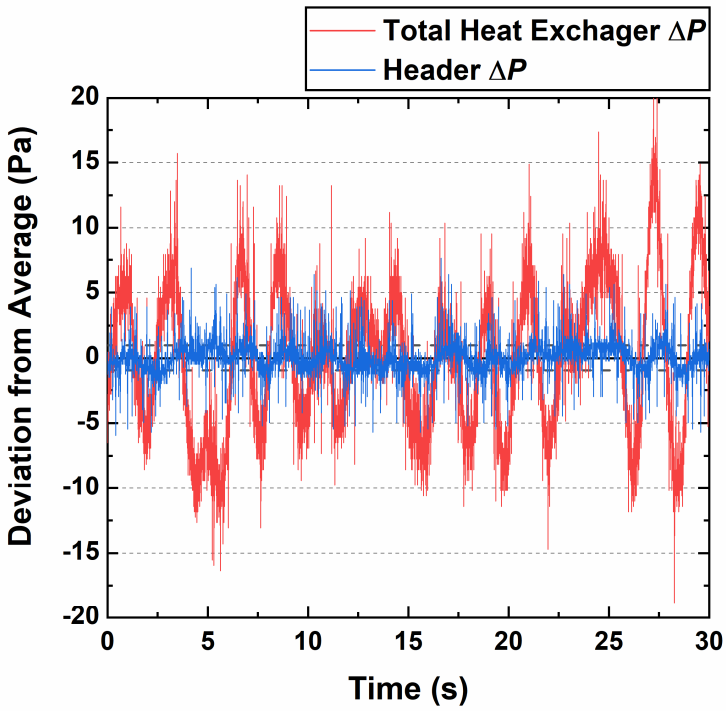

Figure C.2: Deviations in the pressure drop measurements over time (G_{in} = 59.8, x_{in} = 0.30)

The standard deviations of the heat exchanger pressure drop measurements over time are shown as a function of the inlet quality in Figure C.3. The standard deviations of the pressure drop measurements are less than 9 Pa across the entire quality range, again suggesting that significant flow instabilities are not present in these experiments. There is no attempt in the present work to characterize or model potential flow instabilities in the condenser because no evidence of instabilities that would have a large impact of flow distribution were observed.

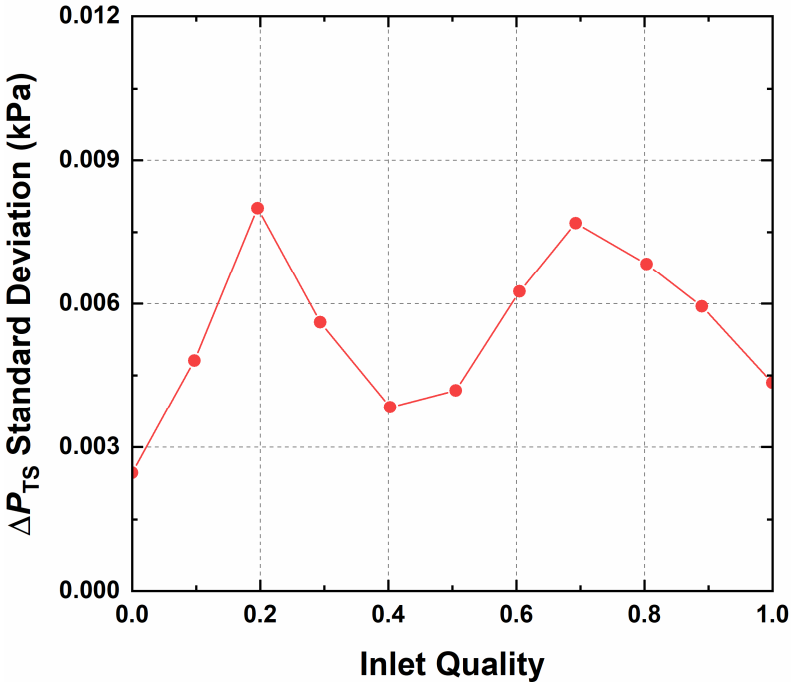

Figure C.3: Standard deviation of the test section pressure drop measurement over 30 seconds

REFERENCES

Ablanque, N., C. Oliet, J. Rigola, C. D. Pérez-Segarra and A. Oliva (2010), "Two-Phase Flow Distribution in Multiple Parallel Tubes," *International Journal of Thermal Sciences* Vol. 49(6) pp. 909-921 DOI: 10.1016/j.ijthermalsci.2009.11.005.

Ahmad, M., G. Berthoud and P. Mercier (2009), "General Characteristics of Two-Phase Flow Distribution in a Compact Heat Exchanger," *International Journal of Heat and Mass Transfer* Vol. 52(1–2) pp. 442-450 DOI: 10.1016/j.ijheatmasstransfer.2008.05.030.

Ajdari, A., N. Bontoux and H. A. Stone (2006), "Hydrodynamic Dispersion in Shallow Microchannels: The Effect of Cross-Sectional Shape," *Analytical Chemistry* Vol. 78(2) pp. 387-392 DOI: 10.1021/ac0508651.

Anbumeenakshi, C. and M. R. Thansekhar (2016), "Experimental Investigation of Header Shape and Inlet Configuration on Flow Maldistribution in Microchannel," *Experimental Thermal and Fluid Science* Vol. 75 pp. 156-161 DOI: 10.1016/j.expthermflusci.2016.02.004.

Andresen, U. C., S. Garimella, B. Mitra, Y. Jiang and B. M. Fronk (2015), "Pressure Drop During near-Critical-Pressure Condensation of Refrigerant Blends," *International Journal of Refrigeration* Vol. 59 pp. 1-13 DOI: 10.1016/j.ijrefrig.2015.07.016.

Aris, R. (1956), "On the Dispersion of a Solute in a Fluid Flowing through a Tube," *Proceedings of the Royal Society of London A: Mathematical, Physical and Engineering sciences*, The Royal Society, pp. 67-77.

Ashauer, M., H. Glosch, F. Hedrich, N. Hey, H. Sandmaier and W. Lang (1999), "Thermal Flow Sensor for Liquids and Gases Based on Combinations of Two Principles," *Sensors and Actuators A: Physical* Vol. 73(1-2) pp. 7-13 DOI: 10.1016/s0924-4247(98)00248-9.

Aslam Bhutta, M. M., N. Hayat, M. H. Bashir, A. R. Khan, K. N. Ahmad and S. Khan (2012), "Cfd Applications in Various Heat Exchangers Design: A Review," *Applied Thermal Engineering* Vol. 32 pp. 1-12 DOI: 10.1016/j.applthermaleng.2011.09.001.

Baroczy, C. J. (1965a), "Correlation of Liquid Fraction in Two-Phase Flow with Application to Liquid Metals," *Chemical Engineering Progress Symposium Series* Vol. 61 pp. 179-191

Baroczy, C. J. (1965b). *Correlation of Liquid Fraction in Two-Phase Flow with Application to Liquid Metals*. Chemical Engineering Progress Symposium Series, Vol. 61 pp. 179-191.

Bassiouny, M. K. and H. Martin (1984), "Flow Distribution and Pressure Drop in Plate Heat Exchangers - I U-Type Arrangement," *Chemical Engineering Science* Vol. 39(4) pp. 693-700 DOI: 10.1016/0009-2509(84)80176-1.

Berthet, H., J. Jundt, J. Durivault, B. Mercier and D. Angelescu (2011), "Time-of-Flight Thermal Flowrate Sensor for Lab-on-Chip Applications," *Lab on a Chip* Vol. 11(2) pp. 215-223 DOI: 10.1039/C0LC00229A.

Bowers, C. D., P. Hrnjak and T. Newell (2006). *Two-Phase Refrigerant Distribution in a Micro-Channel Manifold*. International Refrigeration and Air Conditioning Conference. West Layfayette, USA, Purdue University Libraries, Vol. 743.

Byon, C. (2015), "Numerical and Analytic Study on the Time-of-Flight Thermal Flow Sensor," *International Journal of Heat and Mass Transfer* Vol. 89 pp. 454-459 DOI: 10.1016/j.ijheatmasstransfer.2015.05.011.

Byun, H.-W. and N.-H. Kim (2015), "Two-Phase Refrigerant Distribution in an Intermediate Header of a Parallel Flow Minichannel Heat Exchanger," *International Journal of Refrigeration* Vol. 59 pp. 14-28 DOI: 10.1016/j.ijrefrig.2015.06.023.

Chen, J. S., Y. H. Liu, C. P. Liang, C. W. Liu and C. W. Lin (2011), "Exact Analytical Solutions for Two-Dimensional Advection-Dispersion Equation in Cylindrical Coordinates Subject to Third-Type Inlet Boundary Condition," *Advances in Water Resources* Vol. 34(3) pp. 365-374 DOI: 10.1016/j.advwatres.2010.12.008.

Cho, H., K. Cho and Y.-S. Kim (2003). *Mass Flowrate Distribution and Phase Separation of R-22 in Multi-Microchannel Tubes under Adiabatic Condition*. International Conference on Microchannels and Minichannels. Rochester, NY, The American Society of Mechanical Engineers, Vol. ICMM2003 pp. 527-533.

Churchill, S. W. (1977a), "Comprehensive Correlating Equations for Heat, Mass and Momentum Transfer in Fully Developed Flow in Smooth Tubes," *Industrial & Engineering Chemistry Fundamentals* Vol. 16(1) pp. 109-116

Churchill, S. W. (1977b), "Friction-Factor Equation Spans All Fluid-Flow Regimes," *Chemical Engineering* Vol. 84(24) pp. 91-92

Dario, E. R., L. Tadrist, J. L. G. Oliveira and J. C. Passos (2015), "Measuring Maldistribution of Two-Phase Flows in Multi-Parallel Microchannels," *Applied Thermal Engineering* Vol. 91 pp. 924-937 DOI: 10.1016/j.applthermaleng.2015.08.103.

Dharaiya, V. V., A. Radhakrishnan and S. G. Kandlikar (2009). *Evaluation of a Tapered Header Configuration to Reduce Flow Maldistribution in Minichannels and Microchannels*. International Conference of Nanochannels, Microchannels, and Minichannels. Pohang, South Korea, ASME pp. 771-777.

Eaton, J. K., R. V. Westphal and J. P. Johnston (1981), "Two New Instruments for Flow Direction and Skin-Friction Measurements in Separated Flows," *ISA Transactions* Vol. 21 pp. 69-78

Fei, P. and P. S. Hrnjak (2004). Adiabatic Developing Two-Phase Refrigerant Flow in Manifolds of Heat Exchangers. University of Illinois at Urbana-Champaign, ACRC Technical Report TR225p.

Forinash, D. (2015). *Novel Air-Coupled Heat Exchangers for Waste Heat-Driven Absoprtion Heat Pumps*. Mechanical Engineering, Georgia Insitute of Technology, Vol. Master of Science in Mechanical Engineering.

Friedel, L. (1979), "Improved Friction Pressure Drop Correlations for Horizontal and Vertical Two Phase Pipe Flow (Paper E2)," *European Two Phase Flow Group Meeting*, Ispra, Italy

Garimella, S., A. Agarwal and J. D. Killion (2005), "Condensation Pressure Drop in Circular Microchannels," *Heat Transfer Engineering* Vol. 26(3) pp. 28-35 DOI: 10.1080/01457630590907176.

Ghiaasiaan, S. M. (2017). *Two-Phase Flow, Boiling, and Condensation in Conventional and Miniature Systems*. 2nd Ed. Cambridge, UK, Cambridge University Press.

Guerrero, J. S. P., L. C. G. Pimentel, T. H. Skaggs and M. T. van Genuchten (2009), "Analytical Solution of the Advection-Diffusion Transport Equation Using a Change-of-Variable and Integral Transform Technique," *International Journal of Heat and Mass Transfer* Vol. 52(13-14) pp. 3297-3304 DOI: 10.1016/j.ijheatmasstransfer.2009.02.002.

Habib, M. A., R. Ben-Mansour, S. A. M. Said, J. J. Al-Bagawi and K. M. Al-Mansour (2008), "Correlations of Flow Maldistribution Parameters in an Air Cooled Heat Exchanger," *International Journal for Numerical Methods in Fluids* Vol. 56(2) pp. 143-165 DOI: 10.1002/fld.1518.

Hahn, D. W. and M. N. Ozisik (2012). *Heat Conduction*, John Wiley & Sons.

Handford, P. M. and P. Bradshaw (1989), "The Pulsed-Wire Anemometer," *Experiments in Fluids* Vol. 7(2) pp. 125-132 DOI: 10.1007/bf00207305.

Hewitt, G. F., G. L. Shires and T. R. Bott (1994). *Process Heat Transfer*. New York, NY, USA, CRC Press.

Hwang, S. T., H. M. Soliman and R. T. Lahey (1988), "Phase Separation in Dividing Two-Phase Flows," *International Journal of Multiphase Flow* Vol. 14(4) pp. 439-458 DOI: http://dx.doi.org/10.1016/0301-9322(88)90021-3.

Hwang, Y., D.-H. Jin and R. Radermacher (2007), "Refrigerant Distribution in Minichannel Evaporator Manifolds," *HVAC&R Research* Vol. 13(4) pp. 543-555 DOI: 10.1080/10789669.2007.10390971.

Jiang, H., F. Liu, I. Turner and K. Burrage (2012), "Analytical Solutions for the Multi-Term Time-Space Caputo-Riesz Fractional Advection-Diffusion Equations on a Finite Domain," *Journal of Mathematical Analysis and Applications* Vol. 389(2) pp. 1117-1127 DOI: 10.1016/j.jmaa.2011.12.055.

Jones, B. J., P.-S. Lee and S. V. Garimella (2008), "Infrared Micro-Particle Image Velocimetry Measurements and Predictions of Flow Distribution in a Microchannel Heat Sink," *International Journal of Heat and Mass Transfer* Vol. 51(7) pp. 1877-1887 DOI: 10.1016/j.ijheatmasstransfer.2007.06.034.

Kærn, M. R., W. Brix, B. Elmegaard and L. F. S. Larsen (2011), "Performance of Residential Air-Conditioning Systems with Flow Maldistribution in Fin-and-Tube Evaporators," *International Journal of Refrigeration* Vol. 34(3) pp. 696-706 DOI: 10.1016/j.ijrefrig.2010.12.010.

Kakaç, S. and Y. Yener (1973), "Exact Solution of the Transient Forced Convection Energy Equation for Timewise Variation of Inlet Temperature," *International Journal of Heat and Mass Transfer* Vol. 16(12) pp. 2205-2214 DOI: 10.1016/0017-9310(73)90007-0.

Kattan, N., J. R. Thome and D. Favrat (1998), "Flow Boiling in Horizontal Tubes: Part 1—Development of a Diabatic Two-Phase Flow Pattern Map," *Journal of Heat Transfer* Vol. 120(1) pp. 140-147 DOI: 10.1115/1.2830037.

Keinath, B. L. and S. Garimella (2018), "High-Pressure Condensing Refrigerant Flows through Microchannels, Part II: Heat Transfer Models," *Heat Transfer Engineering* pp. 1-14 DOI: 10.1080/01457632.2018.1443258.

Kim, D. K., A. Majumdar and S. J. Kim (2007), "Electrokinetic Flow Meter," *Sensors and Actuators A: Physical* Vol. 136(1) pp. 80-89 DOI: 10.1016/j.sna.2006.10.022.

Kim, N.-H. and S.-P. Han (2008), "Distribution of Air–Water Annular Flow in a Header of a Parallel Flow Heat Exchanger," *International Journal of Heat and Mass Transfer* Vol. 51(5) pp. 977-992 DOI: 10.1016/j.ijheatmasstransfer.2007.05.028.

Kim, N.-H., D.-Y. Kim and H.-W. Byun (2011), "Effect of Inlet Configuration on the Refrigerant Distribution in a Parallel Flow Minichannel Heat Exchanger," *International Journal of Refrigeration* Vol. 34(5) pp. 1209-1221 DOI: 10.1016/j.ijrefrig.2010.05.018.

Kim, N.-H., E.-J. Lee and H.-W. Byun (2012), "Two-Phase Refrigerant Distribution in a Parallel Flow Minichannel Heat Exchanger Having Horizontal Headers," *International Journal of Heat and Mass Transfer* Vol. 55(25) pp. 7747-7759 DOI: 10.1016/j.ijheatmasstransfer.2012.07.082.

Kim, N.-H., E.-J. Lee and H.-W. Byun (2013), "Improvement of Two-Phase Refrigerant Distribution in a Parallel Flow Minichannel Heat Exchanger Using Insertion Devices," *Applied Thermal Engineering* Vol. 59(1) pp. 116-130 DOI: 10.1016/j.applthermaleng.2013.05.026.

Kim, N.-H. and T.-R. Sin (2006), "Two-Phase Flow Distribution of Air–Water Annular Flow in a Parallel Flow Heat Exchanger," *International Journal of Multiphase Flow* Vol. 32(12) pp. 1340-1353 DOI: 10.1016/j.ijmultiphaseflow.2006.07.005.

Kim, S.-M. and I. Mudawar (2012), "Universal Approach to Predicting Two-Phase Frictional Pressure Drop for Adiabatic and Condensing Mini/Micro-Channel Flows," *International Journal of Heat and Mass Transfer* Vol. 55(11) pp. 3246-3261 DOI: 10.1016/j.ijheatmasstransfer.2012.02.047.

Kim, S.-M. and I. Mudawar (2013), "Universal Approach to Predicting Heat Transfer Coefficient for Condensing Mini/Micro-Channel Flow," *International Journal of Heat and Mass Transfer* Vol. 56(1) pp. 238-250 DOI: 10.1016/j.ijheatmasstransfer.2012.09.032.

Klein, S. (2018). *Engineering Equatino Solver*, F-Chart Software, Vol. V10.294-3D.

Kumar, A., D. K. Jaiswal and N. Kumar (2010), "Analytical Solutions to One-Dimensional Advection-Diffusion Equation with Variable Coefficients in Semi-Infinite Media," *Journal of Hydrology* Vol. 380(3-4) pp. 330-337 DOI: 10.1016/j.jhydrol.2009.11.008.

Kuo, J. T. W., L. Yu and E. Meng (2012), "Micromachined Thermal Flow Sensors-a Review," *Micromachines* Vol. 3(3) pp. 550-573 DOI: 10.3390/mi3030550.

Lahey, R. T. (1990), "The Analysis of Phase Separation and Phase Distribution Phenomena Using Two-Fluid Models," *Nuclear Engineering and Design* Vol. 122(1) pp. 17-40 DOI: https://doi.org/10.1016/0029-5493(90)90194-3.

Lammerink, T. S. J., N. R. Tas, M. Elwenspoek and J. H. J. Fluitman (1993), "Micro-Liquid Flow Sensor," *Sensors and Actuators A: Physical* Vol. 37-8 pp. 45-50 DOI: 10.1016/0924-4247(93)80010-E.

Lee, J. K. (2009), "Two-Phase Flow Behavior inside a Header Connected to Multiple Parallel Channels," *Experimental Thermal and Fluid Science* Vol. 33(2) pp. 195-202 DOI: 10.1016/j.expthermflusci.2008.03.009.

Lee, J. K. and S. Y. Lee (2004), "Distribution of Two-Phase Annular Flow at Header–Channel Junctions," *Experimental Thermal and Fluid Science* Vol. 28(2) pp. 217-222 DOI: 10.1016/S0894-1777(03)00042-6.

Li, G., S. Frankel, J. E. Braun and E. A. Groll (2005), "Application of Cfd Models to Two-Phase Flow in Refrigerant Distributors," *HVAC&R Research* Vol. 11(1) pp. 45-62 DOI: 10.1080/10789669.2005.10391125.

Li, W. and Z. Wu (2010), "A General Correlation for Adiabatic Two-Phase Pressure Drop in Micro/Mini-Channels," *International Journal of Heat and Mass Transfer* Vol. 53(13) pp. 2732-2739 DOI: 10.1016/j.ijheatmasstransfer.2010.02.029.

Liu, F., P. Zhuang, V. Anh, I. Turner and K. Burrage (2007), "Stability and Convergence of the Difference Methods for the Space-Time Fractional Advection-Diffusion Equation," *Applied Mathematics and Computation* Vol. 191(1) pp. 12-20 DOI: 10.1016/j.amc.2006.08.162.

Liu, Y., W. Sun, W. Wu and S. Wang (2017), "Gas-Liquid Two-Phase Flow Distribution in Parallel Micro-Channels with Different Header and Channels' Orientations," *International Journal of Heat and Mass Transfer* Vol. 112 pp. 767-778 DOI: 10.1016/j.ijheatmasstransfer.2017.05.029.

Lomas, C. G. (1986). *Fundamentals of Hot Wire Anemometry*. New York, NY, Cambridge University Press.

Luan, H. B., J. P. Kuang, Z. Cao, Z. Wu, W. Q. Tao and B. Sundén (2017), "Cfd Analysis of Two Types of Welded Plate Heat Exchangers," *Numerical Heat Transfer, Part A: Applications* Vol. 71(3) pp. 250-269 DOI: 10.1080/10407782.2016.1264761.

Mahvi, A. J. and S. Garimella (2017), "Visualization of Flow Distribution in Rectangular and Triangular Header Geometries," *International Journal of Refrigeration* Vol. 76 pp. 170-183 DOI: 10.1016/j.ijrefrig.2017.02.002.

Manikanda Kumaran, R., G. Kumaraguruparan and T. Sornakumar (2013), "Experimental and Numerical Studies of Header Design and Inlet/Outlet Configurations on Flow Mal-Distribution in Parallel Micro-Channels," *Applied Thermal Engineering* Vol. 58(1–2) pp. 205-216 DOI: 10.1016/j.applthermaleng.2013.04.026.

Marchitto, A., F. Devia, M. Fossa, G. Guglielmini and C. Schenone (2008), "Experiments on Two-Phase Flow Distribution inside Parallel Channels of Compact Heat Exchangers," *International Journal of Multiphase Flow* Vol. 34(2) pp. 128-144 DOI: 10.1016/j.ijmultiphaseflow.2007.08.005.

Marchitto, A., M. Fossa and G. Guglielmini (2012), "The Effect of the Flow Direction inside the Header on Two-Phase Flow Distribution in Parallel Vertical Channels," *Applied Thermal Engineering* Vol. 36 pp. 245-251 DOI: 10.1016/j.applthermaleng.2011.10.008.

Marshall, D. C. (1958), "Measurement of Sap Flow in Conifers by Heat Transport," *Plant Physiology* Vol. 33(6) pp. 385-396 DOI: 10.1104/pp.33.6.385.

Miller, T. E. and H. Small (1982), "Thermal Pulse Time-of-Flight Liquid Flow Meter," *Analytical Chemistry* Vol. 54(6) pp. 907-910 DOI: 10.1021/ac00243a016.

Mishima, K. and T. Hibiki (1996), "Some Characteristics of Air-Water Two-Phase Flow in Small Diameter Vertical Tubes," *International Journal of Multiphase Flow* Vol. 22(4) pp. 703-712 DOI: 10.1016/0301-9322(96)00010-9.

Mojtabi, A. and M. O. Deville (2015), "One-Dimensional Linear Advection-Diffusion Equation: Analytical and Finite Element Solutions," *Computers & Fluids* Vol. 107 pp. 189-195 DOI: 10.1016/j.compfluid.2014.11.006.

Moser, K. W., R. L. Webb and B. Na (1998), "A New Equivalent Reynolds Number Model for Condensation in Smooth Tubes," *Journal of Heat Transfer* Vol. 120(2) pp. 410-417 DOI: 10.1115/1.2824265.

Murphy, D. L. (2014). *Condensation Heat Transfer and Pressure Drop of Propane in Vertical Minichannels*. G.W.W. School of Mechanical Engineering, Georgia Institute of Technology, Vol. Master of Science in Mechanical Engineering.

Nellis, G. and S. Klein (2009). *Heat Transfer*. New York, NY, USA, Cambridge University Press.

Nielsen, K. K., K. Engelbrecht, D. V. Christensen, J. B. Jensen, A. Smith and C. R. H. Bahl (2012), "Degradation of the Performance of Microchannel Heat Exchangers Due to Flow Maldistribution," *Applied Thermal Engineering* Vol. 40 pp. 236-247 DOI: 10.1016/j.applthermaleng.2012.02.019.

O'Neill, L. E., I. Mudawar, M. M. Hasan, H. K. Nahra, R. Balasubramaniam and J. R. Mackey (2018), "Flow Condensation Pressure Oscillations at Different Orientations," *International Journal of Heat and Mass Transfer* Vol. 127 pp. 784-809 DOI: https://doi.org/10.1016/j.ijheatmasstransfer.2018.07.072.

Panghat, K. and S. Mehendale (2016). *A Critical Assessment of Two-Phase Flow Distribution in Microchannel Heat Exchangers*. 16th International Refrigeration and Air Conditioning Conference. West Lafayette, USA, Purdue University Libraries, Vol. 2089 pp. 1-10.

Pérez Guerrero, J. S., E. M. Pontedeiro, M. T. van Genuchten and T. H. Skaggs (2013), "Analytical Solutions of the One-Dimensional Advection–Dispersion Solute Transport Equation Subject to Time-Dependent Boundary Conditions," *Chemical Engineering Journal* Vol. 221 pp. 487-491 DOI: 10.1016/j.cej.2013.01.095.

Raithby, G. D. and K. G. T. Hollands (1998). *Natural Convection in the Handbook of Heat Transfer*. 3rd Ed. New York, NY, McGraw-Hill.

Rodrigues, R. J. and R. Furlan (2009), "Time-of-Flight Flow Microsensor Using Free-Standing Microfilaments," *Journal Integrated Circuits and Systems* Vol. 4(2) pp. 84-88

Rohsenow, W. M., J. P. Hartnett and Y. I. Cho (1998). *The Handbook of Heat Transfer*. 3rd Ed. New York, NY, McGraw-Hill.

Rong, X., M. Kawaji and J. G. Burgers (1995), "Two-Phase Header Flow Distribution in a Stacked Plate Heat Exchanger," *Gas Liquid Flows* Vol. 225 pp. 115-122

Ruspini, L. C., C. P. Marcel and A. Clausse (2014), "Two-Phase Flow Instabilities: A Review," *International Journal of Heat and Mass Transfer* Vol. 71 pp. 521-548 DOI: 10.1016/j.ijheatmasstransfer.2013.12.047.

Sabaté, N., J. Santander, L. Fonseca, I. Gràcia and C. Cané (2004), "Multi-Range Silicon Micromachined Flow Sensor," *Sensors and Actuators A: Physical* Vol. 110(1) pp. 282-288 DOI: 10.1016/j.sna.2003.10.068.

Said, S. A. M., R. Ben-Mansour, M. A. Habib and M. U. Siddiqui (2015), "Reducing the Flow Mal-Distribution in a Heat Exchanger," *Computers & Fluids* Vol. 107 pp. 1-10 DOI: 10.1016/j.compfluid.2014.09.012.

Shah, M. M. (1979), "A General Correlation for Heat Transfer During Film Condensation inside Pipes," *International Journal of Heat and Mass Transfer* Vol. 22(4) pp. 547-556 DOI: 10.1016/0017-9310(79)90058-9.

Shah, M. M. (2009), "An Improved and Extended General Correlation for Heat Transfer During Condensation in Plain Tubes," *HVAC&R Research* Vol. 15(5) pp. 889-913 DOI: 10.1080/10789669.2009.10390871.

Smith, S. M., B. S. Taft and J. Moulton (2014), "Contact Angle Measurements for Advanced Thermal Management Technologies," *Frontiers in Heat and Mass Transfer* Vol. 5(6) pp. 1-9 DOI: dx.doi.org/10.5098/hmt.5.6.

Smoglie, C. and J. Reimann (1986), "Two-Phase Flow through Small Branches in a Horizontal Pipe with Stratified Flow," *International Journal of Multiphase Flow* Vol. 12(4) pp. 609-625 DOI: 10.1016/0301-9322(86)90063-7.

Tae, S.-J. and K. Cho (2006), "Two-Phase Split of Refrigerants at a T-Junction," *International Journal of Refrigeration* Vol. 29(7) pp. 1128-1137 DOI: 10.1016/j.ijrefrig.2006.02.004.

Taitel, Y. and A. E. Dukler (1976), "A Model for Predicting Flow Regime Transitions in Horizontal and near Horizontal Gas-Liquid Flow," *AIChE Journal* Vol. 22(1) pp. 47-55 DOI: 10.1002/aic.690220105.

Tillner-Roth, R. and H. D. Baehr (1994), "An International Standard Formulation for the Thermodynamic Properties of 1,1,1,2-Tetrafluoroethane (Hfc-134a) for

Temperatures from 170 K to 455 K and Pressures up to 70 Mpa," *Journal of Physical and Chemical Reference Data* Vol. 23(5) pp. 657-729 DOI: 10.1063/1.555958.

Tong, J. C. K., E. M. Sparrow and J. P. Abraham (2009), "Geometric Strategies for Attainment of Identical Outflows through All of the Exit Ports of a Distribution Manifold in a Manifold System," *Applied Thermal Engineering* Vol. 29(17) pp. 3552-3560 DOI: 10.1016/j.applthermaleng.2009.06.010.

Tuo, H. and P. Hrnjak (2013), "Effect of the Header Pressure Drop Induced Flow Maldistribution on the Microchannel Evaporator Performance," *International Journal of Refrigeration* Vol. 36(8) pp. 2176-2186 DOI: 10.1016/j.ijrefrig.2013.06.002.

Vist, S. (2004). *Two-Phase Flow Distribution in Heat Exchanger Manifolds*. Energy and Process Engineering, Norwegian University of Science and Technology, Vol. PhD p. 306.

Vist, S. and J. Pettersen (2004), "Two-Phase Flow Distribution in Compact Heat Exchanger Manifolds," *Experimental Thermal and Fluid Science* Vol. 28(2–3) pp. 209-215 DOI: 10.1016/S0894-1777(03)00041-4.

Watanabe, M., M. Katsuta, K. Nagata and K. Sakuma (1995), "General Charactertistics of Two-Phase Flow Distribution in a Multipass Tube," *Heat Transfer - Japanese Research* Vol. 24(1) pp. 32-44

Webb, R. L. and K. Chung (2005), "Two-Phase Flow Distribution to Tubes of Parallel Flow Air-Cooled Heat Exchangers," *Heat Transfer Engineering* Vol. 26(4) pp. 003-018 DOI: 10.1080/01457630590916239.

Wijayanta, A. T., T. Miyazaki and S. Koyama (2017), "Refrigerant Distribution in Horizontal Headers with Downward Minichannel-Branching Conduits: Experiment, Empirical Correlation and Two-Phase Flow Pattern Map," *Experimental Thermal and Fluid Science* Vol. 81 pp. 430-444 DOI: 10.1016/j.expthermflusci.2016.09.011.

Yang, C., M. Kummel and H. Soeberg (1988), "A Transit-Time Flow Meter for Measuring Milliliter Per Minute Liquid Flow," *Review of Scientific Instruments* Vol. 59(2) pp. 314-317 DOI: 10.1063/1.1140247.

Yang, C. and H. Søeberg (1992), "Monolithic Flow Sensor for Measuring Millileter Per Minute Liquid Flow," *Sensors and Actuators A: Physical* Vol. 33(3) pp. 143-153 DOI: 10.1016/0924-4247(92)80160-5.

Yates, S. R. (1990), "An Analytical Solution for One-Dimensional Transport in Heterogeneous Porous Media," *Water Resources Research* Vol. 26(10) pp. 2331-2338 DOI: 10.1029/WR026i010p02331.

Yuan, P., G. B. Jiang, Y. L. He and W. Q. Tao (2016), "Performance Simulation of a Two-Phase Flow Distributor for Plate-Fin Heat Exchanger," *Applied Thermal Engineering* Vol. 99 pp. 1236-1245 DOI: 10.1016/j.applthermaleng.2016.01.096.

Zhang, L., H. T. Bi, D. P. Wilkinson, J. Stumper and H. Wang (2008), "Gas–Liquid Two-Phase Flow Patterns in Parallel Channels for Fuel Cells," *Journal of Power Sources* Vol. 183(2) pp. 643-650 DOI: 10.1016/j.jpowsour.2008.05.080.

Zhang, Z. and Y. Li (2003), "Cfd Simulation on Inlet Configuration of Plate-Fin Heat Exchangers," *Cryogenics* Vol. 43(12) pp. 673-678 DOI: 10.1016/S0011-2275(03)00179-6.

Zoppou, C. and J. H. Knight (1997), "Analytical Solutions for Advection and Advection-Diffusion Equations with Spatially Variable Coefficients," *Journal of Hydraulic Engineering* Vol. 123(2) pp. 144-148 DOI: 10.1061/(Asce)0733-9429(1997)123:2(144).

Zou, Y. and P. S. Hrnjak (2013), "Experiment and Visualization on R134a Upward Flow in the Vertical Header of Microchannel Heat Exchanger and Its Effect on Distribution," *International Journal of Heat and Mass Transfer* Vol. 62 pp. 124-134 DOI: 10.1016/j.ijheatmasstransfer.2013.02.068.

Zou, Y. and P. S. Hrnjak (2016). *Cfd Simulation of R134a and R410a Two-Phase Flow in the Vertical Header of Microchannel Heat Exchanger*. International Refrigeration and Air Conditioning Conference. West Lafayette, USA, Purdue University Libraries, Vol. 2367 pp. 1-10.